REPORT DOCUMENTATION PAGE

Form Approved
OMB No. 0704-0188

1. REPORT DATE (DD-MM-YYYY)	2. REPORT TYPE	3. DATES COVERED (From - To)
02/09/2009	Final	07/01/2008 – 05/31/2009

4. TITLE AND SUBTITLE
SPRING NanoEnergetics Hub at UT Dallas

5a. CONTRACT NUMBER

5b. GRANT NUMBER
FA9550-06-1-0403

5c. PROGRAM ELEMENT NUMBER

6. AUTHOR(S)

Dr. John P. Ferraris

5d. PROJECT NUMBER

5e. TASK NUMBER

5f. WORK UNIT NUMBER

7. PERFORMING ORGANIZATION NAME(S) AND ADDRESS(ES)

The University of Texas at
Dallas
800 W. Campbell Road, MP15
Richardson, TX 75080

8. PERFORMING ORGANIZATION REPORT NUMBER

9. SPONSORING / MONITORING AGENCY NAME(S) AND ADDRESS(ES)
AF Office of Scientific
Research
875 N. Randolph St., Room 3112
Arlington, VA 22203

10. SPONSOR/MONITOR'S ACRONYM(S)

USAF, AFRL

11. SPONSOR/MONITOR'S REPORT NUMBER(S)
FA9550-06-1-0403

12. DISTRIBUTION / AVAILABILITY STATEMENT

13. SUPPLEMENTARY NOTES

14. ABSTRACT

The research emphasis of the SPRING NanoEnergetics facility at The University of Texas at Dallas is the synthesis and processing of advanced nanostructured materials, the structure and property characterization needed for materials optimization, the fabrication of sophisticated structures, and device testing in the areas of energy harvesting, storage, transmission, and conversion. SPRING IV funds have thus far been used to support five $150K (for two years) seed grants.

15. SUBJECT TERMS

16. SECURITY CLASSIFICATION OF:			17. LIMITATION OF ABSTRACT	18. NUMBER OF PAGES	19a. NAME OF RESPONSIBLE PERSON Dr. John Ferraris
a. REPORT	b. ABSTRACT	c. THIS PAGE		122	19b. TELEPHONE NUMBER (include area code) 972-883-2905

Standard Form 298 (Rev. 8-98)
Prescribed by ANSI Std. Z39.18

Progress Report for the SPRING Project on *MECHANICAL ENERGY ON DEMAND FROM HIGH STRAIN ACTUATORS* (October 2006 - May 2008)

PRINCIPAL INVESTIGATOR: Ray H. Baughman
CO-PRINCIPAL INVESTIGATOR: Richard Vaia

I INTRODUCTION

Specific needs for the Department of Defense for *Energy on Demand*, include small volume, low weight, energy-efficient actuators that provide very large strokes and very high power densities. These are required for such diverse uses as deployable structures, morphing wings on aircraft, micro-air vehicles, exoskeletons for future soldiers, autonomous robots, and smart surfaces to increase the efficiency and performance of aircraft and marine vehicles. The program plan goal is to demonstrate both fundamentally new and dramatically improved mechanisms for actuation.

The greatest program success was in the demonstration of two mechanisms for achieving giant stroke actuation of nanotube sheets. These mechanisms require no electrolyte, and provide actuator strokes of up to 500% and response rates of up to 10^4%/s for temperatures from below 77 K to above 1900 K. A patent application will be filed on this broad technology and a manuscript is being prepared for publication in *Science*.

Work was conducted in another exciting proposed technology for giant stroke actuation, though success has not yet been achieved. This second technology, *non-thermal electrical shape memory actuation*, is revolutionary in concept and performance; electrochemical double-layer charge injection in a high-surface-area shape memory metal causes a shift in the martensitic phase transition – thereby providing about 5% strain at applied voltages of a few volts and over 100% strains at these applied voltages for shape memory wire springs. While ordinary shape memory actuators have giant power densities, far above other artificial muscles, they are thermal engines. Hence, their efficiency is limited by the Carnot efficiency of a heat engine.

The third investigated technology (*low voltage elastomer actuators*) is evolutionary in terms of mechanism, but revolutionary in terms of performance. The elastomer-based artificial muscle technology developed by Stanford Research Institute and Artificial Muscles, Inc. provides high efficiencies and high power densities, but requires the use of several thousand volts for actuation. We can decrease this voltage by up to two orders of magnitude by replacing the current thick conducting grease electrodes with 50 nm thick, highly elastomeric nanotube electrodes invented at UTD.

Fundamentally *new types of fuel-powered artificial muscles*, which result in electrical dopant intercalation in conducting polymers, were invented, and a corresponding international patent application was filed.

II. PROGRAM PROGRESS

A. GIANT STROKE AND RATE CARBON NANOTUBE SHEET ACTUATORS

We have discovered that solid-state fabricated carbon nanotube aerogels sheets provide an unusual state of matter, which behaves as a low modulus enthalpic rubber for stretch in the width direction and has higher gravimetric strength than steel plate for stretch in the length direction, which is the nanotube orientation direction. More importantly for the present program, we have discovered that these aerogel sheets can be electrically operated in air as artificial muscles that provide strokes and stroke rates as high as 500% and 10^4%/s, respectively. Charge-driven, current-driven, and both dc and resonant linear actuation were demonstrated, which utilize voltages ranging from volts to kilovolts, and produce either electrically driven expansion or contraction from below 77 K to above 1900 K. Actuation can decrease aerogel density to below 10^{-4} g/cm^3 which is ten times lower than the previous record for a self-supporting aerogel. The actuated state of the nanotube sheets can be permanently frozen, which enables tuning nanotube structure for device applications, such as for solar cell electrodes. Observed Poisson's ratios (~9) are ~30 times usual values, which causes confinement of muscle length to profoundly effect lateral actuation.

B. NON-THERMAL ELECTRICAL SHAPE-MEMORY ACTUATION

Development of giant surface area shape memory materials is the key challenge for demonstrating this fundamentally new high-stroke actuator mechanism, which is not limited by either the Carnot efficiency constraints of thermally actuated shape memory materials or the low actuator strains of magnetically operated shape memory materials. This challenge is not yet solved. However, initial research progress has been made on developing new methods for the production of the required giant surface area shape memory materials. The first new method is by electrochemical growth of 50 nm or smaller diameter shape memory wires that are over 50 microns long via electrodeposition using MHz square wave pulses. Norm Barisci of our NanoTech Institute worked with Brett Fanders group of Oklahoma State University (who is an expert on this nanowire fabrication route), and a joint paper on achieved results for conducting polymer nanowires will be submitted. The second method starts with 25 micron diameter NiTi wires and dramatically decreases wire diameter (or thickness in the thinnest direction) by a combination of mechanical draw, mechanical conversion of the shape memory wire to a ribbon, and electrochemical erosion. Other methods are also being pursued, like deposition of 10 nm thick shape memory films by sputtering (followed by substrate removal in selected area) to provide a micro actuator having giant surface-to-volume ratio.

C. LOW VOLTAGE ELASTOMER ACTUATORS
Our collaborative program work with Artificial Muscles, Inc. has provided significant new results on the application of highly elastomeric carbon nanotube sheets as electrodes for low voltage elastomer electrodes. First, it is important that the elastomeric carbon nanotube electrodes do not significantly hinder actuation of the dielectric polymer sheets. Measurement results showed that this was the case for our water-densified, elastomeric nanotube sheet electrodes that provided below 700 ohm/sq sheet resistance. Second, it is important that the nanotube sheet electrodes become resistive in the vicinity of pinholes in the dielectric polymer (so that catastrophic failure by electrical breakdown does not occur). Unfortunately, we find that MWNTs did not provide this self-healing feature. This problem is that the multi-walled nanotubes (MWNTs) in our elastomeric sheets do not vaporize – thereby interrupting current flow at pin holes. The problem fix that we will use is to deploy either single walled nanotubes (SWNTs) of few walled nanotubes (FWNTs) in our solid-state fabricated sheets. Extension of our sheet fabrication process to SWNTs and FWNTs is in progress.

III. AWARDS IN PROGRAM AREA SINCE PROGRAM START

1. *Nano50 Award* of Nanotech Briefs Magazine for Fuel Powered Artificial Muscles (2007)

2. Kapitza Metal of the Russian Academy of Natural Sciences for discoveries on artificial muscles (2007).

IV. PATENT FILING INCLUDING PROGRAM RESULTS

 1. "Fuel Powered Actuators", V. H. Ebron, Z. Yang, D. J. Seyer, M. Kozlov, J. Oh, H. Xie, J. Razal, J. P. Ferraris, A. G. MacDiarmid and R. H. Baughman, Filed PCT International Application (2007), PCT US 2007/063241.

V. ACTUATOR PUBLICATIONS SINCE PROGRAM START

 1. "Electrochemical Actuation of Carbon Nanotube Yarns", T. Mirfakhrai, J. Oh, M. Kozlov, E. C. W. Fok, M. Zhang, S. Fang, R. H. Baughman, and J. D. Madden, Invited Paper in *Journal of Smart Materials and Structures* **16**, S243-S249 (2007).

 2. "Polymer Artificial Muscles", T. Mirfakhrai, J. D. W. Madden and R. H. Baughman, invited review for *Materials Today* **10**, 30-38 (2007).

3. "Capacitive Charging and Background Processes in Carbon Nanotube Yarn Actuators", T. Mirfakhrai, M. Kozlov, M. Zhang, S. Fang, R. H. Baughman, and J. D. W. Madden, *Proceedings of SPIE*, Vol. **6524**, 65241H, 1-12 (2007).

4. "Carbon Nanotube Electroactive Polymer Materials: Opportunities and Challenges", L. Qu, Q. Peng, L. Dai, G. M. Spinks, G. G. Wallace, and R. H. Baughman, *Materials Research Society Bulletin* **33**, 215-224 (2008)

VI. INVITED TALKS ON ACTUATORS SINCE PROGRAM START

"New Technologies from UTD's NanoTech Institute: From High Performance Nanotube Yarns and Sheets to Fuel-Powered Artificial Muscles", The 6th Emerging Information Technology Conference (Dallas, Texas, August 10-11, 2006).

"Fuel Powered Artificial Muscles", NanoBio Convergence Group Lecture Series (Sept. 13, 2006, Menlo Park, CA).

"NanoTech Institute Inventions: From Multifunctional Carbon Nanotube Yarns and Transparent Metallic Sheets to Fuel-Powered Muscles and Devices for Energy Harvesting, Storage, and Conversion", NanoTX'06 Conference on *The Promise of Tomorrow, The Business of Nanotechnology* (Sept. 27-28, 2006, Dallas, TX)

"From Multifunctional Carbon Nanotube Yarns and Transparent Sheets to Fuel-Powered Muscles and Devices for Energy Harvesting, Storage, and Conversion". *Carnegie Mellon University* (Nov. 21, 2006, Pittsburgh, PA).

"From Electrical to Fuel Powered Artificial Muscles", *Fall Materials Research Society Meeting* (Nov. 29-Dec. 1, Boston, Massachusetts).

"NanoTech Institute Inventions: From Multifunctional Carbon Nanotube Yarns and Transparent Metallic Sheets to Fuel-Powered Muscles and Devices for Energy Harvesting, Storage, and Conversion", *International Conference on Nanoscience and Nanotechnology* (Dec. 7-8, 2006, Guangji, Korea).

"From Electrical to Fuel Powered Artificial Muscles", KITECH (Dec. 8, 2006, Seoul, Korea).

"From Electrical to Fuel Powered Artificial Muscles", Hanyang University (Dec. 11, 2006, Seoul, Korea).

"From Electrical to Fuel Powered Artificial Muscles", *2006 International Workshop on Innovations and Advanced Studies –Energy, Biomedicine, Enabling Materials and Micro-Nano Science and Technology*, National Cheng Kung Univ. (Dec. 13-15, 2006, Tainan, Taiwan).

"From Electrical to Fuel Powered Artificial Muscles", Award Lecture for Kapitza Metal (Jan. 18, 2007, Moscow, Russia).

"From Multifunctional Carbon Nanotube Tarns and Transparent Sheets to Fuel-Powered Muscles and Devices for Energy Harvesting, Storage, and Conversion", *Honeywell Corporation* (January 22, 2007, Morristown, New Jersey).

"Strain Amplification for Artificial Muscles and Sensors Using Giant Poisson Ratios and Giant Linear Compressibilities", *2nd International Symposium on Electromaterials Science* (Feb. 7-9, 2007, Wollongong, Australia).

"From Electrical to Fuel Powered Artificial Muscles", *Euroconference on Electronic Properties of Novel Materials* (March 10-16, 2007, Kirchberg, Austria).

"Autonomous Carbon Nanotube and Shape Memory Yarn, Sheet, and Wire Systems", *SPIE Smart Structures and Materials Symposium* (March 18-22, 2007, San Diego, CA).

"New Technologies from UTD's NanoTech Institute", Banquet Lecture for *Raytheon's 7th Electro-Optical Systems Technology Network Conference* (May 15-16, 2007, Richardson, Texas).

"From Multifunctional Carbon Nanotube Tarns and Transparent Sheets to Fuel-Powered Muscles and Devices for Energy Harvesting, Storage, and Conversion", Dinner Lecture for *Institute for Innovation and Invention* (June 14, 2007, Richardson, Texas).

"From Electrical to Fuel Powered Artificial Muscles", Southern Methodist University (July 13, 2007, Dallas, Texas).

"NanoTech Institute Inventions: From Multifunctional Carbon Nanotube Yarns and Transparent Metallic Sheets to Fuel-Powered Muscles and Devices for Energy Harvesting, Storage, and Conversion", Evening lecture for *The Indus Entrepreneurs* (June 14, 2007, Dallas, TX).

"From Electrical to Fuel Powered Artificial Muscles", *Texas-Korea Nano Workshop* (August 6-8, 2007, Richardson, TX).

"NanoTech Institute Inventions: Transparent Metallic Sheets, Fuel-Powered Muscles and More", *MetroCon (IEEE) Conference* (Oct. 10, 2007, Arlington, TX).

"From Multifunctional Carbon Nanotube Yarns and Transparent Sheets to Fuel-Powered Muscles and Devices for Energy Harvesting, Storage, and Conversion", *General Electric* (Oct. 23, 2007, Niskayuna, NY).

"Nanotechnology for Fun and Profit", *Carnegie Mellon University Lecture Series* - Lecture preceding receipt of 2007 Distinguished Alumni Award (Oct. 26, 2007, Pittsburgh, PA).

"From Electrical to Fuel-Powered Artificial Muscles", Plenary Lecture at *2007 National Nano Engineering Conference*, prior to receiving Nano 50 Award for Fuel-Powered Artificial Muscles (Nov. 14, 2007, Boston, Massachusetts).

"Nanotechnology for Fun and Profit", *Petersen Institute of NanoScience and Engineering, University of Pittsburgh* (Feb 4, 2008, Pittsburgh, PA).

"Diverse Carbon Nanotube Artificial Muscles Meet an Exciting New Family Member", *Monash University* (Feb. 21-22, 2008, Melbourne, Australia).

"Diverse Carbon Nanotube Artificial Muscles Meet an Exciting New Family Member", *US AFRL-Israeli Bio/Nano Workshop for Materials* (March 24-25, 2008, San Francisco, CA).

"Diverse Carbon Nanotube Artificial Muscles Meet an Exciting New Family Member", *ChemOnTubes 08*, (April 6-9, 2008, Zaragoza, Spain).

"Diverse Carbon Nanotube Artificial Muscles Meet an Exciting New Family Member", *Nano for Defense Applications* (April 21-23, 2008, Arlington, Virginia).

Electronic Textile Sensors for Stress Measurement in Soldiers

PIs: Bruce Gnade, Roozbeh Jafari and Chris Gintz

Abstract

This project focused on building a platform with electronic textile and wearable sensors to detect acute stress level in human. Our earlier investigation and literature search indicate that several physiological parameters can be used to identify stress. They include: 1) nature of physical activities the subject is engaged in, 2) skin conductance and 3) heart-beat variability. To detect these parameters, we proposed a wearable system with 1) inertial sensors (accelerometers and gyroscopes) and flex sensors, 2) galvanic skin response sensors and 3) pizeo-electric film sensors.

We built a wearable platform with multiple tiny sensor units. Each unit is composed of a microcontroller (Texas Instrument MSP430), a radio module, several analog and digital interfaces and a flash memory. We designed and implemented a software infrastructure that performs data collection, and enables on-board and collaborative signal processing.

We integrated motion and flex sensors to detect a set of physical activities (stand to sit, sit to lie, kneeling and grasping, reach up with two hands, turning crotch counter clockwise, jumping on footrest, lifting object from table, bend and grasp, going upstairs, kneeling) and investigated several challenges including: 1) sensor optimization (where the sensors need to be placed), 2) light-weight and real-time signal processing techniques that interpret sensor readings into indispensable information for users (i.e. what type of activity was performed, for how long,…etc).

We used an off-the-shelf galvanic skin response sensor to detect the skin conductance. We designed and built an interface to connect the galvanic skin response sensor to our wearable platform.

We integrated piezo-electric film sensor into our system for detecting the heartbeat rate. We built an analog interface that consists of amplifiers and filters. This interface performs signal conditioning and generates a suitable output for the analog interface of our wearable platform.

We collected data from several participants and established the effectiveness of the system and signal processing. A maximum accuracy of 94% was achieved for movement classification while the effectiveness of other sensors was established.

1. Introduction

Our research focuses on determining stress level using several small wearable sensors. First, we must clearly define the types of stress and examine their causes, symptoms, and effects. After that, we will explain our methodology for exploiting the immediate biological effects of stress to determine the the wearer's level of stress. Then, we will present the sensor systems and signal processing techniques we developed to measure these effects and report experimental validation of these techniques. Finally we will detail our continued research strategy for developing a complete stress evaluation system.

1.1 Definition of Stress

Stress is the sum of the physical, mental, and emotional tensions on a person. It is caused by a number of stressors, which are stimuli or events that provoke a stress response in an organism. Stressors include physical factors such as temperature or pain as well as psychological factors including relationships with friends and work. The body's immediate response to stress is to prepare for combat or retreat. Periodic exposure to stress is healthy, but frequent or chronic exposure to stress can be psychologically damaging and lead to health problems.

1.3. Types of Stress

Acute stress: This is the most common form of stress. It comes from demands and pressures of the recent past and anticipated demands and pressures of the near future. Acute stress can be thrilling and exciting in small doses, but too much is exhausting. Because it is short-term, acute stress doesn't have enough time to do the extensive damage associated with long-term stress. This type of stress may appear in anyone's life, and is highly treatable and manageable. The effects are immediate and easily differentiable from normal body responses.

The effects can include emotional stress (anger, irritability, anxiety, depression), muscular problems (tension headaches, back pain, and muscular tensions), digestive disorders (heartburn, diarrhea, flatulence, constipation), general arousal symptoms (rapid heartbeat, sweaty palms, heart palpitations, dizziness, and cold hands).

Acute stress is easily measured because of the immediate and drastic biological effects. This is the primary stress our system is capable of observing.

Episodic Acute Stress: Frequent exposure to acute stress is Episodic Acute Stress. This can result from high stress jobs, poor organizational skills, or over-commitment. People who perpetually experience this type of stress can be irritable and abrupt, and have problems maintaining relationships,

The symptoms of episodic acute stress are those of extended over-arousal: persistent tension headaches, migraines, hypertension, chest pain, and heart disease. Often, lifestyle and personality issues are so ingrained and habitual with these individuals that they see nothing wrong with the way they conduct their lives. They often blame their woes on other people and external events. Frequently, they see their lifestyle, their patterns of interacting with others, and their ways of perceiving the world as part of who and what they are.

Treating episodic acute stress requires intervention on a number of levels, generally requiring long-term professional help. However, sufferers can be fiercely resistant to change. Only the promise of relief from pain and discomfort of their symptoms can keep them in treatment and on track in their recovery program.

Our system would be able to observe frequent exposure to acute stress and flag individuals who experience this for examination, but a psychiatrist is required for accurate diagnosis and treatment.

Chronic Stress: While acute stress can be thrilling and exciting, chronic stress is not. This is the grinding stress that wears people away day after day, year after year. Chronic stress destroys bodies,

minds and lives. It wreaks havoc through long-term attrition. It's stress of poverty, of dysfunctional families, unhappy marriages, or despised jobs. Chronic stress comes when a person never sees a way out of a miserable situation. It's the stress of unrelenting demands and pressures for seemingly interminable periods of time. The worst aspect of chronic stress is that people become accustomed to it. They forget it's there. People are immediately aware of acute stress because it is new; they ignore chronic stress because it is old, familiar, and sometimes, almost comfortable.

Chronic stress kills through suicide, violence, heart attack, and stroke. Because physical and mental resources are depleted through long-term attrition, the symptoms of chronic stress are difficult to treat and may require extended medical as well as behavioral treatment and stress management.

Common causes of chronic stress include poverty and financial worries; long-term unemployment; dysfunctional family relationships; caring for a chronically ill family member; feeling trapped in unhealthy relationships or career choices; living in an area besieged by war, ethnic rivalry, or criminal violence; bullying or harassment; and perfectionism.

Because this stress is so integral to an individual's life, our system would be completely unable to differentiate between chronic stress and normal behavior.

1.3. Biological Effects of Acute Stress

The focus of our research is acute stress, as that is most easily measured. Of particular interest is the immediate biological response to acute stress. In many cases, this response produces effects which can be measured with sensors placed on different parts of the body. This is particularly true with heart, lungs, and skin.

Brain's Response to Acute Stress: In humans, the biochemical response to acute stress is known as the "fight-or-flight" reaction. It begins with the activation of a section of the brain called the hypothalamic-pituitary-adrenal system, or HPA. This system first activates the release of steroid hormones, which are also known as glucocorticoids. These hormones include cortisol, the primary stress hormone in humans. The HPA system then releases a set of neurotransmitters known as catecholamines, which include dopamine, norepinephrine, and epinephrine (also known as adrenaline). Catecholamines. These hormones have three important effects:

- Activation of the amygdala, an almond-shaped structure in the limbic system that triggers an emotional response of fear.
- Signaling the hippocampus, another part of the limbic system, to store the emotional experience in longterm memory.
- Suppression of activity in parts of the brain associated with short-term memory, concentration, and rational thinking. This suppression allows a human to react quickly to a stressful situation, but it also lowers ability to deal with complex social or intellectual tasks that may be part of the situation.

Response of the Heart, Lungs, and Circulation: The stress response also affects the heart, lungs, and circulation. As stress increases, the heart rate increases and becomes less erratic, and blood pressure also increases instantaneously. Breathing becomes rapid and the lungs take in more oxygen. Furthermore, the spleen discharges red and white blood cells, allowing the blood to transport more oxygen throughout the body. Blood flow may actually increase 300% to 400%, priming the muscles, lungs, and brain for added demands.

Response of the Immune System: The effect on the immune system from confrontation with stress is similar to marshaling a defensive line of soldiers to potentially critical areas. The steroid hormones dampen parts of the immune system, so that specific infection fighters (including important white blood cells) or other immune molecules can be redistributed. These immune-boosting troops are sent to the body's front lines where injury or infection is most likely, such as the skin, the bone marrow, and the lymph nodes.

Response of the Mouth and Throat: In response to stress, fluids are diverted from nonessential locations, including the mouth. This causes dryness and difficulty in talking. Stress can also cause spasms of the throat muscles, making it difficult to swallow.

Response of the Skin: The stress effect diverts blood flow away from the skin to support the heart and muscle tissues. The physical effect is a cool, clammy, sweaty skin. The scalp also tightens so that the hair seems to stand up. (temporary acne is also a result of stress)

We have suspicion that Skin Conductance and Heart Rate are promising signs for detecting stress level using flexible electronics. Although these two signals have potentials for our target application, they would be affected by other physical and environmental parameters. In particular, the level of stress in a human would change under different physical activity conditions, temperature and humidity. Therefore, we believe that the system needs to be embedded with other types of sensors to capture signals correlated with Skin Conductance and Heat Rate.

2. System Components

Most biomedical applications, including stress level recognition, require a set of sensors that are spatially distributed because of (a) diversity for sensitivity, performance, accuracy, and robustness, and (b) constraints posed by the location of the desirable sensing points on the surface of the human body. The sensors are responsible for collecting data, while the processing units provide filtering and noise reduction on the signals. Due to the nature and usage of our sensor concepts, the processing units must be fairly simple, because the devices and circuits will be fabricated using organic semiconductors. Our system is composed of processing units, sensors and a gateway station.

2.1. Processing units

The most important components of our system are distributed processing units that can support various types of sensors for physiological readings from the human body. These blocks are responsible for reading from the sensors, executing preprocessing (filtering, segmentation,…etc), feature extraction, and local classification. Furthermore, they enable communications that will lead to global classification on a centralized node. At the current, we have been sending out the raw data for off-line processing. The processing units that we utilize are Telos-B motes developed at University of California, Berkeley.

2.2. Sensors

We have investigated and purchased several types of off-the-shelf sensors that can be potentially used for stress evaluation:

2.2.1. Fully Integrated Sensors

- **Fingertip skin conductance (flexible electronic sensor):** Skin conductance is considered to be a function of sweat gland activity and skin pore size, both of which are controlled by the sympathetic nervous system. Sweat glands are activated when the sympathetix nervous system is aroused in response to stress or anxiety. As sweat is produced, the skin's capacity to conduct current is enhanced and the measured conductance is increased. For this particular sensor, a small voltage is applied to the skin between two sensors and the skin's current conduction is measured. We have used this sensor extensively for our experiments. We measure the output voltage on our processing units. Figure 1 shows a typical skin conductance sensor attached to our processing unit.

Figure 1. Fingertip skin conductance sensor and a processing unit

- **Flex sensor (flexible electronic sensor):** The Flex Sensor is a unique component that changes resistance when bent. An un-flexed sensor has a nominal resistance of 10,000 ohms (10 K). As the flex sensor is bent the resistance gradually increases. When the sensor is bent at 90 degrees its resistance will range between 30-40 K ohms. We use this sensor to measure the level of activity in a human. A sample flex sensor is shown in Figure 2.

Figure 2. Flex Sensor

- **Inertial sensors (rigid sensors):** Inertial sensors are used to continuously track the position, orientation, and velocity (direction and speed of movement) of an object without the need for external references. Examples of motion sensor include Accelerometers and Gyroscopes. An accelerometer is a device for measuring the acceleration and gravity induced reaction forces it experiences. Single- and multi-axis models are available to detect magnitude and direction of the acceleration as a vector quantity. Accelerometers can be used to sense inclination, vibration, and shock. They are increasingly present in portable electronic devices. A gyroscope is a device for measuring or maintaining orientation, based on the principles of angular momentum. We use inertial sensors (as shown in Figure 3.) to measure the level of activities.

Figure 3. Inertial sensors attached to a processing unit using custom-designed board

- **Humidity and Temperature sensors:** The humidity and temperature sensors are used to measure effects of environment on bio-signals. In particular, humidity and temperature affect the skin conductance. We are required to integrate these environmental sensors to the system to compensate their effects. Fortunately, some processing units are equipped with temperature and humidity sensors. We are using a sensor board shown in Figure 4.
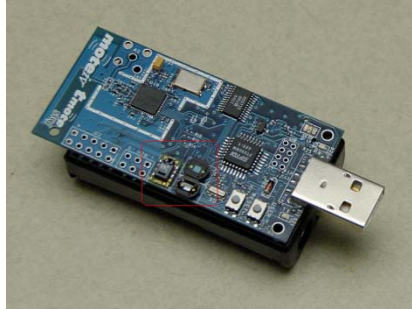

Figure 4. A processing unit integrated with humidity and temperature sensors.

2.2.1. Sensors under development

- **Piezoelctric film sensor:** Piezoelectric sensors measure the electrical potential caused by applying mechanical force to a piezoelectric material. Piezoelectric sensors are used in a variety of pressure-sensing applications.

Figure 5. Piezoelectric sensor

Figure 5 shows a typical piezoelectric film sensor that we tested in this project for detecting heart beat.

Figure 6 shows our custom-designed circuit board. The board is designed to interface with the piezoelectric sensor and the sensor platform. It is designed to reduce environmental noise and amplify the low-amplitude input signal. It is built with a TLV2764 TI amplifier which is a single supply operational amplifier and provides 500 kHz bandwidth from only 20 uA**,** while operating down to 1.8 V over the

industrial temperature range. Our amplifier circuit is made to capture signal readings from four piezoelectric sensors. The schematic of this 4-channel amplifier is shown is Figure 7 .
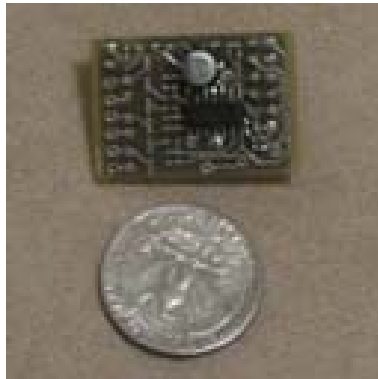

Figure 6. Our custom-designed amplifier circuit

We built the amplifier circuit and tested it while it was powered at 3.0 V by a typical power supply. The piezoelectric film was attached to the wrist with athletic tape, while the circuit output was monitored with an oscilloscope. It was placed over the pulse point to capture the subject's heart rate. As of now, the output we are experiencing has a very low SNR, and the noise has several different sources. After several rounds of modification, we managed to read and amplify heartbeat, as shown in Figure 8.
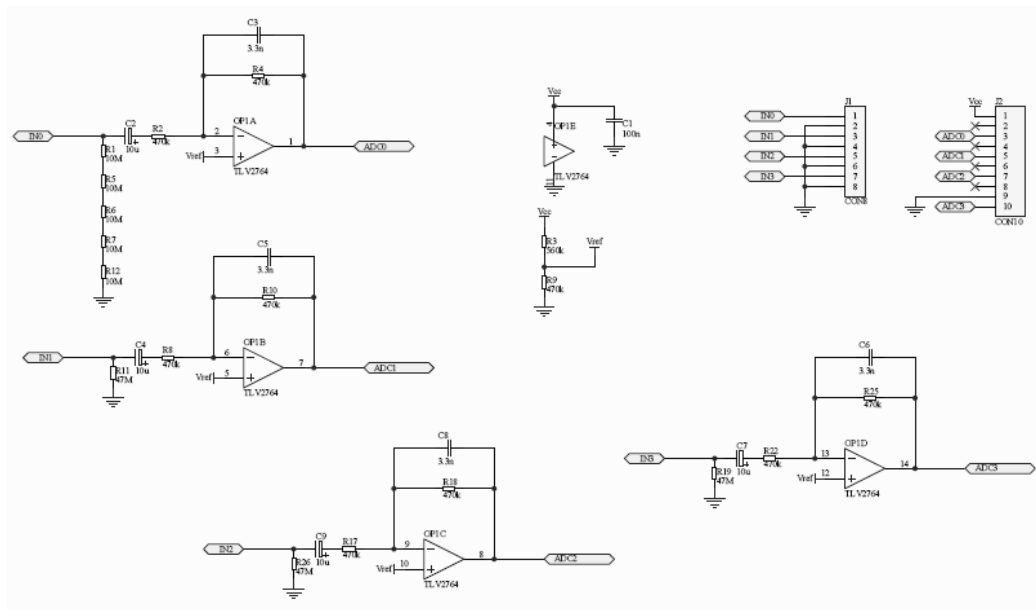

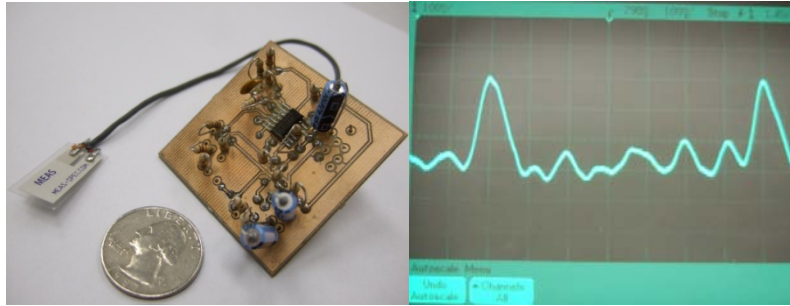**Figure 7. Schematic diagram of the amplifier circuit**

Figure 8. Piezo-electric Prototype and Heartbeat Output

2.3 Gateway

A pocket PC**,** mobile phone, or laptop can be used to collect data from processing units and classify them. In our experiments, we have been using a laptop as a gateway only to log the data for off-line signal processing and analysis.

3. Signal Processing

We propose the following framework, as shown in Figure 9, for stress assessment and classification of activities. Given the goal of classifying behavior based on a subject's sensor readings, the functionality of our automated pattern recognition system is divided into three basic tasks: the pre-processing and filtering**;** the description task which generates attributes of a movement using feature extraction techniques**;** and the classification task which classify ~~this~~ the movement based on its attributes.
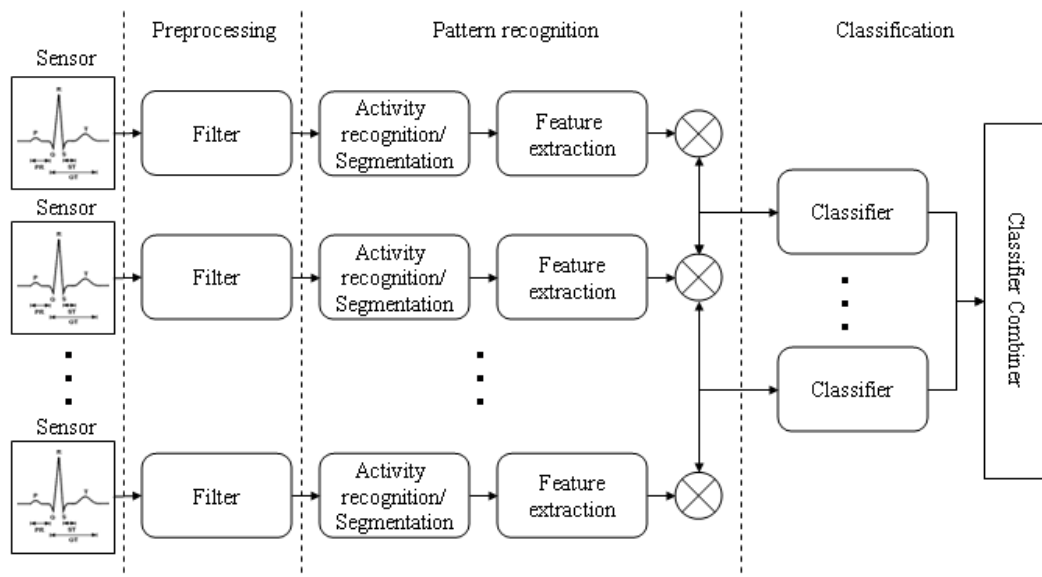

Figure 9. System architecture of distributed sensing platform for stress evaluation

3.1. Preprocessing

Currently, we only obtain readings from the fingertip sensors. The preprocessing step involves splitting the signal into periods of activity. This can be accomplished by a thresholding scheme that attempts to find any sharp changes in the pattern of the signal. For the results presented in this work, we adopted a manual annotation scheme to mark the start and end of each activity period.

3.2. Feature extraction

We consider the following features on fingertip skin conductance sensor readings:
i.   Mean: mean of the signal segment.
ii.   Start-to-end Amplitude: the amplitude change across the signal segment.
iii. STD: standard deviation of the signal segment.
iv.   Peak-to-peak amplitude: max–min value of the signal segment.
v.   RMS: root mean square of the signal segment.
vi.   Morphology: we select k points that are evenly distributed from the start to end of each activity segment. The distance between two morphological features is defined as the area between two morphologies. This allows us to compare the shape of segments, independent of their durations.

3.3. Classification

We will utilize k nearest neighbor (k-NN) algorithm to classify movements. We adopt k-NN classifiers due to 1) the simplicity of implementation, 2) small number of training samples required and small memory usage, and 3) its effectiveness. The k-NN classifier has been fully implemented and tested in MATLAB.

4. Skin Conductance Experiments

We have integrated fingertip skin conductance sensors in our system. Preliminary experiments have been carried out on three subjects, one female and two males. The system has been setup to read from the sensors every 10 seconds. A raw sensor reading for a female subject is shown in Figure 10. The Y-axis is normalized while the X-axis corresponds to time (unit: minute).

A: Working in the lab with a PC
B: Leaving the lab, walking through stairs, inside building
C: Leaving the building, walking around campus
D: Sitting (peak is due to observing a cockroach!)
E: Walking home
F: At home (watching TV…etc)
G: Going to bed

The diagram clearly illustrates changes in sensor readings from one action to another. The signal processing described in Section 3 has not been incorporated yet, although the software modules for pattern recognition has been implemented and tested in MATLAB. This is because the pulse wave sensor, which measures the heartbeat variability (HRV), is essential for our system and has not been yet integrated. Features from HRV sensors are crucial classifying stressful conditions. In the next months, pulse wave sensors will be integrated into our system and several experiments will be carried out.

Furthermore, we will develop sensor elements that can be integrated on ribbons. The initial phase is to develop skin conductance and piezoelectric sensors that will measure stress and heartbeat rate. These sensors will be placed on fabric and inside a glove.
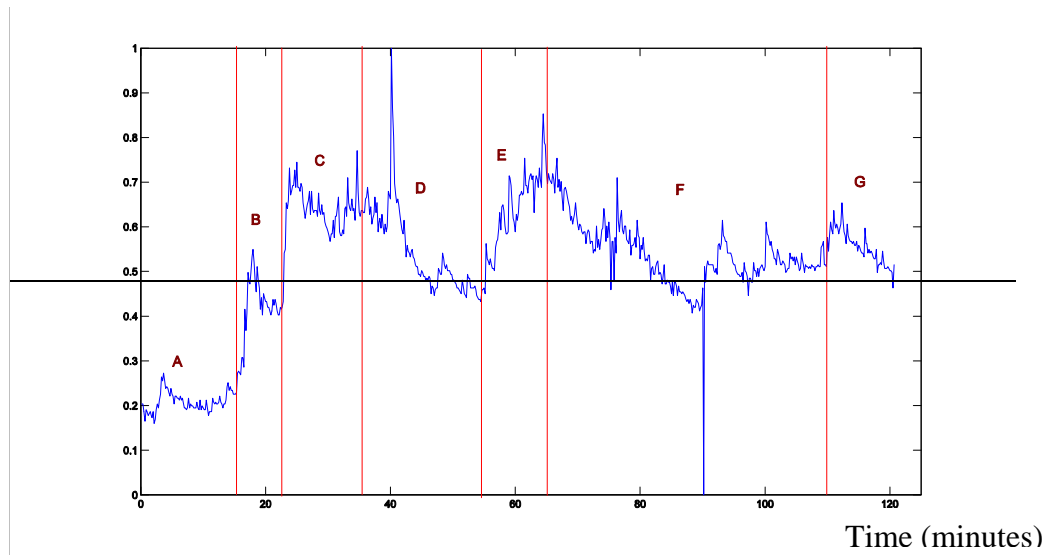
Time (minutes)

Figure 10. Skin conductance reading (female subject)

5. Physical Activity Level Experiments

The activity level can be used to determine external physical stressors and to determine the degree to which skin conductance and heartbeat relate to physical activity versus stress. Traditionally, inertial sensors are used to measure activity level. The most popular inertial sensors for this purpose are accelerometers and gyroscopes, which, as mentioned, measure acceleration and angular velocity respectively. Here we explore the use of flex sensors for this application. Flex sensors provide less information than inertial sensors, but offer many advantages. For both sensor types, sensors must be distributed across the body. Inertial sensors are constructed and deployed on a rigid surface, while researchers are developing flex sensors that can be woven into fabric. Flex sensors are less vulnerable to impact damage, and are small enough that redundant sensors may be placed to decrease vulnerability to damage and compensate for misplacement. These properties make flex sensors (and other fabric-embeddable sensors) much more desirable for deployment on athletic individuals who are involved in rigorous activities. Furthermore, the power requirements for flex sensors are considerably less: they use about 1/100 of the power required for gyroscopes, and 1/10 of that required for accelerometers. An improved circuit design could further widen the power gap. Finally, the cost per sensor is less for flex sensors.

For these validation experiments, we use a test system based on commercially available flex sensors. These sensors are a quarter inch wide, and not embeddable in fabric. However, the results will largely apply to a system utilizing such sensors. Figure 8 shows the flex sensor on the outside of the elbow pad for illustration purposes, as the sensor is actually under the pad. Figure 11 shows as subject wearing inertial and flex sensors. The sensors are placed on different joints including right-elbow, right-knee, left-elbow and left-knee.

Figure 11. Subject wearing Flex sensor and Motion sensor

A sample waveform for movement 'Stand to Sit' is shown in Figure 12. In this movement, the joints of right and left knees are mostly involved. The waveform shows that signals produced by sensors placed on the knees are more intensive.
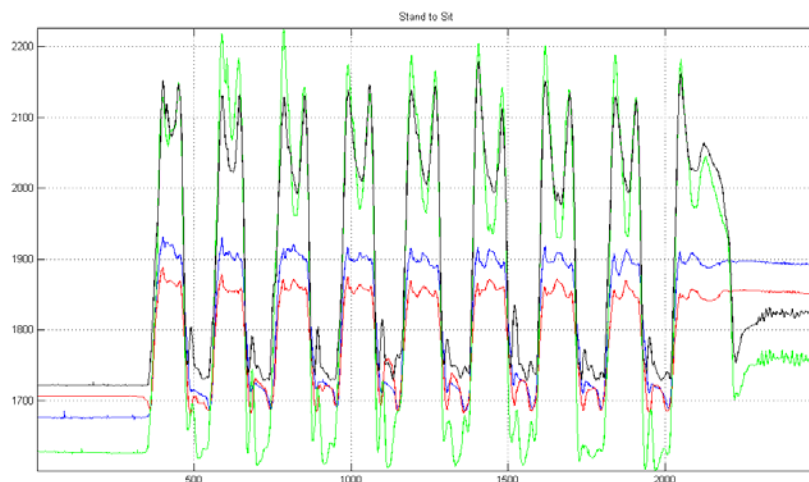

Figure 12. A sample waveform for 'Stand to Sit' performed 10 times

5.1. Activity Recognition/Automatic Segmentation

Before movements can be properly classified, discrete movements must be separated from other movements and from rests. We developed a method for segmenting movements based on standard deviation. The sensor data from the sensors tends to change rapidly when the subject is performing an action and slowly when the subject is not. We previously validated this technique using gyroscope and accelerometer data, but here we show the results using flex sensor data acquired in the aforementioned experiment.

The basic technique is to determine the activity level for a given sensor and time. The activity levels from each sensor on a given sensor node are added together. Any activity level above a threshold is considered an action and anything below is a rest. Not every sensor can accurately determine what is happening, therefore the sensor nodes transmit the times and durations of all actions they have detected individually. The base-station then determines a global segmentation by voting among the sensors: if at least 3/8 of the sensors think an action occurs at a given time, it is considered an action. Any actions or rests that are too short are considered transients and are removed.

The activity level is computed from the standard deviation of values from a single sensor in a window around the current point. The amplitude of this signal is adjusted using dynamic gain control to account for residual motion in rest states.
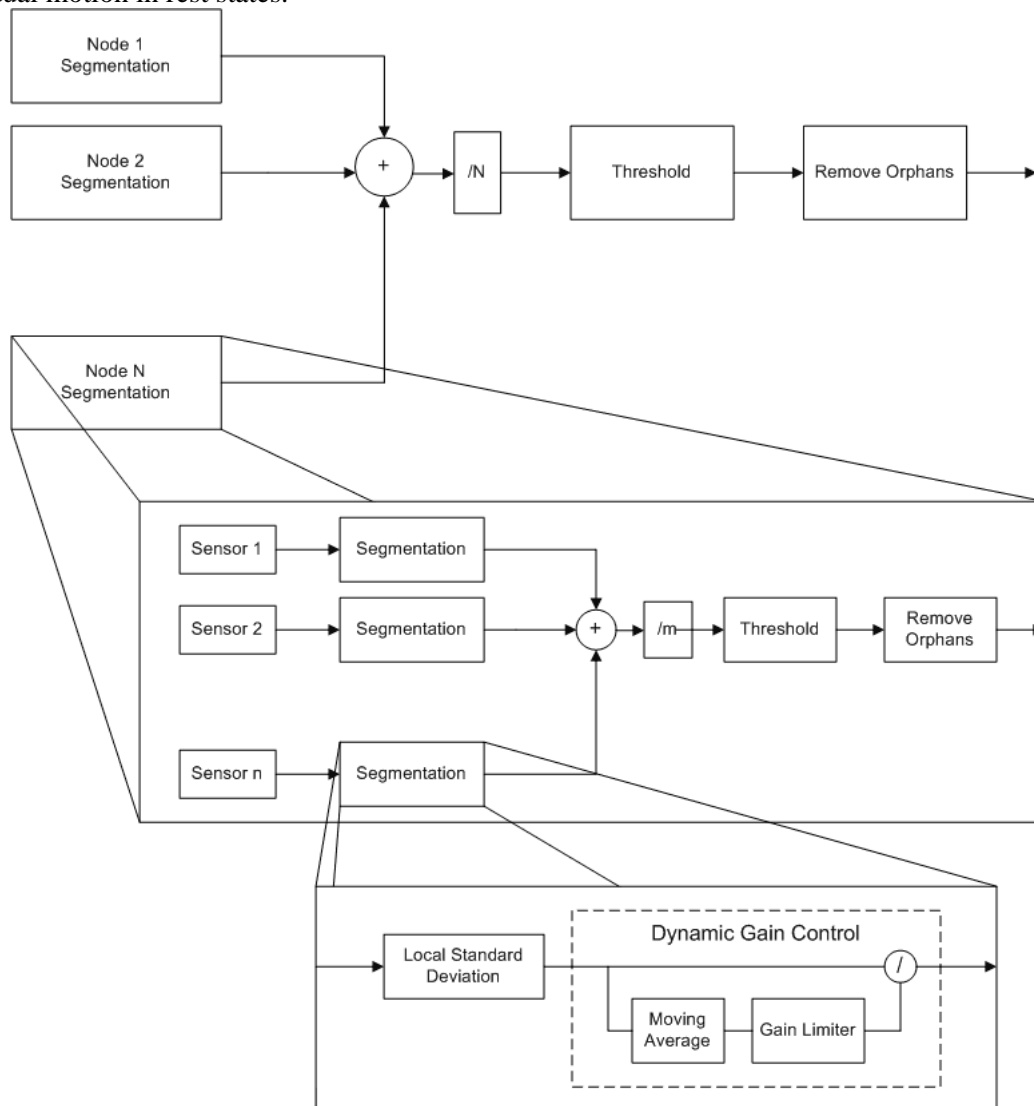
Figure 13. Segmentation Signal Processing

This technique has several limitations: it cannot segment continuous movements such as walking or running; it often divides a single event into several segments, and it falsely considers several close events to be a single event. For walking, we have developed an effective segmentation technique in which is not discussed in this report. The other two problems can be compensated for by changing what we consider to be the event: perhaps a movement does have four parts. This is not always an effective solution. Therefore, we are developing a new algorithm to address these issues.

Figure 14. Segmentation results for kneeling

Figure 15. Results for lifting an object

Figure 14 shows segmentation results for kneeling. The green signal is the signal from the sensor, and the red illustrates the activity level. The blue rectangles are the per-node segmentation, and the red rectangles on top show the global segmentation. In Figure 14, the segmentation is perfect: it correctly considers kneeling to be one action and standing up anoth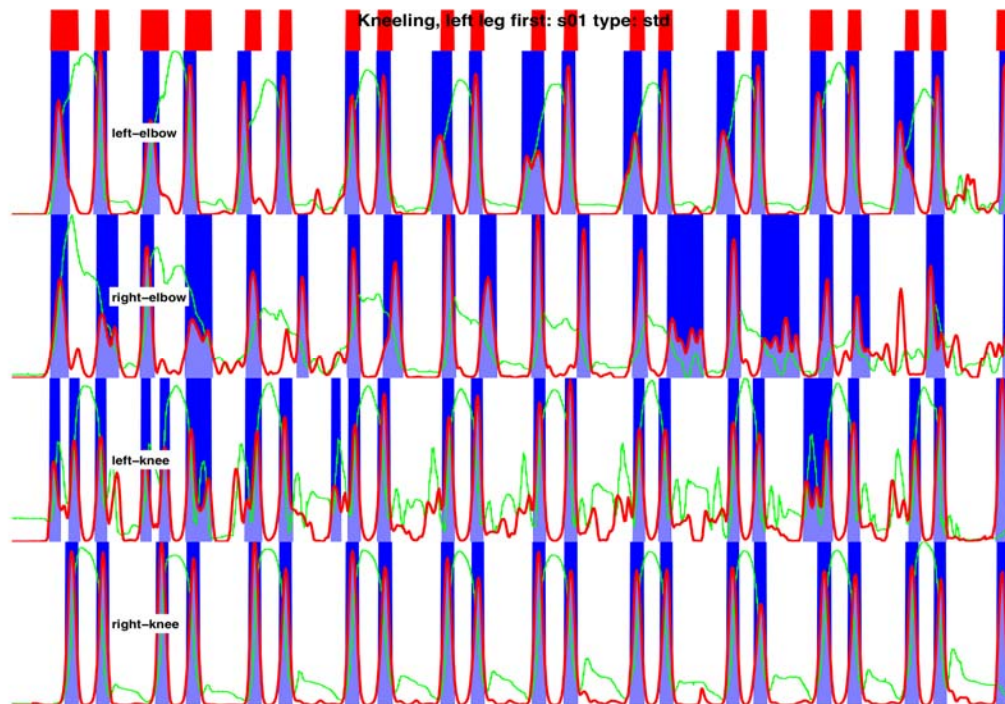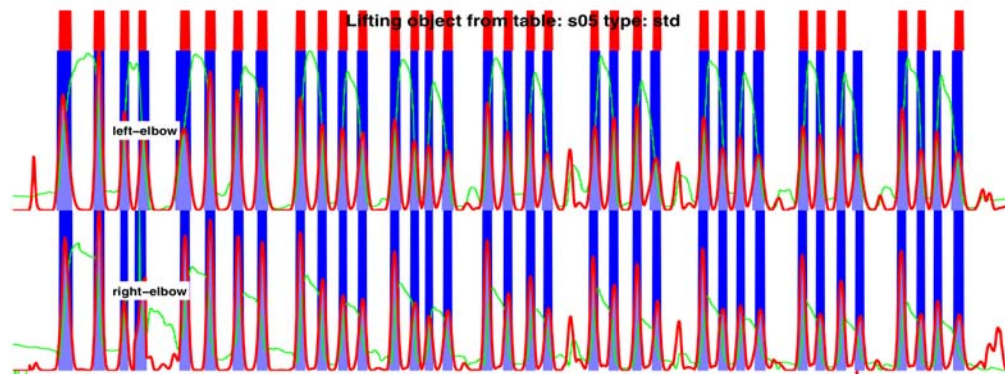er. A good example of an incorrect separation is shown in Figure 15. Even if we split the movement "lifting an object from table" into four sub-actions, there are still several cases where one of those sub-actions is missing. The signals from the leg sensors weren't shown as they were consistently below the threshold for action identification.

Overall, the segmentation was less effective than in previous experiments involving inertial sensors. Moreover, many of these actions featured sequential rather than simultaneous limb movements that led to false splits and joins. For instance, in the movement "bend and grasp" the legs bend first then stay still while the arms bend. This appears to be two movements, although it is incorporated as one. Table 1 was compiled by manually judging how many false positives, false negatives, joins (two separate actions considered one action), and splits (a single action split into two or more separate actions). Even if one action was split into 4 pieces, it would be counted as one split. For movements six to fifteen, a sensor failed on one of the subjects, resulting in fewer total movements listed.

Table 1. Segmentation results

No	Total	FP	FN	Joins	Splits
1	55	5	0	0	3
2	58	6	0	0	24
3	60	T	2	8	11
6	40	4	6	1	11
9	40	0	2	0	0
10	44	0	7	0	1
11	19	0	0	0	19
12	42	5	0	1	0
13	38	7	0	0	0
14	40	1	1	0	0
15	32	0	0	0	0

5.2. Feature Selection

Electronic textiles are highly constrained in terms of computation and memory usage. That is, the signal processing on the fabrics is limited to low processing and storage. Since the number of attributes presented in the 'feature extraction' stage would directly affect system requirement in terms of computation and memory, selecting a small feature space that maintains acceptable classification accuracy while conforming system constraints would be very important. Therefore, we have tried to select a very small feature space that achieves good classification accuracy. We use a heuristic algorithm, so-called Relief, that works based on a feature weighting scheme and finally provides direct insights into choosing highly-relevant features. A brief description of the Relief algorithm follows.

Relief uses a statistical method to select relevant features. It is a feature weight-based algorithm inspired by instance-based learning algorithms. From the set of training instances, it first chooses a sample of instances. Relief randomly picks this sample of instances, and for each instance in it finds *Near Hit* and *Near Miss* instances based on a Euclidean distance measure. *Near Hit* is the instance having minimum Euclidean distance among all instances of the same class as that of the chosen instance; *Near Miss* is the instance having minimum Euclidean distance among all instances of different class. It updates

the weights of the features that are initialized to zero in the beginning based on an intuitive idea that a feature is more relevant if it distinguishes between an instance and its *Near Miss*, and less relevant if it distinguishes between an instance and its *Near Hit*. After exhausting all instances in the sample, it chooses all features having weight greater than or equal to a threshold. This threshold can be automatically calculated using a function that uses the number of instances in the sample; it can also be determined by inspection (all features with positive weights are selected). Relief works for noisy and correlated features, and runs in linear time relative to the number of given features and number of samples considered for feature selection. It works both for nominal and continuous data. One major limitation is that it does not help with redundant features and, hence, generates a non-optimal feature set size in the presence of redundant features. This can be overcome by a subsequent exhaustive search over the subsets of all features selected by Relief. Relief works only for binary classes. This limitation is overcome by Relief-F that also tackles the problem of incomplete data.

For feature conditioning, we first extracted the following features on flex sensor readings.
1. Mean: mean of the signal segment.
2. Max: maximum amplitude of the signal segment.
3. Min: minimum amplitude of the signal segment.
4. Peak-to-peak amplitude: max–min value of the signal segment.
5. VAR: statistical variance of the signal.
6. STD: standard deviation of the signal segment.
7. RMS: root mean square of the signal segment.
8. Start-to-end Amplitude: the amplitude change across the signal segment.
9. Median: the middle sample data of the signal segment.
10. Slope: the slope of the signal segment.

11-20. Morphology: we selected 10 points that are evenly distributed from the starting to the end of each activity segment. The distance between two morphological features is defined as the area between two morphologies. This assists us to compare the shape of segments independent from their time durations.

We used the data collected in the experiments mentioned above (three subjects and four sensor nodes), and we fed only the training set (50% of the collected data) into the feature conditioning system. The input of the system was a training set containing 80 features (20 for each sensor nodes). We performed a feature selection using Relief algorithm and selected only the first four significant features. The resulting features are listed in Table 2.

Table 2. Significant Features

No	Feature Name	Sensor Number	Weight
1	VAR	2	100
2	VAR	3	98
3	VAR	1	87
4	VAR	4	28

To test the effectiveness of our feature selection algorithm, we fed the rest of the collected data into our test set to a central k-NN classifier in which we achieved 82% accuracy. We then compared this number with the classification results reported for the flex sensor in Table 4 (85%) which was attained using 80 dimensional feature space.

5.3. Activity Level Analysis

For the experimental setup, we asked three subjects aged between 20 and 35 to perform eleven movements listed in Table 3; ten trials each.

Table 3. Movements List for Experiments with Flex Sensors

No.	Description
1	Stand to sit
2	Sit to lie
3	Kneeling and grasping (left leg)
4	Reach up with two hands
5	Turning crotch counter clockwise
6	Jumping on footrest
7	Lifting object from table
8	Bend and grasp
9	Going upstairs (1 step, right leg first)
10	Kneeling, left leg first
11	Kneeling, right leg first

The raw data is collected from each of the five sensors on each of the eight sensor nodes at 40Hz. The data is filtered with a five-point moving average. We determine the portion of the signal that represents a complete action. For experimental purposes, this is done by manually segmenting the actions. Since we are developing different parts of the system concurrently, we have not integrated our automatic segmentation module into the classification tool. Furthermore, at this step of our project, we avoid integrating errors of automatic segmentation to the classification results. For the feature selection, single value features are extracted. We transform sensor readings into a set of informative attributes as described before. After preprocessing is completed, each sensor node transmits its local features to the gateway. This node is responsible for making the final decision on the type of action done. We use the k-Nearest Neighbor (k-NN) classifier due to its simplicity and scalability. The final decision can be made using either a data fusion or a decision fusion scheme. We utilize the former method by feeding features from all sensor nodes into the central classifier.

To verify the effectiveness of flex sensors in human motion detection, we compare the results of motion classification using flex sensors with the results using motion sensors. We used 50% of collected data for training the classifier and the rest for testing the functionality of the system. Figure 16 shows the per-action accuracy of the classification using a k-NN classifier where k=1.

While motion sensors (including one 3-axis accelerometer and one 2-axis gyroscope per sensor node) achieve a better classification accuracy (overall accuracy 91%), flex sensors have a reasonable ability to detect certain movements. While the flex sensors have less accuracy in identifying some movements (e.g. 1, 5 and 11), their classification accuracy is equivalent to motion sensors' for several movements (e.g. 4, 8 and 9) and even higher for some other movements (e.g. 7 and 10).

Classification Accuracy
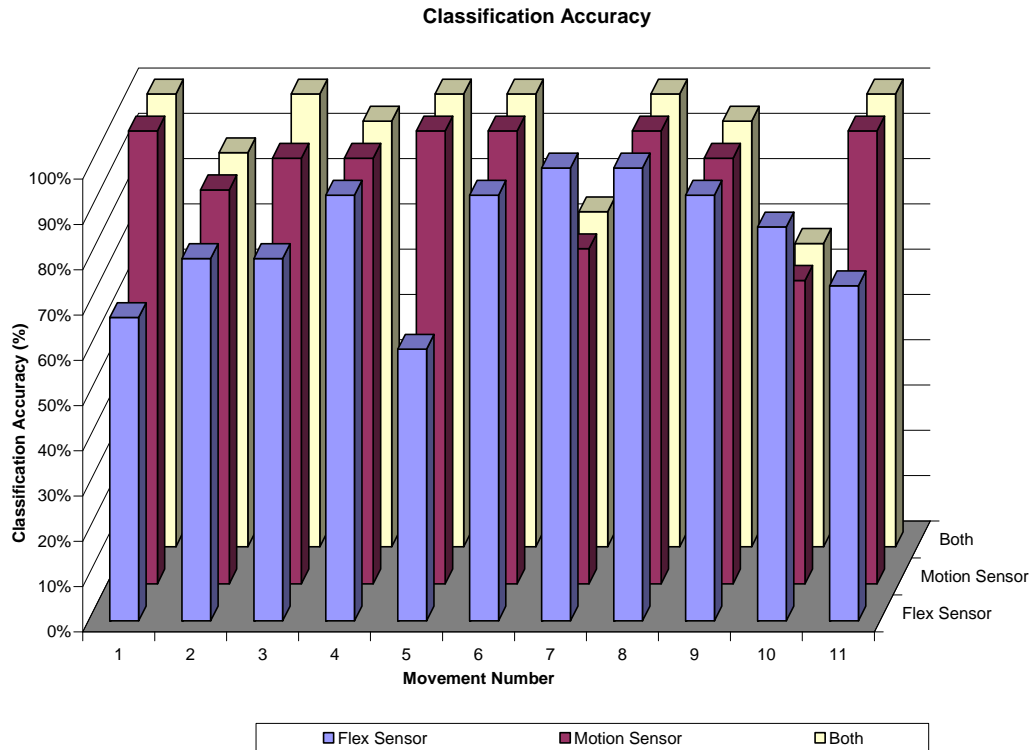
Figure 16. Classification Accuracy using Flex sensor and Motion sensor

In Table 4, the overall accuracy (using 11-movement data set) is shown. Considering a 1-NN classifier, when using only flex sensors, the amount of reduction in accuracy is %6 compared to the case of motion sensors.

Table 4. Overall classification accuracy (11 actions)

K	Flex sensor	Motion sensors	Both
1	%85	%91	%92
2	%78	%92	%93
3	%80	%93	%94
4	%77	%90	%90
5	%76	%88	%89

5.4. Sensitivity to Misplaced Sensors

Soldiers can experience a very high level of activity everyday. The sensors may move during the day. Therefore, calibrating sensor nodes to compensate for misplaced electronics would play an important role in designing this system for use by soldiers. To test the effectiveness of flex sensors in such environments, one of our subjects wore the sensor platform as before, but with the flex sensors misplaced. We consider two scenarios: in the first, the sensors placed on the right hand side of the body are moved

up, making them unable to capture the whole action. In the second scenario, we moved the flex sensors down toward the ground. The subject did all 11 movements again. The collected data in this way was fed into a classifier to determine if the system could detect the movements with misplaced sensors. Figure 17 shows the classification results. The overall accuracy for misplaced scenario was 74%.

Classification Accuracy
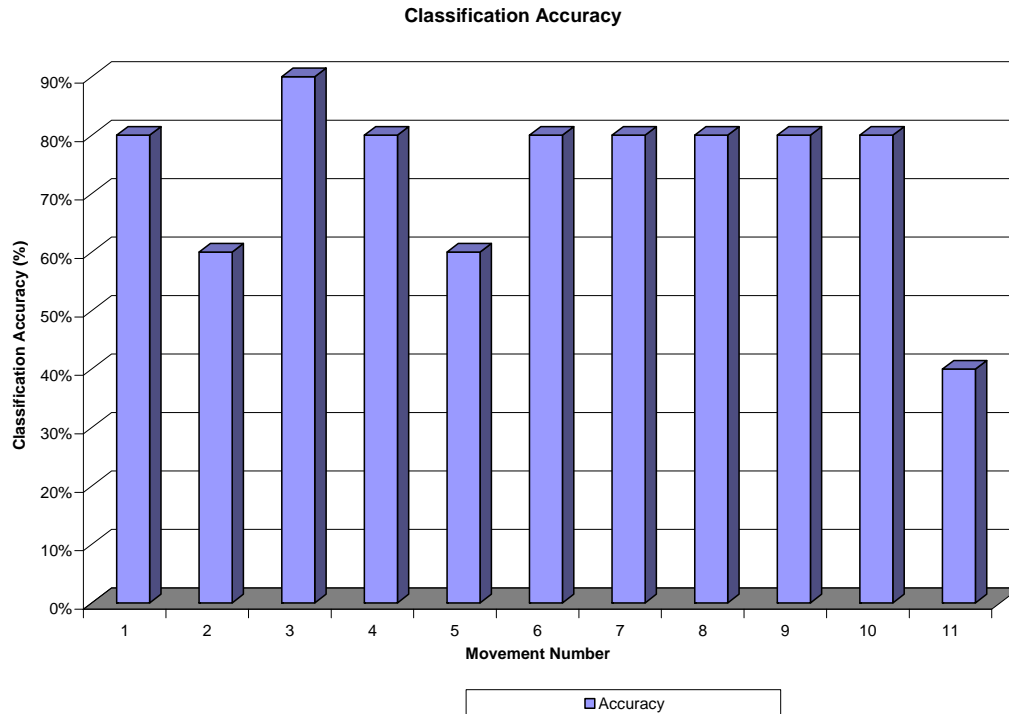
Figure 17. Classification accuracy for misplaced situation (flex sensor)

6. Conclusion

We have invested considerable effort into developing the individual pieces necessary for a wearable stress evaluation system. Our experimental results show that the system is effective at measuring the individual parameters necessary to determine stress level. The piezo-electric heart rate sensor was the most difficult component of the system, however, its functionality was successfully verified.

UTD-SPRING

Annual Report

June 20st 2007 – May 11th 2009

Dr. Walter Hu, Krutarth Trivedi, Mukti Aryal

Contact: walter.hu@utdallas.edu

Department of Electrical Engineering

Erik Jonsson School of Engineering and Computer Science

University of Texas at Dallas

Date: May 11, 2009

Primary Investigator: **Walter Hu**, assistant professor of Electrical Engineering

Student supported: **Krutarth Trivedi**, graduate student of Electrical Engineering.

Student partially supported: **Mukti Aryal**, graduate student of Physics Department.

Summary

Over the duration of the SPRING IV funding period, we have completed two projects, leading to three journal publications (one submitted and two under preparation). First, we have developed a fast and reproducible method for fabrication of nanoscale light sources with relatively inexpensive organic light emitting materials which alleviates charge spreading – a phenomenon that has been determined to be a limitation in scaling organic light emitting diodes (OLEDs) down to nanoscale (manuscript submitted to *Nanotechnology*). Second, we have fully characterized nanoimprint induced, geometry dependent, 3-D chain alignment in imprinted P3HT nanostructures. We show preferential alignment of P3HT in imprinted grating nanostructures which would allow efficient charge transport in devices with electric fields both parallel (organic field effect transistors) and perpendicular (solar cells) to the substrate (manuscript in preparation). Finally, we have developed a novel process to fabricate nanogratings over large areas with dimensions as small as 10 nm or less (manuscript in preparation).

I. *High density nano-channel organic light emitting diodes*

Krutarth Trivedi, Unnat Bhansali, Bruce Gnade and Walter Hu

Indium tin oxide (ITO) coated glass (Delta Technologies) served as OLED device substrates. Identical devices were fabricated on silicon for cross sectional SEM imaging of the device stack. The substrates were cleaned in acetone and isopropyl alcohol, treated with oxygen plasma and patterned by photolithography to define separate device areas. Nano-channel OLED devices with line and space gratings (100 nm each) were defined in SU-8 photo resist on top of the patterned ITO by NIL as shown in Fig. 1. SU-8 is expected to be stable during device operation as it has a post-crosslink glass transition temperature of over 200 ℃. In addition to having superior post-crosslink insulating and mechanical properties, it offers easy, low temperature fabrication (55-85 ℃) by NIL. The SU-8 was imprinted with a silicon mold (Nanonex), containing a large area of 100 nm line and space gratings with an average depth of 95 nm (Fig. 2a). The mold was treated with perfluorodecyltrichlorosilane (FDTS) to prevent adhesion of SU-8 to the mold during imprint. The imprinted SU-8 patterns were cured under UV (450 mJ/cm^2) and baked to facilitate cross-linking of SU-8. We found an initial spin-coated SU-8 film thickness of 95 nm results in uniform 75-85 nm tall features with a residue layer of 30 nm over an area of 4 cm^2 (Fig. 2b). Thickness of the residue layer increases with initial film thickness. Therefore, it is possible to control final SU-8 structure height after residue etching without changing the mold height. To expose ITO between SU-8 gratings, the residue layer must be etched while maintaining overall grating profile integrity. However, etching of the residue layer without protecting the imprinted features would result in a decrease in pattern height as well as rounding of the top surface of the imprinted features which could lead to conformal coating of the active materials. To selectively etch the residue layer, a hard masked residue

etching process was developed using oblique angle evaporation of chrome (Fig. 1c) at an angle of 10°, which allows selective coating of metal only on the top surfaces of SU-8 gratings. Figure 2b shows a SEM micrograph of imprinted patterns after oblique angle Cr deposition. The residue layer was etched in an inductively coupled oxygen plasma (5 mTorr, 25 °C, 300 watt ICP power, 100 watt bias power). The samples were etched for 10 seconds to account for any non-uniformity in the residue layer, assuring complete residue removal. The bulk of the residue is likely etched away in approximately three seconds while the ITO is further cleaned by the oxygen plasma for the remainder of the etch. Figure 2c shows a SEM micrograph of the imprinted SU-8 patterns after residue etch, with Cr remaining on top of the patterns. After residue etching, the samples undergo a two minute wet etch with CR-9S Cr wet etchant to remove the Cr mask, leaving only isolated SU-8 nano-channel gratings with ITO exposed between gratings. CR-9S Cr etchant is routinely used in photomask fabrication and is not expected to damage oxides such as ITO. This process produces rectangular gratings with sharp and vertical sidewalls, which is expected to prevent highly conformal coating during thermal evaporation of organics. In addition to nano-channel SU-8 gratings, we fabricated micrometer scale SU-8 line and space patterns with dimensions of two, five and ten micrometers by a standard photolithography process. Initial film thickness was calibrated to yield SU-8 gratings with the same height as nano-channel gratings.

Next, N,N'-Bis(naphthalen-1-yl)-N,N'-bis(phenyl)benzidine (NPB), tris-(8-hydroxyquinoline) aluminum (Alq_3), calcium (Ca), and silver (Ag) were deposited into the nano-channel and microscale SU-8 gratings by thermal evaporation, which is expected to produce uniform but more non-conformal filling in the SU-8 nanotrenches without significant sidewall coating. For all devices, 30 nm of NPB was deposited, followed by 75 nm of Alq3, 50 nm of Ca and 100 nm of Ag. The thickness of the individual organic materials inside the nano-channel gratings was carefully calibrated, as it can be vastly different from blanket deposition, which is used in conventional OLED device fabrication. Significant shadowing, caused by angled incident flux of organics inside the high aspect ratio trenches of nano-channel devices can occur during thermal evaporation as material is deposited in between and on top of the SU-8 gratings, resulting in non-uniform coating inside trenches. Consequently, the effect of shadowing increases as more material is deposited on top of the SU-8 gratings, as there is an effective increase in the aspect ratio of the trenches. Problematic shadowing can be alleviated by holding the substrates stationary over the organic sources during thermal evaporation. Devices fabricated on silicon, with identical nano-channel patterns, are placed alongside devices made on ITO coated glass in order to examine the filling inside the gratings with cross sectional SEM. Figure 2d shows a SEM micrograph of a typical nano-channel OLED device. The organics are deposited in the trenches as well as on top of the SU-8 gratings. However, in contrast to spin-coated active materials, the organic materials are deposited in a highly non-conformal manner, with a negligible amount of material on the sidewalls. The grating dimensions and filling properties are expected to be similar for devices fabricated on ITO coated glass.

All devices underwent electrical and optical characterization with a Keithley 2400 power supply and a photoresearch PR-650 Spectra Photometer interfaced with Labview. The OLED devices were biased only up to 10 volts to increase the lifetime of the device for repeated testing. Figure 3 shows the electrical and optical characteristics of nano-channel and microscale OLED devices fabricated on ITO coated glass. As seen in Fig. 3a, the current density of nano-channel OLED devices is observed to be higher than that of microscale devices. Current in OLED

devices is dependent on various parameters such as materials used and active layer thickness but less current in nano-channel OLED devices could be attributed to reduction of charge spreading by successful isolation of light emitting trenches from non-emitting SU-8 gratings, which is desired for discrete nanoscale light sources. Fig. 3b shows luminescence of microscale grating devices to be higher than the nano-channel OLED devices. The data shows that light output from the 2 µm grating device is not only brighter than the 5 and 10 µm grating devices, but the nano-channel devices as well. Hence, there is no clear geometry dependence in the brightness of OLED devices of varying grating size. At low bias, the nano-channel devices exhibited slightly lower brightness than the microscale grating devices while having a higher current density. However, nano-channel devices were brighter than microscale grating devices at higher current densities, beyond applied bias of 10 volts, reaching luminescence values exceeding 1000 Cd/m^2 at 15 volts. The observed higher current density paired with relatively lower luminescence at low bias are not related to scaling down of the dimension of light emitting trenches. Slight variation between devices is likely due to processing conditions from sample to sample. The process flow and conditions can certainly be optimized for better device performance. The electrical and optical characterization data of the nano-channel OLEDs show no geometry dependence and, therefore, indicate that miniaturization of OLEDs to nanoscale would result in similar performance as microscale devices, which makes them feasible as nanoscale light sources for near-field applications.

SPM was performed under ambient conditions with white light on both microscale and nano-channel OLED devices without metal cathodes. Metal was not deposited so that the surface of the organics can be scanned across the morphology of the devices. A Veeco Dimension V atomic force microscope system was set up for amplitude modulation (AM mode) SPM with a conductive 1Ω silicon tip having a spring constant of 40 N/m. An a.c voltage of 4 volts was superimposed on the tip, while a d.c voltage of 8 volts was applied to the sample, which caused the tip to oscillate in response to the electrostatic forces on the surface of the sample. During the surface potential scan, the tip is held 5 nm above the surface of the sample as the surface potential is recorded. Figure 4 shows SPM micrographs of the surface potential across several gratings of the microscale and nano-channel OLED devices as well as light emission profiles taken under an optical microscope (insets). The change in surface potential corresponds to the grating topography. A distinct difference in the surface potential on top of the SU-8 gratings and the trenches is immediately visible. In all devices, a higher surface potential is observed on top of the SU-8 structures, indicating a non-uniform charge distribution between the top of the SU-8 gratings and the trenches. Table I shows the same recorded average difference in surface potential (ΔSP) of organics on top of SU-8 gratings and inside trenches for all devices, regardless of geometry. The slight reduction in contrast and image quality for nano-channel gratings (Fig. 4d) is expected in AM mode as it is carried out in ambient conditions. More importantly, long range electrostatic forces affect the readings in AM mode, making it difficult to differentiate changes in surface potential that are too closely-spaced. The SPM measurements presented show a periodic difference in surface potential of organics inside trenches and on top of SU-8 gratings. This distinct periodic difference in surface potential can be attributed to electrical separation of the organic stacks inside trenches and on top of the SU-8 gratings. Furthermore, electrical separation of organic stacks is evident in the light emission profiles of microscale grating devices (insets of Fig. 4,b,c,d). Light is only output from the trenches, indicating electron-hole recombination is clearly confined to the organics inside trenches. This absolute confinement of the recombination region can be attributed to the

confinement of holes to the NPB inside trenches despite any thin layer of NPB on the sidewalls. It is apparent from the light emission profiles of microscale grating devices that charge spreading is not a problem in devices fabricated only with thermally evaporated NPB. Unfortunately, due to diffraction limitations of optical microscopy similar discrete light emission profile from nano-channel OLED devices cannot be observed directly. Nevertheless, the similar ΔSP observed in the microscale and nano-channel OLED devices indicates that light emission profile of nano-channel OLED devices should also be discrete with light output only from the nanoscale trenches in between the SU-8 gratings, much like light emission from microscale devices.

II. *Nanoimprint induced, geometry dependent 3-D alignment in imprinted P3HT nanostructures*

Mukti Aryal, Krutarth Trivedi and Walter Hu

Uniform 80 nm thin films of P3HT were prepared on a silicon substrate and soft-baked at 150 ˚C for 5 minutes on a hot plate. The films were imprinted with nanograting and nanoporous molds coated with 1H,1H,2H,2H-perfluorodecyltrichlorosilane (FDTS) as per the process flow shown in Fig. 5. The nanograting mold consists of 200 nm deep, 65 nm wide gratings at a period of 200 nm (Fig. 6a) while the nanoporous mold consists of a hexagonal array of 350 nm deep nanopores with 80 nm diameter (Fig. 6b). Nanoimprinting was done at 170 C for 10 minutes, after which the samples were de-moled at 25 C. P3HT nanogratings and nanopillar structures were obtained after releasing the mold from the sample (Fig. 7). With careful control of spin-coating and imprint conditions it is possible to control the thickness of the residue layer of imprints. As seen in the figure, the residue layer is controlled to be 20 nm.

P3HT crystallization and chain orientation were studied by in-plane and out-of-plane grazing incident XRD measurements. With this measurement only the lattice distances in the z-direction are detected with the (001) peak generally not detectable in any case. The schematic of face-on and chain-on orientations is given in the inset in Fig. 8a, ii and iii, respectively. The graph in Fig 8b. shows out-of-plane measurement of imprinted and non-imprinted thin film samples. Only the (100) peak, corresponding to lattice parameter a=1.69 nm, is observed, indicating edge-on orientation (Fig. 8a, iii) is dominant in all samples. . However, the lower intensity of the (100) peak for the nanoimprinted samples (gratings and pillars) indicates re-ordering of P3HT chains during nanoimprint. In-plane measurement is conducted to investigate the precise ordering of chains with respect to grating direction. As seen in figure 9, the (010) peak at 23.4^o, corresponding to the lattice parameter b=0.38nm, was detected for the non-imprinted thin film sample, consistent with the (100) peak observed in the out-of-plane measurement in Fig. 8 (blue curve). This is because edge on orientation observed in out of plane measurement means to π-staking parallel to the substrate or x-y plane which could be observed in in-plane measurement. Therefore both measurements show the dominance of edge on orientation in non imprinted P3HT film. The reordering of polymer chain nanopillar structures is proved since (100) peak in the graph of this sample (blue) dominates the same for the non imprinted sample (black). The increase in (100) peak intensity nanopillar structures compared to the thin film in in-plane measurement means that the lattice parameter a which was observed in z-direction in thin film reordered to become parallel to the substrate. The lattice parameter b is parallel to the substrate since (010) was detected only in the in-plane. With this, c-axis must be normal to the substrate. Therefore the polymer chain re-ordering of c-axis normal or the chain alignment with vertical polymer backbone was conformed in nanopillar structure. However, the chain ordering in nanograting structure is entirely different.

The intensity of the peak (100) varies with the sample rotation in nanograting sample. When the sample was scanned placing it in the thin film stage making grating direction parallel to the source the peak (100) intensity becomes huge and the intensity drops to noise level while the sample was placed making nanograting direction perpendicular to the source. Just opposite of this, the intensity of (010) peak was detected while scanning in perpendicular direction and that was dropped to noise level when scanning in parallel direction. This means the reordering of polymer chain depends on the geometry of the nanostructures. The chain alignment in nanopillar structure is isotropic in x-y plane since the sample rotation does not make any difference in the (100) peak intensity while the difference in (100) peak intensity in nanograting corresponding to sample rotation shows the anisotropy of chain orientation in x-y plane. While scanning parallel to the nanograting direction XRD detects chain ordering corresponding to the lattice parameter a i.e. side chain faces to x-direction as shown in Fig. 5.a.ii. and while scanning perpendicular to the nanograting direction XRD detects chain ordering corresponding to the lattice parameter b i.e. p-stacking faces to x direction as given in Fig. 5.a.iii. This only means that, 1) π-stacking direction corresponding to lattice parameter b is along the line grating direction parallel to the substrate, 2) the lattice parameter a is perpendicular to the line grating direction and parallel to the substrate, and 3) the lattice parameter c is normal to the substrate or the chains are vertically aligned.

Further to investigate the distribution of anisotropic chain orientation nanogratings, an azimuthal (ϕ) in plane prefer orientation scan with detector fixed at an angle $2\theta\chi$ 5.2^o corresponding to (100) peak was performed. The sample was rotated from -40° to 115° i.e. ϕ goes from -40° to 115°. The peak maximum was observed when the angle between the source and nanograting is about 3°. It shows that a-axis orientation centered perpendicular to the line grating direction and the distribution ranges from -20 and +20 which is shown in the Fig. 10.

Ordering of P3HT chains inside nanostructures during nanoimprint can be assesed by considering several fundamental theories from literature. There are three underlying reason behind the ordering of P3HT chains in nanostrucures: 1) Flow induced ordering into nanoscale dimensions at molten state under high pressure; 2) Nanoscale confinement of polymer and hydrophobic interaction between side walls of the Si mold and P3HT side chains due to surface treatment effects; 3) Self assemby of polymer due to side chain-side chain interaction and interaction. Polymer disentanglment commences with the application of heat during nanoimprint, followed by flow in the nanoscale. As this process continues, polymer chains start aligning along the flow direction, and most prominently along the sidewalls of the nanostrucures. At high temperatures (170 C in our experiments), individual molecular chains rotate freely along the backbone, with the hydrophobic side chains preferably turning towards the FDTS treated side walls of the nanostrucures on the mold. Thus, crystallization begins when the hydrophobic side chains of P3HT interact with the sidewalls of the mold, and this effect is cascaded throughout the imprinted P3HT. This cascade effect continues throughout theduration of the imprint, while reaching completion as the temperature is cooled down to room temperature. The chains cease to move as the temperature is reduced, forming comb-like polymeric structures. Finally, the rod–like segments are ordered in a parallel lamella-type stack with interdigitized alkyl side chains to achieve maximum van der Waals interactions. Therefore the π–π interchain interactions and the side chain hydrophobic interactions assist in formation of RR-P3Htcrystallites and hence stable 3-D chain alignment is possible. The effect of geometry is evident in the case of nanogratings, which exhibit preferential orientation of π-stacking along the nanograting. The less intense (100) peak for nanopillar structures compared to the parallel orientation of nanograting by in-plane

measurement (Fig. 9) indicates that the P3HT side chains in naopillar structures turn around the walls of nanopores and hence becomes isotropic in the x-y plane. Since most of the P3HT chains which were edge on oriented in P3HT film are reordered to c-axis normal, the out of plane (100) peaks for nanograting and nanopillar structures are less intensive than that of the thin film as shown in Fig.8. However, the presence of (100) peak, though less intensive, indicates the presence of highly crystalline edge on oriented P3HT chain.

The gaussian-like curve in figure 10 shows the distribution of alignment modes in the nanogratings. The distribution ranges from -20° to $+20^o$ which means that the π-stacking are tilting up to 20° with the side wall on both sides. Highly ordered polymer chain induced by polymer flow into nanostructures and nanoconfinement with in hydrophobic surface has been clearly observed. Regio-random polymer chains present in the nanostructures causes the kink or chain folding so that the continuous crystalinity breaks to form crystal domains with amorphous boundries. Therefore nanoimprinting was proven to have dominant effect on polymer chain alignment and the nanoimprinting conditions such as time, tempearture, pressure and starting film thickness can be controlled. Another important factor is the geometry effect which is seen in nanopillar and nanograting structures.

In summary, we have shown that P3HT chain ordering is significantly impacted by nanoconfinement in nanostrutured geometries during nanoimprint lithogprahy. The extent and morphology of chain ordering can be controlled by mold geometry as well as nanoimprint process conditions. The mechanism of ordering and alignment is discussed and is found to be supported by fundamental studies conducted by several authors. Preferential chain alignment and control of 3-D morphology was achieved and clearly examined by XRD. The resulting aligned P3HT nanostrucures are believed to offer superior charge transport properties in both solar cell and FET applications. We believe that the $\pi-\pi$ stacking along the nanograting would enhance mobility FETs while the vertical (c-axis normal) alignment and $\pi-\pi$ stacking across the nanograting would facilitate enhanced charge separtation in solar cells. Further enhancement of polymer alignment and crsytallinity can be achieved by fine-tuning imprint conditions as well as polymer quality.

III. *Dimension reduction of gratings by controlled reflow of patterned polymer mask*

Krutarth Trivedi and Walter Hu

In this project, we have also developed a simple and well controlled process of dimension reduction to single-digit nanometer regime by controlled reflow of lithographically (nanoimprint lithography) defined polymer lines to reduce the slope of the grating sidewall, followed by oblique angle metal evaporation and inductively coupled plasma (ICP) etching (Fig. 11). This low-temperature method offers good dimensional control and is applicable to a wide variety of materials. One application to make nanoimprint molds with narrow trenches (~10 nm) is demonstrated. First, 50K PMMA is imprinted with a mold containing a large area of 100 nm line and space gratings (Nanonex). Then, the sample is heated above the glass transition temperature of PMMA, causing partial melting of the imprinted PMMA gratings while still preserving the overall imprinted profile. Extent of melting, characterized by the change in sidewall slope of imprinted lines, can be well controlled by duration (Fig. 12) and temperature of

heating. Then, a metal layer is deposited onto the sloped PMMA gratings by oblique angle evaporation. By adjusting the angle during metal evaporation, it is possible to control the size of the opening in the metal coating on the imprint profile (Fig. 13). The metal serves as a mask for etching of exposed PMMA, between openings in the metal, by oxygen ICP as well as transfer of patterns to the oxide layer by ICP etching in a mixture of C_4F_8, CHF_3 and Ar. Using this process, the trench width can be precisely controlled down to as small as 10 nm or less (reduced from original 100 nm line and space PMMA gratings) and resulting patterns exhibit excellent quality and controllability (Fig. 14).
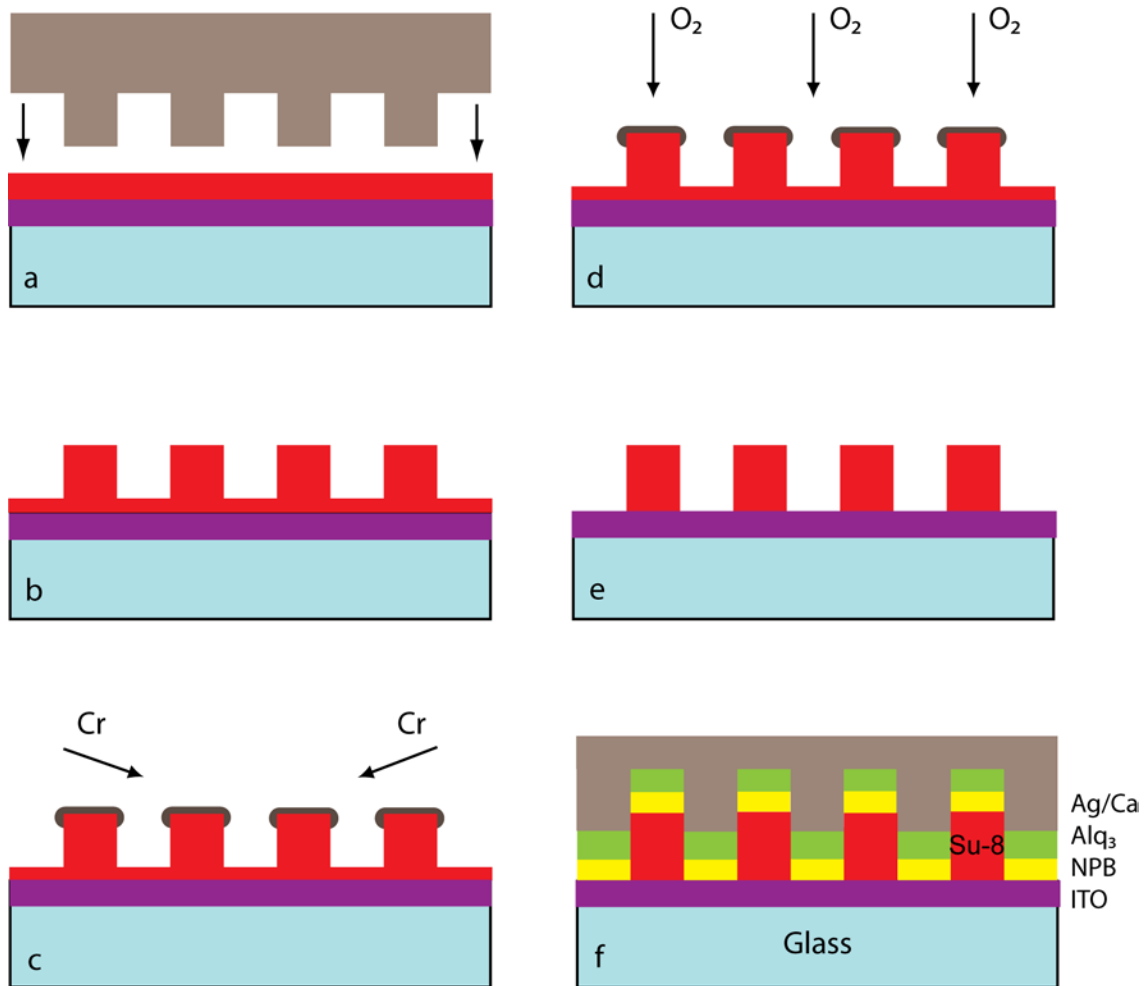
Figures and Tables:

Figure 1: Nano-channel OLED process flow a) Si mold is pressed into the SU-8 film on ITO coated glass; b) the mold is removed, leaving imprinted SU-8 gratings; c) Cr is coated on top of the imprinted SU-8 gratings at an oblique angle; d) the residue is etched by O_2 plasma, with the Cr protecting the SU-8 gratings; e) the imprinted SU-8 gratings are isolated after O_2 plasma etch; f) organics and metal are deposited by thermal evaporation.
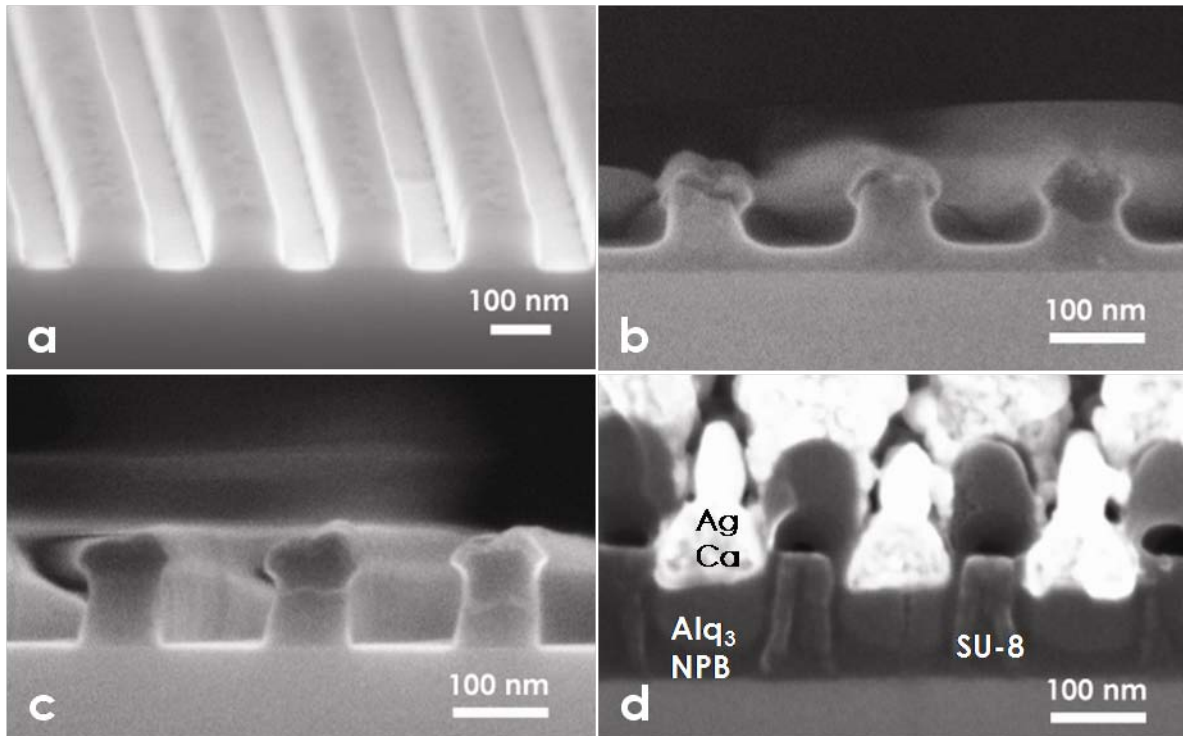
Figure 2: SEM micrographs showing cross sections of a) the Si mold used to imprint the SU-8; b) imprinted SU-8 gratings after oblique angle Cr evaporation; c) isolated SU-8 gratings with Cr on top after O_2 plasma etch; d) a typical nano-channel OLED device after thermal evaporation of organics and metal.
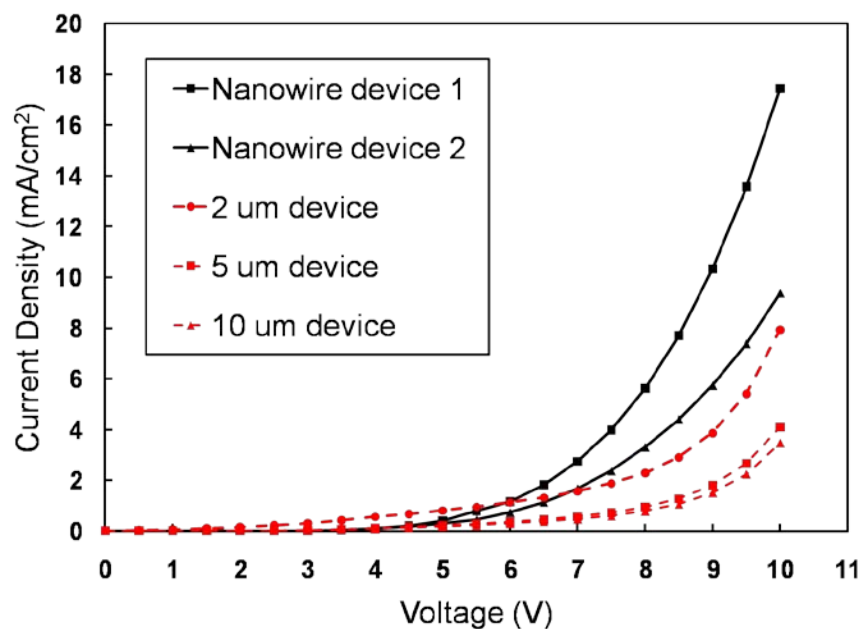
(a)
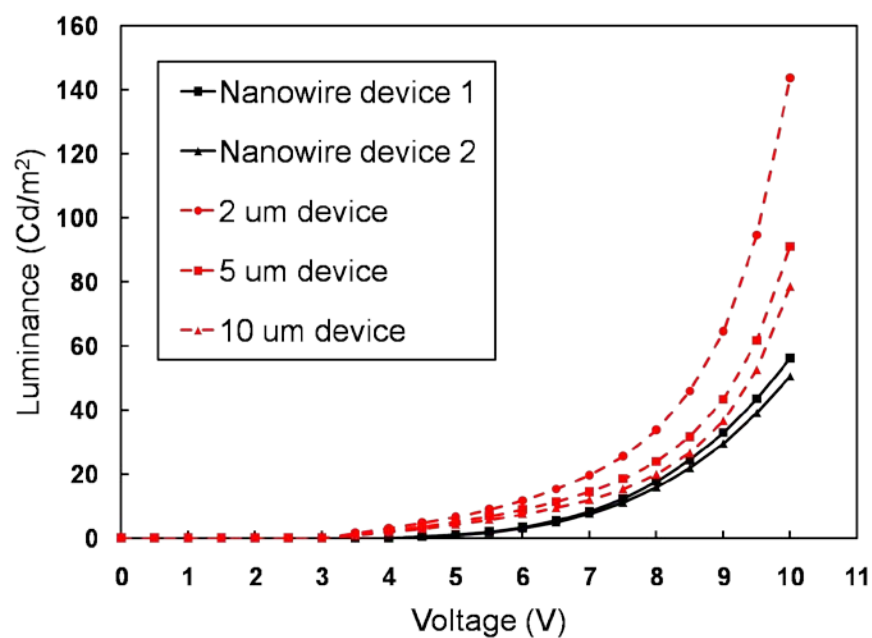
(b)

Figure 3: Electrical characterization data showing a) current density vs. voltage characteristics; and b) luminescence vs. voltage characteristics of microscale and nano-channel OLED devices.
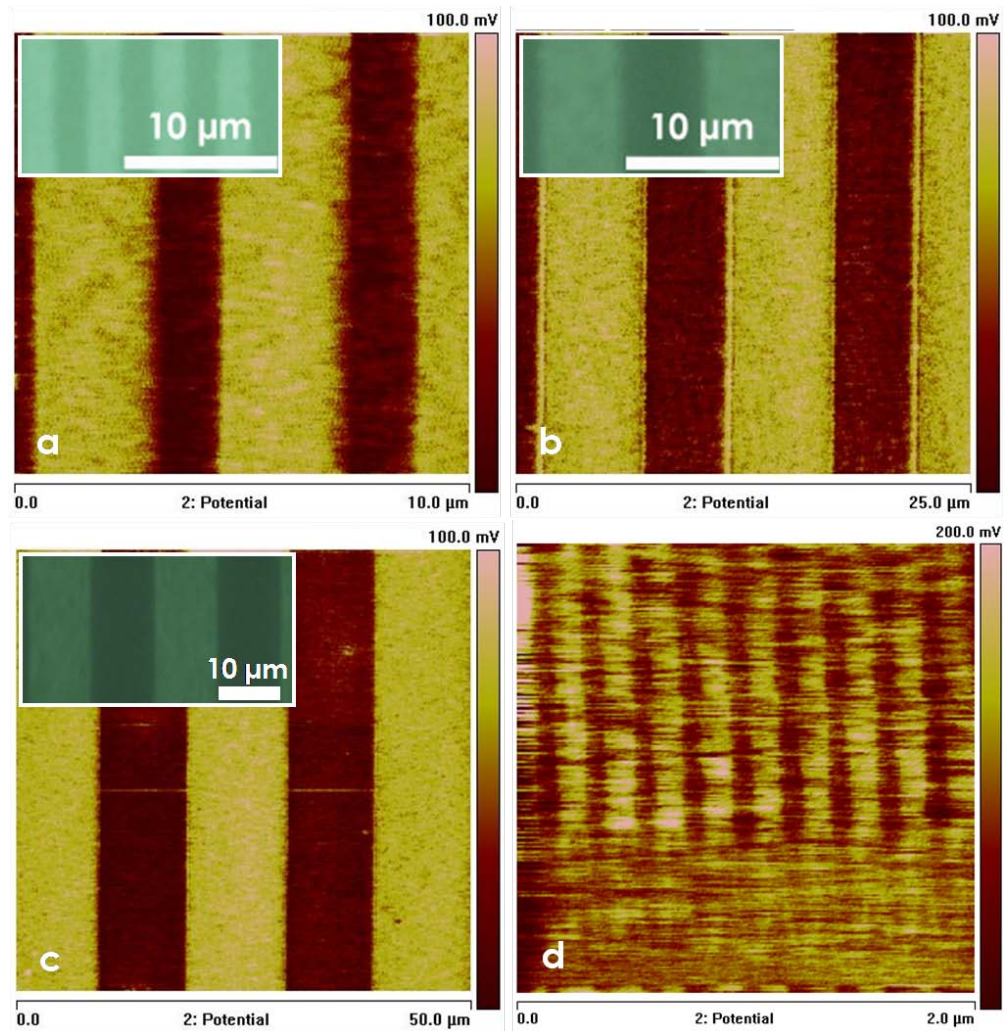
Figure 4: Surface potential micrographs with insets showing light emission profile under optical microscope of a) 2 µm grating; b) 5 µm grating; c) 10 µm grating; and d) nano-channel OLED devices.

Table I

Grating Dimension	Average ΔSP
10 µm gratings	64 mV
5 µm gratings	63 mV
2 µm gratings	68 mV
100 nm gratings	65 mV
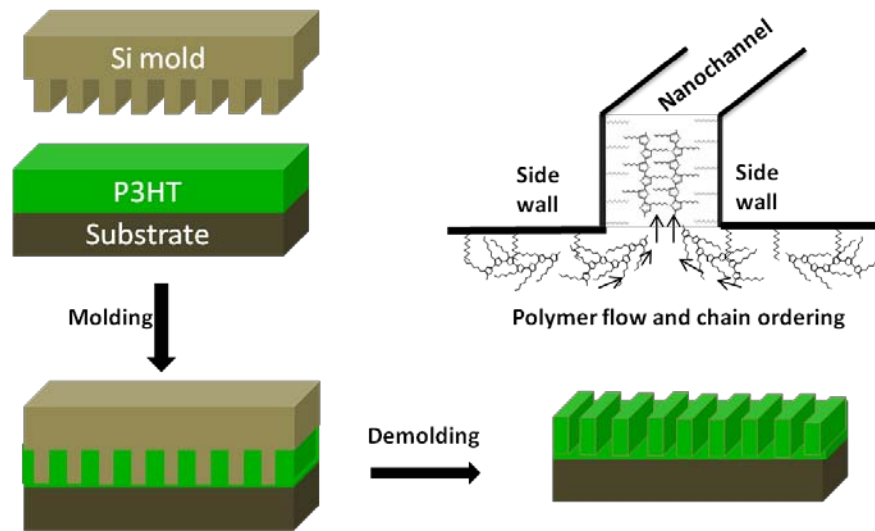
Figure 5: Schematic of nanoimprinting process and P3HT chain alignment during flow into nano-gratings of the mold.
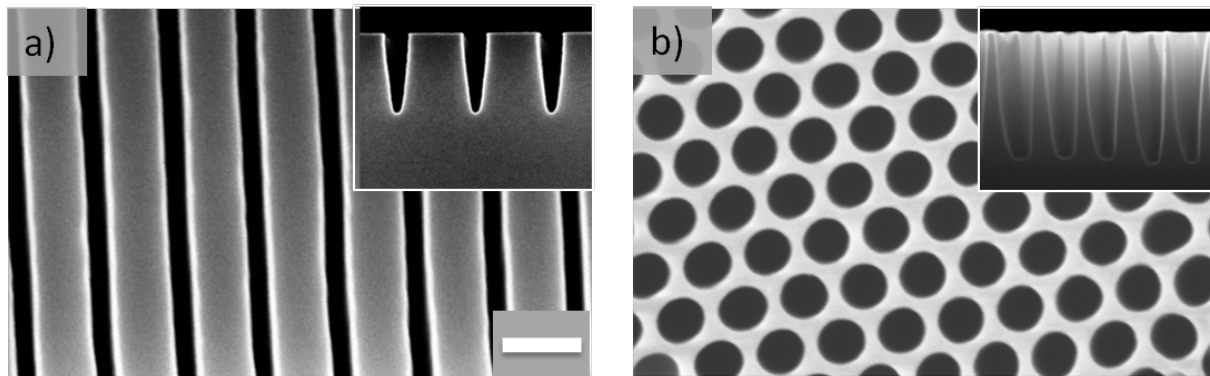
Figure 6: SEM top view of Si molds a) nanogratings of period 200 nm, width 65 nm and depth 200 nm b) hexagonal array of nanopores of diameter 80 nm and height 350 nm, separation of 30 nm. Insets show cross sectional views. Scale bar 200 nm.
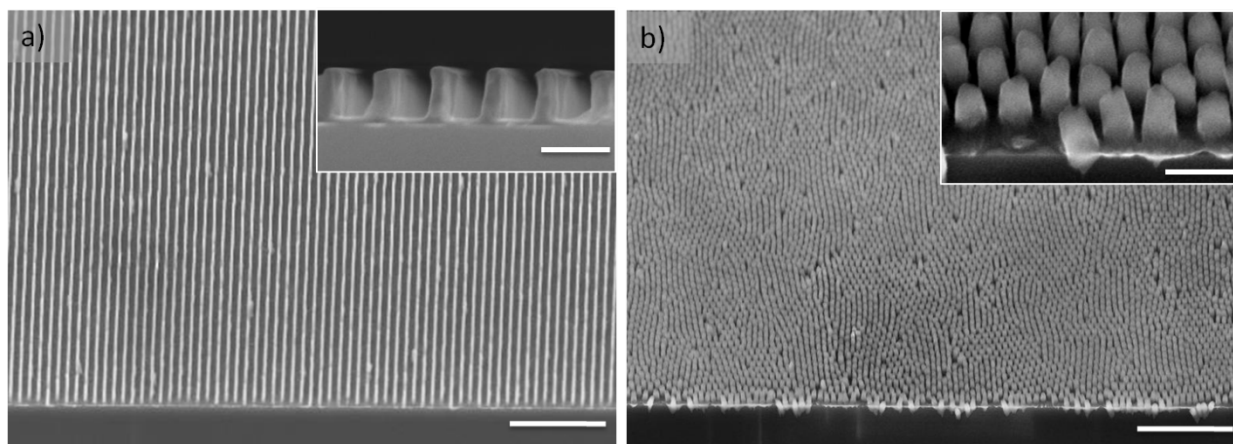
Figure 7: SEM images of 45° tilted view of P3HT a) nanogratings of period 200 nm, width 65 nm, height 200 nm and the residual layer of 20 nm, b) hexagonal array of nanopillars of diameter 80 nm and height 150 nm, separation of 30 nm, with residual layer of 20 nm. Insets show cross sectional views. Scale bar is 2 µm and 200 nm for the tilted view and insets, respectively.
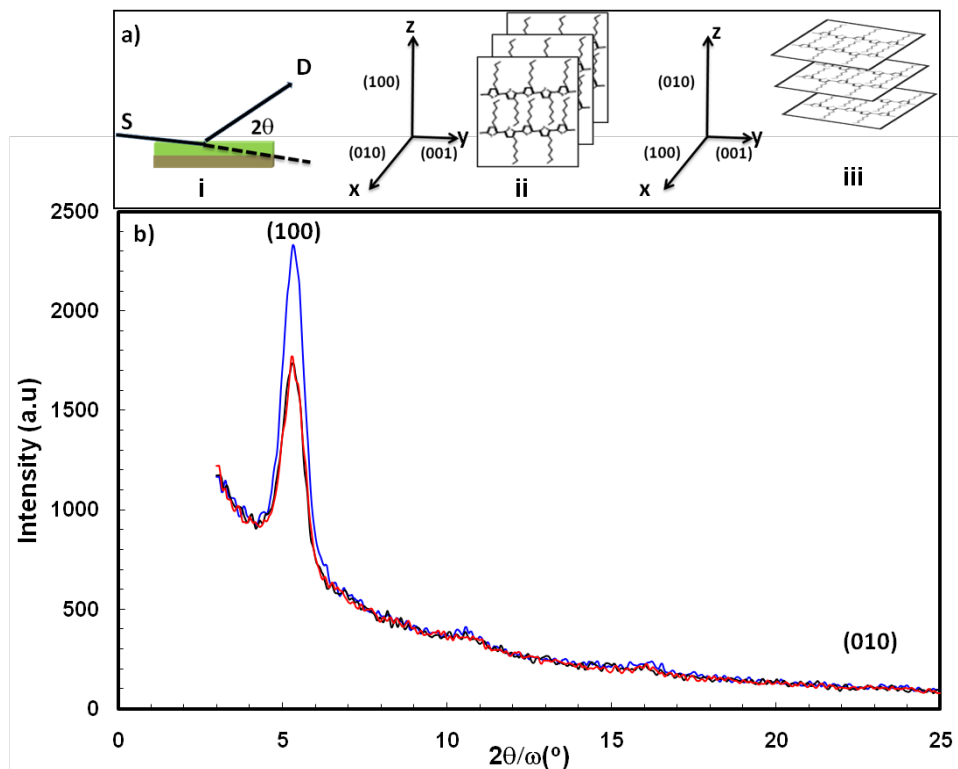
Figure 8: a) Schematic of i) out of plane measurement with fixed source (S) and detector (D) moving in the vertical plane, ii) edge on orientation iii) face on orientation for the detection of lattice in z direction b) out of plane XRD measurement for the detection of lattice normal to the substrate. The detection of edge on orientation conforms edge on chain alignment of P3HT structures for thin film (blue), nanogratings (black) and nanopillar (red). The decrease in (100) peak intensity indicates the rearrangement of P3HT chain due to nanoimprinting.
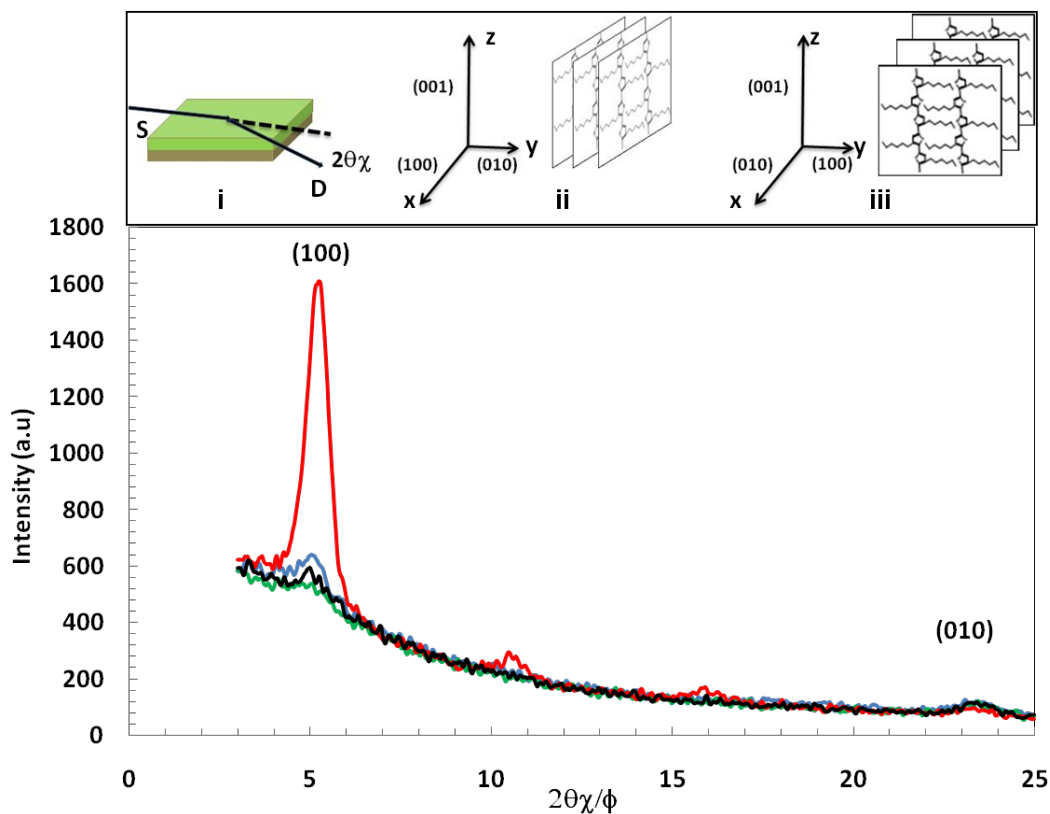
Figure 9: a) Schematic of XRD i) in-plane measurement with fixed source (S) and detector (D) moving in the horizontal plane; detection of ii) (100) and iii) (010) lattice orientation on x-direction, b) out in-plane XRD measurement for the detection of lattice along x-direction. Red curve for the nanograting when aligned along y-direction and green for that when aligned along x-direction, blue is for nanopillars and black for the film. The difference between red and green curve conforms the preferential chain orientation of P3HT chain in nanograting as shown in schematic a).
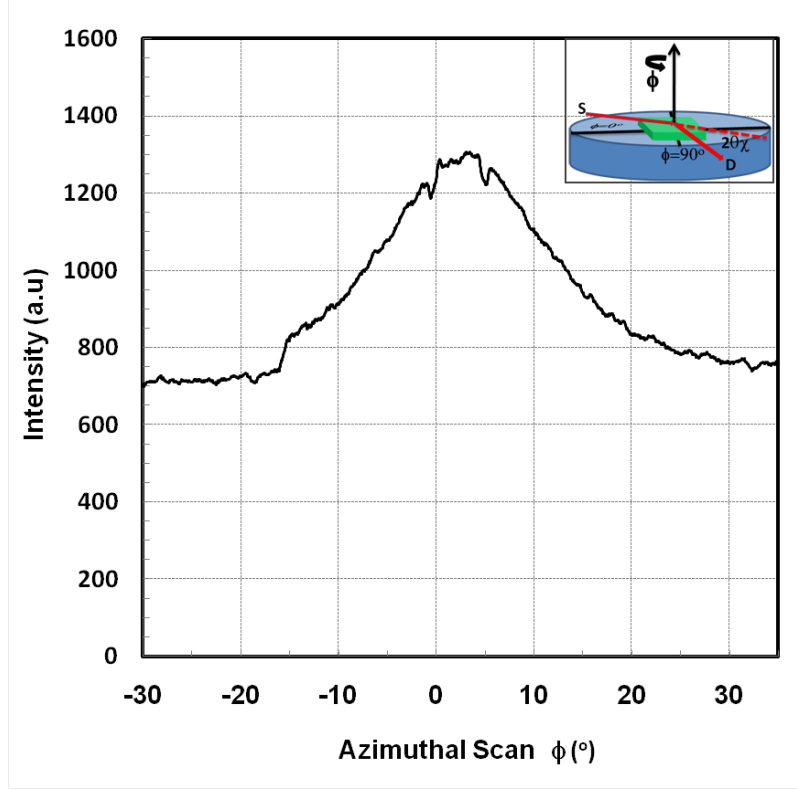
Figure 10: XRD in-plane ϕ scan measurement for the grating structures. Inset shows the schematic of the measurement. The sample is placed so that when ϕ=0° the sample is aligned with ϕ=0° cross hair position as shown and the nanograting become parallel to the incident beam. The incident beam makes an angle ϕ with the direction of nanograting when the thin film stage rotated through an angle ϕ. The detector is fixed at 2 θ = 5.2^o.
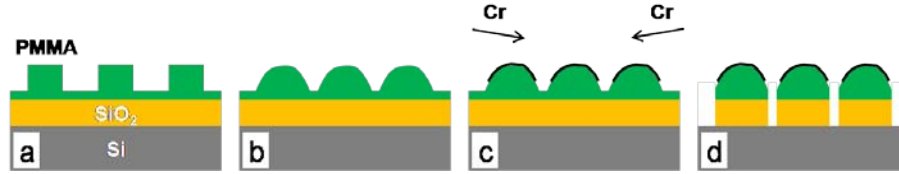
Figure 11: Schematic showing imprinted (a), and then melted PMMA lines (b), oblique angle metal evaporation on melted lines (c) and ICP etch to substrate (d).
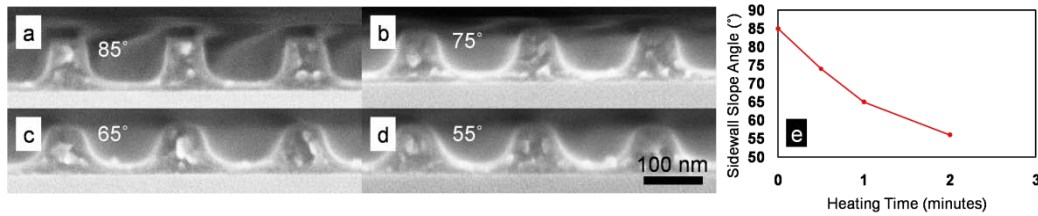
Figure 12: SEM X-section showing imprint profiles with measured sidewall slope angle before (a) and after heat treatment at 125˚C for 30 seconds (b), 1 minute (c), and 2 minutes (d) (scale bar is shared); (e) Sidewall slope angle of imprinted gratings heated at 125˚C as a function of heating time.
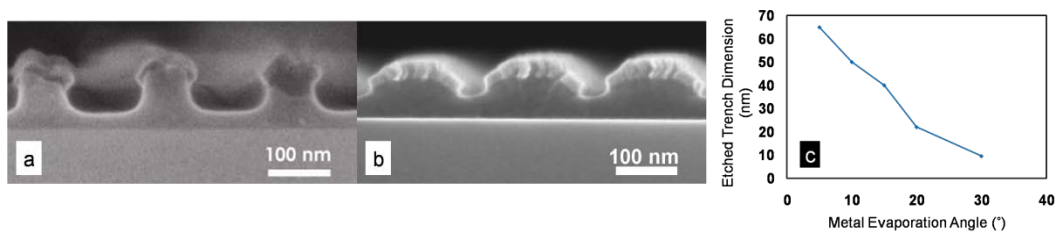
Figure 13: SEM X-section showing imprinted profiles after oblique angle Cr evaporation on gratings without heat treatment (a) and with heat treatment (b); (c) Etched trench dimension in oxide as a function of metal evaporation angle.
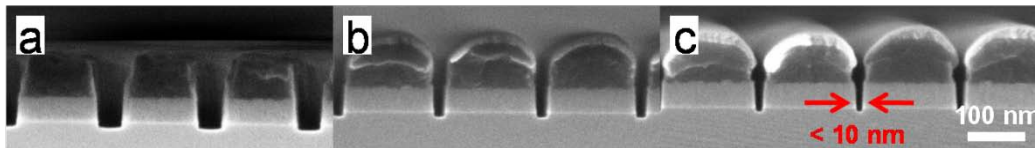
Figure 14: SEM X-section showing patterns etched into oxide after oblique angle Cr evaporation on melted imprint profile at 10˚ (a), 20˚ (b) and 30˚ (c).

19

Final Report

SPECTROSCOPY OF ELECTRONIC EXCITATIONS OF CARBON NANOTUBES IN POLAR ENVIRONMENTS

UTD-SPRING/AFOSR Project

PI: *Dr. Yuri Gartstein* (Department of Physics)

I. Overiview

The scope of our work in this Project has been theoretical studies and modeling of charged and neutral excitations of carbon nanotubes and related one-dimensional (1D) semiconductor nanostructures (such as nanowires and conjugated polymers) as affected by surrounding polarizable environments. A particular focus has been on the effect of solvation of excess charge carriers by the slow (orientational) polarization of the surrounding polar solvent. This is the situation of particular relevance to applications and processes involving fundamental redox reactions, including (photo)electrochemistry. It should be noted that redox chemistry of carbon nanotubes has been deemed in the literature as "emerging field of nanoscience" and solvatochromic effects are being increasingly researched. As a result of solvation, excess charge carriers can become self-localized forming large-radius 1D adiabatic polarons whose properties are distinctly different from the parent band electronic states. The energetic significance of the solvation has been emphasized by finding that the binding energy of the resulting 1D polarons could reach a substantial fraction, roughly one third, of the binding energy of Wannier-Mott excitons, the well-known primary photoexcitations in many 1D semiconductors. This may lead to enhanced charge separation. On the other hand, the mobility of solvated charge carriers is drastically reduced due to the dissipative drag of the medium. Our emphasis was on clarifying some conceptual issues and, mostly, on working out experimentally testable signatures of such solvation-induced polarons.

We have been keeping our counterparts at Rice University abreast of our findings that could serve as theoretical expectations for future experiments. In turn, experimental data from Rice on the effects of hydrocarbon environments on excitonic transition in carbon nanotubes is being currently employed by us in evaluations of the dynamical dielectric effects on electron- and hole-quasiparticles.

1. Personnel involved

The following personnel received various amounts of financial support from the funds provided by this grant: (1) Yuri Gartstein (PI); (2) Tony Bustamante (undergraduate student); (3) Michael Mayo (graduate student); (4) Geoffrey Ussery (graduate student).

Due to the mismatch of the project period endings (April 30) and the official UTD semester duration dates, no student support during Spring semesters was possible to arrange. This resulted in leftover personnel support funds, which could be used to support the in-progress research, should a no-cost extension be granted.

2. Student training and development

All students involved in the project have been receiving training expanding their knowledge of related physical and chemical aspects of the problems. No less important, they

1

substantially improved their practicing skills, both conceptual and computational, and had multiple opportunities to appreciate the synergy of ideas and methods characteristic of modern nanoscience.

Their research within the framework of the project has also resulted in important personal development steps as signified in submitted theses/proposals:

- Tony Bustamante, Senior Honors Thesis "Environmental and Geometrical Effects on Excitons in Carbon Nanotubes" defended in 2007.

- Geoffrey Ussery, PhD Thesis Proposal "Physical properties of solvated charge carriers on one-dimensional semiconductors" submitted. PhD defence is expected in the Summer 2009.

- Michael Mayo, PhD Thesis Proposal "Model ab initio study of excess charge carrier solvation on conjugated carbon chains" submitted. PhD defence is expected in the Fall 2009.

3. Peer-reviewed publications of the completed work

The following papers have already been published acknowledging support from UTD-SPRING Research and Nanotechnology Transfer Program:

- Yu.N. Gartstein, T. D. Bustamante and S. Ortega Castillo, "Polarons and excitons on a cylinder: a simplified model for nanotubes in polar environments", *Journal of Physics: Condensed Matter* **19**, 156210 (2007).

- Yu.N. Gartstein and V.M. Agranovich, "Excitons in long molecular chains near the reflecting interface", *Physical Review B* **76**, 115329 (2007).

- Yu.N. Gartstein and G.L. Ussery, "One-dimensional semiconductor in a polar solvent: Solvation and low-frequency dynamics of an excess charge carrier", *Physics Letters A* **372**, 5909 (2008).

- M.L. Mayo and Yu.N. Gartstein, "Charge carrier solvation and large polaron formation on a polymer chain revealed in model *ab initio* computations", *Physical Review B* **78**, 073402 (2008).

- G.L. Ussery and Yu.N. Gartstein, "Optical absorption from solvation-induced polarons on nanotubes", *Journal of Chemical Physics* **130**, 014701 (2009).

- M.L. Mayo and Yu.N. Gartstein, "Model *ab initio* study of excess charge carrier solvation and large polaron formation on conjugated carbon chains", *Journal of Chemical Physics* **130**, 134705 (2009).

4. Presentations of the completed work

Scientific results of the project have been presented at several venues:

- Yuri Gartstein and Tony Bustamante, "Nanotubes in Polar Media: Polarons and Excitons on a Cylinder", UTD-Technion Workshop; UTD, January 2007

- Yuri Gartstein and Tony Bustamante, "Nanotubes in polar environments: polarons vs excitons", Oral presentation at the 7th International Conference on Optical Probes of Conjugated Polymers and Functional Self-Assemblies; Turku, Finland, June 2007

- Geoffrey Ussery and Yuri Gartstein, "Nanotubes in polar environments: Solvated charge carriers and their dynamics", APS March Meeting; New Orleans, March 2008

- Michael Mayo and Yuri Gartstein, "Charge carrier solvation on a polymer chain revealed in ab initio computations", APS March Meeting; New Orleans, March 2008

- Michael Mayo and Yuri Gartstein, "Model *ab initio* studies of solvation and excess charge localization on conjugated carbon chains", APS March Meeting; Pittsburg, March 2009

- Geoffrey Ussery and Yuri Gartstein, "Nanotubes in polar solvents: Solvation and physical properties of excess charge carriers", 2009 Spring Meeting of the Texas Sections of the APS, AAPT, and SPS; Stephenville, Texas, April 2009

5. The work in progress and future plans

In addition to the completed work cited above, there is an intense ongoing work that will continue until an acceptable level of fruition is achieved. The following tasks are being currently addressed:

- *Electron transfer between 1D semiconductors (nanotubes) and small molecular species.* Classic descriptions of the electron transfer as applied to chemical reactions in solutions and to electrochemistry include Marcus theory of the transfer between small molecular species and Marcus-Gerischer model of the transfer to bulk semiconductor electrodes. In the former, the solvent fluctuations affect the discrete electronic levels of both constituents while in the latter, the band structure of the semiconductor is considered rigid thereby represented by the bare density of electronic states. The strong solvation effect we have studied for excess charge carriers on 1D semiconductors requires a description "in between" those two as the solvent fluctuations "smear" the rigid electronic structure and produce localized molecular orbitals with intragap energies. We are working on the corresponding theoretical development.

- *Ab initio studies of solvation.* In order to better evaluate the role of many-electron effects, we are pursuing a systematic comparative study of polaronic effects at different levels of the theory. Compared will be various hybrid DFT and pure Hartree-Fock computations. Also under consideration is application of time-dependent PCM schemes dubbed recently "a new frontier for quantum-mechanical continuum models". We also explore types of charged excitations other than simple polarons, such as kink-solitons and bipolarons.

- *Modulation of the exciton energies in carbon nanotubes by various dielectric environments.* The observable exciton energy is determined by both the gap energy for individual electron and hole quasi-particles and their binding energy. We are currently evaluating the effects on quasi-particle excitations that result from the fast polarization components in order to compare them to corrections from the exchange interactions previously discussed in the literature. Also of interest here is the modulation of the excitonic effects by vibrational modes of the environment whose energies are close to the exciton binding energy.

We believe the scope of our studies is of relevance and potential importance for various applications of carbon nanotubes and related 1D nanostructures. We intend to use results derived during this project to apply for further funding opportunities to be able to continue this line of research. We have already submitted one proposal entitled "Quantum chemistry of electron solvation on conjugated polymers" (Welch Foundation), and more is in the planning stage.

II. Synopsis of some scientific results

A comprehensive discussion of our results is available on the following pages. In this section we attempt to briefly introduce and comment on some of the results.

- *Comparing polarons and excitons: the energetic significance of the effect of solvation.* Within a simplified model of charge carriers on semiconducting nanotubes in sluggish polar environments (such as common solvents), we compared the binding energies E_b^{exc} of the Wannier-Mott exciton (a closely bound electron-hole pair) and of the polaron, E_b^{pol}. Our variational study demonstrated a non-monotonic dependence of the ratio of the binding energies $E_b^{\text{pol}}/E_b^{\text{exc}}$ on the radius of the nanotubes and that this ratio may reach values as large as about 0.35. As the exciton dissociation under these conditions would occur into a polaron pair, the thermal activation energy $E_b^{\text{exc}} - 2E_b^{\text{pol}}$ for the dissociation is thereby decreased by a factor of about 3 compared to the bare exciton binding, evidently a very substantial effect. It is expected that this should result in enhanced separation of charge carriers and could be an attractive proposition for applications requiring both strong excitonic transitions and the relative ease of exciton dissociation. We believe we elucidated the basic physics behind this behavior that we characterized as the crossover effect occurring in systems crossing over "between" pure 3D, 2D or 1D. Hence, we conjecture the relevance for other semiconducting nanostructures (quantum wells, quantum wires) in contact with polar environments and the possibility to judiciously exploit other geometries. Another generic implication is the possibility to influence some excitations more than the other by geometrical means, that is, by selectively matching the geometry to the size of the desired excitation.

- *Coherent optical properties of exciton-polaritons in 1D molecular systems in the vicinity of a metallic substrate*, an environment characterized by a strong and fast polarization. In this study, we focus on a more tractable model of (small-radius) Frenkel excitons. With a proper modification for specifics, however, results are expected applicable to various systems including nanotubes and quantum wires. The metallic substrate acts as to modify the inherent optical properties, hence the systems of this composition may be of relevance for optoelectronic and plasmonic applications. Our results indeed showed a strong modification of patterns of the radiative decay and elucidated the dependence of the effects on the polarization and energy of the excitons as well as on the distance from the interface. A major channel of the decay has been found to be the excitation of surface plasmons of the substrate. In an idealized system, the exciton-polaritons form two branches in their spectrum: one is "super-radiant" with respect to surface-plasmon emission and the other is non-emissive representing bound exciton-surface-plasmon states. Taking into account the realistic dissipation of in the substrate modifies the idealized picture in two regards. First, as the wave vector of surface plasmons acquires a finite uncertainty, there is no clean-cut separation into emissive and non-emissive branches. Second, the excitons can decay in a non-coherent way via Joule losses in the metal. The results suggest that one could control the relative importance of the processes by the variation of the distance to the substrate.

- *Mobility and low-frequency dynamics of polarons.* A simplified dynamical model has been developed that allowed to study the formation and low-frequency properties of polarons as solvated charge carriers. The model embarks from the combined microscopic dynamics of the excess electron charge density and the surrounding Debye solvent to result in a macroscopic Langevin dynamics of the polaron center of mass. This way

we have been able to derive a closed-form solution for such an important characteristic as polaron mobility and find its functional dependence on the properties of the semiconductor and the solvent. Importantly, numerical estimates indicate that polaron mobilities can be orders of magnitude lower than the intrinsic mobilities. We have also identified local solvent dielectric relaxation modes forming around the polaron that may play a role in the low-frequency absorption.

- *Optical absorption from polarons.* Another testable experimental signature of polarons is the higher-frequency (infrared) absorption from a local polaron level. We performed calculations of such absorption based on a simplified model of solvated carriers on nanotubes. The calculations show that over a wide range of system parameters, the major contribution (oscillator strength of about 0.85-0.9) to the absorption corresponds to the promotion of a charge carrier to the next local level (rather than to the band states) within the polarization potential well. The transition energy was evaluated as a function of system parameters that should assist in prospective experimental studies. We have also shown that thermal fluctuations of the environment result in a substantial (order-of-magnitude larger than the thermal energy) broadening of this transition. Gross features of the resulting absorption line shapes have been illustratively calculated.

- *Ab initio studies of excess charge carrier solvation.* Using state-of-the-art hybrid DFT calculations in conjunction with the Polarizable Continuum Model (PCM) as implemented in Gaussian 03, we have been able to accomplish a first - to the best of our knowledge - *ab initio* demonstration of the solvation-induced self-consistent localization of the excess charge leading to 1D large-radius polaroninc states. As these computations are quite demanding, this demonstration relied on conceptually prototypical but structurally simpler systems of conjugated polyynic carbon chains. Both electron- and hole-polarons have been shown to be emerging entirely due to solvation but even larger degrees of charge localization can occur when accompanied by carbon atom displacements. *Ab initio* computations are expected to help in clarification of the role played by many-electron interactions, and in fact, our results indicate the reorganization of valence band electrons taking place upon the polaron formation. From a theoretical standpoint, our demonstration can also be thought of as a new avenue for applications of quantum-mechanical continuum solvation models.

Polarons and excitons on a cylinder: a simplified model for nanotubes in polar environments

Yu N Gartstein[1], T D Bustamante[1] and S Ortega Castillo[2]

[1] Department of Physics, The University of Texas at Dallas, PO Box 830688, FO23, Richardson, TX 75083, USA
[2] FAMAT, University of Guanajuato, Guanajuato, Mexico

Abstract

Excess charge carriers on semiconducting nanotubes immersed in sluggish polar environments can undergo self-localization into polaronic states. Using a simplified model of electrons and holes of equal effective masses and confined to a cylindrical surface in the three-dimensional polar medium, we evaluate the binding energy E_b^{pol} of adiabatic Fröhlich–Pekar polarons and compare it to the corresponding exciton binding energy E_b^{exc}. The ratio E_b^{pol}/E_b^{exc} is found to be a non-monotonic function of the cylinder radius R which, in an idealized model, can reach values of about 0.35, substantially larger than values of about 0.2 for two-dimensional (2D) or three-dimensional (3D) systems. We argue that these findings represent a more general crossover effect that could manifest itself in other semiconductor nanostructures in 3D polar environments. As a result of the strong polaronic effect, the activation energy of exciton dissociation into polaron pairs is significantly reduced, which may lead to enhanced charge separation.

1. Introduction

Low-dimensional semiconductor structures such as quantum wells, quantum wires, nanotubes and conjugated polymers are important for practical applications and interesting scientifically. It is known that the confinement of the motion of charge carriers in some directions leads to increased effects of the Coulomb interaction on system excitations. In this paper we are concerned with two types of such effects: *excitonic* and *polaronic*. The excitonic effect refers to the formation of Coulombically bound electron–hole pairs, Wannier–Mott excitons, which progressively affect optical properties of semiconductors: the exciton binding energy E_b^{exc} increases from its 3D value to 2D and, further on, to quasi-one-dimensional (1D) magnitudes (E_b^{exc} diverges in pure 1D) [1]. The polaronic effect occurs in polar media, where the Coulomb field of an individual charge carrier causes the polarization (deformation) of its surroundings, resulting in the carrier self-localization into polaronic states. Such polarons have been extensively studied especially in the context of 3D ionic crystals and polar

semiconductors [2–5]. The polaronic effect also grows with the confinement: the polaron binding energy $E_{\rm b}^{\rm pol}$ in 2D is larger than in 3D and would diverge in pure 1D [6, 7]. Multiple aspects of the excitonic and polaronic effects have been explored in many publications for various specific low-dimensional systems.

Of particular interest to us is a relationship between $E_{\rm b}^{\rm exc}$ and $E_{\rm b}^{\rm pol}$, each of the binding energies understood as being measured from the band edges in the absence of the polaronic effect. The ratio $E_{\rm b}^{\rm pol}/E_{\rm b}^{\rm exc}$ of the binding energies has a clear significance for the relative energetics of closely bound and well-separated electron–hole pairs that is expected to affect practically important processes of charge separation and recombination. The bare value $E_{\rm b}^{\rm exc}$ signifies the ionization energy, whether thermal or photo, required for 'unbinding' of the exciton into a well-separated band-edge electron and hole. In the presence of the polaronic effect, however, the thermal ionization (dissociation) would occur into a distant electron–polaron and hole–polaron so that the exciton thermal ionization energy is reduced from $E_{\rm b}^{\rm exc}$ to $E_{\rm b}^{\rm exc} - 2E_{\rm b}^{\rm pol}$. We are interested in how much of this relative reduction might be possible to achieve due to the formation of *strong-coupling* (adiabatic) polarons. Our discussion here is restricted to systems with equal electron and hole effective masses, $m_{\rm e} = m_{\rm h} = m$, so that the electron–polaron and hole–polaron have the same binding energies while the closely bound exciton is neutral both globally and locally and therefore does not polarize the sluggish component of the medium in the adiabatic approximation [8, 9].

It is instructive to look at the ratio $E_{\rm b}^{\rm pol}/E_{\rm b}^{\rm exc}$ based on the results known for isotropic systems of 'well-defined' dimensionality, that is, for purely 3D, 2D and 1D systems. One would then find that, while each of the binding energies increases with more confinement, their growth occurs nearly 'in proportion' so that the ratio does not change significantly. Indeed, the classic Pekar's result [10] for 3D adiabatic polarons would translate into the maximum ratio of about 0.22. The exciton binding in 2D increases by a factor of four from its 3D value [1] but the polaron binding energy in 2D increases by almost as much [6], resulting in the ratio $\simeq 0.20$. Moreover, if the divergent purely 1D binding energies are taken (parametrically) for their ratio, then the result of [7] would translate into a maximum $E_{\rm b}^{\rm pol}/E_{\rm b}^{\rm exc}$ of approximately 0.17.

From the standpoint of this data, the results of our recent *model* quasi-1D calculations [11] for polarons and excitons on nanotubes immersed in a 3D polar medium, yielding $E_{\rm b}^{\rm pol}/E_{\rm b}^{\rm exc}$ in excess of 0.3, appear quite surprising. In the particular case of the tubular geometry, charge carriers are confined to motion on a cylindrical surface. Our study [11] was restricted to relatively small cylinder radii R. In this paper we will use a direct variational approach to calculate adiabatic polarons for arbitrary R, thereby enabling an assessment of the evolution of the ratio $E_{\rm b}^{\rm pol}/E_{\rm b}^{\rm exc}$ between the purely 2D ($R \to \infty$) and quasi-1D regimes. The corresponding calculations for excitons on a cylindrical surface have been performed recently [12, 13] and are very much in line with our exciton data. We will demonstrate explicitly (see figure 2(b)) that the ratio of the polaron and exciton binding energies exhibits non-monotonic behaviour as a function of the cylinder radius and can achieve values as large as about 0.35 at intermediate R, where the cylinder circumference is roughly comparable to an appropriate Bohr radius. We believe that our demonstration of $E_{\rm b}^{\rm pol}/E_{\rm b}^{\rm exc}$ ratios above the values in purely 3D and 2D systems can be rationalized by invoking simple physical arguments. These arguments also suggest that the *relative* increase in the polaronic effect that is found may reflect a general behaviour that might be characterized as a crossover effect.

Consider a gradual increase in the confinement, e.g. by starting to decrease the radius of a very large cylinder in going from the purely 2D system towards quasi-1D or by starting to decrease the thickness of a very thick quantum well in going from the purely 3D system towards 2D. Stated simplistically, the spatial size (extent) of a still unconfined polaron wavefunction

is larger than that of an unconfined exciton. As the confinement increases, therefore, the polaron can start experiencing substantial growth in its binding energy due to the confinement before a 'proportionally' substantial growth of the exciton binding energy sets in. With yet further increase in confinement, both polaron and exciton binding energies will reflect fuller confinement effects, resulting in the corresponding trend of the decreasing ratio E_b^{pol}/E_b^{exc}. Of course, quantitative aspects of the evolution can vary for different systems and need to be evaluated accordingly. We also stress that the above consideration tacitly assumed the existence of a uniform 3D polarizable medium, with the confinement affecting *only* the motion of charge carriers. Strong violations of this assumption can significantly affect the outcome for the ratio of binding energies.

While serving as a suggestive illustration of possibly general behaviour, it is polarons and the relationship of polarons and excitons on a cylindrical surface that are the subjects of our direct interest in this paper. Organic and inorganic tubular (nano)structures (see, e.g., [14, 15]) attract a great deal of attention and are considered to be candidate systems for important applications like (photo)electrochemical energy conversion and the (photo)catalytic production and storage of hydrogen, as well as in optoelectronics. On the one hand, their extended size along the tube axis can facilitate very good electron transport in that direction. On the other hand, tubes can expose large areas of both exterior and interior surfaces to facilitate surface-dependent reactions. Many of these applications involve contact with polar liquid environments such as common aqueous and non-aqueous solvents and electrolytic solutions which can provide conditions appropriate for the strong polaronic effect [11], thereby changing the nature of charge carriers. A widely known example of the tubular geometry is single-walled carbon nanotubes (SWCNTs) and, in fact, redox chemistry of carbon nanotubes is an 'emerging field of nanoscience' [16]. We note that the importance of the excitonic effects in the optics of semiconducting SWCNTs is well established now, with binding energies E_b^{exc} experimentally measured in some SWCNTs to be in the range of 0.4–0.6 eV [17–19]. There is also growing evidence of environmental effects on the electronic properties of SWCNTs [20–22].

It can be anticipated that the polaronic effect that we discuss would have an influence on both charge-transfer reactions and charge carrier dynamics on the tubes. In the context of our discussion of the relative energetics, a substantial reduction in the activation energy due to the polaronic effect should be expected for electric-field-assisted exciton dissociation and charge separation on semiconducting nanotubes.

Our illustrative calculations of the polaronic effect in this paper do not take into account details of the electronic band structure and polarizability of different nanotubes but, instead, are restricted to a simplest model of electrons and holes confined to a cylindrical surface in the 3D dielectric medium. The assumption of equal electron and hole effective masses is a reasonable approximation, e.g. for SWCNTs as well as for boron nitride tubes [23].

2. Exciton and polaron energy functionals

As noted above, our basic model, following references [12] and [13], assumes that electron and hole are particles of the same effective mass m whose motion is restricted to the surface of the cylinder of radius R. The cylindrical surface itself is immersed in the uniform 3D dielectric continuum characterized, as is common in studies of the polaron [2–4] and solvation [24–26] effects, by two magnitudes of the dielectric permittivity: the high-frequency (optical) value of ϵ_∞ and the low-frequency (static) value of ϵ_s. In the case of liquid polar media, the slow component of the polarization is ordinarily associated with the orientational polarization of the solvent dipoles, and it is typical [25, 11] that $\epsilon_s \gg \epsilon_\infty$. The fast component of the polarization follows charge carriers instantaneously. The slow component of the polarization, on the other

hand, is considered to be static in the adiabatic picture to determine the electronic states; the slow component then responds to the averaged electronic charge distribution.

With $m_e = m_h$, there is no net charge density associated with the ground state of the neutral exciton that would cause a static polarization of the slow component ('non-polarizing exciton'). The Coulomb interaction between the electron and the hole in the exciton is screened only by the high-frequency dielectric response ϵ_∞ [8, 9, 27]. The total energy of the exciton as a function of the normalized wavefunction $\psi(\mathbf{r})$ of the electron–hole relative motion (reduced mass $m/2$) is then

$$\mathcal{E}^{\mathrm{exc}}\{\psi\} = K^{\mathrm{exc}} - U^{\mathrm{exc}}$$
$$= \frac{\hbar^2}{m} \int d\mathbf{r} \, |\nabla\psi(\mathbf{r})|^2 - \frac{e^2}{\epsilon_\infty} \int d\mathbf{r} \, \frac{|\psi(\mathbf{r})|^2}{D(\mathbf{r})}, \tag{1}$$

whose global minimum determines the exciton ground-state wavefunction and its binding energy. For our geometry, position vector $\mathbf{r} = (x, y)$ is confined to the cylindrical surface, where we choose x to be along the cylinder axis and $-\pi R < y < \pi R$ to be along the circumferential direction; $|\nabla\psi(\mathbf{r})|^2 = (\partial\psi/\partial x)^2 + (\partial\psi/\partial y)^2$. Coulomb interaction is determined by the physical distance in the 3D space; in the flat geometry it would be $D(\mathbf{r}) = |\mathbf{r}|$, for the points on the cylindrical surface

$$D(\mathbf{r}) = \left(x^2 + 4R^2 \sin^2 \frac{y}{2R} \right)^{1/2}. \tag{2}$$

Optimization of the functional (1) for the ground state of the exciton on a cylinder has been performed in [12] and [13], with the results being in very good agreement with our data to be used in the comparison with the polaron.

The polarons that we discuss here are of the large-radius Fröhlich–Pekar type, where the Coulomb field of an individual charge carrier supports a self-consistent dielectric polarization pattern surrounding the carrier. The formation of large-radius polarons (self-localization, self-trapping) occurs due to the interaction of charge carriers with the 'slow' component of polarization. As the fast component of polarization does not contribute to the polaronic effect, it is the effective dielectric constant ϵ^*:

$$1/\epsilon^* = 1/\epsilon_\infty - 1/\epsilon_s, \tag{3}$$

which affects the coupling strength [2–4, 24–26]. In the adiabatic approximation, the normalized wavefunctions $\psi(\mathbf{r})$ of a self-localized charge carrier correspond to the minima of the following polaron energy functional:

$$\mathcal{E}^{\mathrm{pol}}\{\psi\} = K^{\mathrm{pol}} - U^{\mathrm{pol}}$$
$$= \frac{\hbar^2}{2m} \int d\mathbf{r} \, |\nabla\psi(\mathbf{r})|^2 - \frac{e^2}{2\epsilon^*} \int d\mathbf{r}_1 \, d\mathbf{r}_2 \, \frac{|\psi(\mathbf{r}_1)|^2 \, |\psi(\mathbf{r}_2)|^2}{D(\mathbf{r}_1 - \mathbf{r}_2)}, \tag{4}$$

whose global minimum we will be seeking for the ground state of the polaron. The functional (4) has the form that is well known for the large strong-coupling polarons [5, 9] and is a result of the optimization of the total adiabatic energy functional with respect to the polarization of the medium, thereby exhibiting an effective self-interaction of the electron [4, 9, 11]. Correspondingly, the U^{pol} term in equation (4) is known to be 'made of' two parts: $-U^{\mathrm{pol}} = -U^{\mathrm{pol}}_{\mathrm{el}} + U^{\mathrm{pol}}_{\mathrm{d}}$, where $U^{\mathrm{pol}}_{\mathrm{el}}$ represents the magnitude of the potential energy of the electron in the polarization field and $U^{\mathrm{pol}}_{\mathrm{d}}$ represents the energy required to create this polarization ('deformation energy'); with the optimal polarization, $U^{\mathrm{pol}}_{\mathrm{d}} = U^{\mathrm{pol}}_{\mathrm{el}}/2$.

Both energy functionals (1) and (4) assume that the electron and hole energies are measured from the band edges.

It is convenient to factor out dependences on physically relevant combinations of parameters by introducing appropriate units of energy and length. We will choose such units based on combinations for the exciton Bohr radius and binding energy (effective Rydberg) in 3D:

$$a_0 = 2\epsilon\hbar^2/me^2, \qquad \mathrm{Ryd} = e^2/2\epsilon a_0. \tag{5}$$

For the exciton problem, equation (1), one uses $\epsilon = \epsilon_\infty$ in equation (5), and for the polaron problem, equation (4), one uses $\epsilon = \epsilon^*$. We use superscript indices 'exc' and 'pol' to distinguish between the corresponding units (5). With all the coordinates (x, y for the cylinder) measured in appropriate a_0, one arrives at dimensionless energy functionals, $\mathcal{E}_0^{\mathrm{exc}} = \mathcal{E}^{\mathrm{exc}}/\mathrm{Ryd}^{\mathrm{exc}}$ and $\mathcal{E}_0^{\mathrm{pol}} = \mathcal{E}^{\mathrm{pol}}/\mathrm{Ryd}^{\mathrm{pol}}$, where

$$\mathcal{E}_0^{\mathrm{exc}}\{\psi\} = \int \mathrm{d}\mathbf{r}\ |\nabla\psi(\mathbf{r})|^2 - 2 \int \mathrm{d}\mathbf{r}\ \frac{|\psi(\mathbf{r})|^2}{D_0(\mathbf{r})} \tag{6}$$

and

$$\mathcal{E}_0^{\mathrm{pol}}\{\psi\} = \frac{1}{2} \int \mathrm{d}\mathbf{r}\ |\nabla\psi(\mathbf{r})|^2 - \int \mathrm{d}\mathbf{r}_1\, \mathrm{d}\mathbf{r}_2\ \frac{|\psi(\mathbf{r}_1)|^2\ |\psi(\mathbf{r}_2)|^2}{D_0(\mathbf{r}_1 - \mathbf{r}_2)}. \tag{7}$$

The dimensionless $D_0(\mathbf{r})$ in equations (6) and (7) features the same behaviour as equation (2) but with R replaced by the corresponding $R_0 = R/a_0$.

The global minima of equations (6) and (7), $-E_0^{\mathrm{exc}}$ and $-E_0^{\mathrm{pol}}$ respectively, would determine the dimensionless binding energies. As the units (5) already establish the scaling rules, in what follows we will be comparing E_0^{exc} and E_0^{pol} at the same values of R_0. The ratio $E_0^{\mathrm{pol}}/E_0^{\mathrm{exc}}$ would have a direct physical meaning of the maximum achievable when $\epsilon_s \gg \epsilon_\infty$ and $\epsilon^* \simeq \epsilon_\infty$ in equation (3). As we mentioned earlier, this can be a typical situation for many polar solvents.

Before proceeding with the analysis for a cylindrical surface, we recall in more detail the benchmarks known for isotropic d-dimensional systems ($D_0(\mathbf{r}) = |\mathbf{r}| = r$) briefly described in the introduction. The exact isotropic excitonic ground state $\psi(r)$ corresponding to equation (6) is given by the solution of the Schrödinger equation,

$$-E_0^{\mathrm{exc}}\psi = -\frac{\partial^2\psi}{\partial r^2} - \frac{(d-1)}{r}\frac{\partial\psi}{\partial r} - \frac{2}{r}\,\psi,$$

yielding well-known

$$\psi(r) \propto \exp\left(-\frac{2r}{d-1}\right), \qquad E_0^{\mathrm{exc}} = \frac{4}{(d-1)^2}. \tag{8}$$

With our choice of units, $E_0^{\mathrm{exc}} = 1$ in 3D.

The polaronic ground-sate wavefunctions and energies corresponding to equation (7) are known from variational calculations for d-dimensional systems. It is customary in the polaronic literature to express energies in terms of the coupling constant $\alpha_c = \left(me^4/2\epsilon^{*2}\hbar^3\omega\right)^{1/2}$ and phonon frequency ω. Note that the combination $\alpha_c^2\hbar\omega$ appearing in the results for strong-coupling (adiabatic) polarons corresponds to $2\mathrm{Ryd}^{\mathrm{pol}}$, as defined in equation (5). Thus the well-known Pekar's result [10] for the 3D polaron translates into $E_0^{\mathrm{pol}} \simeq 0.218$ and into the same magnitude of the ratio $E_0^{\mathrm{pol}}/E_0^{\mathrm{exc}}$ in 3D.

The 2D polaron has been studied in great detail in [6], with the best result of $E_0^{\mathrm{pol}} \simeq 0.809$ for the adiabatic case being achieved with Pekar-type trial wavefunctions. Since $E_0^{\mathrm{exc}} = 4$ in 2D, the ratio $E_0^{\mathrm{pol}}/E_0^{\mathrm{exc}} \simeq 0.202$, which is only slightly smaller than in 3D. The 2D case represents the limit $R \to \infty$ for a cylindrical surface and is particularly important for our
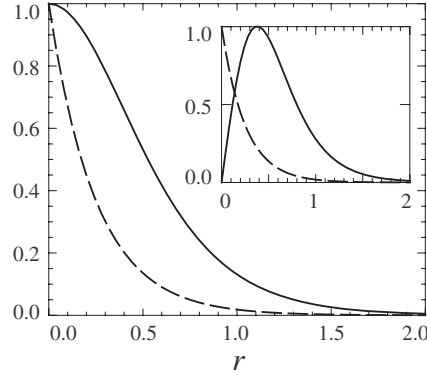
Figure 1. The spatial distribution of unnormalized density $|\psi(r)|^2$ for the exciton (dashed line) and the polaron (solid line) in 2D. The polaron wavefunction is as per equation (9). The inset shows the corresponding spatial distribution $U(r)$ of the potential energy in $U = \int U(r)\,dr$.
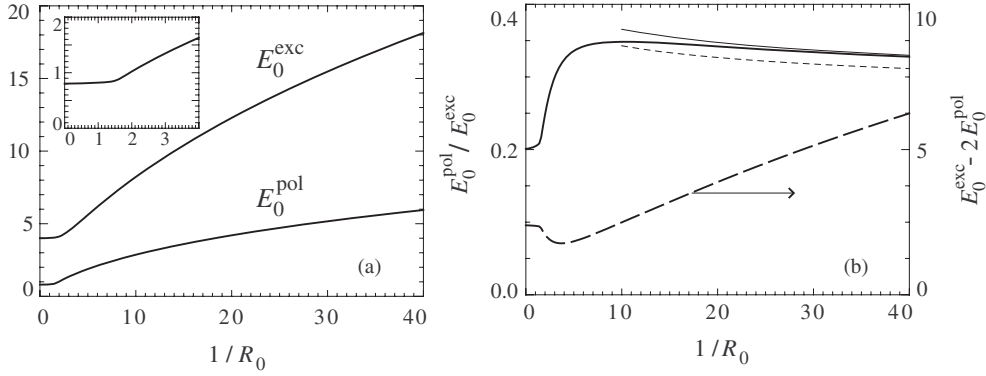

Figure 2. (a) The dimensionless exciton and polaron binding energies as functions of the dimensionless inverse cylinder radius $1/R_0$. The inset shows the behaviour of the polaron binding energy in more detail at small $1/R_0$. (b) The ratio of the binding energies $E_0^{\mathrm{pol}}/E_0^{\mathrm{exc}}$ of the excitations on a cylinder is shown as a thick solid line. A thin solid line displays this ratio as is obtained in the quasi-1D calculation with the effective tube potential (15). A thin short-dash line shows the quasi-1D result for this ratio if the effective interaction, instead, was that of a quantum wire, equation (16). A thick long-dash line displays the dimensionless activation energy $E_0^{\mathrm{exc}} - 2E_0^{\mathrm{pol}}$.

analysis. We have looked at simpler one-parametric trial wavefunctions that would make a good representation of the 2D adiabatic polaron and found that the wavefunction

$$\psi(r) \propto \frac{1}{\cosh(\alpha r)} \tag{9}$$

with $\alpha \simeq 1.674$ yields a very good optimization for the energy: $E_0^{\mathrm{pol}} \simeq 0.804$, which is quite accurate for our purposes. Figure 1 compares the spatial structure of the 2D exciton and polaron.

As both exciton and polaron binding energies diverge in pure 1D, the following comparison might be of a dubious nature but is still interesting. Specifically, reference [7] discussed the calculation of the 1D polaron in terms of the renormalized coupling constant $\alpha_c' = \alpha_c/(d-1)$, where $d \to 1$. The best variational result achieved for the adiabatic polaron was $E_b^{\mathrm{pol}} \simeq$

$0.333 \, (\alpha_c'^2 \hbar \omega)$. As the diverging d-dependence in this expression is the same $(d-1)^{-2}$ as in the exciton case (8), the ratio of the binding energies in 1D could then be interpreted as $E_0^{\mathrm{pol}}/E_0^{\mathrm{exc}} \simeq 0.167$.

3. Variational analysis for a cylinder

When on a cylindrical surface, both exciton and polaron ground states need to be determined numerically. Our variational analysis of the energy functionals (6) and (7) has been performed on the following classes of the trial wavefunctions[3]. For the exciton problem we have used three-parametric (α, β and γ) wavefunctions

$$\psi(x, y) \propto \exp\left[-\left(\alpha^2 x^2 + \beta^2 y_1^2 + \gamma^2\right)^{1/2}\right]. \tag{10}$$

The polaron problem is much more demanding on computation time, so we chose two-parametric (α and β) wavefunctions

$$\psi(x, y) \propto \frac{1}{\cosh\left(\alpha^2 x^2 + \beta^2 y_1^2\right)^{1/2}}. \tag{11}$$

The functional dependences in equations (10) and (11) are such that they can recover, in the limit of $R_0 \to \infty$, wavefunctions (8) and (9) found for the 2D systems—similarly to the earlier exciton calculations [12, 13].

We explored two choices for the effective coordinate y_1 in equations (10) and (11): 'arc-based' (as in [13])

$$y_1 = y, \tag{12}$$

$-\pi R_0 < y < \pi R_0$, and 'chord-based' (as in [12])

$$y_1 = 2 R_0 \sin\left(y / 2 R_0\right). \tag{13}$$

Both choices can be thought of as, respectively, $n \gg 1$ and $n = 1$ limits of more general

$$y_1 = \pi R_0 \left\{ \frac{2}{\pi} \sin\left[\frac{\pi}{2} \left(\frac{y}{\pi R_0} \right)^n \right] \right\}^{1/n}$$

which could be used in future refinements as being more flexible in terms of the shape of the wavefunction being periodic in the circumferential direction. In this paper we resorted to just choosing the best results among those obtained with equations (12) and (13).

Wavefunctions (10) and (11) feature two parameters α and β having the meaning of inverse lengths, thereby explicitly allowing for anisotropy of the wavefunction extent in the axial and circumferential directions [13]. What we will later be referring to as quasi-1D results corresponds to $\beta = 0$ when the wavefunctions are uniform around the cylinder circumference.

The main quantitative results of this paper are displayed in figure 2, showing the optimized variational outputs for the exciton and polaron binding energies as well as their ratio $E_0^{\mathrm{pol}}/E_0^{\mathrm{exc}}$. Our exciton data is very close to the results of [12] and [13], where the reader can find extensive discussions.

Just as in the exciton case, the polaron binding energy exhibits very little change from its 2D value ($\simeq 0.8$) due to the curvature of up to $R_0 \sim 1$ (see the inset in figure 2(a)) where it starts rising, relatively earlier and more rapidly than the exciton dependence. This immediately translates into a substantial increase in the ratio $E_0^{\mathrm{pol}}/E_0^{\mathrm{exc}}$ with decreasing R_0, as shown in figure 2(b). The maximum of the ratio $\simeq 0.35$ is achieved in the region of $1/R_0 \sim 10$, after

[3] All numerical integrations and optimizations have been performed by using IMSL numerical libraries, as provided with the PV-WAVE Advantage package, http://www.vni.com.
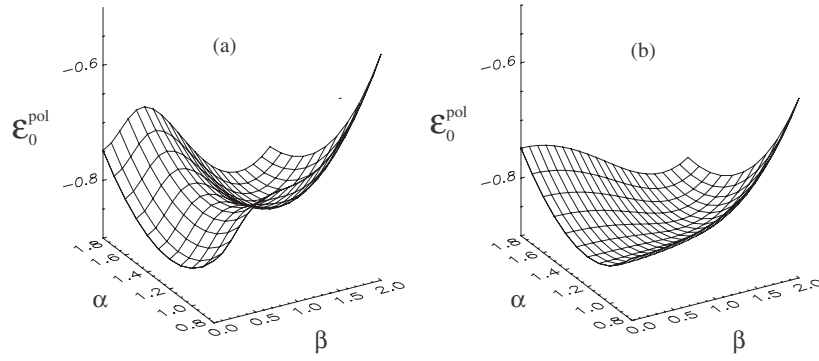
Figure 3. The behaviour of the functional (7) at $R_0 = 0.65$ with the trial wavefunctions (11) as a function of the variational parameters α and β for two choices of the effective coordinate y_1: (a) as in equation (12) and (b) as in equation (13).

which the ratio starts slowly decreasing with $1/R_0$. While, of course, larger ratios $E_0^{\text{pol}}/E_0^{\text{exc}}$ lead to larger relative reductions in the effective activation energy $E_0^{\text{exc}} - 2E_0^{\text{pol}}$, it is quite interesting that the *absolute* value of this activation energy, also shown in figure 2(b), exhibits a non-monotonic dependence on $1/R_0$. A region around the minimum of this curve indicates specific tube sizes where the activation energy would be at its lowest.

Our variational results have shown that the the dependence of E_0^{pol} on $1/R_0$ collapses onto the corresponding quasi-1D curve practically right away after the onset of a substantial rise in binding. This is different from the exciton case, where deviations from the quasi-1D behaviour persist all the way into the region of $1/R_0 > 20$. In other words, the polaron spreads uniformly around the cylinder at much smaller curvatures than the exciton does. We note that the quasi-1D variational results for the polaron binding using trial wavefunctions (11) and (10) differ very little and are in good agreement with our analysis in [11], where no assumptions have been made about the wavefunction shape and the nonlinear optimizing equation has been solved numerically. The thin solid line in figure 2(b) shows the ratio $E_0^{\text{pol}}/E_0^{\text{exc}}$ using quasi-1D results for the binding energies, and its deviation from the variational result for a cylinder is entirely due to underestimation of the exciton binding.

As with all variational calculations, we, of course, cannot exclude that some details in the results shown in figure 2 may undergo slight modifications upon further improvements of variational wavefunctions. Importantly, possible improvements would be inconsequential for our main observations of a non-monotonic dependence of the ratio $E_0^{\text{pol}}/E_0^{\text{exc}}$ on $1/R_0$ and of the magnitude of the ratio reaching values well above the 2D value of $\simeq 0.2$. We found that a rise in the ratio above 0.3 is obtainable even if the polaron wavefunctions are not specifically optimized for a range of given R_0 but the 2D optimal values of $\alpha = \beta \simeq 1.67$ are used. For very small tubes with $1/R_0 < 20$, the results of exact numerical calculations in [11] complement the picture.

The transitional region of $R_0 \sim 1$ is likely to be especially sensitive to the choice of trial wavefunctions. So, reference [12] reported an improvement of a few percent for the exciton binding energy in the region of $1 < 1/R_0 < 2.5$ with certain trial functions. Similar improvements could perhaps be found for the polaron binding energies. Figure 3 illustrates the behaviour of the polaron functional (7) in the transitional region, at $R_0 = 0.65$, as a function of the variational parameters α and β. A curious feature of the 'landscape' in figure 3(a) is a clear coexistence of two minima, one corresponding to a polaronic state that

is uniformly distributed (delocalized) around the cylinder circumference, and the other where the circumferential distribution is non-uniform. While this appears as an interesting possibility, it could also be an artefact of a restricted nature of a specific class of the trial wavefunctions; compare visually, for example, to the landscape of figure 3(b). A much more careful study would be needed to explore the possibility of coexisting polaronic states requiring an analysis of actual adiabatic potential surfaces. An example of an analogous analysis can be found in [28], where we proved a coexistence of different polarons in certain quasi-1D systems.

4. Discussion

Both in this paper and in [11] we have shown that the strong polaronic effect occurring in sluggish polar environments substantially affects the relative energetics of closely bound and well-separated electron–hole pairs on a cylindrical surface of nanotubes. The binding energy $E_{\rm b}^{\rm pol}$ of an individual polaron can, in an idealized model, reach as much as about 0.35 of the binding energy $E_{\rm b}^{\rm exc}$ of the exciton. This would translate into a reduction in the activation energy $E_{\rm b}^{\rm exc} - 2E_{\rm b}^{\rm pol}$ for exciton dissociation by a factor of about three from the value $E_{\rm b}^{\rm exc}$ that it would have in a non-polar environment with the same value of the high-frequency dielectric constant ϵ_∞. Note that, in our earlier study [11], we have not found any additional energy barriers between the exciton and distant polaron-pair states. One should expect that enhanced separation of charges and a corresponding luminescence quenching would then result, for example, in experiments probing the effects of electric field on the luminescence. It is needless to say that additional factors omitted in our simplified analysis here can make the reduction magnitude smaller (see, e.g., a comparison in [11] of cases with different 'electrostatic conditions').

Polar liquid environments such as many common solvents may be good candidates for providing conditions necessary for the strong polaronic effect, as they can exhibit both high values of the static dielectric constant $\epsilon_{\rm s}$ and a relatively slow response of the orientational polarization (longitudinal relaxation times can be on the order of 1 ps and longer) [25, 11]. Quite fittingly, there is an ongoing intense research effort on various applications of nanotubes in contact with such environments, and we hope that direct experimental verifications of our qualitative conclusions will be possible. We note that a comprehensive mapping of luminescence versus absorption spectra of individual SWCNTs was in fact achieved in aqueous suspensions [29, 30]. Interestingly, numerical estimates in [13] indicate that the dimensionless radius R_0 for a range of SWCNTs may be close to 0.1, which corresponds to the region of maximum $E_0^{\rm pol}/E_0^{\rm exc}$ ratios in figure 2(b).

We have demonstrated that the ratio of the binding energies $E_{\rm b}^{\rm pol}/E_{\rm b}^{\rm exc}$ has a non-monotonic dependence on the cylinder curvature $1/R$. As argued in the introduction, our particular observation for the cylindrical geometry can be a manifestation of a more general crossover effect that would be common for other structures in 3D polar media when the increasing confinement of the electron motion causes a 'transition' between d-dimensional systems, such as between 3D and 2D (quantum wells) or between 3D and 1D (quantum wires). Basically, the origin of this effect can be related to the fact that the spatial extent of an unconfined polaron is larger than the size of an unconfined exciton (see figure 1 for the 2D case), thereby making the polaron 'respond' to the initially increasing confinement in a more pronounced way than the exciton. Only after the exciton experiences a fuller effect of the confinement, the ratio of the binding energies starts decreasing. Elaborating more on this idea, the inset in figure 1 shows the spatial distribution of the potential energy terms U: $\mathcal{E} = K - U$, for unconfined excitations. It is evident that the 'longer-range' contributions to the polaron potential energy are relatively more important than for the exciton. This is why the effect of increasing confinement on the
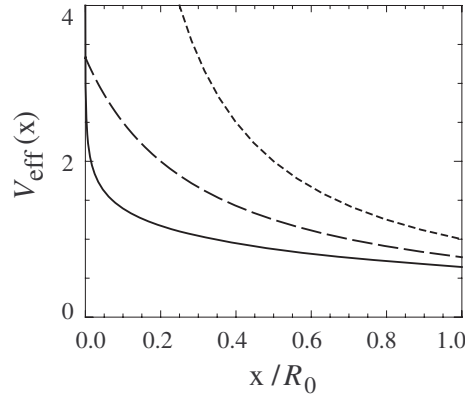
Figure 4. Distance dependence of the effective 1D Coulomb potentials for charges on a cylinder, equation (15), solid line, and in a quantum wire, equation (16), long-dash line, in comparison with the original Coulomb interaction (14), short-dash line.

polaron is initially stronger. In the particular case of the cylindrical geometry, the curvature changes remote physical distances (chords instead of arcs, equation (2)) more than it does close distances.

A meaningful parallel can be drawn with the behaviour of the ratio U/K of the potential and kinetic energy terms in confined systems. The virial theorem for the Coulombically bound states in unconfined d-dimensional systems states that $U/K = 2$, independent of d, which, of course, also follows directly from scaling of both functionals (1) and (4) provided that $D(\mathbf{r}) = |\mathbf{r}| = r$. In particular, polarons in such systems are known [31, 9, 4] to satisfy the following ratios for various energy terms: $E_{\rm b}^{\rm pol}:K^{\rm pol}:U^{\rm pol}:U_{\rm el}^{\rm pol}:U_{\rm d}^{\rm pol} = 1{:}1{:}2{:}4{:}2$. Some of these relationships are violated in confined systems. As studied in [32], the virial theorem ratio $U^{\rm exc}/K^{\rm exc}$ for excitons in quantum wells and quantum wires is larger than 2 and, in fact, a non-monotonic dependence of $U^{\rm exc}/K^{\rm exc}$ has been demonstrated for quantum wells transitioning between 3D and 2D limits. We have found a non-monotonic behaviour of the ratio U/K for both polarons and excitons on a cylinder as a function of the curvature $1/R$. In agreement with our qualitative arguments, at smaller $1/R$ this ratio grows much more quickly for the polaron than for the exciton. At large curvatures, however, the trend is reversed and the exciton has larger ratios U/K than the polaron.

It is useful to continue a qualitative reasoning by discussing the quasi-1D limit of our results, that is, the case of stronger but still finite degrees of confinement. One can then use the notion of the effective Coulomb potentials [1, 32], here as a function of the 1D (axial) distance x. (The effective Coulomb potentials for 2D can be similarly introduced [32]). Figure 4 compares three potentials in units such that, at very large distances, the potentials behave as

$$V_{\rm eff}(x) = R_0/x. \tag{14}$$

In this limit the electron wavefunction on a cylinder is delocalized around its circumference and the effective interaction becomes that of rings of charge given by

$$V_{\rm eff}(x) = \frac{2}{\pi \left[(x/R_0)^2 + 4\right]^{1/2}} K\left[\frac{4}{(x/R_0)^2 + 4}\right], \tag{15}$$

where $K(m) = \int_0^{\pi/2}(1 - m\sin^2\theta)^{-1/2}\,{\rm d}\theta$ is a complete elliptic integral of the first kind. If, instead of a tube, we dealt with a quantum wire, the electron wavefunction would be delocalized

throughout the cross-section of the wire, with the effective interaction approximated as [1]

$$V_{\text{eff}}(x) = \frac{1}{(x/R_0) + 0.3}. \tag{16}$$

Both effective tube (15) and wire (16) 1D potentials feature modifications of the shorter-range interaction from the original Coulomb (14) due to the transverse spread of wavefunctions, thereby eliminating a pure 1D divergence of the ground states for excitons and polarons. As we discussed above, the role of the longer-distance interactions is more important for the polaron than for the exciton. Since the relative modification of the original Coulomb to the effective potentials is increasing towards shorter distances, it is then clear that the ratio $E_{\text{b}}^{\text{pol}}/E_{\text{b}}^{\text{exc}}$ in systems with modified interactions should be larger than values of about 0.2 in systems with pure Coulomb interaction. Moreover, following the same logic, one should expect that the larger modification is from the original Coulomb distance dependence, the larger will be the $E_{\text{b}}^{\text{pol}}/E_{\text{b}}^{\text{exc}}$ ratios. Figure 4 shows that deviations from the Coulomb dependence for the effective wire potential are smaller than for the tube potential (over a relevant spatial range). We have performed a quasi-1D variational optimization of the polaron and exciton binding energies with the wire potential (16). The resulting ratios, $E_0^{\text{pol}}/E_0^{\text{exc}}$, are shown in figure 2(b) with a short-dash thin line and are, indeed, smaller than the ratios calculated with the tube potential (15)—solid thin line in that figure.

These qualitative arguments, while confirmed by specific model calculations, do not appear to be restricted to this specific situation. We therefore expect that findings of larger magnitudes of the ratio $E_{\text{b}}^{\text{pol}}/E_{\text{b}}^{\text{exc}}$ and of a non-monotonic dependence of this ratio on the degree of confinement represent a crossover effect that can be common to semiconductor nanostructures in 3D polar environments. Further calculations with different geometric structures are needed to validate this conjecture and evaluate its quantitative aspects, including in non-uniform polar environments.

We would like to reiterate that numerical data that we arrived at in this paper are based on a simplified model; more accurate calculations would have to take into account specific aspects of the nanotube band structure and the tube's own polarizability. Optical studies of SWCNTs particularly indicate the dependence of the exciton binding not only on R but also on the chirality of the tubes; see the discussion and multiple citations in [33]. The latter reference also shows separately the effect on excitons of tube's polarizability; our earlier quasi-1D calculations are consistent with their findings, and we refer the reader to [11] for illustrations of this effect on polarons.

Another interesting subject for future research is an assessment of the activation energy for exciton dissociation in confined semiconductors with unequal electron and hole masses, $m_{\text{e}} \neq m_{\text{h}}$. In this case, electron–polarons and hole–polarons have different binding energies and, in addition, the exciton itself can cause an adiabatic polarization of the environment [8, 27]. The corresponding 'polaronic' corrections to the exciton binding in quantum-well wires have been studied, for example, in [34]. From a general standpoint, one would also like to extend the analysis of the effects of polar media on the dissociation of confined excitons to the intermediate-coupling [2–4] regime.

References

[1] Haug H and Koch S W 2004 *Quantum Theory of the Optical and Electronic Properties of Semiconductors* (New Jersey: World Scientific)
[2] Fröhlich H 1954 *Adv. Phys.* **3** 325
[3] Kuper C G and Whitfield G D (ed) 1963 *Polarons and Excitons* (New York: Plenum)
[4] Appel J 1968 *Solid State Physics* vol 21, ed F Seitz, D Turnbull and H Ehrenreich (New York: Academic) p 193
[5] Alexandrov A S and Mott N 1995 *Polarons and Bipolarons* (Singapore: World Scientific)
[6] Wu X, Peeters F M and Devreese J T 1985 *Phys. Rev.* B **31** 3420
[7] Peeters F M and Smondyrev M A 1991 *Phys. Rev.* B **43** 4920
[8] Dykman I M and Pekar S I 1952 *Dokl. Akad. Nauk SSSR* **83** 825
[9] Rashba E I 1987 *Excitons, Selected Chapters* ed E I Rashba and M D Sturge (Amsterdam: North Holland) p 273
[10] Pekar S I 1946 *Zh. Eksp. Teor. Fiz.* **16** 335
     Pekar S I 1946 *Zh. Eksp. Teor. Fiz.* **16** 341
[11] Gartstein Yu N 2006 *Phys. Lett.* A **349** 377
[12] Kostov M K, Cole M W and Mahan G D 2002 *Phys. Rev.* B **66** 075407
[13] Pedersen T G 2003 *Phys. Rev.* B **67** 073401
[14] Tenne R 2002 *Semiconductor Electrodes and Photoelectrochemistry* ed S Licht (Weinheim: Wiley–VCH) p 238
[15] Zhao X S, Bao X Y, Guo W and Lee F Y 2006 *Mater. Today* **9** 32
[16] O'Connell M J, Eibergen E E and Doorn S K 2005 *Nat. Mater.* **4** 412
[17] Wang F, Dukovic G, Brus L E and Heinz T F 2005 *Science* **308** 838
[18] Ma Y-Z, Valkunas L, Bachilo S M and Fleming G R 2005 *J. Phys. Chem.* B **109** 15671
[19] Wang Z, Pedrosa H, Krauss T and Rothberg L 2006 *Phys. Rev. Lett.* **96** 047403
[20] Fantini C, Jorio A, Souza M, Strano M S, Dresselhaus M S and Pimenta M A 2004 *Phys. Rev. Lett.* **93** 147406
[21] Hertel T, Hagen A, Talalaev V, Arnold K, Hennrich F, Kappes M, Rosenthal S, McBride J, Ulbricht H and Flahaut E 2005 *Nano Lett.* **5** 511
[22] Lu M P, Hsiao C Y, Lo P Y, Wei J H, Yang Y S and Chen M J 2006 *Appl. Phys. Lett.* **88** 053114
[23] Mele E J and Král P 2002 *Phys. Rev. Lett.* **88** 056803
[24] Kuznetsov A M and Ulstrup J 1999 *Electron Transfer in Chemistry and Biology* (Chichester: Wiley)
[25] Fawcett W R 2004 *Liquids, Solutions and Interfaces* (Oxford: Oxford University Press)
[26] Nitzan A 2006 *Chemical Dynamics in Condensed Phases* (New York: Oxford University Press)
[27] Pekar S I, Rashba E I and Sheka V I 1979 *Sov. Phys.—JETP* **49** 129
[28] Gartstein Yu N and Zakhidov A A 1986 *Solid State Commun.* **60** 105
[29] O'Connell M J, Bachilo S M, Huffman C B, Moore V C, Strano M S, Haroz E H, Rialon K L, Boul P J, Noon W H, Kittrell C, Ma J, Hauge R H, Weisman R B and Smalley R E 2002 *Science* **297** 593
[30] Weisman R B, Bachilo S M and Tsyboulski D 2004 *Appl. Phys.* A **78** 1111
[31] Pekar S I 1951 *Research in the Electron Theory of Crystals* (Moscow: Gostekhizdat)
[32] Zhang Y and Mascarenhas A 1999 *Phys. Rev.* B **59** 2040
[33] Jiang J, Saito R, Samsonidze Ge G, Jorio A, Chou S G, Dresslhaus G and Dresslhaus M S 2007 *Phys. Rev.* B **75** 035407
[34] Degani M H and Hipólito O 1987 *Phys. Rev.* B **35** 9345

Excitons in long molecular chains near the reflecting interface

Yu. N. Gartstein[1] and V. M. Agranovich[2,3]

[1]*Department of Physics, The University of Texas at Dallas, Richardson, Texas 75083, USA*
[2]*UTD-NanoTech Institute, The University of Texas at Dallas, Richardson, Texas 75083, USA*
[3]*Institute of Spectroscopy, Russian Academy of Science, Troitsk, Moscow, Russia*

We discuss coherent exciton-polariton states in long molecular chains that are formed due to the interaction of molecular excitations with both vacuum photons and surface excitations of the neighboring reflecting substrate. The resonance coupling with surface plasmons (or surface polaritons) of the substrate can substantially contribute to the retarded intermolecular interactions leading to an efficient channel of the decay of one-dimensional excitons with small momenta via emission of surface excitations. The interface also modifies the radiative decay of excitons into vacuum photons. In an idealized system, excitons with higher momenta would not emit photons or surface waves. For a dissipative substrate, additional exciton quenching takes place owing to Joule losses as the electric field of the exciton polarization penetrates the substrate. We discuss how these effects depend on the polarization of molecular excitations, their frequency, and the distance of the chain from the substrate.

I. INTRODUCTION

The interaction of the electromagnetic field with a molecular excitation in an aggregate of identical molecules leads, on the one hand, to the delocalization of the excitation over the aggregate and, on the other hand, to a modification of its radiative decay.[1] Both notions of excitons and polaritons are used in the literature on such delocalized excitations. In crystalline structures, the excitation can be spatially coherent and then it is characterized by its wave vector as a proper quantum number. In this paper we discuss how electric-dipole-active coherent excitations in linear crystals are affected by the presence of a neighboring metallic or dielectric half-space.

A variety of one-dimensional (1D) electronic systems available nowadays, such as conjugated polymers, J and H aggregates, semiconducting quantum wires, and carbon nanotubes, exhibit interesting optical properties and are considered for potential applications in optoelectronics; their spectroscopy is an active research area. Successes at the synthesis and fabrication of these systems have resulted in a continuously improving quality and an increase of their "conjugation length" L which may exceed the appropriate electromagnetic wave length λ. Perhaps one of the most noteworthy achievements in this regard is the recent observation[2] of a macroscopic coherence of a single exciton in polydiacetylene chains of $L \simeq 10$ μm that allowed one to discuss the issue of an "ideal 1D quantum wire."[3] It is also relevant to note a physically very different but conceptually related class of excitations in chains of "dipole-coupled" nanoparticles (see, e.g., the recent work in Ref. 4 and multiple references therein) studied for photonic and plasmonic applications.

Long before the modern experimental advances, it was shown[1,5] that the coherent interaction of low-dimensional (1D and 2D) excitons with an electromagnetic field is drastically different than in 3D systems. The radiative decay of low-dimensional excitons is strongly enhanced in the region

of their wave vectors $|\mathbf{q}| \lesssim k$, where $k = \omega/c$ (c is the speed of light in vacuum) is determined self-consistently by the excitation energy $E(\mathbf{q}) = \hbar\omega$, while the excitations with $|\mathbf{q}| > k$ would not radiate, as is required by energy and momentum conservation for an exciton-photon system. More specifically, for 1D excitons in the molecular chain in vacuum, the radiative width $\Gamma = \hbar/\tau$ (τ being the decay time) depends on the wave vector q as

$$\Gamma^{\mathrm{v}}(k,q) = \frac{\pi p^2}{a}[2(k^2 - q^2)\cos^2\theta + (k^2 + q^2)\sin^2\theta]\Theta(k - |q|),$$
$$(1)$$

where p is the magnitude of the molecular dipole transition moment $\mathbf{p}$ that makes an angle θ with the chain axis, a the intermolecular spacing along the chain, and Θ the step function. As compared with the radiative width

$$\Gamma^0(k) = 4p^2k^3/3 \qquad (2)$$

of a single molecule, Eq. (1) exhibits an enhancement factor of $\sim \lambda/a = 2\pi/ka \sim 10^2 - 10^3$ in the optical region of the spectrum ("superradiant" states). This enhancement has been discussed in the context of various systems (see, e.g., Refs. 6–9 and references therein). Equation (1) also shows how the polarization of the transition dipole affects the q dependence of the decay rate.

Importantly for applications, it is possible to manipulate the optical properties of molecular excitations and to form new hybrid excitations by putting molecules or molecular aggregates in the vicinity of interfaces and in dielectric microcavities.[10] Well known, e.g., is an oscillating dependence of the radiative width on the distance of a single molecule from the planar interface resulting from the interference of the radiative fields of a molecular transition and its image.[10,11] The dipole-dipole interaction also gets modified in the vicinity of a surface or in the cavity.[12–14] In the case of a linear molecular crystal, the environment can lead to qualitatively interesting coherent effects as it is the interaction of
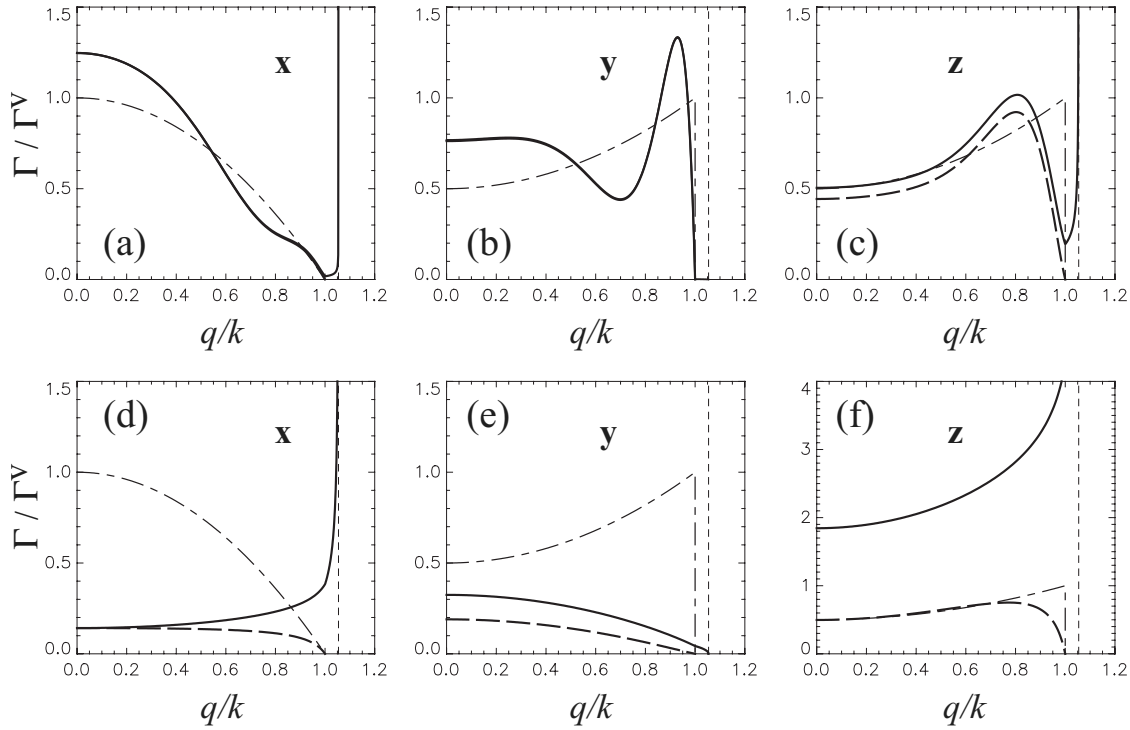
FIG. 1. Decay width $\Gamma(k,q)$ of 1D exciton polaritons as a function of the reduced wave vector q/k for a fixed value of $k = 2\pi/400a$ and substrate's dielectric constant $\epsilon = -10$. Two rows correspond to different dipole–to–image-dipole distances d: upper panels (a)–(c) are for $d = 600a$, lower panels (d)–(f) for $d = 10a$. All distances are measured in units of intermolecular spacing in the chain, a. Each of the trio of panels in a row corresponds to different exciton polarization, indicated by the boldface letters. The chain is parallel to the x axis and situated above the substrate whose surface is the xy plane. Decay width is shown with respect to $\Gamma^v = 2\pi p^2 k^2/a$ which is the radiative width of the **x**-polarized exciton in vacuum at $q = 0$, Eq. (2). The overall vacuum benchmark results (1) are shown with the dash-dotted lines. The total decay width is displayed by thick solid lines; the dashed solid lines (when distinguishable) show the part of the width due to the decay into vacuum photons only. The vertical dash lines indicate the position of the surface plasmon wave vector, κ_p/k, Eq. (4).

many molecular transition dipoles (and their images) that would determine the properties of the excitation. Philpott,[6] for instance, pointed out that by placing a linear chain near a transparent substrate, one could probe some of the otherwise nonradiant polariton states via emission of bulk substrate photons. It was also studied how the radiative decay properties of quantum wire excitons get modified when the wire is embedded in a microcavity—that is, via emission of cavity photons (Refs. 8 and 15 and references quoted there). As one-dimensional arrays are considered for directed energy transfer applications, their interaction with the environment may also be used to achieve certain purposes such as, e.g., to counteract losses by embedding the array in the gain medium.[16]

In this paper we discuss 1D coherent dipole excitations that are formed in the neighborhood of the planar reflecting substrate in the range of frequencies ω where the dielectric constant of the substrate medium $\epsilon(\omega) < 0$ and the substrate does not support bulk photon modes. This is the situation that is most easily implementable in the vicinity of a metallic surface and which, in fact, has recently received a considerable attention in the context of both organic excitons[17] and dipole excitations of nanoparticles (Ref. 18 and references therein). The substrate in general affects both the dispersion of the excitons and their lifetime. We will show that the presence of the substrate may result in new interference patterns and leads to a plethora of behaviors depending on the polarization and frequency of the excitation as well as on the distance from the interface. For the decay width, this is illustrated in Fig. 1 that exemplifies substantial differences with the vacuum result (1) and is discussed in more detail later. This figure demonstrates not only a modification of the exciton decay into vacuum photons, but also the decay into substrate surface plasmon (SP) modes [which occur for $\epsilon(\omega) < -1$], the significance of the latter channel strongly increasing upon approach to the interface.

The importance of the coupling of an individual dipole excitation to substrate SP modes and of associated resonance decay and scattering phenomena have already been stressed for both molecules[19–21] and nanoparticles.[18] This coupling strongly increases as the exciton transition frequency approaches the "resonance" region of the substrate in which $\epsilon(\omega)$ is close to -1. The increase is, of course, what should be expected from the theory of electrostatic image forces[22] which features the combination factor

$$Q_0 = (1 - \epsilon)/(1 + \epsilon) \qquad (3)$$

for the magnitude of image charges. One should be aware, however, that this is also the region where both retardation[19,20] and dissipation[11] effects are particularly important. The corresponding enhancement of the decay of 1D
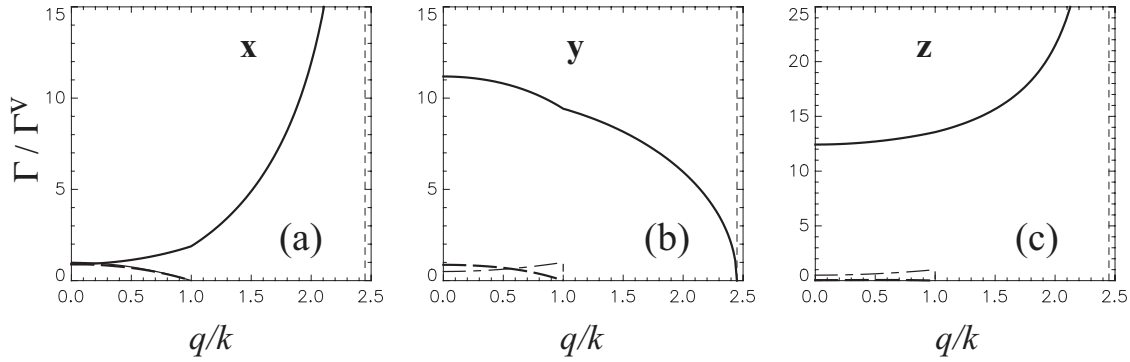
FIG. 2. As in Fig. 1 but for $d=50a$ and $\epsilon=-1.2$. Note that despite the distance here being 5 times larger than in panels (d)–(f) of Fig. 1; the decay into substrate surface plasmons is much stronger.

excitons into SPs is seen in the illustration of Fig. 2 ($\epsilon=-1.2$) where, in comparison with Fig. 1 ($\epsilon=-10$), it clearly is a dominant decay channel; consequently, the fluorescence efficiency is greatly reduced.[20] One also appreciates the fact that the resonant enhancement, as shown, occurs over the already "superradiant" vacuum decay rate.

Both Figs. 1 and 2 have been calculated with negligible exciton scattering and substrate losses (see Sec. IV for a discussion of dissipation effects); hence, they are reflective of the full conservation laws for our exciton-photon-SP system. So excitons with wave vectors $|\mathbf{q}|>k$ cannot decay into vacuum photons, while emission of SPs can occur only for $|q|<\kappa_p(k)$ where

$$\kappa_p = k[\epsilon/(\epsilon+1)]^{1/2} \tag{4}$$

is the well-known (e.g., Ref. 10) wave vector of the SP at an appropriate frequency. In such an idealized system, exciton polaritons with $|q|>\kappa_p(k)$ would be nonemissive. An example of the corresponding qualitative picture of the dispersion spectrum of exciton polaritons in the chain near the substrate is shown schematically in Fig. 3. As the radiative decay rate vanishes at $|q|=k-0$ (see Figs. 1 and 2), no branch splitting takes place upon the polariton spectrum crossing the vacuum photon line. The branching instead occurs in the region of would-be crossing the SP dispersion curve [this splitting, however, is absent for **y**-polarized excitons whose decay rate into SPs vanishes at $|q|=\kappa_p(k)-0$]. The nonemissive branch 2 in the figure can be thought of as of excitations representing a coherent mix of the exciton, photons and SPs of the same momentum projection along the chain, the relative weight contributions depending on this momentum. We cannot exclude that surface plasmon guiding by chains of nanoparticles found in recent numerical simulations[23] is related to the formation of the discussed bound exciton-SP states.

As the SPs are surface states characterized by 2D wave vectors, the inverse square-root singular behavior in the decay rates of 1D excitons upon $q\rightarrow\kappa_p$ seen in Figs. 1 and 2 has a "dimensionality" origin similar to the one taking place for 2D (quantum well) excitons decaying into 3D vacuum photons[1,5,24,25] and 1D (quantum wire) excitons decaying into 2D cavity photons.[8]

In what follows we will elaborate on the interaction of 1D excitons with the neighboring reflecting substrate using the simplest model of a chain of molecules with a single molecular dipole transition (Frenkel-like excitons). We note that some resulting features would be generically valid for Wannier-Mott excitons as well. We however do not pursue here an explicit analysis of the Wannier-Mott excitons that would require specific modifications for their bare dispersion as well as the influence of the substrate on the exciton binding and oscillator strength. While we chose, for certainty, to use an example of the metallic substrate and the corresponding surface plasmon excitations, it should be clear that the same effects would occur for a dielectric substrate whenever it can feature the region of negative $\epsilon(\omega)$ and surface polariton excitations.
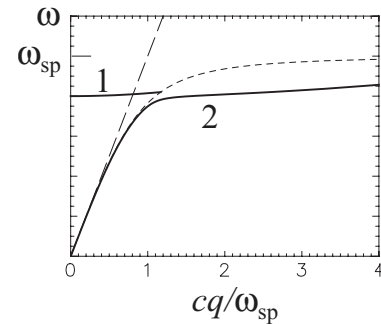
FIG. 3. Schematically (not to scale), an example of the possible idealized dispersion of **x**-polarized 1D exciton polaritons in the form of their frequency $\omega=E(q)/\hbar$ as a function of the wave vector q. This spectrum is a result of the interaction of the bare excitons with vacuum photons, whose spectrum is reflected in the limiting long-dashed line, and with substrate surface plasmons, whose spectrum is reflected in the limiting short-dashed line (ω_{sp} is the asymptotic SP frequency). The exciton-polariton spectrum (solid lines) is split into two branches. The states of branch 2 are nonemissive while the states of branch 1 can decay via emission of photons and/or SPs. The photon emission can take place only for states of branch 1 with $|q|<k$—that is, where branch 1 lies above the shown vacuum photon line; exactly at their crossing, the radiative decay rate vanishes and stays zero afterwards.

II. FRENKEL EXCITON POLARITONS IN A MOLECULAR CHAIN: VACUUM RESULTS

Renormalization of a single-molecule transition of energy E_f and the formation of an electric-dipole exciton band in a molecular aggregate can be derived in various frameworks (see, e.g., Refs. 1 and 26) with identical results. Here we will use a simple and physically transparent description having a clear underlying semiclassical analogy. In the Heitler-London approximation (energy E_f is much larger than all other energies involved), the exciton Hamiltonian for interacting identical molecules can be written as

$$H = (E_f + V_0) \sum_n B_n^\dagger B_n + \sum_{n>m} V_{n-m}(B_n^\dagger B_m + \text{H.c.})$$
$$= \sum_q E(q) B_q^\dagger B_q,$$

where $B_n^\dagger$ creates an excitation on the nth molecule whereas $B_q^\dagger = N^{-1/2} \sum_n e^{iqna} B_n^\dagger$ creates an excitation of the wave vector q in a chain of N molecules with the intermolecular spacing a. Correspondingly, the exciton energy

$$E(q) = E_f + V_0 + 2 \sum_{n>0} V_n \cos(qna), \qquad (5)$$

where V_0 represents a possible renormalization for a single molecule,[31] while V_n the *effective* intermolecular interaction as mediated by the electromagnetic field. The interaction is handily expressed via the semiclassical expression

$$V_n = -\mathbf{p} \cdot \mathbf{E}(na\hat{\mathbf{x}}), \qquad (6)$$

with $\mathbf{p}$ being the molecular transition dipole moment and $\mathbf{E}(na\hat{\mathbf{x}})$ the electric field produced by the dipole $\mathbf{p} = p\hat{\mathbf{p}}$ at the distance na along the chain axis chosen to be along x (we use hatted letters to denote unit vectors).

If the electric field $\mathbf{E}$ is the total retarded field, however, it is in fact also a function of the oscillating dipole frequency $\omega = ck$ and has both real and imaginary parts. Equation (5) then has to be rewritten as a more general equation

$$E(q) = E' - i\Gamma/2 = E_f + \Sigma(k,q), \qquad (7)$$

involving the self-energy correction $\Sigma(k,q)$, the real-space transform of which

$$\Sigma(k,x) = -\mathbf{p} \cdot \mathbf{E}(k,x\hat{\mathbf{x}}) \qquad (8)$$

serves to replace Eq. (6). Equation (7) self-consistently (via $k = E/\hbar c$) determines both the dispersion $E'(q) = E_f + \text{Re}\{\Sigma(k,q)\}$ and the decay width $\Gamma(q) = -2 \text{Im}\{\Sigma(k,q)\}$ of the exciton-polariton states as a function of their wave vector q. This simple approach, alternatively formulated in terms of Green's functions, is both physically appealing and powerful as it involves only classically calculable electric fields; various aspects of it have been used for different geometries (e.g., Refs. 10, 11, and 14 and references therein). In this paper we will not pursue solving specific self-consistent problems that may depend on a multitude of parameters and, instead, be discussing the self-energy for a given *real* value of parameter k (that is, the oscillating frequency) for different values of the excitation wave vector q. For our numerical

illustrations in this paper we chose a representative value of k corresponding to the wavelength $\lambda = 2\pi/k = 400a$, a reasonable magnitude for the optical region of the spectrum given typical spacing $a \sim 10$ Å. Understandably, typical values for nanoparticle systems would be different.[4] With retardation effects neglected (purely electrostatic fields), the value of k would have to be set equal to zero.

Let us briefly review the application to a molecular chain in vacuum (see also Refs. 6 and 4). Consider the standard[22] retarded electric field at the point $\mathbf{r} = r\hat{\mathbf{r}}$ from the oscillating point dipole in vacuum,

$$\mathbf{E}^{\text{v}}(k,\mathbf{r}) = \frac{e^{ikr}}{r} \left\{ k^2 [\mathbf{p} - \hat{\mathbf{r}}(\hat{\mathbf{r}} \cdot \mathbf{p})] + \left(\frac{1}{r^2} - \frac{ik}{r} \right) [3\hat{\mathbf{r}}(\hat{\mathbf{r}} \cdot \mathbf{p}) - \mathbf{p}] \right\}, \qquad (9)$$

and the corresponding

$$\Sigma^{\text{v}}(k,\mathbf{r}) = -\mathbf{p} \cdot \mathbf{E}^{\text{v}}(k,\mathbf{r}).$$

This expression turns out to be directly applicable even for the decay of a single molecule (see also Ref. 10): indeed, calculating $-2 \text{Im}\{\Sigma^{\text{v}}(k,\mathbf{r} \to 0)\}$ immediately leads to the well-known decay width (2). To derive the decay rate for a 1D exciton state with wave vector q, one augments this decay by the sum of contributions from other molecules:

$$\Gamma^{\text{v}}(k,q) = \Gamma^0(k) - 4 \sum_{n>0} \cos(qna) \text{Im}\{\Sigma^{\text{v}}(k,na\hat{\mathbf{x}})\},$$

resulting, after evaluation of the sum, in already quoted Eq. (1). Exemplifying a general feature of self-energy corrections, a direct inspection easily verifies that, for a fixed k, Eqs. (1) and (2) satisfy, as expected,

$$\sum_q \Gamma^{\text{v}}(k,q) = N\Gamma^0(k). \qquad (10)$$

With the real part of the field (9), one immediately obtains the effective resonant interaction matrix element:

$$\frac{1}{p^2} \text{Re}\{\Sigma^{\text{v}}(k,x)\} = (1 - 3\cos^2\theta) \left[\frac{\cos(kx)}{x^3} + \frac{k\sin(kx)}{x^2} \right]$$
$$- (1 - \cos^2\theta) \frac{k^2 \cos(kx)}{x}, \qquad (11)$$

exactly the same result that would be derived in the picture of the virtual photon exchange.[26] Calculating the corresponding sums with $n > 0$ (and disregarding the irrelevant single-molecule renormalization[31]) for many molecules in the long-wavelength, $|qa| \ll 1$, expansion, one arrives at

$$\frac{a}{p^2} \text{Re}\{\Sigma^{\text{v}}(k,q)\} \simeq \frac{(1 - 3\cos^2\theta)}{2} \left[\frac{4\zeta(3)}{a^2} + k^2 - 3q^2 \right.$$
$$\left. - (k^2 - q^2)b \right] + (1 - \cos^2\theta)k^2 b, \quad (12)$$

where $\zeta(3) \simeq 1.202$ and $b = \ln(|k^2 - q^2|a^2)$. [It is useful to note that approximation (12) actually works very well over a sizable portion of the exciton Brillouin zone.] The known logarithmic divergence in Eq. (12) upon $|q| \to k$ signifies the splitting of the exciton-polariton spectrum into two

branches[5–7] as caused by the radiative zone component of the field at $\cos\theta \neq 1$ in Eq. (11). Of course, corresponding to this divergence there is a nonvanishing decay rate at $|q|=k-0$ in Eq. (1). The vanishing of the latter takes place only at $\cos\theta=1$, and in this case the exciton dispersion exhibits a single-branch behavior with a cusp at $|q|=k$.

The electrostatic part of Eq. (12) features a nonparabolic behavior $\propto q^2\ln(qa)^2$ at $|q| \gg k$ due to the long-range nature of the dipole-dipole interaction, making the exciton dispersion "steeper," the behavior that recently attracted attention in the context of exchange-interaction effects for excitons in carbon nanotubes.[27] The overall width of the bare exciton zone as seen in Eq. (12) is scaled with the energetic parameter

$$J = p^2/a^3, \tag{13}$$

establishing the unit for the nearest-neighbor electrostatic dipole-dipole interaction. To appreciate the scale of energies involved: with $p=1$ D and $a=10$ Å, for instance, $J \simeq 0.014$ eV. With reasonable variations of values of p and a, J could reach magnitudes ~ 0.1 eV.

III. MOLECULAR CHAIN NEAR THE INTERFACE

In the vicinity of the interface with a metallic or dielectric body, the total electric field can be conveniently represented as a sum of the primary, vacuum, field, discussed in Sec. II and the secondary field due to the induced response of that body: $\mathbf{E} = \mathbf{E}^v + \mathbf{E}^s$. Correspondingly, the self-energy of the exciton polaritons is also represented as $\Sigma = \Sigma^v + \Sigma^s$. In what follows we discuss the induced contribution $\Sigma^s(k,q)$ coming from a half-space characterized by the dielectric constant $\epsilon = \epsilon(\omega)$ taken at the frequency $\omega = ck$ in the geometry of the molecular chain (along $\mathbf{x}$), being parallel to the separating interface (xy plane) at the distance $z_0 = d/2$ from it (d is the distance between a dipole and its image).

The problem of an electric dipole near a metallic or dielectric half-space is a classical problem first treated by Sommerfeld[10,28] and whose solution is available in different forms. Here we find it convenient to adopt the expressions for the electric field as derived in Ref. 29. In the context of our application for fields along the chain, it matters how the dipoles are oriented with respect to both the chain and the interface. For a chain of electric dipoles of an arbitrary polarization $\hat{\mathbf{p}}$, one easily finds that

$$\Sigma^s(k,x) = \hat{p}_x^2\Sigma_\mathbf{x}^s(k,x) + \hat{p}_y^2\Sigma_\mathbf{y}^s(k,x) + \hat{p}_z^2\Sigma_\mathbf{z}^s(k,x),$$

where axes-related components can be rewritten from results in Ref. 29 as follows:

$$\frac{1}{p^2}\Sigma_\mathbf{x}^s(k,x) = \int_0^\infty \kappa d\kappa\, e^{-\gamma d}\left(\frac{\gamma Q}{2}J_-(\kappa x) + \frac{k^2 P}{2\gamma}J_+(\kappa x)\right) \tag{14}$$

for $\mathbf{x}$-polarized dipoles,

$$\frac{1}{p^2}\Sigma_\mathbf{y}^s(k,x) = \int_0^\infty \kappa d\kappa\, e^{-\gamma d}\left(\frac{\gamma Q}{2}J_+(\kappa x) + \frac{k^2 P}{2\gamma}J_-(\kappa x)\right) \tag{15}$$

for $\mathbf{y}$-polarized dipoles, and

$$\frac{1}{p^2}\Sigma_\mathbf{z}^s(k,x) = \int_0^\infty \kappa d\kappa\, e^{-\gamma d}\frac{\kappa^2 Q}{\gamma}J_0(\kappa x) \tag{16}$$

for $\mathbf{z}$-polarized dipoles. In Eqs. (14)–(16),

$$J_\pm(x) = J_0(x) \pm J_2(x)$$

are composed of Bessel functions of the first order while parameters

$$Q = \frac{\gamma_\epsilon - \epsilon\gamma}{\gamma_\epsilon + \epsilon\gamma}, \quad P = \frac{\gamma_\epsilon - \gamma}{\gamma_\epsilon + \gamma} \tag{17}$$

and

$$\gamma = (\kappa^2 - k^2)^{1/2}, \quad \gamma_\epsilon = (\kappa^2 - \epsilon k^2)^{1/2} \tag{18}$$

[for negative $u < 0$, $u^{1/2} = -i(-u)^{1/2}$ should be used in Eq. (18)]. One can straightforwardly verify that the no-retardation limit ($k=0$) of the above expressions leads to the usual electrostatic fields of image dipoles.

Representations (14)–(16) are quite meaningful physically. One immediately observes that the pole in the parameter Q in Eqs. (17) occurs at κ equal to κ_p in Eq. (4), the wave vector of the surface plasmon (surface polariton) whenever real $\epsilon < -1$. Together with p-polarized photons, SPs make the Q-containing contributions in Eqs. (14)–(16). The parameter P-containing terms, on the other hand, correspond to contributions to the electric fields from s-polarized photons. Expressions (14)–(16) taken at the source point $x=0$ would describe the effect of the half-space on the electronic transition in a single molecule as studied in Refs. 19 and 20.

We now turn to the q-dependent self-energy of an exciton in a long chain of molecules. Restricting ourselves to chain-to-interface distances larger than the intermolecular spacing, $d \gg a$, one can safely use a continuum description of the half-space response:

$$\Sigma^s(k,q) = 2\int_0^\infty \frac{dx}{a}\Sigma^s(k,x)\cos(qx). \tag{19}$$

As with the vacuum case, all results are clearly even functions of q; to simplify the expressions, we will therefore continue assuming $q > 0$. The transformation (19) for individual dipole contributions (14)–(16) is facilitated by the integrals[30]

$$\int_0^\infty dx\,\cos(qx)J_0(\kappa x) = \frac{1}{(\kappa^2 - q^2)^{1/2}}\Theta(\kappa - q), \tag{20}$$

$$\int_0^\infty dx\,\cos(qx)J_2(\kappa x) = \frac{1 - 2q^2/\kappa^2}{(\kappa^2 - q^2)^{1/2}}\Theta(\kappa - q), \tag{21}$$
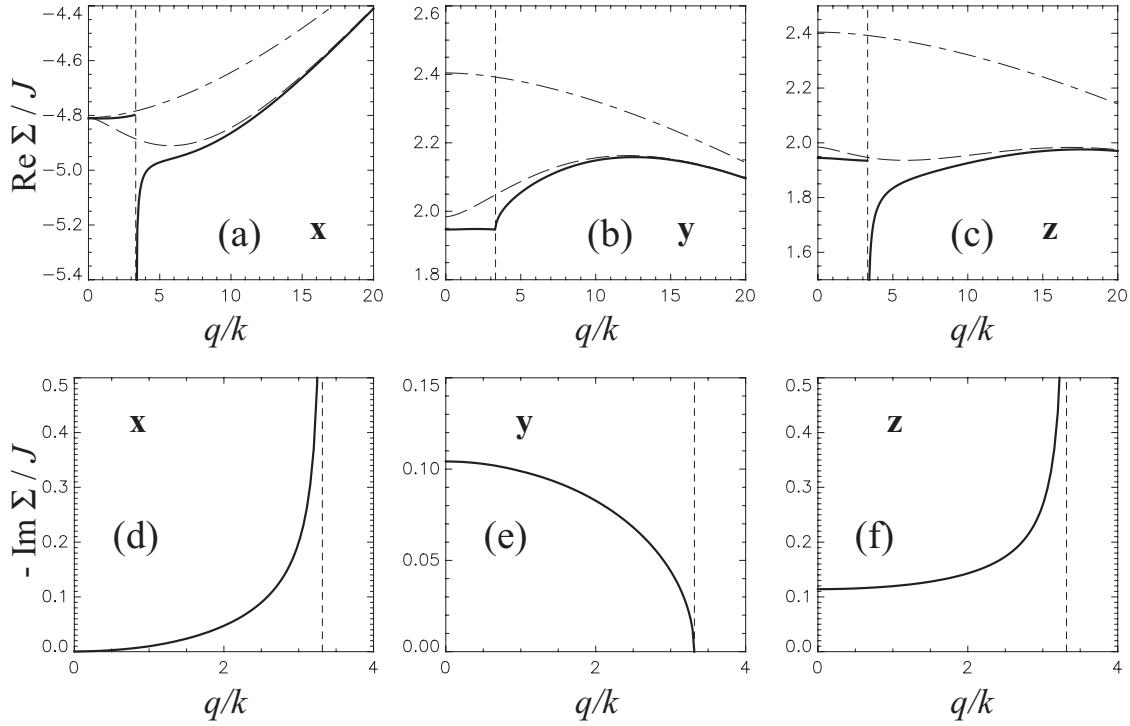
so that Eq. (16), e.g., is transformed into

FIG. 4. Real (upper panels) and imaginary (lower panels) of the self-energy $\Sigma(k,q)$ of exciton polaritons as functions of the reduced wave vector q/k for a fixed value of $k=2\pi/400a$, $\epsilon=-1.1$, and $d=10a$. Self-energy is shown with respect to J from Eq. (13). The vertical short-dashed lines show the position of the surface plasmon wave vector, κ_{p}/k. In the upper panels, the long-dashed lines show the electrostatic (no-retardation) results, dash-dotted lines the electrostatic results for the exciton dispersion in vacuum.

$$\frac{a}{p^2}\Sigma^{\mathrm{s}}_{\mathbf{z}}(k,q)=2\int_q^\infty \frac{\kappa^3 Q e^{-\gamma d}}{\gamma(\kappa^2-q^2)^{1/2}}d\kappa \qquad (22)$$

and similarly for Eqs. (14) and (15). The step functions in Eqs. (20) and (21), as is also reflected in Eq. (22), have a clear physical significance of the energy-and-momentum conservation limitation.

It is also useful and meaningful to note the no-retardation limit ($k=0$) of the above expressions, when Q in Eq. (17) becomes equal to the electrostatic combination (3), and the exciton dispersion would be affected by the image dipoles as

$$\frac{a}{Q_0 p^2}\Sigma^{\mathrm{s}}_{\mathbf{x}}(q)=2q^2\int_q^\infty \frac{e^{-\kappa d}}{(\kappa^2-q^2)^{1/2}}d\kappa=2q^2 K_0(qd), \quad (23)$$

$$\frac{a}{Q_0 p^2}\Sigma^{\mathrm{s}}_{\mathbf{y}}(q)=2\int_q^\infty (\kappa^2-q^2)^{1/2}e^{-\kappa d}d\kappa=\frac{2q}{d}K_1(qd), \quad (24)$$

and

$$\Sigma^{\mathrm{s}}_{\mathbf{z}}(q)=\Sigma^{\mathrm{s}}_{\mathbf{x}}(q)+\Sigma^{\mathrm{s}}_{\mathbf{y}}(q), \qquad (25)$$

where $K_0(x)$ and $K_1(x)$ are the modified Bessel functions.

The effects of these real image corrections are displayed in Fig. 4 showing an example of the total q-dependent exciton self-energy $\Sigma(k,q)$ including both vacuum and secondary field contributions. The figure is a result of an illustrative calculation for an idealized (no dissipation) system in the resonance region ($\epsilon=-1.1$ so that $\kappa_{\mathrm{p}}\simeq 3.3k$) at a relatively

close ($d=10a$) distance from the interface—to demonstrate a possible magnitude of the effects. The figure shows both the retardation effects as well as the fact that upon the increase of the wave vector q, the exciton dispersion approaches the electrostatic behavior. It is clear that, in principle, the electrostatic image forces may appreciably modify the exciton dispersion.

In an idealized system, the secondary field contributions to the imaginary part of the self-energy (exciton decay) can come only from two sources. First, it is the regions of variable κ in the integrals where the parameter γ, Eqs. (18), is imaginary. As Eq. (22) shows, that happens only for $q<k$—this is the source of the modification by the substrate of the exciton decay into vacuum photons that we explicitly illustrated in Fig. 1. The second, and dominating in Fig. 4, source is the surface plasmon pole $\kappa=\kappa_{\mathrm{p}}$ in the parameter Q in the integrals. As Eq. (22) shows again, this pole contributes only for $q<\kappa_{\mathrm{p}}$, signifying the decay of the exciton into a SP. The pole contributions to $-\mathrm{Im}\{\Sigma(k,q)\}$ are immediately calculable and can be represented by a combination of a common factor

$$\frac{4\pi}{|\epsilon|^{1/2}(1-\epsilon)}\frac{p^2\kappa_{\mathrm{p}}^4}{ak^2}\exp[-d(\kappa_{\mathrm{p}}^2-k^2)^{1/2}] \qquad (26)$$

and polarization- and q-dependent cofactors

$$q^2/\kappa_{\mathrm{p}}(\kappa_{\mathrm{p}}^2-q^2)^{1/2} \qquad (27)$$
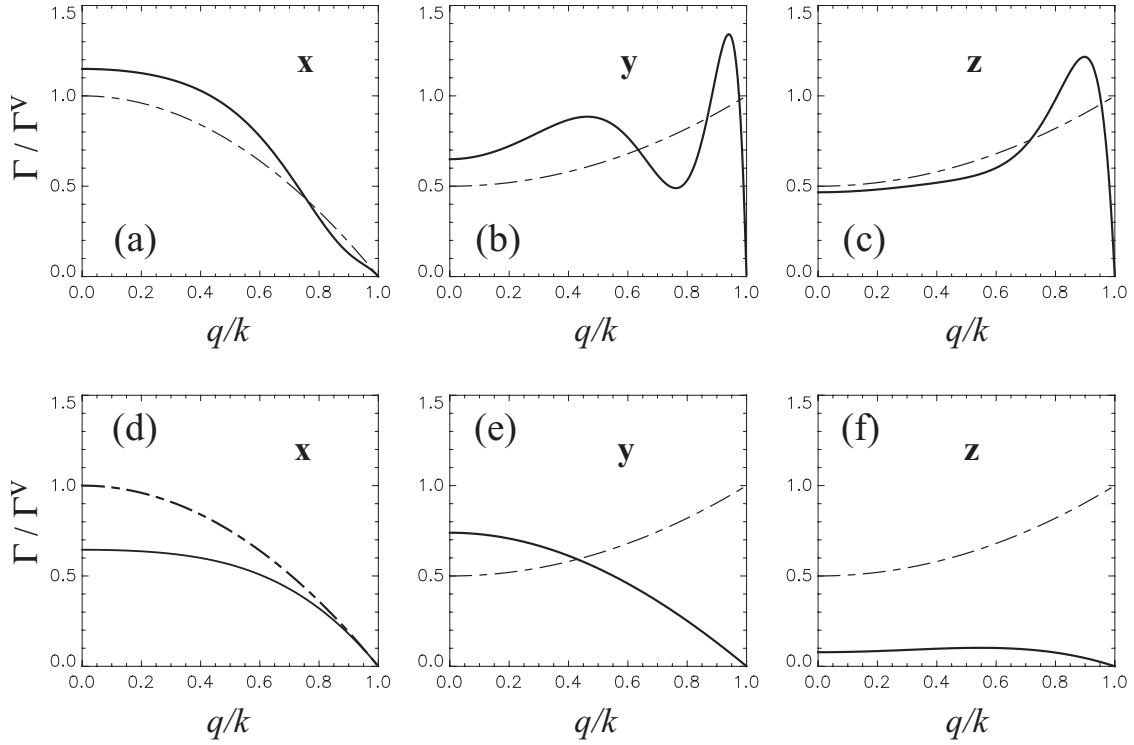
for $\mathbf{x}$ polarization,

FIG. 5. Decay width $\Gamma(k,q)$ of the exciton polariton as a function of the reduced wave vector q/k for a fixed value of k and $\epsilon = -0.8$. Two rows correspond to different dipole–to–image-dipole distances: upper panels (a)–(c) are for $d = 600a$, lower panels (d)–(f) for $d = 10a$. There is no surface plasmon channel here, and the total decay width is due to the vacuum photons only.

$$(\kappa_p^2 - q^2)^{1/2}/\kappa_p \qquad (28)$$

for **y**, and

$$|\epsilon|\kappa_p/(\kappa_p^2 - q^2)^{1/2} \qquad (29)$$

for **z**.

Accompanying decay's inverse square-root singularity in Eqs. (27) and (29), also seen in Figs. 4(d) and 4(f), are the diverging discontinuities in the real parts [panels (a) and (c) of Fig. 4] of the type familiar from the studies of the decay of 2D excitons into 3D vacuum photons.[1,5,24,25] Due to such a discontinuity, the resulting self-consistent dispersion of, e.g., **x**-polarized excitations would split into two branches as shown in Fig. 3. On the contrary, the decay rate of **y**-polarized excitons vanishes at $q \to \kappa_p$ in Eq. (28). This is a consequence of the polarization of SPs whose electric field can have only longitudinal and perpendicular to the interface components (like p-polarized photons). As $q \to \kappa_p$, the surface plasmons would be emitted along the chain direction; hence, their field would have no **y** components to interact with **y** excitons. [There is a similarity here with the decay of **x**-polarized excitons in vacuum, whose decay rate vanishes at $q \to k$, Eq. (1).] Correspondingly, the real part of the self-energy in Fig. 4(b) does not exhibit a discontinuity at $q = \kappa_p$ (the discontinuity is in the derivative) with the resulting exciton spectrum consisting of one branch only. Quite clear is also $\propto q^2$ behavior for **x** excitons in Eq. (27); it has the same origin as in the electrostatic effect (23)—at $q \to 0$, the exciton

polarization of the chain becomes uniform and there would be no polarization charges (a vanishing spatial derivative) to induce images in the substrate.

The SP excitations in the substrate exist in the region of frequencies where $\epsilon(\omega) < -1$. Qualitatively different, therefore, for a reflecting substrate is another region of frequencies in which $-1 < \epsilon(\omega) < 0$. In this case exciton polaritons in the molecular chain can decay only into vacuum photons. The (idealized) substrate then serves as to modify the dispersion of excitons and their radiative decay. An example of the radiative decay modification is shown in Fig. 5 calculated for $\epsilon = -0.8$ and to be compared with Fig. 1. Both figures feature the same distances from the interface but different magnitudes *and* signs of the image charges, Eq. (3). These two facts explain the similarities and differences in the radiative decay patterns for the two examples. Among the important common features, one should notice "oscillating" q dependences of the decay rate at larger distances and the vanishing of the radiative decay at $q \to k$. As the chain is moved farther away from the interface, even more undulations would be observed in the q dependence of the decay rate as a result of the interference with the image dipoles.

IV. EFFECTS OF DISSIPATION IN THE SUBSTRATE

Real metallic (dielectric) substrates are characterized by finite dissipation (losses) that is taken into account phenomenologically via the imaginary part of the dielectric function:
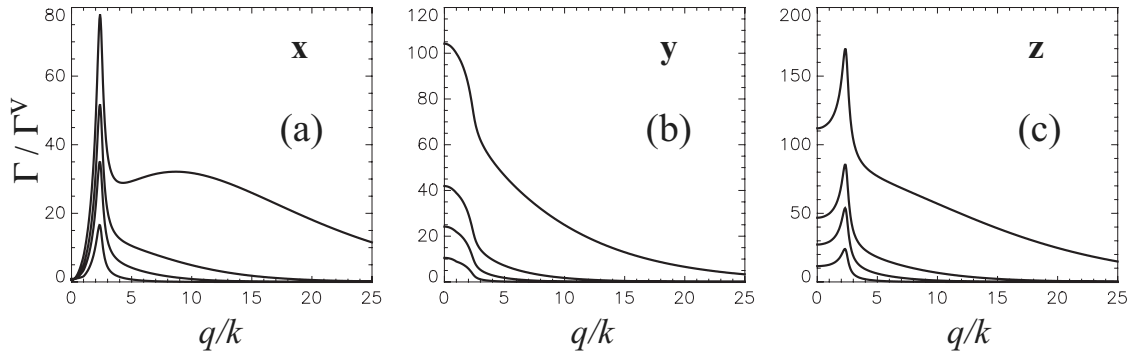
FIG. 6. Decay width $\Gamma(k,q)$ of exciton polaritons as a function of the reduced wave vector q/k for a fixed value of $k=2\pi/400a$ in units of vacuum $\Gamma^{\mathrm{v}}=2\pi p^2 k^2/a$ and for different (indicated in the panels) exciton polarizations. Here substrate's dielectric constant is *complex*: $\epsilon=-1.2+0.05i$. Each of the panels contains four curves corresponding to different distances between the molecular chain and the substrate (top to bottom): parameter $d=10a$, $20a$, $30a$, and $50a$.

$$\epsilon(\omega)=\epsilon'(\omega)+i\epsilon''(\omega).$$

In the context of the effects of ϵ'' on SPs, for a given real frequency ω, wave vectors of the SPs consequently acquire imaginary parts as well:[10]

$$\kappa_{\mathrm{p}}=\kappa_{\mathrm{p}}'+i\kappa_{\mathrm{p}}'',$$

where κ_{p}'' describes the damping of the SP modes. Another way to look at κ_{p}'' is as of the uncertainty (broadening) of the SP's wave vector. Hence the momentum conservation law in the exciton decay into a SP would not be obeyed exactly as in idealized systems discussed so far. One thus should expect a broadening and extension of the range of finite exciton decay rates into the region of the exciton wave vectors $q > \kappa_{\mathrm{p}}'$. Moreover, even with *relatively* small losses, $\epsilon'' \ll |\epsilon'|$, the relative damping of the SP can become substantial in the resonance region of ϵ' close to -1. Indeed, in this case,[10]

$$\kappa_{\mathrm{p}}''/\kappa_{\mathrm{p}}' \simeq \frac{\epsilon''/\epsilon'}{2(\epsilon'+1)}, \tag{30}$$

and the denominator on the right-hand side (rhs) of Eq. (30) could "compensate" for the smallness of ϵ'' and completely destroy the notion of a coherent SP.

Figure 6 shows results of the calculation of the exciton decay for the substrate with the dielectric constant $\epsilon=-1.2+0.05i$ and variable distances to the interface. As compared to the idealized system, one immediately notices very broad, especially at smaller distances, $q \gg \kappa_{\mathrm{p}}'$ regions of the exciton decay. For this particular value of the complex dielectric function, however, the "uncertainty" ratio (30) is only about 0.1. Thus the extremely broadened q region of the exciton decay is not due to the broadening of the SPs themselves; the latter can explain only the formation of the finite-magnitude SP peaks clearly seen in Fig. 6. Of course, with complex dielectric constants, the imaginary part of the exciton self-energy discussed in Sec. III is contributed to, in principle, by the whole integration range in integrals like Eq. (22), rather than just by the around-the-pole region. What is reflected in the broad "wings" in Fig. 6 is the result of the ordinary "incoherent" Joule losses due to the oscillating electric field of the exciton polarization penetrating into the substrate. Es-

pecially illuminating in this regard is a second maximum on the topmost curve in Fig. 6(a). Indeed, similarly to the image-charge effects already discussed in Sec. III, the electrostatic component of the electric field of **x**-polarized excitons has a q and d dependence reflected on the rhs of Eq. (23), the maximum of which is achieved at $q \sim 1/d$. As the distance from the interface increases, the role of such short-range energy transfer from the higher-q excitons to the substrate decreases and one can "tune" it off while still having an appreciable decay rate of the lower-q states into SPs. In addition to the largest-distance curves in Fig. 6, this point is illustrated in Fig. 7, showing clear SP emission effects both close to and away from the resonance region. The distance dependence of the SP emission intensity is governed by the factor (26), and one could likely "optimize" the relationship between the coherent and incoherent energy transfer based on the system regime parameters.

V. DISCUSSION

The modification of the electric fields in the presence of the reflecting substrate leads to substantial changes of the properties of 1D exciton-polaritons in a dipole-coupled chain above the substrate. The substrate modifies the interaction of the exciton with vacuum photons and, in addition, can engage a new and efficient interaction channel—with surface excitations of the substrate. While these statements also apply to a well-studied[19,20] case of a single molecule near the interface, the cooperative interaction of many molecules in the chain and of their images may lead to qualitatively and quantitatively interesting effects. In this paper, we discussed such effects for coherent delocalized 1D exciton polaritons that are well characterized by their wave vectors q. We emphasize that it is actually individual q states that would exhibit qualitatively different coherent properties—if averaged uniformly over all q, a (near) reduction would occur to the effects of the substrate on an individual molecule [similarly to discussed Eq. (10) for a vacuum]. Immediately noticeable in our illustrative examples, for instance, is a difference of the behavior of **x**- and **y**-polarized 1D exciton polaritons— while those cases of the molecular transition dipoles parallel
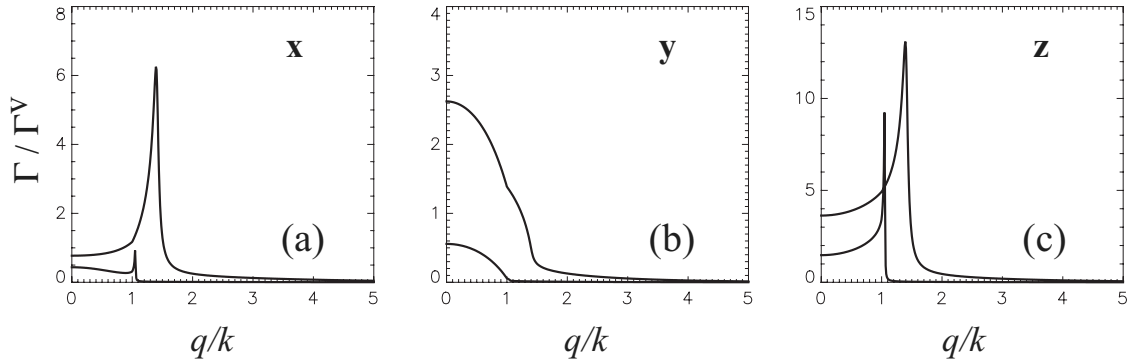
FIG. 7. As in Fig. 6 but for $d=50a$ and two different dielectric functions (top to bottom): $\epsilon=-2.0+0.1i$ and $\epsilon=-10.0+0.5i$.

to the interface would be equivalent for single molecules. The properties of 1D exciton polaritons depend specifically on their polarization, frequency with respect to the substrate dielectric dispersion, and distance from the interface. We reiterate that, while our illustrations used parameters appropriate for molecular systems, qualitatively similar effects are expected for other systems such as chains of nanoparticles.

A common feature for all exciton polarizations and conditions considered (see Figs. 1, 2, and 5) is that the rate of the radiative decay into vacuum photons in the presence of the substrate vanishes as $|q|$ approaches $k=\omega/c$ from the lower side—that is, where the exciton dispersion curve would cross the vacuum photon dispersion line (see, e.g., Fig. 3). This is distinctly different from the case of the chain in the vacuum where the radiative decay rate (1) generally remains finite at $|q|=k-0$ and discontinuously goes to zero at $|q|=k+0$; in vacuum, only excitons polarized parallel to the chain exhibit continuous vanishing at $|q|=k$. The consequence of this effect of the image dipoles is that, near the substrate, no branch splitting occurs for the chain polaritons at $|q|=k$. At distances from the interface comparable to the wavelength $2\pi/k$ of vacuum photons, the interference with the radiative fields of the image dipoles results in undulated patterns of the radiative decay [panels (a)–(c) of Figs. 1 and 5] as functions of q; the larger the distance, the more undulations would take place.

It is important to note that, as a result of integration (19) over many molecules in the chain, the magnitudes of these and some other q-dependent features fall off with distance from the interface slower than their averages characteristic of single molecules. Consider, e.g., the electrostatic exciton energy shifts due the interaction of the molecular dipole(s) with their image(s). For a single molecule, the corresponding transition energy shift is $\sim p^2/d^3$. The maximum of q-dependent shifts, however, as Eqs. (23)–(25) show, would be $\sim p^2/ad^2$—that is, much larger at distances $d \gg a$ (not in the immediate proximity of the interface). This may provide an opportunity for easier experimental identification of such shifts than for individual molecules.

While the distance dependence (26) of the decay rate of the excitons into surface plasmons is the same as for single

molecules, q-dependent enhancing factors (27) and (29), seen as the peaks in our illustrations, may facilitate better experimental verifications. As the rate of the emission of SPs is q dependent, we speculate that the chain excitons could perhaps serve as directional sources of SPs—in expectation of a more efficient emission along the chain for **x**- and **z**-polarized excitons and perpendicular to the chain for **y**-polarized excitons. We recall that these polarization assignments stem from the fact that the electric field of the SPs lies in the plane made by the wave vector and the normal to the interface. As the small-q exciton decay into SPs can be strongly enhanced in comparison with the decay into vacuum photons, it is likely that the inverse process of the excitation of the chain by SPs could also be exploited. Nonemissive exciton polaritons with larger q may also present an opportunity to be used for SP guiding.[23]

Various scattering and dissipation processes are known to be able to strongly affect features characteristic of idealized systems. We particularly discussed the chain exciton quenching due to the "incoherent" energy transfer to the substrate—and this does not exhaust the list. It suffices to also mention, e.g., the scattering by phonons in molecular chains or Joule losses in the chains of metallic nanoparticles. The fast scattering between different q states would result in the thermalized population of the exciton polaritons so that the observed decay rates are thermally averaged (see Refs. 7, 9, and 27 for some specific 1D applications). We therefore presume that the best conditions to experimentally address finer q-dependent effects we discussed in this paper would be low-temperature spectroscopic measurements.

[1] V. M. Agranovich, *Theory of Excitons* (Nauka, Moscow, 1968), updated English language edition is in preparation by Oxford University Press.

[2] F. Dubin, R. Melet, T. Barisien, R. Grousson, L. Legrand, M. Schott, and V. Voliotis, Nat. Phys. **2**, 32 (2006).

[3] H. Bässler, Nat. Phys. **2**, 15 (2006).

[4] V. A. Markel and A. K. Sarychev, Phys. Rev. B **75**, 085426 (2007).

[5] V. M. Agranovich and O. A. Dubovsky, JETP Lett. **3**, 223 (1966).

[6] M. R. Philpott, J. Chem. Phys. **63**, 485 (1975).

[7] D. S. Citrin, Phys. Rev. Lett. **69**, 3393 (1992).

[8] Y. N. Chen and D. S. Chuu, Europhys. Lett. **54**, 366 (2001).

[9] C. D. Spataru, S. Ismail-Beigi, R. B. Capaz, and S. G. Louie, Phys. Rev. Lett. **95**, 247402 (2005).

[10] L. Novotny and B. Hecht, *Principles of Nano-Optics* (Cambridge University Press, Cambridge, England, 2006).

[11] R. R. Chance, A. Prock, and R. Silbey, Adv. Chem. Phys. **37**, 1 (1978).

[12] M. Cho and R. J. Silbey, Chem. Phys. Lett. **242**, 291 (1995).

[13] H. R. Stuart and D. G. Hall, Phys. Rev. Lett. **80**, 5663 (1998).

[14] R. L. Hartman and P. T. Leung, Phys. Rev. B **64**, 193308 (2001).

[15] Y. N. Chen, D. S. Chuu, T. Brandes, and B. Kramer, Phys. Rev. B **64**, 125307 (2001).

[16] D. S. Citrin, Opt. Lett. **31**, 98 (2006).

[17] J. Bellessa, C. Bonnand, J. C. Plenet, and J. Mugnier, Phys. Rev. Lett. **93**, 036404 (2004).

[18] T. Søndergaard and S. I. Bozhevolnyi, Phys. Rev. B **69**, 045422 (2004).

[19] H. Morawitz and M. R. Philpott, Phys. Rev. B **10**, 4863 (1974).

[20] M. R. Philpott, J. Chem. Phys. **62**, 1812 (1975).

[21] W. H. Weber and C. F. Eagen, Opt. Lett. **4**, 236 (1979).

[22] J. D. Jackson, *Classical Electrodynamics* (Wiley, New York, 1975).

[23] A. B. Evlyukhin and S. I. Bozhevolnyi, Laser Phys. Lett. **3**, 396 (2006).

[24] L. C. Andreani and F. Bassani, Phys. Rev. B **41**, 7536 (1990).

[25] S. Jorda, U. Rössler, and D. Broido, Phys. Rev. B **48**, 1669 (1993).

[26] D. P. Craig and T. Thirunamachandran, *Molecular Quantum Electrodynamics* (Academic Press, London, 1984).

[27] V. Perebeinos, J. Tersoff, and P. Avouris, Nano Lett. **5**, 2495 (2005).

[28] A. Sommerfeld, *Partial Differential Equations in Physics* (Cambridge University Press, Cambridge, England, 2006).

[29] R. W. P. King and G. S. Smith, *Antennas in Matter* (MIT Press, Cambridge, MA, 1981).

[30] A. P. Prudnikov, Y. A. Brychkov, and O. I. Marichev, *Integrals and Series. Special Functions* (OPA, Amsterdam, 1990).

[31] Single-molecule renormalization is, to a large extent, not important for our interest in this paper, and we refer the reader to numerous studies dedicated to it. We will completely disregard the vacuum real energy shift of a single molecule which can be thought of as absorbed in E_f. By the same token, we do not discuss any modifications of E_f in the presence of the interface that may take place due to the interactions outside of our scope.
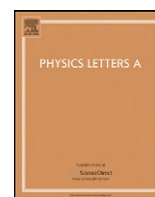
One-dimensional semiconductor in a polar solvent: Solvation and low-frequency dynamics of an excess charge carrier

Yu.N. Gartstein[*], G.L. Ussery

Department of Physics, The University of Texas at Dallas, PO Box 830688, FO23 Richardson, TX 75083, USA

ABSTRACT

Due to solvation, excess charge carriers on 1d semiconductor nanostructures immersed in polar solvents undergo self-localization into polaronic states. Using a *simplified* theoretical model for small-diameter structures, we study low-frequency dynamical properties of resulting 1d adiabatic polarons. The combined microscopic dynamics of the electronic charge density and the solvent leads to macroscopic Langevin dynamics of a polaron and to the appearance of local dielectric relaxation modes. Polaron mobility is evaluated as a function of system parameters. Numerical estimates indicate that the solvated carriers can have mobilities orders of magnitude lower than the intrinsic values.

© 2008 Elsevier B.V. All rights reserved.

1. Introduction

One-dimensional (1d) semiconductor (SC) nanostructures like nanowires and nanotubes are fascinating objects offering a promise for various applications, including electronics, energy harvesting and sensors. The properties of excess charge carriers are fundamental for these applications. A customary picture used to describe charge carriers in nanowires [1] and nanotubes [2] is that of band electron states with very high, nearly ballistic [3], intrinsic mobilities. Many applications, however, such as photoelectrochemical energy conversion [4,5], feature SC nanostructures in contact with polar liquid environments. We have recently pointed out [6, 7] that excess carriers on 1d SCs immersed in the sluggish polar medium can drastically change their nature. Due to the long-range Coulomb interaction with the slow (orientational) polarization of the medium, a charge carrier (an electron or a hole) gets solvated forming a localized electronic state surrounded by a self-consistent dielectric polarization pattern as shown schematically in Fig. 1. In physical parlance, self-trapped states formed by this mechanism are traditionally called polarons, extensively studied in 3d ionic crystals and polar SCs [8,9]. Another related 3d notion is that of the solvated electron in liquids [10–12].

The formation of 1d polarons is expected to have an impact on various processes such as electron–hole separation from bound excitonic states [6,7], charge transfer reactions, local optical absorption [13] and charge carrier transport. As we discuss the low-frequency polaron dynamics in this Letter within a *simplified* theoretical framework, it will be particularly illustrated that the mobili-

ties of the solvated carriers can be orders of magnitude lower than the intrinsic values. We note that the system we consider appears an interesting model realization in the general context of quantum particles interacting with a dissipative environment [14]. While we restrict our discussion to rigid SC nanostructures with good intrinsic electronic properties and favoring the formation of continuum adiabatic polarons, the generic aspects apply to other systems as well. Basko and Conwell [15] emphasized a conceptually similar formation of hole polarons in DNA in aqueous electrolyte solutions and discussed the effect of water drag on their mobility [16].

The parametric scales for the spatial extent and the binding energy of the 3d polaron are established by the 3d Coulomb center problem where, for a carrier of charge q and effective mass m in the uniform medium of effective dielectric constant ϵ^*, the corresponding 3d Bohr radius and Rydberg are[1]

$$a_B = \epsilon^* \hbar^2 / mq^2, \qquad Ry = q^2 / 2\epsilon^* a_B. \tag{1}$$

As a result of the confinement of charge carrier motion to the 1d SC, the effects of Coulomb interactions are generally known [17] to get amplified, and, in fact, the binding energy E_b^{pol} of the confined polaron can increase substantially in comparison with the 3d binding [6,7]. Our interest is in the strong confinement regime: $a_B \gg R$ (R is the transverse radius of the 1d structure), when the resulting longitudinal spatial extent of the polaron is much larger than R (see Fig. 2(b)) and the self-localized charge carrier can be adequately described by the 1d wave function $\psi(x)$, x being the coordinate along the structure axis.

---

[1] As we do not compare polarons and excitons in this Letter, our definitions here are based on the electron mass rather than on the exciton reduced mass used in Refs. [6,7].
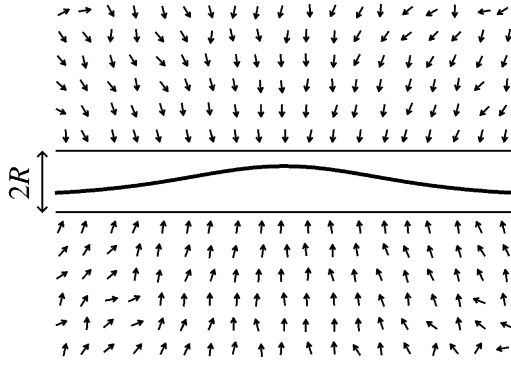
* Corresponding author.
E-mail address: yuri.gartstein@utdallas.edu (Yu.N. Gartstein).

Fig. 1. Schematically: Solvated excess electron charge density (thick line) along the 1d semiconductor nanostructure which is surrounded by a pattern of the orientational polarization of solvent molecules.

We consider the polaron to be formed due to the interaction of an excess carrier with the slow polarization component of the Debye solvent described by the frequency ω-dependent dielectric function

$$\epsilon(\omega) = \epsilon_\infty + \frac{\epsilon_s - \epsilon_\infty}{1 - i\omega\tau_D}, \tag{2}$$

for which the effective dielectric constant in Eq. (1) would be determined from the well-known [8,11,12] relationship

$$1/\epsilon^* = 1/\epsilon_\infty - 1/\epsilon_s, \tag{3}$$

with $\epsilon_s \gg \epsilon_\infty$ for typical solvent values of static ϵ_s and high-frequency ϵ_∞ constants [18]. The characteristic time τ_D in Eq. (2) is the Debye (transverse) relaxation time, for the problem at hand, however, the solvent response occurs at generally much shorter time scales corresponding to the longitudinal relaxation time [12, 18,19]

$$\tau_L = \frac{\epsilon_\infty}{\epsilon_s} \tau_D. \tag{4}$$

Typical solvents are characterized by a wide range of τ_L ranging from fractions to tens of ps [6,18]. With the estimated polaron binding energies E_b^{pol} on the order of 0.1 eV, the dynamic adiabaticity is ensured by $\hbar/\tau_L \ll E_b^{\text{pol}}$. For room temperatures T, on the other hand, one can also have $k_B T \ll E_b^{\text{pol}}$ satisfied, thus making thermal population of higher energy electronic states negligible.

The aim of this Letter is to elucidate the response of such 1d polarons to weak perturbations of low-frequencies ω: $\hbar\omega \ll E_b^{\text{pol}}$, which do not cause transitions between different electronic levels. This, in particular, encompasses such basic phenomena as polaron drift caused by an applied field and polaron diffusion caused by the dielectric fluctuations of the surrounding solvent. We stress that our consideration is limited to a simplified theoretical model whose main purpose is to address elements of the essential physics. We will show how the underlying combined microscopic dynamics of the electronic charge density on the 1d SC and the solvent results in point-particle-like Langevin dynamics of the polaron center. The derived mobility and diffusion coefficient, as should be expected [14], satisfy the Einstein relation. In addition, we demonstrate the existence of local relaxation modes around the polaron whose relaxation times are somewhat longer than bare solvent's τ_L. These modes involve polaron shape variations and presumably could manifest themselves in responses to time-dependent fields as well as in collisions.

2. General adiabatic polaron relationships

In the adiabatic picture, the excess charge carrier instantaneously responds to the electrostatic potential $\phi(x,t)$ that is slowly changing in time by staying in the lowest eigenstate of the *stationary* Schrödinger equation:

$$H\psi(x,t) = E\psi(x,t), \qquad H = -\frac{\hbar^2}{2m}\frac{\partial^2}{\partial x^2} + q\phi(x,t), \tag{5}$$

where time t thus enters only as a parameter. The corresponding time-dependent 1d charge density is

$$\rho(x,t) = q|\psi(x,t)|^2, \tag{6}$$

where q is the charge of the carrier.

The electrostatic potential $\phi(x,t)$, in turn, can be represented as a sum of two contributions:

$$\phi(x,t) = \phi_i(x,t) + \phi_s(x,t), \tag{7}$$

where the first term represents the potential "independent" of the charge carrier itself, that is, the potential that would be there if the charge carrier was absent—as exemplified by applied fields and dielectric fluctuations of the environment. The second term in (7) is the part that is induced by the carrier charge density (6) in the past via the time-dependent medium response:

$$\phi_s(x,t) = \int_0^\infty dt' \int dx' \, \mathcal{G}(x',t')\rho(x-x',t-t'). \tag{8}$$

Eq. (8) assumes the translationally invariant response so that

$$\phi_s(k,\omega) = \mathcal{G}(k,\omega)\rho(k,\omega).$$

in Fourier space. The response function $\mathcal{G}$ is determined from the solutions of the corresponding 3d electrostatic potential problem using the appropriate geometry of elementary charge distributions and of the dielectric environment. Let us denote such a solution derived for a particular value $\epsilon(\omega)$ of the medium dielectric function as $V(k, \epsilon(\omega))$. One, of course, recognizes that $\mathcal{G}$ should *not* include the instantaneous Coulomb interaction of the charge carrier with itself; in the context of the Debye solvent (2), the medium for this case is characterized by ϵ_∞. In these terms,

$$\mathcal{G}(k,\omega) = V(k, \epsilon(\omega)) - V(k, \epsilon_\infty), \tag{9}$$

the relevant response is thus due to the slow (orientational) component of the dielectric polarization of the medium. Explicit examples of such calculations for the nanotube geometry with the account of tube's own polarizability can be found in Ref. [6]. When the dielectric polarization effects are well captured by the model of a uniform 3d medium, which is a good approximation in the strong confinement regime [6,20], the response $\mathcal{G}$ is separable into a product of the spatial and temporal components (all bare Coulomb interactions are simply decreased by a factor of the inverse dielectric constant). We will write this as

$$\mathcal{G}(x,t) = -\mathcal{A}(t)G(x) \quad \text{or} \quad \mathcal{G}(k\omega) = -\alpha(\omega)g(k). \tag{10}$$

To gain more physical insight and obtain explicit simpler relationships, we will restrict our attention in this Letter to this regime. In accordance with Eq. (9), the temporal part for the Debye solvent (2) can be described as

$$\alpha(\omega) = \frac{1}{\epsilon_\infty} - \frac{1}{\epsilon(\omega)} = \frac{\alpha_0}{1 - i\omega\tau_L}, \quad \alpha_0 = \frac{1}{\epsilon^*}. \tag{11}$$

The relaxation time τ_L that determines the pole of the *inverse* dielectric function as well as the familiar combination (3) naturally arise here. As is well known [12,18,19], τ_D characterizes the dielectric relaxation in circumstances controlled by electrostatic potentials (electric fields **E**) while τ_L is appropriate in circumstances

controlled by charge densities (electric inductions **D**). Evidently, the latter is the relevant situation here, and we will use $\tau \equiv \tau_L$ to simplify the notation in what follows. In the time domain, the response function is therefore

$$\mathcal{A}(t) = \int \frac{d\omega}{2\pi} e^{-i\omega t} \alpha(\omega) = \frac{\alpha_0}{\tau} e^{-t/\tau} \Theta(t), \tag{12}$$

where Θ is a step function.

The spatial part $G(x)$ of the response (10) is determined by the specifics of the transverse charge distribution in our 1d SC. For the illustrative calculations below, we will use the case of the nanotube geometry where (see, e.g., Refs. [6,21])

$$g(k) = 2I_0(kR)K_0(kR), \tag{13}$$

with I_0 and K_0 being the modified Bessel functions and R the tube radius. Equation (13) essentially corresponds to the Fourier transform of the Coulomb interaction between two charged rings of radius R.

Taking advantage of the particular simple form (12), the temporal evolution of the potential $\phi(x,t)$, as per Eqs. (7) and (8), can be conveniently converted into the differential (over time) equation:

$$\begin{aligned}&\frac{\partial \phi(x,t)}{\partial t} + \frac{\phi(x,t)}{\tau} \\&= \frac{\partial \phi_i(x,t)}{\partial t} + \frac{\phi_i(x,t)}{\tau} - \frac{\alpha_0}{\tau} \int dx' \, G(x-x')\rho(x',t).\end{aligned} \tag{14}$$

3. The stationary solution and small perturbations around it

One first discusses the dynamics in the absence of the external potential $\phi_i(x,t)$, and the starting point, of course, is the consideration of the ground-state *stationary* polaron problem. In this basic case, the resulting charge density and potential are time-independent, we denote their spatial distributions as $\bar{\rho}(x)$ and $\bar{\phi}(x)$, respectively. Their relationship is determined by the static medium response, or $\alpha(0) = \alpha_0$ in Eqs. (10), (11). That is also immediately seen from Eq. (14):

$$\bar{\phi}(x - x_0) = -\alpha_0 \int dx' \, G(x-x')\bar{\rho}(x'-x_0), \tag{15}$$

where we explicitly emphasized the translational invariance by indicating that the stationary solutions can be centered around arbitrary points x_0. (The negative sign in the r.h.s. of Eq. (15) and in other expressions below signifies that a positive charge density leads to a stabilizing negative potential, and vice versa.) As $\bar{\rho}(x)$ is determined (6) by the ground-state charge carrier wave function $\psi_0(x)$ obeying Eq. (5), the latter wave function is then found from the self-consistent non-linear Schrödinger equation

$$-\frac{\hbar^2}{2m}\frac{\partial^2 \psi(x)}{\partial x^2} - \frac{q^2}{\epsilon^*} \int dx' \, G(x-x')|\psi(x')|^2 \psi(x) = E\psi(x)$$

as corresponding to its lowest eigenvalue $E = E_0$. This, of course, is the same equation one would derive from the optimization of the adiabatic system energy; it results in self-localized (polaronic) solutions as we discussed in Refs. [6,7].

With the ground-state polaron solution in place, one can now consider the effects of *small* potential perturbations $\tilde{\phi}(x,t)$: $\phi(x,t) = \bar{\phi}(x) + \tilde{\phi}(x,t)$, in the stationary Schrödinger problem (5): $H = \bar{H} + V$,

$$\bar{H} = -\frac{\hbar^2}{2m}\frac{\partial^2}{\partial x^2} + q\bar{\phi}(x), \qquad V = q\tilde{\phi}(x,t).$$

The overall approach here is very similar to used in previous studies of small perturbations around 3d [22] and 1d [23–25] optical

polarons. The standard lowest-order perturbation theory with respect to V then results in the perturbed electron density $\rho(x,t) = \bar{\rho}(x) + \tilde{\rho}(x,t)$ with

$$\tilde{\rho}(x,t) = -\int dx' \, L(x,x')\tilde{\phi}(x',t), \tag{16}$$

where the Hermitian kernel

$$L(x,x') = q^2 \sum_{i>0} \frac{\psi_0^*(x)\psi_i(x)\psi_i^*(x')\psi_0(x') + \text{c.c.}}{E_i - E_0}$$

is built out of the solutions of the unperturbed problem

$$\bar{H}\psi_i(x) = E_i \psi_i(x).$$

The density perturbation (16) should self-consistently determine the potential perturbations (8) at future times, that is:

$$\tilde{\phi}(x,t) = \int_0^\infty dt' \int dx' \, \mathcal{G}(x',t')\tilde{\rho}(x-x',t-t'). \tag{17}$$

Together, Eqs. (16) and (17) determine the eigenmodes of the undriven dynamics around the stationary polaron in the case of a general response $\mathcal{G}$. In the separable case (10), the problem of finding eigenmodes evidently reduces to a simpler generalized eigenvalue problem which we write in the form of

$$\rho_n(x) = -\int dx' \, L(x,x')\phi_n(x'), \tag{18a}$$

$$\phi_n(x) = -\lambda_n \alpha_0 \int dx' \, G(x-x')\rho_n(x'). \tag{18b}$$

In practical terms, the generalized problem (18) is easily converted to a normal eigenvalue problem and readily solved in Fourier (wave vector) space. The eigenfunctions of this problem form a complete orthogonal set. To save space on notation, here we choose to normalize this set without extra coefficients as

$$-\int dx \, \rho_m(x)\phi_n(x) = \delta_{nm} \tag{19}$$

(all functions can be chosen real). The eigenvalues $\lambda_n \geqslant 1$ ($n \geqslant 0$), in turn, determine the eigenfrequencies ω_n from

$$\alpha(\omega_n) = \lambda_n \alpha_0. \tag{20}$$

Unlike the oscillating solutions in Refs. [22–25], for the Debye solvent with its dissipative dynamics (11), Eq. (20) leads to a set of relaxation times τ_n:

$$\omega_n = -\frac{i}{\tau_n}, \quad \tau_n = \frac{\tau}{1 - 1/\lambda_n}. \tag{21}$$

The temporal evolution of the eigenfunctions of the dynamical problem would therefore be "ordinarily" decaying:

$$\rho_n(x,t) \propto \rho_n(x)e^{-t/\tau_n}.$$

Fig. 2(a) illustrates how these relaxation times τ_n converge to the "bare" value of τ upon the increase of the mode index n—for this illustrative calculation we used the tubular case (13) with the confinement parameter $a_B/R = 10$. One immediately notices, however, that the dynamics has a very different character for the mode with $\lambda_0 = 1$ corresponding to $\omega_0 = 0$. This is the so-called zero-frequency translational mode whose existence is a general feature of quantum-field models with non-trivial spatial solutions and is a consequence of the translational invariance [26]. As discussed above, the static polaronic solutions are degenerate with respect to the position of the polaron center. An infinitesimal displacement along x corresponds to the spatial derivative of the static solutions
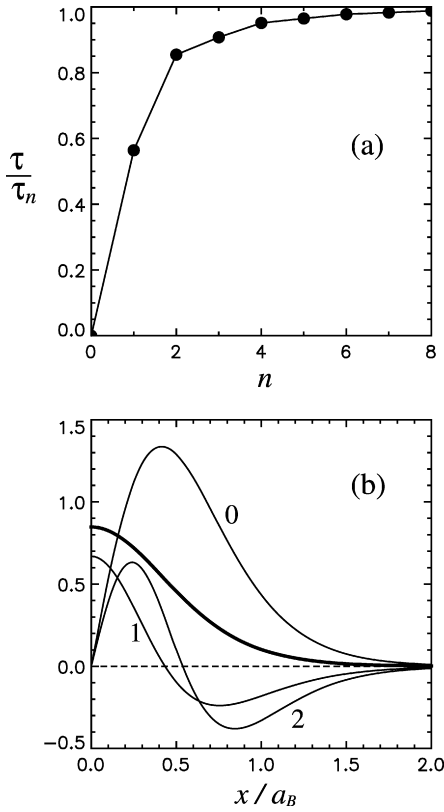
Fig. 2. Illustration of local relaxation modes (tubular geometry with $a_B/R = 10$): (a) Relaxation times for the first $n = 0$ to 8 eigenmodes; (b) Shapes of the spatial density variations $\rho_n(x)$ for the first 3 modes as indicated by values of the index n next to thin lines. These lines are arbitrarily scaled here to be better displayed. The thick line corresponds to the scaled static polaron density $a_B \bar{\rho}(x)/q$.

over x (denoted below with symbol $'$); one indeed easily verifies that

$$\rho_0(x) = \gamma^{-1/2} \bar{\rho}'(x), \qquad \phi_0(x) = \gamma^{-1/2} \bar{\phi}'(x) \qquad (22)$$

satisfy Eqs. (18) with $\lambda_0 = 1$. Here the normalization factor involves

$$\gamma = \int dx \, |\bar{\rho}'(x) \bar{\phi}'(x)|. \qquad (23)$$

As an example, Fig. 2(b) shows spatial patterns corresponding to the first 3 eigenmodes in comparison with the static polaron shape in terms of the charge density. Of course, all density variations satisfy $\int dx \, \rho_n(x) = 0$. Given the numerical nature of the solution, we have confirmed that the translational mode ($n = 0$) precisely follows the spatial derivative of the static polaron shape. The next mode ($n = 1$) can be qualitatively thought of as corresponding to the variation of the polaron width. The convergence pattern in panel (a) and the spatial variations displayed in panel (b) of Fig. 2 are reminiscent of those discussed in connection with 1d optical polarons [23–25].

As is well known [26,27], in the expansions of the arbitrary spatial patterns over the complete set of eigenmodes, the zero-frequency mode should be excluded in favor of the collective coordinate $\xi(t)$ of the polaron center position (polaron centroid). Such expansions for the potential and density variations then take the form of

$$\phi(x,t) = \bar{\phi}\big(x - \xi(t)\big) + \sum_{n \geqslant 1} a_n(t) \phi_n\big(x - \xi(t)\big), \qquad (24a)$$

$$\rho(x,t) = \bar{\rho}\big(x - \xi(t)\big) + \sum_{n \geqslant 1} a_n(t) \rho_n\big(x - \xi(t)\big), \qquad (24b)$$

where the first terms correspond to the shapes of the static solutions that are centered around $\xi(t)$. The set of time-dependent coefficients $a_n(t)$ ($n \geqslant 1$) and the centroid coordinate $\xi(t)$ then constitute complete coordinates of the system and can be conveniently used to describe its dynamics.

Using Eqs. (24) in Eq. (14) for the potential evolution, one converts the latter into

$$-\dot{\xi}\bigg[\bar{\phi}' + \sum_{n \geqslant 1} a_n \phi_n'\bigg] + \sum_{n \geqslant 1}\bigg[\dot{a}_n + \frac{a_n}{\tau_n}\bigg]\phi_n = F(x,t), \qquad (25)$$

where the external perturbation part is

$$F(x,t) = \frac{\partial \phi_i(x,t)}{\partial t} + \frac{\phi_i(x,t)}{\tau}. \qquad (26)$$

As in Eqs. (24), all potential expansion functions in Eq. (25) have the same argument $(x - \xi(t))$.

4. Equations of motion and centroid dynamics

One derives the equations of motion for the set of coordinates $\{\xi(t), a_n(t)\}$ by projecting Eq. (25) with each of $\rho_n(x - \xi(t))$ ($n \geqslant 0$) and utilizing the orthonormality relationships (19). Now note that we are interested in and have been developing our framework to study the lowest-order effects of small perturbations. Correspondingly, the system responses to such perturbations, the centroid velocity $\dot{\xi}(t)$ and shape deformation coefficients $a_n(t)$, are small. Therefore, the second-order term in Eq. (25) (containing products of $\dot{\xi}$ and a_n) can safely be dropped. The result is then a set of fully decoupled equations of motion:

$$\gamma \dot{\xi} = f, \qquad (27)$$

$$\dot{a}_n + a_n/\tau_n = f_n, \quad n \geqslant 1, \qquad (28)$$

where

$$f(\xi,t) = \int dx \, \bar{\rho}'(x) F(x + \xi, t) \qquad (29)$$

and

$$f_n(\xi,t) = -\int dx \, \rho_n(x) F(x + \xi, t).$$

Eqs. (27) and (28) evidently allow one to easily study various dynamic responses. Here we will concentrate on the centroid dynamics.

The external (perturbation) potential $\phi_i(x,t)$ can be represented as a sum of two contributions:

$$\phi_i(x,t) = \phi_a(x,t) + \phi_f(x,t),$$

where $\phi_a(x,t)$ is due to the applied field while $\phi_f(x,t)$ is due to the "bare" fluctuations of the dielectric polarization (here, of course, only its slow, orientational, component is relevant). We will correspondingly use subscript indices a and f.

Let us consider first the motion of the polaron under the action of a constant applied potential $\phi_a(x)$ that can slowly (on the scale of the polaron size) change in space. From Eqs. (26) and (29) it immediately follows that

$$f_a(\xi) = \int dx \, \bar{\rho}'(x) \frac{\phi_a(x+\xi)}{\tau} = -\int dx \, \bar{\rho}(x) \frac{\partial \phi_a(x+\xi)}{\tau \partial \xi}$$
$$\simeq -\bigg(\frac{\partial \phi_a(\xi)}{\tau \partial \xi}\bigg) \int dx \, \bar{\rho}(x) = \frac{q\mathcal{E}(\xi)}{\tau}, \qquad (30)$$

where $\mathcal{E}$ is the electric field acting on the polaron.

On the other hand, the fluctuating contribution $f_f(\xi,t)$ is a random process whose correlations have to be determined from the correlations of $\phi_f(x,t)$ subsequently using definitions (26) and

(29). The bare classical ($k_B T \gg \hbar/\tau$) fluctuations are easily found by using the fluctuation–dissipation theorem for the specified 1d geometry, the result is

$$\langle \phi_f(x,t)\phi_f(x',t')\rangle = \alpha_0 k_B T\, G(x-x')e^{-|t-t'|/\tau}. \tag{31}$$

With Eq. (26), this translates *exactly* into

$$\langle F_f(x,t)F_f(x',t')\rangle = \frac{2\alpha_0 k_B T}{\tau}G(x-x')\delta(t-t'). \tag{32}$$

Given the time-uncorrelated character of Eq. (32), the relevant correlations of f_f are those for the same centroid coordinate:

$$\langle f_f(\xi,t)f_f(\xi,t')\rangle = \frac{2\gamma k_B T}{\tau}\delta(t-t'). \tag{33}$$

To derive Eq. (33) from Eqs. (29) and (32), we have also used Eq. (15) in the following:

$$\int dx\,dx'\,\bar{\rho}'(x)\bar{\rho}'(x')G(x-x') = -\int dx\,\frac{\bar{\rho}'(x)\bar{\phi}'(x)}{\alpha_0} = \frac{\gamma}{\alpha_0}.$$

Introducing the random velocities $\eta(t) = f_f(t)/\gamma$, the equation of motion (27) for the polaron centroid under the action of a constant field can be conveniently rewritten as

$$\dot{\xi} = \mu q\mathcal{E} + \eta(t), \tag{34}$$

where the mobility

$$\mu = 1/\gamma\tau \tag{35}$$

is defined with respect to the dynamical force $q\mathcal{E}$ while the random process $\eta(t)$, as per Eq. (33), satisfies

$$\langle \eta(t)\eta(t')\rangle = 2D\delta(t-t') \tag{36}$$

with the diffusion coefficient

$$D = k_B T/\gamma\tau. \tag{37}$$

Eq. (34) is the standard overdamped Langevin equation [12] for a point particle as consistent with our assumption of the field having practically no spatial variation on the scale of the polaron size. We emphasize that ingredients of Eq. (34) have been *derived* from the underlying microscopic dynamics. Our mobility (35) and diffusion coefficient (37) manifestly obey the Einstein relation

$$D = \mu k_B T,$$

thus ensuring that the macroscopic dynamics of the polaron in the steady state leads to the Boltzmann distribution. We note that expression (35) is similar in form to the one obtained from energy conservation considerations by Basko and Conwell [15,16] but with the important quantitative distinction that our $\tau = \tau_L$ is the longitudinal relaxation time rather than τ_D they used (the difference that can easily exceed an order of magnitude).

Our discussion of the constant applied field is straightforwardly generalized to time-dependent fields. As Eq. (26) suggests, for fields varying as $\mathcal{E}(t) = \mathcal{E}_0\exp(-i\omega t)$, the first term in Eq. (34) would get modified, with $1/\tau$ being replaced by $-i\omega + 1/\tau$. In addition, time-dependent fields would be exciting polaron shape deformations (28) as we will discuss elsewhere.

The calculation of the mobility (35), within the studied model, is thus reduced to the evaluation of Eq. (23) based on the ground-state of the polaron. Fig. 3 displays results of such a calculation for the tubular interaction (13) in the scaled form that separates the specific dependence of the mobility on the confinement parameter a_B/R. Within the shown region of its variation, the behavior exhibited in Fig. 3 may be *approximated* by a power-law:

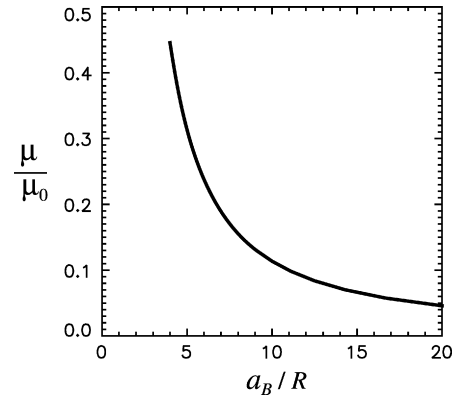$$(\mu/\mu_0) \propto (a_B/R)^{-1.4}. \tag{38}$$

Fig. 3. The polaron mobility in the constant applied field as a function of the confinement parameter a_B/R, here the mobility is measured in units of $\mu_0 = a_B^2/\tau_L Ry$ which itself can strongly depend on system parameters.

For the overall dependence of the polaron mobility on system parameters, one should recall that the reference value of

$$\mu_0 = a_B^2/\tau_L Ry \tag{39}$$

is itself strongly parameter-dependent as per Eqs. (1) and (4).

Using Eqs. (38) and (39), one can establish how the mobility scales when some of system parameters vary. The effect of the radius R on the mobility is already explicit in Eq. (38). For the dependence on the effective mass m, one finds an approximate scaling law

$$\mu \propto m^{-1.6}. \tag{40}$$

The dielectric properties of the solvent are also important here: if one were to separate the effect of τ_L on μ the remaining factor for the mobility would feature the dependence on ϵ^* as

$$\tau_L \cdot \mu \propto (\epsilon^*)^{2.6}. \tag{41}$$

With typical $\epsilon_s \gg \epsilon_\infty$, $\epsilon^* \simeq \epsilon_\infty$. To appreciate the effect on the mobility itself, however, one is reminded that the longitudinal time τ_L (4) is also proportional to ϵ_∞. Eqs. (40) and (41) illustrate a quite understandable general trend: the more strongly bound the polaron is, then the lower its mobility would be.

5. Discussion

One-dimensional semiconductor nanostructures in immediate contact with polar liquids is an interesting class of systems of relevance to many applications, particularly those involving redox reactions [4,28]. Using simplified theoretical models, we have demonstrated [6,7] that the solvation of excess charge carriers due to the solvent polarization can cause carriers on 1d SCs to self-localize. A combination of several factors, small intrinsic effective masses of the carriers, enhanced Coulomb effects in 1d (small-diameter structures) and the sluggish nature of the orientational solvent polarization, creates conditions in these systems that may be favorable for the resulting formation of 1d continuum adiabatic polarons. The physical properties of the polarons are quite different from those of the band states. The energetic significance of the polaronic effect is emphasized by making comparisons with much more studied Wannier–Mott excitons in 1d SCs. When compared theoretically on an equal footing, we have found [6,7] that the polaron binding energy, E_b^{pol}, can be a substantial fraction, roughly one-third for charge-conjugation-symmetric SCs, of the exciton binding energy, E_b^{exc}, in the media with comparable ϵ_∞.

Let us take a widely known example of single-wall carbon nanotubes (SWCNTs). The importance of the excitonic effects in the optics of semiconducting SWCNTs is well established now, with

binding energies E_b^{exc} experimentally measured in some tubes to be in the range of 0.4–0.6 eV [29–31]. That would suggest that polaron binding energies can reach values of 0.1 eV and more, as it also follows from numerical estimates, reaffirming the potential importance of polarons. It would be pertinent to note that redox chemistry of CNTs has been deemed an "emerging field of nanoscience" [32] and solvatochromic effects in CNTs are being intensely researched [33]; interestingly, even the first mapping of luminescence versus absorption spectra of individual SWCNTs has been achieved in aqueous suspensions [34,35].

In an effort to establish experimentally testable signatures of polaron formation, in this Letter we have studied the low-frequency dynamics of 1d large adiabatic polarons. We have shown how the combined microscopic dynamics of the electronic charge density on the 1d SC and the solvent results in macroscopic Langevin dynamics of the polaron centroid. The mobility (35) and diffusion coefficient (37) are thus derivable from the stationary polaron parameters and the solvent dynamic relaxation. We also demonstrated that new local dielectric relaxation modes develop in the presence of the polaron. These modes involve polaron shape deformations and may play a role in time-dependent responses and in polaron collision events.

It is instructive to make some numerical estimates based on the obtained results. If, for instance, one chooses a set of reasonable representative numerical parameters: $m = 0.05 m_e$ (m_e being the free electron mass), $\epsilon^* = 3$ and $\tau_L = 1$ ps, then, by Eq. (1), the resulting $a_B \simeq 32$ Å, $Ry \simeq 76$ meV, and, by Eq. (39), $q \cdot \mu_0 \simeq 1.3$ cm^2 V^{-1} s^{-1}. Using the data of Fig. 3 for $a_B/R = 6$ as an example of a small-diameter structure, this value of μ_0 would then translate into $q \cdot \mu \simeq 0.3$ cm^2 V^{-1} s^{-1}. At $T = 300$ K this yields the value of the diffusion coefficient $D \simeq 8 \times 10^{-3}$ cm^2/s. Of course, with a wide range of variability of the relevant system parameters (suffice to mention values of τ_L), these tentatively estimated values can change substantially for various systems. Still, these numbers strongly indicate that the mobility of the solvated carriers can be orders of magnitudes smaller than the intrinsic carrier mobilities of 10^3–10^5 cm^2 V^{-1} s^{-1} discussed for SC wires and tubes [1,2].

We conclude by reiterating that the illustrative calculations presented in this Letter are based on simplified generic models whose main role is to elucidate the essential physics. While we do not expect substantial changes in the results valid for small-diameter nanostructures (the strong-confinement regime, when most dielectric effects are due to the surrounding medium [6,7,20]), more accurate calculations for specific systems, including a finite size of dielectric cavities, SCs band structure and polarizability, may be required for detailed comparison with prospective experimental data.

References

[1] Y. Li, F. Qian, J. Xiang, C.M. Lieber, Mater. Today 9 (10) (2006) 18.
[2] P. Avouris, J. Chen, Mater. Today 9 (10) (2006) 46.
[3] R. Saito, G. Dresselhaus, M.S. Dresselhaus, Physical Properties of Carbon Nanotubes, Imperial College Press, London, 1998.
[4] P.V. Kamat, J. Phys. Chem. C 111 (2007) 2834.
[5] M. Law, L.E. Greene, J.C. Johnson, R. Saykally, P. Yang, Nature Mater. 4 (2005) 455.
[6] Y.N. Gartstein, Phys. Lett. A 349 (2006) 377.
[7] Y.N. Gartstein, T.D. Bustamante, S. Ortega Castillo, J. Phys.: Condens. Matter 19 (2007) 156210.
[8] C.G. Kuper, G.D. Whitfield (Eds.), Polarons and Excitons, Plenum, New York, 1963.
[9] A.S. Alexandrov, N. Mott, Polarons and Bipolarons, World Scientific, Singapore, 1995.
[10] C. Ferradini, J.P. Jay-Gerin (Eds.), Excess Electrons in Dielectric Media, CRC Press, Boca Raton, FL, 1991.
[11] A.M. Kuznetsov, Charge Transfer in Physics, Chemistry and Biology, Gordon and Breach, Luxembourg, 1995.
[12] A. Nitzan, Chemical Dynamics in Condensed Phases, Oxford, New York, 2006.
[13] G.L. Ussery, Y.N. Gartstein, 2008.
[14] U. Weiss, Quantum Dissipative Systems, World Scientific, Singapore, 1999.
[15] D.M. Basko, E.M. Conwell, Phys. Rev. Lett. 88 (2002) 098102.
[16] E.M. Conwell, D.M. Basko, J. Phys. Chem. B 110 (2006) 23603.
[17] H. Haug, S.W. Koch, Quantum Theory of the Optical and Electronic Properties of Semiconductors, World Scientific, New Jersey, 2004.
[18] W.R. Fawcett, Liquids, Solutions and Interfaces, Oxford Univ. Press, Oxford, 2004.
[19] H. Fröhlich, Theory of Dielectrics, Clarendon, Oxford, 1949.
[20] V. Perebeinos, J. Tersoff, P. Avouris, Phys. Rev. Lett. 92 (2004) 257402.
[21] T. Ando, J. Phys. Soc. Jpn. 66 (1997) 1066.
[22] S.J. Miyaki, J. Phys. Soc. Jpn. 41 (1976) 747.
[23] V.I. Melnikov, Sov. Phys. JETP 45 (1977) 1233.
[24] P.B. Shaw, G. Whitfield, Phys. Rev. B 17 (1978) 1495.
[25] L.A. Turkevich, T.D. Holstein, Phys. Rev. B 35 (1987) 7474.
[26] R. Rajaraman, Solitons and Instantons, North-Holland, Amsterdam, 1982.
[27] T.D. Holstein, L.A. Turkevich, Phys. Rev. B 38 (1988) 1901.
[28] S. Licht (Ed.), Semiconductor Electrodes and Photoelectrochemistry, Wiley–VCH, Weinheim, 2002.
[29] F. Wang, G. Dukovic, L.E. Brus, T.F. Heinz, Science 308 (2005) 838.
[30] Y.-Z. Ma, L. Valkunas, S.M. Bachilo, G.R. Fleming, J. Phys. Chem. B 109 (2005) 15671.
[31] Z. Wang, H. Pedrosa, T. Krauss, L. Rothberg, Phys. Rev. Lett. 96 (2006) 047403.
[32] M.J. O'Connell, E.E. Eibergen, S.K. Doorn, Nature Mater. 4 (2005) 412.
[33] J.H. Choi, M.S. Strano, Appl. Phys. Lett. 90 (2007) 223114.
[34] M.J. O'Connell, et al., Science 297 (2002) 593.
[35] R.B. Weisman, S.M. Bachilo, D. Tsyboulski, Appl. Phys. A 78 (2004) 1111.

Charge carrier solvation and large polaron formation on a polymer chain revealed in model *ab initio* computations

M. L. Mayo and Yu. N. Gartstein

Department of Physics, The University of Texas at Dallas, P.O. Box 830688, FO23, Richardson, Texas 75083, USA
(Received 30 April 2008; published 7 August 2008)

When an excess charge carrier is added to a semiconducting polymer chain, it is well known that the carrier may self-trap into a polaronic state accompanied by a bond-length adjustment pattern. A different mechanism of self-localization is the solvation of charge carriers expected to take place when the polymer chain is immersed in polar media such as common solvents. We use density-functional computations in conjunction with the polarizable continuum model to demonstrate solvation-induced self-consistent charge localization into large-radius one-dimensional (1D) polarons on long $C_N H_2$ carbon chains with the polyynic structure. Within the framework used, the solvation results in a much more pronounced charge localization. We believe this mechanism of polaron formation to be of relevance for various 1D semiconductors in polar environments.

A variety of one-dimensional (1D) wide-band semiconductor (SC) structures—conjugated polymers, nanowires, and nanotubes—attract a great deal of attention. The nature and properties of excess charge carriers on these structures are fundamental for various applications. For our discussion, one distinguishes between nearly free band states of excess carriers and self-localized polaronic[1] states. Self-trapping and the formation of 1D polarons can occur owing to the (strong) interaction of the electronic subsystem with another subsystem such as, e.g., displacements of the underlying atomic lattice, which is the mechanism that has been extensively explored for 1D electron-phonon systems. Here we are concerned with a different, much less studied implementation of the polaronic effect that should take place for 1D SCs immersed in three-dimensional (3D) polar media, the situation particularly common for applications involving fundamental redox processes in polar solvents. In this case of what could be called charge carrier solvation, the long-range Coulomb interaction is expected[2–4] to lead to the formation of a localized electronic state on a SC structure surrounded by a self-consistent pattern of the sluggish (orientational) polarization of the solvent. The main goal that we pursue and achieve in this paper is to substantiate the validity of this picture at the level of *ab initio* computations, that is, with realistic many-electron effects taken into account. To our knowledge, this is a first *ab initio* demonstration of the *solvation-induced* self-consistent localization of the excess charge resulting in large-radius 1D polarons.

The type of systems we consider is an interesting model realization in the general context of quantum particles interacting with dissipative environments.[5,6] The confinement of the electron motion to 1D and its structural separation from the 3D polarizable medium clearly distinguishes such systems from the well-known 3D cases of polarons in polar SCs (Refs. 7–9) and solvated electrons in polar liquids.[9,10] A combination of several factors here creates conditions that may be especially favorable for the formation of 1D continuum adiabatic polarons; these are small effective band masses of the carriers (e.g., ~0.1 of free-electron mass), enhanced Coulomb effects in 1D,[11] and the slow response of the solvent polarization.

The self-trapping of an excess charge carrier (an electron or a hole) is easily described in a *single-particle* picture within a standard 1D continuum adiabatic framework. It corresponds to the localized ground-state solution $\psi(x)$ of the nonlinear Schrödinger equation:

$$-\frac{\hbar^2}{2m}\frac{\partial^2 \psi(x)}{\partial x^2} - \int dx' V(x-x')|\psi(x')|^2\psi(x) = E\psi(x),$$

where x is the coordinate along the structure axis, m the intrinsic effective mass of the carrier, and $V(x)$ the effective self-interaction mediated by another subsystem. In the case of a short-range electron-phonon mediation, the self-interaction can be taken local, $V(x)=g\,\delta(x)$, leading then to the exact result $\psi(x)\propto\text{sech}(gmx/2\hbar^2)$ for a continuum 1D polaron widely known after the pioneering contributions of Rashba[12] and Holstein.[13] In the case of the long-range polarization interaction, the effective $V(x)$ behaves as $1/|x|$ at large distances, while the short-range behavior depends on specific system details such as the actual transverse charge-density distribution and the geometry of the dielectric screening. Numerical studies of this case[3,4] indicate that the binding energy of the resulting polarons could reach a substantial fraction, roughly one third, of the binding energy of the corresponding Wannier-Mott excitons (primary optical excitations in many 1D SCs).

While illuminating the basic physics of the effect, the single-particle description has the drawback of not *explicitly* including valence-band electrons, whose reorganization may substantially affect the outcomes. Such a reorganization can be important even in noninteracting electron models—a nice illustration was given in Ref. 14 that analyzed how polarons of a two-band Peierls dielectric model evolve into single-particle Holstein polarons in the limit of the "frozen valence band" approximation. With realistic Coulomb interactions in place, the role of valence electrons in the formation of the relevant self-consistent potentials would only increase. As applied to electron-phonon polarons in conjugated polymers (CPs), various *ab initio* computational schemes have been found useful to clarify the role of electron-electron interactions on such polarons and their optical properties (we refer

the reader to a recent account[15] for a discussion and multiple references). In what follows we use the GAUSSIAN 03 implemented density-functional theory (DFT) *ab initio* calculations in conjunction with the polarizable continuum model[16,17] (PCM) to study the polaron formation in conjugated linear systems as mediated by the polarization interaction with a surrounding polar solvent.

Since the computational demand increases substantially in DFT-PCM calculations, we have selected structurally simple systems of hydrogen-terminated polyynic linear carbon chains $C_N H_2$ (even N between 20 and 100) for our demonstration. A polyynic structure exhibits in its ground state an alternating pattern of triple $C \equiv C$ and single C-C bonds and is semiconducting. It should be noted that while playing the role of a prototypical example in our study, polyynic chains continue to be the subject of much attention in their own right.[18–22] Interestingly, they were predicted[23] to possess a rich family of electron-lattice self-localized excitations because of the extra degeneracy of molecular-orbital (MO) levels.

The results presented in this paper have been derived by employing DFT computations with the B3LYP hybrid exchange-correlation functional known to include local and nonlocal correlation effects. This functional is commonly used in recent studies of polyynes.[18–21] The $6-311++G(d,p)$ all electron basis set was chosen due to its richness and ability to represent charged systems. We note that our "in vacuum" calculations have been verified to compare well against previously published *ab initio* results on neutral[19] and charged[20] polyynic systems both in terms of energetics and optimized bond lengths. The DFT-PCM ("in solvent") calculations used water as a polar solvent with its *default* parameters in GAUSSIAN 03.

A pertinent quantity for us is the equilibrium *spatial distribution* of the excess charge over the 1D SC, which is naturally related to atomic charges in outputs of *ab initio* calculations. Importantly, these charges represent the effect due to *all* electrons in the system. It is well known[17] that calculations of the atomic charges from many-electron wave functions are dependent on the basis set transformations and sometimes lead to spurious results. Two procedures, due to Mulliken and Löwdin, are used particularly frequently in such calculations.[17] We exercised both and established that while they may lead to different raw atomic charges for individual cases, the results become remarkably close when calculated for unit-cell-based charge *differences* between charged and neutral chains. The unit cells are defined here to consist of pairs of neighboring carbons, with the chain end cells including the hydrogen atomic charges. It is these stable charge differences—that is, excess charge—per cell that are displayed in Figs. 1, 2, and 4(a) using Löwdin numbers. We studied both anionic (an extra electron) and cationic (an extra hole) chains. Their self-localization behavior has been found very similar. Accordingly we restrict our discussion here to the anionic cases, with the excess charge in the figures measured in units of $(-e)$, where e is the magnitude of the fundamental charge.

To be able to clearly separate the effect of the solvation on excess charge localization from the effect of atomic displacements, we start by exploring systems with rigid geometries,
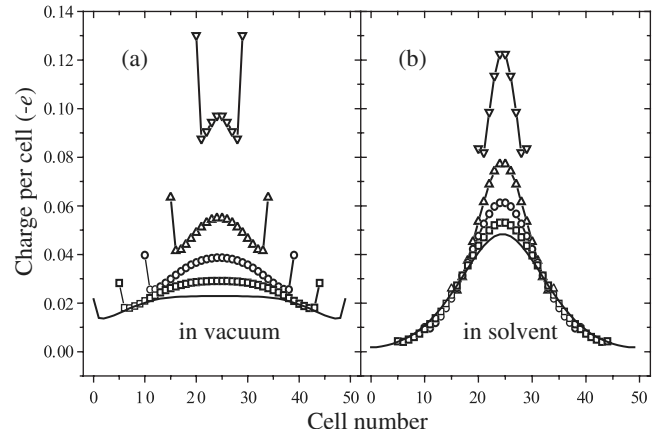

FIG. 1. Excess charge-density spatial distribution on charged $C_N H_2^-$ chains with $N=20$, 40, 60, 80, and 100—top to bottom curves, respectively, in their central parts. All chains feature the same pattern of fixed bond lengths corresponding to RG1 geometry described in text. Panel (a) displays results for chains in vacuum, panel (b) for chains in the solvent environment.

that is, with fixed prescribed atomic positions. Our first geometry, referred to as RG1, features the following fixed lengths: 1.235 Å for the triple bonds, 1.326 Å for the single, and 1.063 Å for the C-H bonds. These lengths have been retrieved from our complete optimization of the neutral $N=80$ chain in vacuum and are therefore expected to be relatively close to optimal values. We now use this geometry to perform DFT calculations for a set of $C_N H_2$ and $C_N H_2^-$ samples with various N to find the excess charge-density distribution both in vacuum and in the solvent environment. The derived results are compared in Fig. 1 whose (a) and (b) panels display clearly distinct trends. Barring the end effects,
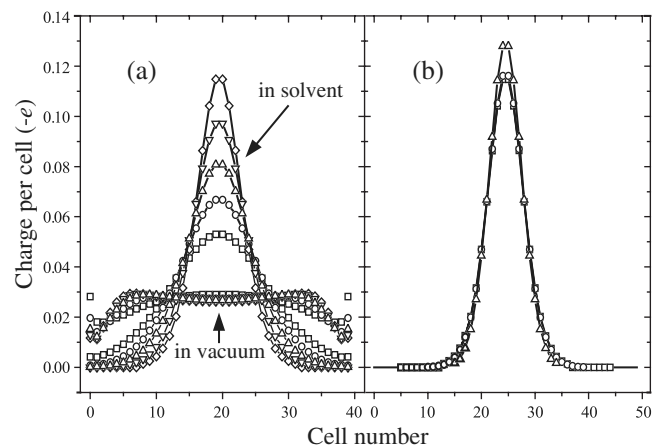

FIG. 2. Excess charge-density spatial distribution on charged $C_N H_2^-$ chains. (a) $N=80$. The evolution of the charge distribution upon stretching the single bonds by 0.1 Å successive increments from 1.326 to 1.726 Å—bottom to top in a group of five clearly distinct curves shown by different connected symbols and denoted "in solvent." The same—but unconnected—data symbols are used to show the results for chains in vacuum; those distributions largely overlap. (b) Comparison of distributions for chains in the solvent with $N=40$, 60, 80 (different data symbols), and 100 (solid line) for the geometry RG2 featuring the longest single bonds.
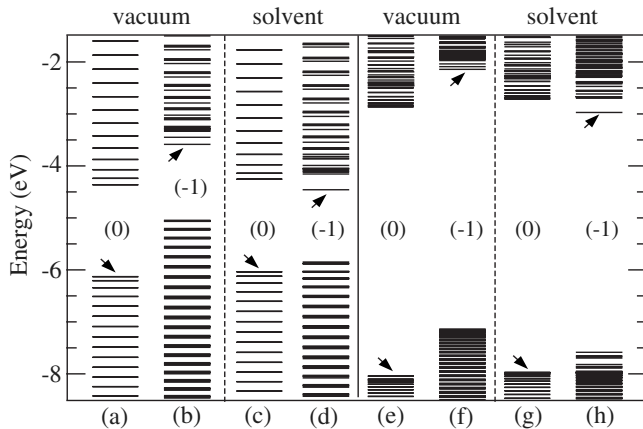
FIG. 3. Molecular-orbital energy levels for neutral (0) and charged (−1) $C_{100}H_2$ chains with rigid RG1 [(a)–(d)] and RG2 [(e)–(h)] geometries both in vacuum and in the solvent. The arrows indicate positions of HOMO levels.

FIG. 4. Comparison of the solvation and bond-length adjustment effects for $C_{40}H_2$. (a) Excess charge distributions in vacuum (△) and in the solvent (□) for RG1 geometry (dashed lines) and for the fully optimized bond-length patterns (solid lines). (b) The corresponding MO energy levels in the solvent for (b1) optimized neutral chain, (b2) charged chain in RG1 geometry, and (b3) optimized charged chain. The arrows show HOMO levels.

vacuum results in panel (a) are reminiscent of the "particle in a box" behavior: as the chain length increases, the excess charge is distributed more and more uniformly over the whole chain. In a sharp contrast, for chains in the solvent, panel (b), the excess charge exhibits much more localized distributions around central parts of the chains. As the chain length increases, those distributions show a tendency toward convergence, albeit not completely achieved within the range of lengths studied.

To further the understanding of the observed behavior, we now attempt to decrease the spatial extent of charge localization. In single-particle models, the size of the polaron is determined by the balance of the gain in the potential energy of the localized carrier and the loss in its kinetic energy. Decreasing the latter leads to a diminished delocalization propensity and is expected to shorten the polaron. This should be achievable with an increased intrinsic effective mass, or with a narrower electron bandwidth. To imitate the effect, we chose to *artificially* stretch all single bonds in our system, thereby making $C \equiv C$ "dimers" more and more separated from each other. Figure 2(a) illustrates a *dramatic* difference in the response of the excess charge distribution to successive single-bond stretchings for chains in vacuum and for chains in solvent. Whereas charge density in vacuum is hardly affected in this process, preserving nearly uniform distributions over the whole chain, for chains in solvent, each successive stretching step results in smaller and smaller localization regions. We refer to the fixed geometry with the longest-stretched single bonds of 1.726 Å as RG2. As the localization size in this geometry appears to be well within the chain length, we compare the excess charge distributions for several chain lengths in Fig. 2(b). The distributions for $N=60$, 80, and 100 practically coincide confirming that they correspond to a fully converged self-consistent pattern of excess charge localization achieved *entirely* due to the interaction with the surrounding solvent.

A comparison of the corresponding molecular-orbital energy-level structures is available in Fig. 3. One immediately notices a much wider (but inconsequential for the effect we consider) band gap in the RG2 geometry. The narrowing
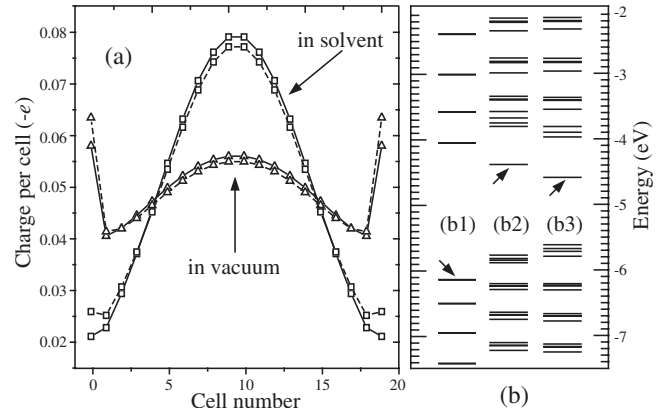
of the bandwidth is, however, relevant and easily detected via a much larger density of states [panels (e) vs (a) and (g) vs (c)]. Disregarding "trivial" (the electrostatic potential with respect to infinity) overall shifts of the levels for the charged chains in vacuum, the important difference with the charged chains in the solvent is that the latter case exhibits local highest occupied molecular orbital (HOMO) levels clearly separated from other states: compare panel (d) to (b) and, especially, panel (h) to (f). This is the behavior expected from single-particle polaron models. One, however, does not observe distinctly separate unoccupied local levels appearing in such models with long-range Coulomb potentials.[3] Also, a reorganization of valence-band electron states is apparent in the band gap upon the formation of the polaron, especially well seen in geometry RG2, panel (h). This is suggestive of a more complex electronic structure of the polaron as affected by many-electron interactions.

To better benchmark the localization due to the solvation, we now turn to bond-length optimization results derived for the $N=40$ system. Figure 4(a) pictures modifications of the excess charge spatial distribution that take place upon changes from the rigid RG1 geometry to fully optimized bond-length patterns both in vacuum and in the solvent. It is evident that for the charge distribution, the effect of the lattice relaxation is much less significant than the effect of the solvation. (The same conclusion has been drawn in our studies of $N=80$ chains.) Figure 4(b) shows how local HOMO and intragap valence levels are affected by the pure solvation and by the combined action of the solvation and lattice displacements. Interestingly, here the effects due to each of the mechanisms appear similar in magnitude despite a much more pronounced effect of the solvation on charge-density localization. This is again likely indicative of the intricacies of many-electron interactions and the screening effects. A more complete understanding of similarities and differences of these mechanisms calls for further studies at various computational levels. The picture of Fig. 4(b) suggests that com-

parative spectroscopy of electronic transitions to and from local HOMO levels should be a helpful experimental tool.

The spatial extent of demonstrated solvation-induced 1D polarons is seen to be on the order of tens of angstroms. We, however, do not feel to be able to reliably evaluate the polaron binding energy except to estimate it at ~0.1 eV based on comparisons of lowest unoccupied molecular orbital (LUMO) levels with the computed electron affinities. Our consideration has been limited to chains with idealized straight structures; various defects including spatial conformations of the chains can lead to the formation of bound polarons with possibly larger binding energies.

While providing a clear conceptual demonstration, the present *ab initio* framework may overestimate the effects of the solvation on self-localization as it does not take a proper account of the frequency dependence of the solvent dielectric function.[3,4,7,9] This issue could possibly be addressed within time-dependent DFT-PCM computational schemes.[24] Another current development, on the scaling description of solvent effects,[25] may also help in studies of large polaron formation. Given the general character of the solvation-induced self-localization with the subsequent decrease of charge carrier mobility,[2,6,26] as well as its expected significance for fundamental redox processes on various 1D SC structures, further studies of this effect seem quite interesting and warranted.

[1] A. S. Alexandrov and N. Mott, *Polarons and Bipolarons* (World Scientific, Singapore, 1995).

[2] D. M. Basko and E. M. Conwell, Phys. Rev. Lett. **88**, 098102 (2002).

[3] Y. N. Gartstein, Phys. Lett. A **349**, 377 (2006).

[4] Y. N. Gartstein, T. D. Bustamante, and S. O. Castillo, J. Phys.: Condens. Matter **19**, 156210 (2007).

[5] U. Weiss, *Quantum Dissipative Systems* (World Scientific, Singapore, 1999).

[6] Y. N. Gartstein and G. L. Ussery, arXiv:0804.1767, Phys. Lett. A (to be published).

[7] *Polarons and Excitons*, edited by C. G. Kuper and G. D. Whitfield (Plenum, New York, 1963).

[8] *Polarons in Ionic Crystals and Polar Semiconductors*, edited by J. T. Devreese (North-Holland, Amsterdam, 1972).

[9] A. M. Kuznetsov, *Charge Transfer in Physics, Chemistry and Biology* (Gordon and Breach, Luxembourg, 1995).

[10] *Excess Electrons in Dielectric Medias*, edited by C. Ferradini and J. P. Jay-Gerin (CRC, Boca Raton, 1991).

[11] H. Haug and S. W. Koch, *Quantum Theory of the Optical and Electronic Properties of Semiconductors* (World Scientific, New Jersey, 2004).

[12] E. I. Rashba, Opt. Spektrosk. **2**, 75 (1957); **2**, 88 (1957);

[13] T. Holstein, Ann. Phys. (N.Y.) **8**, 325 (1959).

[14] D. K. Campbell, A. R. Bishop, and K. Fesser, Phys. Rev. B **26**, 6862 (1982).

[15] A. Ye, Z. Shuai, O. Kwon, J. L. Brédas, and D. Beljonne, J. Chem. Phys. **121**, 5567 (2004).

[16] M. J. Frisch *et al.*, GAUSSIAN 03, Revision D.01, Gaussian, Inc., Wallingford, CT, 2004.

[17] A. Leach, *Molecular Modelling: Principles and Applications* (Prentice-Hall, Englewood Cliffs, NJ, 2001).

[18] S. Yang and M. Kertesz, J. Phys. Chem. A **110**, 9771 (2006).

[19] S. Yang and M. Kertesz, J. Phys. Chem. A **112**, 146 (2008).

[20] L. Hornŷ, N. D. K. Petraco, C. Pak, and Henry F. Schaefer III, J. Am. Chem. Soc. **124**, 5861 (2002).

[21] L. Hornŷ, N. D. K. Petraco, and Henry F. Schaefer III, J. Am. Chem. Soc. **124**, 14716 (2002).

[22] S. Szafert and J. A. Gladysz, Chem. Rev. (Washington, D.C.) **106**, PR1 (2006).

[23] M. J. Rice, A. R. Bishop, and D. K. Campbell, Phys. Rev. Lett. **51**, 2136 (1983).

[24] B. Mennucci, Theor. Chem. Acc. **116**, 31 (2006).

[25] C. S. Pomelli and J. Tomasi, J. Mol. Struct. **537**, 97 (2001).

[26] E. M. Conwell and D. M. Basko, J. Phys. Chem. B **110**, 23603 (2006).

Optical absorption from solvation-induced polarons on nanotubes

G. L. Ussery and Yu. N. Gartstein[a)]

Department of Physics, The University of Texas at Dallas, P.O. Box 830688, EC36, Richardson, Texas 75083, USA

When an excess charge carrier is added to a one-dimensional (1D) wide-band semiconductor immersed in a polar solvent, the carrier can undergo self-localization into a large-radius adiabatic polaron. We explore the local optical absorption from the ground state of 1D polarons using a simplified theoretical model for small-diameter tubular structures. It is found that about 90% of the absorption strength is contained in the transition to the second lowest-energy localized electronic level formed in the polarization potential well, with the equilibrium transition energy larger than the binding energy of the polaron. Thermal fluctuations, however, can cause a very substantial—an order of magnitude larger than the thermal energy—broadening of the transition. The resulting broad absorption feature may serve as a signature for the optical detection of solvated charge carriers. © *2009 American Institute of Physics*. [DOI: 10.1063/1.3046292]

I. INTRODUCTION

One-dimensional (1D) wide-band semiconductor (SC) nanostructures (e.g., nanotubes and nanowires) in contact with polar solvents is an interesting class of systems of particular relevance to applications and processes involving fundamental redox reactions.[1–3] When an excess charge carrier (an electron or a hole) is added to such a structure, the carrier can become solvated resulting in an adiabatic polaron, a self-consistent combination of a localized electronic state and a dielectric polarization pattern of the surrounding medium.[4–8] The long-range Coulomb mechanism of the polaron formation here is analogous to the well-known three-dimensional (3D) polarons in polar SCs (Refs. 9–11) and solvated electrons in polar liquids.[11–13] Distinct from those cases, however, are the confinement of the electron motion in a 1D nanostructure and its structural separation from the 3D polarizable medium.

The physical properties of strong-coupling polarons are quite different from the nearly free band electrons frequently discussed in the context of electronic transport in nanotubes[14,15] and nanowires.[16] We have already emphasized the energetic significance of the solvation by finding[5,6] that the binding energy of the resulting 1D polarons could reach a substantial fraction, roughly one-third, of the binding energy of Wannier–Mott excitons, the well-known primary photoexcitations in many 1D SCs. This may lead to enhanced charge separation. On the other hand, the mobility of solvated charge carriers is drastically reduced due to the dissipative drag of the medium.[4,8,17] In this paper we address qualitative theoretical expectations for the local optical absorption from solvation-induced 1D polarons. This kind of the optical absorption has been a powerful tool in optical detection of electron-lattice polarons in conjugated polymers as well as of 3D solvated electrons.

While the polaronic effect due to solvation and the features we discuss have a generic character, specific illustrative calculations in this paper are done using a simplified model representation for small-diameter tubular structures. A widely known example of such structures is semiconducting single-wall carbon nanotubes (SWCNTs). We note that redox chemistry of CNTs has been deemed an "emerging field of nanoscience" [18] and solvatochromic effects in CNTs are being intensely researched.[19]

As discussed in more detail later, Fig. 1 displays calculated functional dependences for the binding energy, E_b, and the spatial extent, l, of 1D adiabatic polarons in terms of the
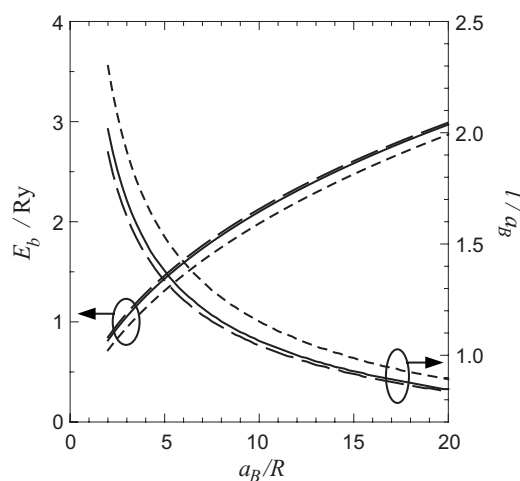

FIG. 1. The binding energy, E_b, and the linear size, l, of 1D adiabatic polarons as a function of the confinement parameter a_B/R. The size l is defined here as the FWHM of the localized electron density. Different curves correspond to different dielectric conditions, as explained more fully in the text: filled (solid lines), hollow (long-dash), and polarizable (short-dash) nanotube screening models.

[a)]Electronic mail: yuri.gartstein@utdallas.edu.

tube radius R and convenient scales of the effective Bohr radius and Rydberg energy for the corresponding 3D Coulomb problem[20]

$$a_B = \epsilon^* \hbar^2 / m q^2, \quad \mathrm{Ry} = q^2 / 2 \epsilon^* a_B. \tag{1}$$

Here q is the carrier charge, m its effective mass, and ϵ^* is the effective dielectric constant of the uniform 3D medium. These scales arise naturally in the analysis (e.g., Refs. 5 and 6 and below in Sec. II) of the polaronic effect due to the long-range polarization interaction. They result from the balance between the carrier delocalization energy loss and the polarization energy gain due to localization. The length l of the polaron has been defined here as the full width at half maximum (FWHM) of the localized 1D electron charge *density*. In what follows we refer to the ratio a_B / R as the confinement parameter. It is well known that the spatial confinement generally results in amplification of the Coulomb binding,[21] and Fig. 1 illustrates both the magnitude and the growth of E_b / Ry for 1D polarons with the increased confinement parameter. For a proper perspective, one should compare[6] those results with the polaron binding energy in higher dimensions, where the classic Pekar's result[22,23] for E_b in 3D is only $\simeq 0.1$ Ry, while in two-dimensional (2D) systems[24] it increases to $\simeq 0.4$ Ry. Our variational calculations[6] for cylindrical surfaces have shown that the transition to a 1D polaron structure (charge uniformly distributed over the tube circumference) takes place at $a_B / R \gtrsim 1$, this is the regime of our interest in this paper. At smaller values of the confinement parameter, nonuniform 2D charge distributions can take place.

As exemplified in Fig. 1, we present our results in a dimensionless form irrespective of numerical values of appropriate scales (1). This way one can allow for uncertainties of values of individual system parameters and, more importantly, study the trends of the system behavior as dependent on relevant combinations and scaling with the confinement parameter. It is, however, useful and interesting to make some *tentative* estimates of representative numerical values in specific cases. The effective dielectric constant in Eq. (1) varies for different solvents and can be determined from the well-known[9,11,13,23] relationship

$$1/\epsilon^* = 1/\epsilon_\infty - 1/\epsilon_s,$$

typical[5,25] static ϵ_s and high-frequency ϵ_∞ constants satisfy $\epsilon_s \gg \epsilon_\infty$ so that $\epsilon^* \simeq \epsilon_\infty$. Wide-band SCs we are interested in are commonly characterized by effective band masses of charge carriers much smaller than the free electron mass m_e (e.g., $\sim 0.1 m_e$). For SWCNTs, in particular, band masses of carriers generally depend both on tube radius and chirality; see, e.g., Ref. 15 for a compilation of some theoretical data. If, for instance, one were to use the band mass of $0.05 m_e$ corresponding to $R \simeq 8$ Å (Ref. 15) for m, along with a representative value of $\epsilon^* = 3$, then Eq. (1) would result in $a_B \simeq 32$ Å and Ry $\simeq 76$ meV. In this particular example, then, $a_B / R \simeq 4$ and $E_b \sim 0.1$ eV. Larger values of m or smaller values of ϵ^* would lead to increased magnitudes of E_b by

virtue of larger values of Ry. The dependence of the band mass on radius R in SWCNTs [roughly $\propto 1/R$ (Ref. 15)], however, would make the confinement parameter in this estimate nearly independent of the radius (see also Sec. IV). We will be employing specific values of $a_B / R = 4$ and 10 for some plots below, which are meant to serve mainly *illustrative* purposes.

Using the band mass for m in the above consideration tacitly assumed that the charge carrier is not affected by interactions with vibrational degrees of freedom of the 1D SC. Meanwhile, electron-phonon (and exciton-phonon) interactions in 1D systems are well-known drivers of the polaronic effect on their own. This includes self-localized strong-coupling polaronic (solitonic) states, e.g., in molecular crystals and conjugated polymers, that have been studied in a great body of work since the pioneering contributions of Rashba[26] and Holstein,[27] as well as various intermediate regimes (see, e.g., an extensive discussion in Ref. 28). The problem of a charge carrier strongly interacting both with displacements of the underlying atomic lattice and with the surrounding solvent is interesting and would require a corresponding self-consistent treatment which we do not address in this paper. The systems of our interest here exhibit instead a *weak* electron-phonon coupling (in the parlance of the theory of polarons[23]) that result only in a relatively slight renormalization of the band parameters. Indeed, first calculations[29] of electron-lattice polarons on SWCNTs due to acoustic vibrations revealed minuscule binding energies of fractions of meV. More refined recent calculations[30] included the interaction with optical phonons: although the band energy shift was now found much larger, on the order of tens of meV, it was at the same time much smaller than the corresponding phonon energy. In accordance with this weak-coupling feature,[23] the renormalization of band velocities in calculations of Ref. 30 was found to be just a few percent. Also consistent with the picture of weak electron-phonon scattering in SWCNTs are the resulting huge, on the order of 10^4–10^5 cm^2/V s, mobilities of charge carriers.[15,30] In contrast, solvated charge carriers are expected to have mobilities orders of magnitudes smaller[8] as follows from the strong interaction with the solvent. The net result of the weak electron-phonon coupling for our carrier solvation problem is therefore a slight, few percent, increase in the effective mass m from its band values in the rigid lattice. Hence, estimates of solvation-induced polaron bindings of 0.1–0.2 eV appear as reasonable representative values. Moreover, it should be noted that such estimates would be in apparent agreement with experimental reports[31–33] of exciton binding energies of 0.4–0.6 eV in SWCNTs and our earlier assessments[5,6] of the relationship between polaron and exciton bindings.

Figure 2 displays an example of the equilibrium 1D polarization potential well resulting from the solvation of an excess charge carrier. The corresponding pattern of the medium polarization is self-consistently stabilized by the electric field of a charge carrier occupying the lowest-energy localized electronic level formed in this well (the ground state of the polaron). Along with that level, also shown are the two next higher-energy empty levels. The results discussed below indicate that it is the transition between the two
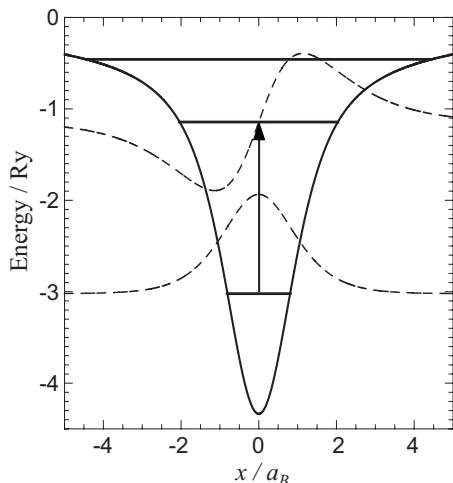
FIG. 2. The equilibrium self-consistent 1D potential well (x is a coordinate along the tube axis) along with the three lowest-energy electronic energy levels calculated for $a_B/R=4$. The optical transition with the largest oscillator strength is indicated by the arrow, the dashed lines showing the localized electronic wave functions of the participating states.

lowest-energy levels that has the largest oscillator strength and dominates the optical absorption in the ground state. The long-range behavior of the potential well is Coulombic, and hence it contains many more higher-energy localized states (not shown in Fig. 2) converging to the onset of the continuum spectrum at zero energy in the figure.

Our consideration in this paper assumes that the polaron binding energy E_b is sufficiently larger than the thermal energy $k_B T$ so that the thermal occupation of higher-energy electronic states can be neglected. Even so, thermal fluctuations are found to very significantly broaden the optical transition in question, as is also the case for 3D solvated electrons.[34] In the presence of the polaron, the fluctuations involve combined dynamics of the electronic charge density and the solvent dielectric polarization. A major contributor to the broadening is the resulting 1D polaron "breathing" mode, qualitatively corresponding to fluctuations of the polaron length. Without pursuing the exact calculation of the absorption line shape, we will provide an approximate estimation of the broadening due to the breathing mode within the classical Franck–Condon framework.[35] The described broad absorption feature could be used for detection of the solvation-induced 1D polarons and an estimate of their binding energy in prospective experimental studies.

II. THE GROUND-STATE AND OPTICAL TRANSITIONS IN EQUILIBRIUM

In the single-particle 1D continuum adiabatic framework, the excess charge carrier is described by the wave function $\psi(x)$; it responds to the electrostatic potential $\phi(x)$ due to the surrounding medium via the corresponding Schrödinger equation:

$$-\frac{\hbar^2}{2m}\frac{\partial^2 \psi_i(x)}{\partial x^2} + q\phi(x)\psi_i(x) = E_i\psi_i(x). \tag{2}$$

The magnitude of the effective mass m here determines the propensity of the charge carrier to delocalize along the 1D SC: the smaller the m the larger the loss in the kinetic energy is due to given spatial localization. In the absence of the potential $\phi(x)$, eigenfunctions of Eq. (2) would be just plane waves $\psi(x) \propto \exp(ikx)$ corresponding to kinetic energies $E(k)=\hbar^2 k^2/2m$ of delocalized charge carriers. As we discussed in Sec. I, a weak electron-phonon coupling results in a slight increase in m with respect to the band mass in a rigid lattice structure.

We now proceed with the discussion of self-localization. In the ground state, the charge carrier occupies the lowest-energy ($i=0$) state so that the resulting 1D electronic charge density is

$$\rho(x) = q|\psi_0(x)|^2. \tag{3}$$

At *equilibrium*, the self-consistency requires that this charge density stabilizes the very electrostatic potential used in Eq. (2):

$$\phi(x) = \int dx' G(x-x')\rho(x'), \tag{4}$$

where kernel G is the appropriate electrostatic response function assuming the translational invariance along the x-axis. Solving Eqs. (2)–(4) together yields the equilibrium 1D polaron distributions that we will be denoting as $\bar{\phi}(x)$ and $\bar{\rho}(x)$. One notes that the equations determining the equilibrium correspond to the minimum of the total adiabatic energy of the system:

$$E_0^{\text{tot}} = E_0 + E_P, \tag{5}$$

consisting both of the electronic energy E_0 in Eq. (2) and the energy stored in the dielectric polarization of the medium:

$$E_P = \frac{1}{2}\int dx dx'\, \phi(x)G^{-1}(x-x')\phi(x'),$$

where G^{-1} is the kernel inverse to G (see also Ref. 5). As the continuum onset in Eq. (2) is set at zero energy, the "depth" of this minimum is the polaron binding energy:

$$\min\{E_0^{\text{tot}}\} = -E_b. \tag{6}$$

The data for E_b and equilibrium $\bar{\rho}(x)$ and $q\bar{\phi}(x)$ have been used in Figs. 1 and 2. Other adiabatic energy surfaces $E_i^{\text{tot}} = E_i + E_P$ are defined similarly to Eq. (5).

The electrostatic potential $\phi(x)$ in Eq. (2) is due to only the slow (orientational) polarization of the surrounding medium and hence should not include the "instantaneous" self-interaction of the charge carrier with itself. A proper separation of the slow polarization response is a standard step in the polaron problem.[11,13,23,35] The kernel G in Eq. (4) can therefore be written as

$$G(x) = G_s(x) - G_\infty(x), \tag{7}$$

where indices s and ∞ denote that the standard electrostatic potential problem (4) is solved with dielectric conditions corresponding respectively to full (static, s) screening or to screening only by "fast" (∞) components of polarization. In

the polaron context, fast means operative on time scales shorter than $\hbar/E_b$. In the model we consider, the continuum solvent is characterized by the corresponding dielectric constants ϵ_s and ϵ_∞. Another fast contributor to the screening is the polarizability of the 1D SC nanostructure itself related to interband electronic transitions.

In Fourier space, $g(k) = \int dx e^{-ikx} G(x)$, Eq. (7) can be conveniently rewritten as

$$g(k) = g_0(k)\left(\frac{1}{\epsilon_s(k)} - \frac{1}{\epsilon_\infty(k)}\right), \tag{8}$$

where the k-dependence of the corresponding dielectric functions reflects a possible spatial dispersion of the screening due to the geometry of the system.

The bare, unscreened, response for the 1D tubular geometry (the "elementary" charge distributions are uniform rings of radius R) is given by[5,36]

$$g_0(k) = 2I_0(kR)K_0(kR), \tag{9}$$

where $I(x)$ and $K(x)$ are the modified Bessel functions appearing in electrostatic problems with cylindrical symmetry.[37] The general form of the corresponding k-dependent dielectric functions can be represented[5] as

$$\epsilon(k) = kR[\epsilon_1 I_1(kR)K_0(kR) + \epsilon_2 I_0(kR)K_1(kR)] + \Pi(k), \tag{}$$

where ϵ_1 is the dielectric constant of the dielectric medium inside the tube, ϵ_2 is the dielectric constant of the unbounded medium outside the tube, and $\Pi(k)$ is the contribution arising from the polarizability of the tubular surface itself.

If the latter contribution is neglected and the media inside and outside are the same (we will be calling this model case "filled"), there would be no spatial dispersion in the screening (uniform medium) and response (8) takes a simple form of

$$g(k) = -g_0(k)/\epsilon^*. \tag{10}$$

With this form, one easily sees how the original problem description provided by Eqs. (2)–(4) and (9) can be converted into a completely dimensionless form employing all lengths measured in units of a_B and all energies in units of Ry, Eq. (1). This way, relevant combinations of system parameters are properly recognized, and the confinement parameter a_B/R appears naturally in the response function (9). For another discussion of energy and length scales, see also Ref. 6 comparing Wannier–Mott and polaron energy functionals.

In order to evaluate the magnitude of the effects arising from different dielectric screening conditions, we also examine the model cases called "hollow," where the interior of the tube does not contain any medium ($\epsilon_1 = 1$), and "polarizable," in which the hollow model is augmented by the tube polarizability. For the model of the latter, we will use the following approximate representation of the polarizability of semiconducting SWCNTs calculated in Ref. 38:

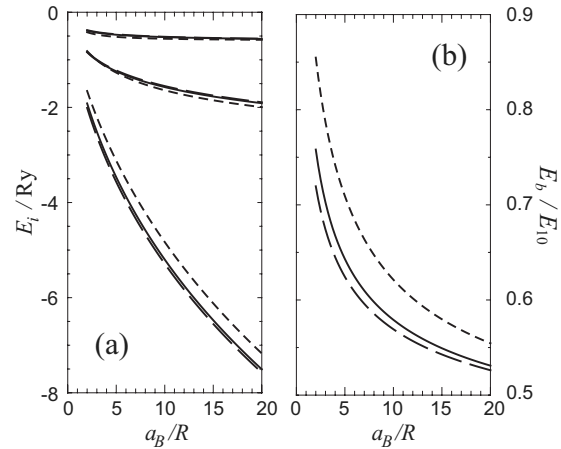$$\Pi(k) = \frac{6.2(kR)^2 I_0(kR)K_0(kR)}{1 + 1.6(kR)^{1.8}}.$$

FIG. 3. (a) The energies E_i of the three lowest electronic energy levels in the ground state equilibrium as a function of the confinement parameter for filled (solid), hollow (long-dash), and polarizable (short-dash) screening models. (b) The ratio of the polaron binding energy, E_b, to the electronic transition energy, E_{10}, in equilibrium calculated with the same models.

Figure 1 compares the results for the ground state of the polaron calculated with the three dielectric screening models, in which we used representative values of $\epsilon_\infty = 3$ and $\epsilon_s = 40$ for the solvent medium. It is evident from the comparison that in the parameter range we study, different screening models do not lead to drastically different results. The variations observed are quite understandable and are largely caused by the effective changes in the magnitude of the fast screening, which is decreased by going from the filled to hollow model and is increased in the polarizable model. Relatively small changes are also observed in the results for individual electronic energy levels displayed in Fig. 3. Panel (a) of that figure just shows the scaling of the three lowest electronic energy levels E_i ($i=0,1,2$) from Eq. (2) as formed in the equilibrium self-consistent potential well (see Fig. 2).

For the optical absorption from the ground state, a Franck–Condon framework discussion requires electronic transition energies

$$E_{i0} = E_i - E_0. \tag{11}$$

The dominant dipole electronic transition turns out to be $i=0 \rightarrow i=1$, and Fig. 3(b) shows the relationship between the polaron binding energy E_b and the equilibrium value of E_{10}. [To compare, the ratio of these energies for 3D Pekar's polaron is about 0.8 (Ref. 23).] More detailed information on this transition for our 1D polaron is displayed in Fig. 4; the most important conclusion from which is that the transition contains nearly 90% of the total absorption strength across a wide range of the confinement parameter. This overall dominance is similar to the one taking place for 3D (Ref. 34) and 2D (Ref. 39) solvated electrons.

Since Eq. (2) has a form of a standard continuum Schrödinger equation, the overall absorption satisfies the optical sum rule familiar from atomic systems[21]
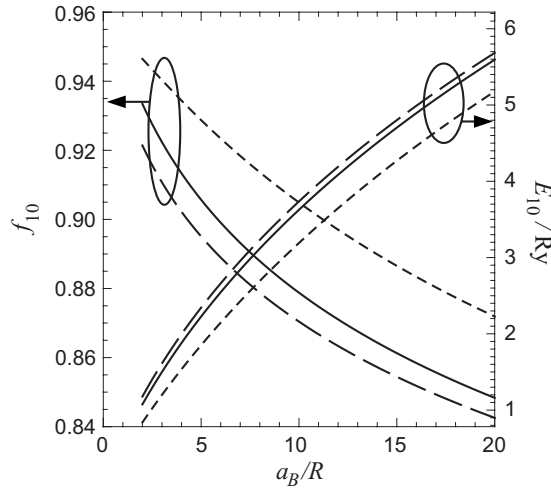
FIG. 4. Oscillator strength and transition energy for the optical transition between $i=0$ and $i=1$ electronic eigenstates in the equilibrium potential well. Calculations done with different screening models are denoted as in Figs. 1 and 3.

$$\sum_i f_{i0} = 1,$$

where the oscillator strength of the transition to the ith state

$$f_{i0} = \frac{2\hbar^2}{mE_{i0}} |\langle \psi_i(x) | \partial/\partial x | \psi_0(x) \rangle|^2. \tag{12}$$

In terms of the frequency ω-dependent oscillator strength density,[40] the sum rule *per one* polaron reads

$$\int_0^\infty f(\omega) d\omega = 1, \tag{13}$$

where, for sharp, discrete transitions (11),

$$f(\omega) = \sum_i f_{i0}\delta(\omega - \omega_{i0}), \quad \omega_{i0} = E_{i0}/\hbar. \tag{14}$$

We will discuss in Sec. III how the thermal broadening of these transitions occurs resulting in a continuous $f(\omega)$.

As Eq. (12) clearly indicates, the optical absorption in our case is due to the electric field polarized *parallel* to the tube axis. The data in Fig. 4 have been derived by calculating matrix elements in Eq. (12) between the states in the equilibrium potential well (and the sum rule verified in all cases).

III. THERMAL BROADENING OF THE OPTICAL ABSORPTION

In the Franck–Condon framework, the optical absorption from the polaron is realized by virtue of "vertical" electronic transitions between the adiabatic potential surfaces E_i^{tot}, meaning that the polarization state of the environment does not change while the transition takes place. This picture of *slow* modulating dynamics of the environment leads to what is called inhomogeneous broadening of the absorption line shape (see Chapter 5 of Ref. 35 for an extensive discussion) and is well justified for our application to the case of the orientational solvent polarization. Indeed, the parameter range of our interest and practical significance corresponds to the regime of $E_b > k_B T > \hbar/\tau_L$, and, hence,

$$\tau_L \gg \hbar(k_B T E_b)^{-1/2},$$

which is a condition of the applicability of the semiclassical Franck–Condon picture.[35] Here τ_L is the longitudinal relaxation time of the solvent defining the relevant time scale for the solvent orientational dynamics and equal to[13,25,41]

$$\tau_L = (\epsilon_\infty/\epsilon_s)\tau_D$$

for the Debye solvent described by the ω-dependent dielectric function

$$\epsilon(\omega) = \epsilon_\infty + \frac{\epsilon_s - \epsilon_\infty}{1 - i\omega\tau_D}. \tag{15}$$

Typical solvents are characterized by a wide range of τ_L ranging from fractions to tens of picoseconds.[5,25]

Thermal fluctuations result in variations of the potential distribution $\phi(x)$ in Eq. (2) from the equilibrium pattern $\bar{\phi}(x)$ discussed in the previous section, thereby modulating electronic wave functions and transition energies (11). Averaging over various fluctuations would thus lead to broadening of the discrete transitions in Eq. (14). In the discussed semiclassical picture, the weighting of various fluctuations in the ground state is described by the Boltzmann factor associated with fluctuations of the *total* adiabatic energy (5) from the minimum equilibrium value (6). Of course, fluctuations in the presence of the polaron are not the fluctuations of the solvent alone but rather combined fluctuations of the medium and localized electronic charge density.

One can get an insight into the nature of thermal fluctuations of the polaron shape by using explicit results derived in Ref. 8 for *small-amplitude* fluctuations in a simplified model of the charge carrier interacting with the Debye solvent (15) with response function (10). Within that model, shape fluctuations are governed by amplitudes $a_n(t)$ in the expansion of the time-dependent electric potential $\phi(x,t)$ and self-localized carrier charge density $\rho(x,t)$ over the normal dielectric relaxation modes:

$$\phi(x,t) = \bar{\phi}(x - \xi(t)) + \sum_{n\geq 1} a_n(t)\phi_n(x - \xi(t)), \tag{16a}$$

$$\rho(x,t) = \bar{\rho}(x - \xi(t)) + \sum_{n\geq 1} a_n(t)\rho_n(x - \xi(t)), \tag{16b}$$

where the first terms in the right hand side of Eq. (15) correspond to the equilibrium static patterns. Both equilibrium patterns and normal modes are centered around arbitrary polaron centroid positions $\xi(t)$. The dynamics of $\xi(t)$ results in the diffusion of the polaron as a whole and does not affect the optical absorption line shape. The spatial patterns of the

normal modes, $(\phi_n(x), \rho_n(x))$, follow from the solutions of the generalized eigenvalue (λ_n) problem:

$$\rho_n(x) = -\int dx' L(x, x') \phi_n(x'), \tag{17a}$$

$$\phi_n(x) = -\frac{\lambda_n}{\epsilon^*} \int dx' G_0(x - x') \rho_n(x'), \tag{17b}$$

where spatial kernel L is determined by the response of the electronic subsystem (see Ref. 8 for more detail). Equations (16) yield shape-modulating modes $(n \geq 1)$ with growing eigenvalues $\lambda_n > 1$ as well as the zero-frequency translational mode with $\lambda_0 = 1$, which is excluded in Eq. (15) in favor of the collective coordinate $\xi(t)$.

For our purposes here, it is convenient to choose the normalization of the modes as

$$-\int dx \rho_m(x) \phi_n(x) = \frac{1}{\lambda_n} \delta_{nm}, \tag{18}$$

note that coefficients $a_n(t)$ are then measured in units of the square root of energy. The equations of motion for so normalized modes read[8]

$$\dot{a}_n + a_n / \tau_n = \eta_n, \tag{19}$$

where mode relaxation times τ_n are given by

$$\tau_L / \tau_n = 1 - 1/\lambda_n \tag{20}$$

and perturbations η_n by

$$\eta_n(\xi, t) = -\lambda_n \int dx \rho_n(x) F(x + \xi, t). \tag{21}$$

As the eigenvalues λ_n grow with the mode index n, the relaxation times τ_n in Eq. (20) converge to the solvent longitudinal relaxation time τ_L (see Ref. 8 for an illustration of this convergence).

For thermal dielectric fluctuations, $F(x, t)$ in Eq. (21) is a random process with a vanishing average and correlations established by "bare" solvent fluctuations[8]

$$\langle F(x, t) F(x', t') \rangle = \frac{2k_B T}{\epsilon^* \tau_L} G_0(x - x') \delta(t - t'). \tag{22}$$

It then follows from Eqs. (18), (21), and (22) that different modes n and m exhibit no dynamic correlations, and the only relevant (for the same centroid coordinate) nonzero correlation is

$$\langle \eta_n(\xi, t) \eta_n(\xi, t') \rangle = 2D \delta(t - t'), \quad D = k_B T / \tau_L,$$

with the effective diffusion coefficient D independent of the mode index with the chosen normalization.

The random dynamics described by Eq. (19) is thus the Ornstein–Uhlenbeck process,[42] which leads, at times $t \gg \tau_n$, to the Gaussian distribution of a_n with the variance established by

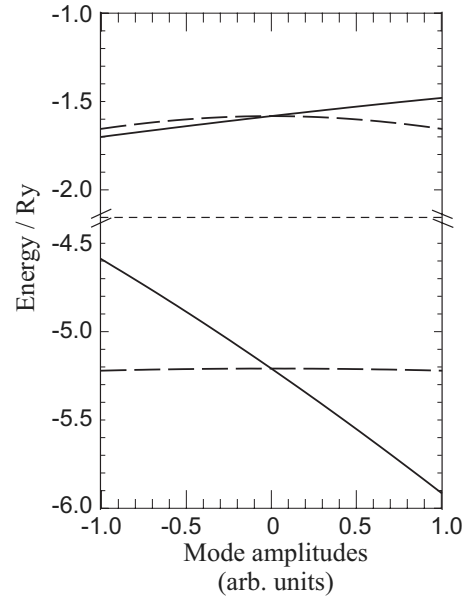$$\langle a_n^2 \rangle = D \tau_n,$$

the probability

FIG. 5. Modulation of the two lowest electronic energy levels E_0 and E_1 by the normal fluctuations modes, Eq. (15), as a function of mode amplitudes in arbitrary units. The solid lines show the modulation by the even mode $n = 1$ and long-dash lines by the odd mode $n = 2$. The confinement parameter used for this illustration is $a_B / R = 10$.

$$P(a_n) \propto \exp\left(-\frac{U_n(a_n)}{k_B T}\right), \quad U_n(a_n) = \frac{a_n^2}{2}\left(1 - \frac{1}{\lambda_n}\right). \tag{23}$$

Equation (23) features the classic Boltzmann distribution for independent fluctuation modes with the effective potential energies $U_n(a_n)$. The behavior of U_n is consistent with behavior (20) of relaxation times.

As the normal mode index n grows, the interaction of the solvent polarization with the electronic density in the ground state generally decreases, likewise the modulation effect on the transition energy E_{10} generally diminishes. The largest modulation effect occurs due to the even normal fluctuation mode $n = 1$, corresponding to the shallowest potential energy U_1. This modulation is illustrated in Fig. 5 comparing the effects of two normal modes on the electronic energies E_0 and E_1. It is evident that the major contribution comes from the modulation of the ground state level E_0 by the $n = 1$ mode. As discussed in Ref. 8, the spatial pattern of this mode corresponds qualitatively to the modulation of the polaron length l, we will accordingly call this the breathing mode.

While illuminating the character of the fluctuations and their modulation effects, the small-amplitude description may be insufficient for realistic T on the order of room temperature. In this paper we do not pursue a comprehensive analysis of the absorption line shape that would then be required. Instead, we will provide a qualitative assessment of the effect of the polaron breathing using a simplistic single-parameter scaling description similar in the spirit to the approach used in recent studies of continuum adiabatic models of 3D electron solvation[43] and of electron localization at dielectric-metal interfaces.[39] In this description, the fluctuations are restricted to modulate the electrostatic potential via a scaling ansatz of the equilibrium pattern
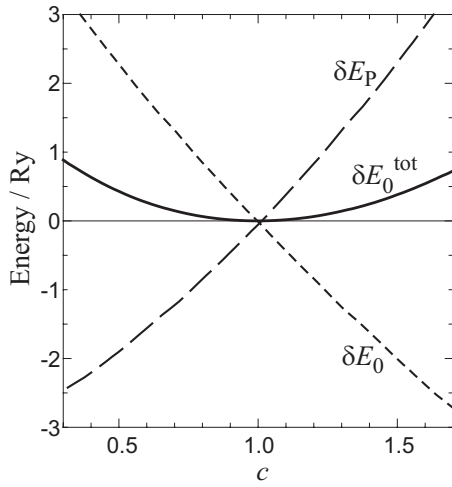
FIG. 6. Variations of the electronic energy δE_0, polarization energy δE_P, and the total adiabatic energy δE_0^{tot} with the scaling parameter c. The confinement parameter used for this illustration is $a_B/R = 10$.

$$\phi(x) = c\,\bar{\phi}(cx), \tag{24}$$

where $c \geq 0$ is the scaling parameter. Its deviation from the value of $c = 1$ results in variations of all quantities relevant for the optical absorption. It should be noted that the results of small deviations from $c = 1$ turn out to be quite close to the results we derived with exact small-amplitude breathing fluctuations.

Figure 6 displays variations of different energies $\delta E(c) = E(c) - E(c = 1)$ with the scaling parameter c. It is evident that the shallow response of the total energy δE_0^{tot} to fluctuations around the equilibrium is a result of a near compensation of much larger variations of the polarization energy δE_P and the purely electronic energy δE_0, as indeed should be the case for the ground state adiabatic surface. It is this strong variability of E_0 in response to the polaron breathing that has already been noted in Fig. 5 and is largely responsible for the resulting enhanced broadening of the line shape. The "mechanism" of the enhancement is also illustrated in Fig. 7 displaying two adiabatic energy surfaces, E_0^{tot} and E_1^{tot}, be-
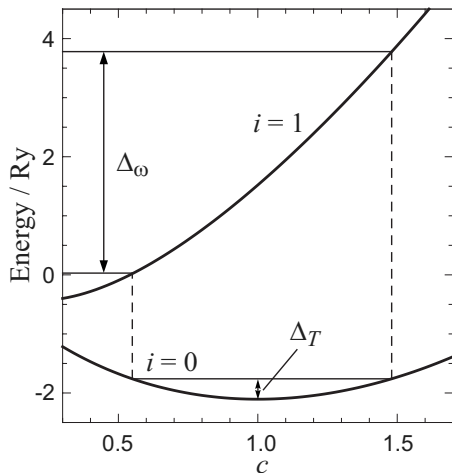

FIG. 7. Total adiabatic energies E_0^{tot} and E_1^{tot} as functions of the scaling parameter c calculated here for the confinement parameter $a_B/R = 10$. The plot illustrates how fluctuations of small energy Δ_T translate into much larger variations Δ_ω of the electronic transition energies.
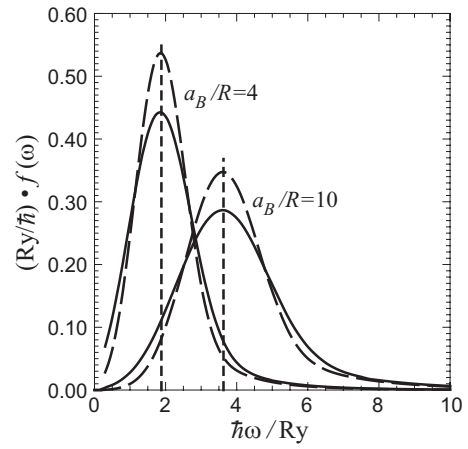

FIG. 8. The model absorption line shapes calculated as described in the text for $a_B/R = 4$ and $a_B/R = 10$ and for two different temperatures: $k_BT = 0.2$ Ry (long-dash curves) and $k_BT = 0.3$ Ry (solid curves). Vertical short-dash lines show the positions of the respective electronic transition energies E_{10} in the equilibrium configurations. The low-frequency tail of $f(\omega)$ for the case of $a_B/R = 4$ is not shown completely as the computational scheme used becomes inadequate.

tween which the dominant optical transitions take place. The behavior of E_1^{tot} here reflects large variations δE_P of the polarization energy without a comparable compensation of the electronic energy that occurs for E_0^{tot}. Figure 7 shows how a population on E_0^{tot} within a relatively small energetic broadening Δ_T translates into a much broader distribution Δ_ω of the transition energies.

To model the absorption line shape as a function of frequency ω, we work with an ensemble average over various fluctuations represented by different values of the scaling parameter c in Eq. (24). The resulting oscillator strength density in Eq. (13) is then a Boltzmann average of Eq. (14) taking the form of

$$f(\omega) = \int dc\, P(c) \sum_i f_{i0}(c)\, \delta(\omega - \omega_{i0}(c)), \tag{25}$$

where the probability

$$P(c) = \exp\left(-\frac{\delta E_0^{tot}(c)}{k_BT}\right) \bigg/ \int dc\, \exp\left(-\frac{\delta E_0^{tot}(c)}{k_BT}\right)$$

determines the weighting of fluctuations on the ground state adiabatic surface E_0^{tot}. Both transition frequencies $\omega_{i0}(c)$ and oscillator strengths $f_{i0}(c)$ in Eq. (25) are functions of the scaling parameter c.

Figure 8 shows examples of the absorption line shapes calculated with Eq. (25) for two values of the confinement parameter and two different values of temperature T. The results are broad peaks around the respective equilibrium transitions frequencies E_{10}. The broadening of the absorption lines, as we discussed, is strongly enhanced, roughly an order of magnitude larger than the thermal energies in our examples. Note that both photon energy $\hbar\omega$ and thermal energy k_BT in Fig. 8 are measured in units of the energy scale Ry, Eq. (1). If we were to use lower temperatures than shown in the figure, say $k_BT = 0.1$ Ry, the broadening would decrease in comparison to Ry but would still be very substantial in comparison with k_BT itself. Of course, the essence of the

enhancement mechanism here is generic. A similar, order-of-magnitude-enhanced, broadening have been reported for 3D solvated electrons.[34] It is this large and confinement-parameter-dependent broadening that is the emphasis of Fig. 8 rather than details of the model line shapes.

IV. CONCLUSIONS

As a result of solvation by the surrounding sluggish polar medium, excess charge carriers on 1D SC nanostructures can undergo self-localization into 1D polarons whose properties are quite different from band carriers. In an effort to establish experimentally testable signatures of the polaron formation, in this paper we examined the local optical absorption from solvation-induced 1D polarons within a simplified single-particle adiabatic framework for tubular structures.

The calculations indicate that a new broad absorption feature is expected, the peak energy of which is comparable with (but larger than) the binding energy of the polaron and whose width is much larger than the thermal energy. This feature arises mostly due to the electronic transition between two lowest-energy localized electronic levels formed in the polarization potential well. We identified the polaron length fluctuations (breathing mode) as the major source of the broadening.

Similarly to the enhanced binding of 1D excitons,[21] the binding of 1D polarons is stronger than in higher dimensions, and we explored polaron structure and optical transitions as a function of the confinement parameter a_B/R, where a_B is the effective 3D Bohr radius (1) and R the radius of the tubular structure. Of particular relevance for the optical absorption is the equilibrium transition energy E_{10}, which approximately determines the position of the absorption peak (Fig. 8). Within the range shown in Fig. 4, the scaling of this energy may be *approximated* as

$$E_{10}/\text{Ry} \propto (a_B/R)^{0.7}. \tag{26}$$

Note that the relation between E_{10} and the binding energy E_b also changes with the confinement parameter (Fig. 3). Together with the parametric dependence (1) of the Rydberg energy Ry, Eq. (26) allows to assess how the position of the absorption peak scales with system parameters [compare to scaling of excitons in SWCNTs (Refs. 44 and 45). It follows then that the effective dielectric constant ϵ^* of the solvent affects it as

$$E_{10} \propto (\epsilon^*)^{-1.3}.$$

If the effective mass m of the carrier was independent of the tube radius R, then Eq. (26) would result in

$$E_{10} \propto m^{0.3}.$$

In SWCNTs, however, m does depend on tube radius, and, for not very small radius tubes, this dependence is roughly $m \propto 1/R$.[15,44] In this regime, the confinement parameter becomes practically independent of R, and the transition energy scales as

$$E_{10} \propto m \propto R^{-1}.$$

For the specific numerical example provided in Sec. I, the absorption peak could then be expected at energy close to 0.15 eV. For a tube half as wide, under the same dielectric conditions the peak could be at about 0.3 eV. These numerical examples should, however, be considered only as representative, as they are subject to variations of the effective system parameters and model details. We note that a strong infrared absorption has also been predicted for the 2D electrons localized at the metal-polar-dielectric interface.[39]

To reiterate, illustrative results in this paper have been derived using simplified model considerations. More accurate treatments, particularly of temperature effects, may be needed for detailed comparisons with experimental data when it becomes available.

ACKNOWLEDGMENTS

[1] *Semiconductor Electrodes and Photoelectrochemistry*, edited by S. Licht (Wiley-VCH, Weinheim, Germany, 2002).
[2] P. V. Kamat, J. Phys. Chem. C **111**, 2834 (2007).
[3] M. Law, L. E. Greene, J. C. Johnson, R. Saykally, and P. Yang, Nature Mater. **4**, 455 (2005).
[4] D. M. Basko and E. M. Conwell, Phys. Rev. Lett. **88**, 098102 (2002).
[5] Y. N. Gartstein, Phys. Lett. A **349**, 377 (2006).
[6] Y. N. Gartstein, T. D. Bustamante, and S. Ortega Castillo, J. Phys.: Condens. Matter **19**, 156210 (2007).
[7] M. L. Mayo and Y. N. Gartstein, Phys. Rev. B **78**, 073402 (2008).
[8] Y. N. Gartstein and G. L. Usery, Phys. Lett. A **372**, 5909 (2008).
[9] *Polarons and Excitons*, edited by C. G. Kuper and G. D. Whitfield (Plenum, New York, 1963).
[10] *Polarons in Ionic Crystals and Polar Semiconductors*, edited by J. T. Devreese (North-Holland, Amsterdam, 1972).
[11] A. M. Kuznetsov, *Charge Transfer in Physics, Chemistry and Biology* (Gordon and Breach, Luxembourg, 1995).
[12] *Excess Electrons in Dielectric Media*, edited by C. Ferradini and J. P. Jay-Gerin (CRC, Boca Raton, FL, 1991).
[13] A. Nitzan, *Chemical Dynamics in Condensed Phases* (Oxford, New York, 2006).
[14] P. Avouris and J. Chen, Mater. Today **9**, 46 (2006).
[15] G. Pennington and N. Goldsman, Phys. Rev. B **71**, 205318 (2005).
[16] Y. Li, F. Qian, J. Xiang, and C. M. Lieber, Mater. Today **9**, 18 (2006).
[17] E. M. Conwell and D. M. Basko, J. Phys. Chem. B **110**, 23603 (2006).
[18] M. J. O'Connell, E. E. Eibergen, and S. K. Doorn, Nature Mater. **4**, 412 (2005).
[19] J. H. Choi and M. S. Strano, Appl. Phys. Lett. **90**, 223114 (2007).
[20] Our definitions here are based on the electron mass rather than on the exciton reduced mass used in Refs. 5 and 6.
[21] H. Haug and S. W. Koch, *Quantum Theory of the Optical and Electronic Properties of Semiconductors* (World Scientific, New Jersey, 2004).
[22] S. I. Pekar, Zh. Eksp. Teor. Fiz. **16**, 341 (1946).
[23] J. Appel, in *Solid State Physics*, edited by F. Seitz, D. Turnbull, and H. Ehrenreich (Academic, New York, 1968), Vol. 21, p. 193.
[24] W. Xiaoguang, F. M. Peeters, and J. T. Devreese, Phys. Rev. B **31**, 3420 (1985).
[25] W. R. Fawcett, *Liquids, Solutions and Interfaces* (Oxford, Oxford, 2004).
[26] E. I. Rashba, Opt. Spektrosk. **2**, 75 (1957).
[27] T. Holstein, Ann. Phys. **8**, 325 (1959).
[28] G. Venzl and S. F. Fischer, Phys. Rev. B **32**, 6437 (1985).
[29] M. Verissimo-Alves, R. B. Capaz, B. Koiller, E. Artacho, and H. Chacham, Phys. Rev. Lett. **86**, 3372 (2001).
[30] V. Perebeinos, J. Tersoff, and P. Avouris, Phys. Rev. Lett. **94**, 086802 (2005).
[31] F. Wang, G. Dukovic, L. E. Brus, and T. F. Heinz, Science **308**, 838 (2005).

[32] Y.-Z. Ma, L. Valkunas, S. M. Bachilo, and G. R. Fleming, J. Phys. Chem. B **109**, 15671 (2005).

[33] Z. Wang, H. Pedrosa, T. Krauss, and L. Rothberg, Phys. Rev. Lett. **96**, 047403 (2006).

[34] J. Schnitker, K. Motakabbir, P. J. Rossky, and R. A. Friesner, Phys. Rev. Lett. **60**, 456 (1988).

[35] V. May and O. Kühn, *Charge and Energy Transfer Dynamics in Molecular Systems* (Wiley-VCH, Weinheim, Germany, 2004).

[36] T. Ando, J. Phys. Soc. Jpn. **66**, 1066 (1997).

[37] J. D. Jackson, *Classical Electrodynamics* (Wiley, New York, 1998).

[38] J. Jiang, R. Saito, G. G. Samsonidze, A. Jorio, S. G. Chou, G. Dresslhaus, and M. S. Dresslhaus, Phys. Rev. B **75**, 035407 (2007).

[39] A. A. Zharikov and S. F. Fischer, J. Chem. Phys. **126**, 134707 (2007).

[40] L. D. Landau and E. M. Lifshitz, *Electrodynamics of Continuous Media* (Butterworth-Heinemann, Oxford, 1984).

[41] H. Fröhlich, *Theory of dielectrics* (Clarendon, Oxford, 1949).

[42] M. Le Bellac, F. Mortessagne, and G. G. Batrouni, *Equilibrium and Non-Equilibrium Statistical Thermodynamics* (Cambridge University Press, Cambridge, 2004).

[43] A. A. Zharikov and S. F. Fischer, J. Chem. Phys. **124**, 054506 (2006).

[44] T. G. Pedersen, Phys. Rev. B **67**, 073401 (2003).

[45] V. Perebeinos, J. Tersoff, and P. Avouris, Phys. Rev. Lett. **92**, 257402 (2004).

Model *ab initio* study of charge carrier solvation and large polaron formation on conjugated carbon chains

M. L. Mayo and Yu. N. Gartstein[a)]
Department of Physics, The University of Texas at Dallas, P.O. Box 830688, EC36, Richardson, Texas 75083, USA

Using long C_NH_2 conjugated carbon chains with the polyynic structure as prototypical examples of one-dimensional (1D) semiconductors, we discuss self-localization of excess charge carriers into 1D large polarons in the presence of the interaction with a surrounding polar solvent. The solvation mechanism of self-trapping is different from the polaron formation due to coupling with bond-length modulations of the underlying atomic lattice well known in conjugated polymers. Model *ab initio* computations employing the hybrid B3LYP density functional, in conjunction with the polarizable continuum model, are carried out demonstrating the formation of both electron and hole polarons. Polarons can emerge entirely due to solvation but even larger degrees of charge localization occur when accompanied by atomic displacements. © *2009 American Institute of Physics*. [DOI: 10.1063/1.3105337]

I. INTRODUCTION

One-dimensional (1D) semiconductor (SC) structures such as π-conjugated polymers (CPs), nanotubes, and nanowires are interesting nanoscopic objects that can be exploited in various areas including (opto)electronics, energy harvesting, and sensors. The nature and properties of excess charge carriers on these structures are fundamental for many applications. As covalent bonds provide for wide electronic bands and effective band masses much smaller than the free electron mass, intrinsically excess charge carriers in these systems have a high propensity for delocalization and a potential for high mobilities. If not for extrinsic defects, inherent limitations on the mobility arise due to interactions of charge carriers with other subsystems—most commonly with displacements of the underlying atomic lattice of the 1D SC structure. This electron-phonon coupling has been a subject of numerous studies for various specific 1D systems. It is well known that, as a result of the interaction with lattice phonons, excess charge carriers may undergo self-localization into polaronic states. Such polarons have been extensively discussed in the context of CPs, where they are believed to be accompanied by localized bond-length modulation patterns and new features in the optical absorption (see, e.g., Refs. 1 and 2 for reviews and original references).

A different and much less explored implementation of the strong polaronic effect can take place when a 1D SC is immersed in a three-dimensional (3D) polar medium, the situation is of particular relevance to applications and processes involving fundamental redox reactions in polar solvents. In this case of excess charge carrier *solvation*, the long-range Coulomb interaction, as has been recently discussed within simplified theoretical models,[3–7] can result in the formation of 1D adiabatic large-radius polarons, where a localized electronic state on a SC structure is surrounded by

a self-consistent pattern of the sluggish (orientational) polarization of the solvent. The Coulomb mechanism of the polaron formation here is analogous to the well-known 3D polarons in polar SCs[8–11] and solvated electrons in polar liquids.[11–13] Distinct from those cases are the confinement of the electron motion in a 1D nanostructure and its structural separation from the 3D polarizable medium. The energetic significance of the solvation has been emphasized by finding[4,5] that the binding energy of the resulting 1D polarons could reach a substantial fraction, roughly one-third, of the binding energy of Wannier–Mott excitons, the well-known primary photoexcitations in many 1D SCs. This may lead to enhanced charge separation. On the other hand, the mobility of solvated charge carriers is drastically reduced due to the dissipative drag of the medium.[3,6,14] New optical absorption signatures are also expected as a result of solvation.[7,15]

Given the generic character of the solvation mechanism of charge carrier self-localization and its potential implications for carrier mobilities and redox processes on 1D SC nanostructures, this effect appears interesting and important enough to warrant studies at various computational levels. As a step in that direction, we have attempted a first—to our knowledge—model *ab initio* study reported in a recent communication[15] that would demonstrate the formation of *solvation-induced* 1D large-radius polarons. In this paper we elaborate on that brief report discussing features of solvation-induced self-localization of excess charges on finite linear conjugated carbon chains C_NH_2 (polyyne oligomers) as derived within density-functional theory (DFT) computations in conjunction with the polarizable continuum model (PCM).[16–18]

Ab initio calculations are expected to be helpful in elucidating the role played by valence electrons and many-electron interactions in accommodation of an extra charge carrier. It should be noted that a reorganization of valence

---

a)Electronic mail: yuri.gartstein@utdallas.edu.

band electrons can be important even in noninteracting electron models—a nice illustration was given in Ref. 19 that analyzed how polarons of a two-band Peierls dielectric model evolve into single-particle Holstein[20] polarons in the limit of the "frozen valence band" approximation. With realistic Coulomb interactions in place, the role of valence electrons in the formation of the relevant self-consistent potentials would only increase. Interestingly enough, despite a relatively long history of first-principles studies of electron-phonon polarons in CPs (see, e.g., multiple references in Refs. 21 and 22), certain questions have been raised recently regarding the applicability of different *ab initio* frameworks to describe the formation of those polarons. That pertains to the failure of the local-density-approximation and generalized-gradient-approximation DFT schemes to detect self-localized charge density distributions in various charged oligomers, while Hartree–Fock (HF), parametrized semi-empirical and possibly hybrid-functional DFT methods have been reported to lead to charge localization in the middle of oligomers (e.g., Refs. 22–25). Quite different level-of-theory-dependent magnitudes of the effective electron-phonon coupling have also been found even in neutral polymeric systems (see, e.g., a comparative discussion in Refs. 26 and 27). A caution therefore has to be exercised in the interpretation of at least the quantitative aspects of various *ab initio* results.

As first-principles calculations are applied to the effect of solvation on charge carrier self-localization within the PCM framework, it would also be desirable to have a comprehensive comparison of different computational approaches. Such a study is currently underway and we are planning to report its results elsewhere. Reassuringly, the effect of solvation on excess charge localization appears qualitatively robust in those computations. While providing an illustrative example of comparison with HF computations, in this paper we rather focus on a more modest goal to discuss trends that are derived within a single computational scheme. Specifically, we employ DFT calculations with the B3LYP hybrid exchange-correlation density functional.[28] This functional is known to include both local and nonlocal effects and has been commonly used in recent studies[26,27,29,30] of polyyne and its oligomers.

By exploring model systems with prescribed carbon atom positions, we will be able to illustrate excess charge carrier (an electron or a hole) localization and the resulting formation of large 1D polarons entirely due to the polarization of the surrounding solvent. Examples of self-consistent—that is, practically independent of the chain length—polaron structures will thereby be also given. Within the confines of the computational scheme used, "realistic" geometries of carbon atom arrangements are those that optimize the total energy of the system. We have performed such geometrical optimizations for polyyynic chains both in vacuum and in solvent. In the range of chain lengths studied (up to $N = 100$ of carbon atoms) with the B3LYP hybrid functional, we have not been able to detect a clear trend toward excess charge self-localization due to the electron-phonon interaction *alone*—as the chain length increased, the bond-length modulation pattern would only become flatter in the

middle of the chain. On the contrary, in the presence of the Coulomb interaction with the solvent, clearly localized patterns of bond-length alternation (BLA) have been found to act as to boost the degree of excess charge localization, possibly reflecting synergistic effects from both mechanisms in this case.

II. SYSTEMS, COMPUTATIONS, AND DATA ANALYSIS

Since the computational demand increases substantially in DFT-PCM calculations, we have selected structurally simple 1D semiconducting systems of hydrogen-terminated polyyynic linear carbon chain $C_N H_2$ for our demonstration. It should be stressed however that, while playing the role of a prototypical example in our study, polyyynic chains continue to be the subject of much attention in their own right (see Refs. 26, 27, 31, and 32 and multiple references therein). Interestingly, they were predicted[33,34] to possess a rich family of electron-lattice self-localized excitations because of the extra degeneracy of molecular orbital (MO) levels.

The subject of our attention in this paper is the long chain $C_N H_2$ with even number of carbons N (N between 20 and 100). It is well established now[26,27,29,35,36] that even-N long ($N \gtrsim 10$) neutral chains have their ground state with the polyyynic structure, that is, they feature a (nearly uniform) alternating pattern of triple $C \equiv C$ and single $C–C$ bonds leading to a gap in the electronic spectrum. The ground state of odd-N chains would exhibit a kinklike "defect" in the bond-alternation pattern with associated mid-gap states,[33,30] which we do not discuss here. Having neutral chain $C_N H_2^0$ as a benchmark, we have studied both negatively charged $C_N H_2^-$ (an extra electron) and positively charged $C_N H_2^+$ (an extra hole) chains. As illustrated below, their self-localization behavior has been found very similar, with the excess charge measured correspondingly in units of $(−e)$ or (e), where e is the magnitude of the fundamental charge. To save space, some of the results, therefore, would be shown only for the negatively charged systems.

For the *ab initio* engine in this study, we employ DFT within the GAUSSIAN 03 (Ref. 16) set of programs. The majority of the results presented in this paper have been derived with the B3LYP hybrid exchange-correlation functional which includes the HF exchange along with DFT correlation.[28] In order to investigate the effects of solvation in a polar medium, GAUSSIAN 03 (Ref. 16) offers its implementation of the PCM described in original publications.[37–40] A rich $6-311++G(d,p)$ all electron basis set has been employed throughout. It should be noted that the results of our "in vacuum" calculations have been verified to compare well against the previously published *ab initio* data on neutral[27] and charged[29] polyyynic systems both in terms of energetics and optimized bond lengths. For all DFT-PCM ("in solvent") calculations, water has been chosen as a polar solvent with its default parameters in GAUSSIAN 03. We remind the reader that the focus of this paper is to compare results obtained in vacuum and in solvent environments within the same computational scheme rather than compare various computational approaches.
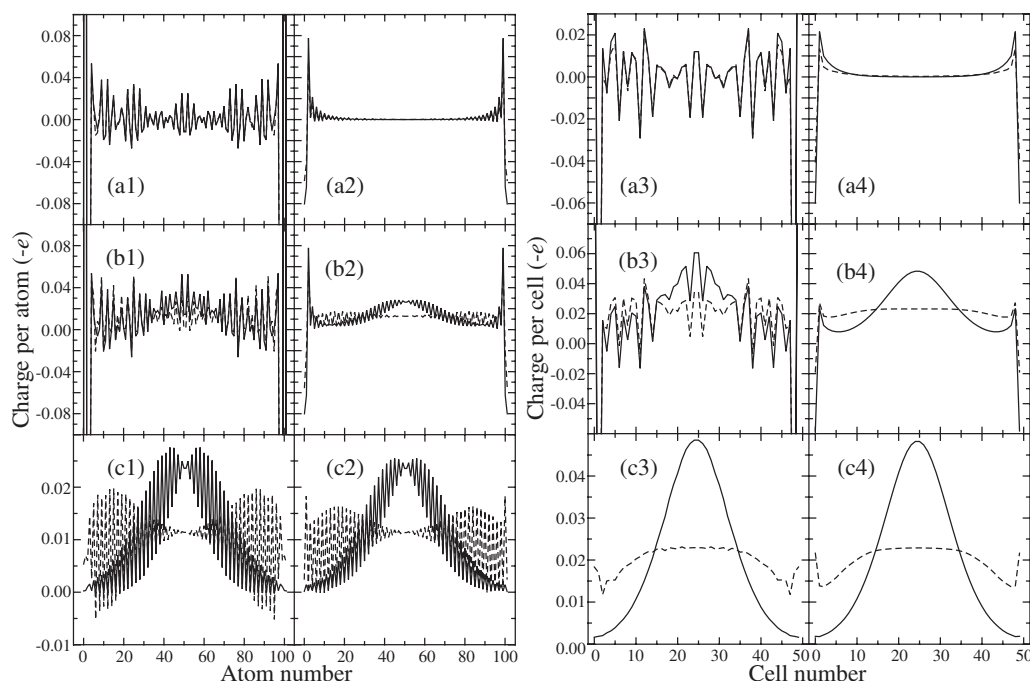
In order to be able to clearly discern the effects due to

FIG. 1. Spatial charge distributions on $N=100$ polyynic chains with RG1 geometry derived by using atomic charges from Mulliken (panel columns indexed 1 and 3) and Löwdin (panel columns 2 and 4) procedures. Panel row (a) is for the totally neutral chains, row (b) for the negatively charged chains with one added electron, and row (c) depicts the distribution of *excess* charge defined as a difference of the data in rows (b) and (a). Two left columns (1 and 2) depict charges per atom, two right columns (3 and 4) yield charges per unit cell. In each of the panels, solid lines show the results for chains in solvent, whereas dashed lines (when distinguishable) for chains in vacuum. It is evident that cell-centric excess charge distributions in panels (c3) and (c4) are nearly identical despite substantial differences between Mulliken and Löwdin charges observed in other panel pairs.

the solvation and provide conceptual proofs and illustrations (see Sec. III), we will be exploring both systems with the full geometric optimization of the underlying atomic lattice and systems with *model* rigid geometries, that is, with prescribed atomic positions. One of such rigid geometries, referred to as RG1, features the following fixed lengths: 1.235 Å for the triple bonds, 1.326 Å for the single, and 1.063 Å for the C–H bonds. These lengths have been retrieved from our complete optimization of the neutral $N=80$ chain in vacuum and are in fact relatively close to optimal values (see Sec. IV). Other rigid geometries have also been explored where all single C–C bonds are artificially stretched in successive increments of 0.1 Å up to the final length of 1.726 Å, the latter geometry is denoted as RG2. This artificial stretching is used to study the effect of narrower electronic bandwidths (larger band effective masses) on the charge localization.

A very relevant quantity for our discussion is the equilibrium *spatial charge distribution* over the 1D SC, which is naturally related to atomic charges in outputs of *ab initio* calculations. Importantly, these charges are calculated from many-electron wave functions and thereby reflect responses due to *all* electrons in the system. Two procedures, due to Mulliken and Löwdin, are widely used for charge population analysis.[17] It is well known[17] that calculations of atomic charges depend on the basis set transformations and sometimes lead to artifacts and spurious results. Such artifacts are in fact apparent in our illustration in Fig. 1 that compares various results we obtained for $N=100$ chains. Differences between Mulliken and Löwdin charges are especially clearly seen for raw charge populations separately on neutral [row (a)] and charged [row (b)] chains, whether they are atomic or

unit-cell centric. Comparison of panels (c1) and (c2), however, indicates that certain cancellation effects take place and both methods lead to less dissimilar results when one is interested in the spatial distribution of the *excess* charge derived as the difference in charge densities on charged and neutral chains. Still those atomic-centric results exhibit possibly spurious oscillations which may be artifacts related to the presence of bond-oriented charge density waves in our system. This suggests "averaging" of the charge over the unit cells consisting of pairs of neighboring carbons (for convenience, the chain end cells are defined here to include the hydrogen atomic charges). Panels (c3) and (c4) show that various artifacts indeed practically disappear, and the unit-cell-based excess charge distributions calculated by Mulliken and Löwdin procedures become remarkably close. We confirmed this conclusion for many other cases of interest. Accordingly, it is these stable results for excess charge per cell that will be displayed in our results below (using raw Löwdin charges).

III. SOLVATION-INDUCED SELF-CONSISTENT CHARGE LOCALIZATION IN MODEL SYSTEMS

In real systems, both atomic displacements and polarization of the surrounding medium are expected to take place in order to accommodate an excess charge carrier. Moreover, given the nonlinear nature of the polaronic effect, both subsystems may act in a synergistic way. In order to better understand the contribution coming from the solvation, we therefore start from studying model systems with rigid ge-
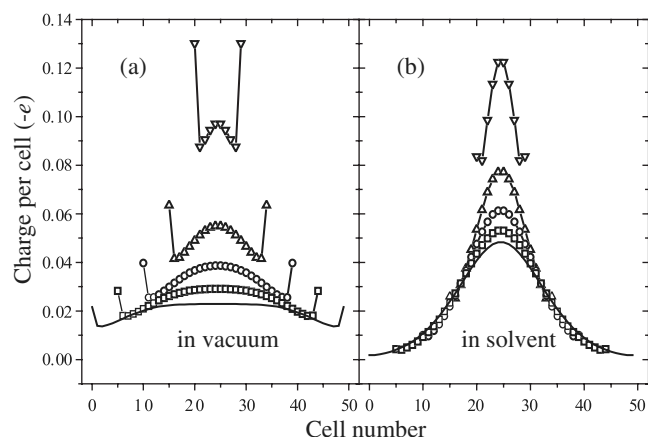
FIG. 2. Excess charge density spatial distribution on negatively charged $C_NH_2^-$ chains with $N=20$, 40, 60, 80, and 100—top to bottom curves, respectively, in their central parts. All chains feature the same pattern of fixed bond lengths corresponding to RG1 geometry described in text. Panel (a) displays results for chains in vacuum, panel (b) for chains in the solvent environment.

ometries, where no localized bond-alternation patterns are allowed, while the medium "adjusts" its state of polarization.

A. Spatial distribution of the excess charge

Figures 2 and 3 compare excess charge density distributions, negative and positive, respectively, calculated as described in Sec. II for chains of varying lengths both in vacuum and in solvent. It is evident that panels (a) and (b) of each of the figures display quite distinct trends. Disregarding the end effects (end cells include charges on hydrogens), vacuum results in panel (a) reflect the "particle in a box" behavior: as the chain length increases, the excess charge is distributed more and more uniformly over the whole chain. In a sharp contrast, for chains in the solvent, panel (b), the excess charge exhibits much more localized distributions around the central parts of the chains to the extent that no appreciable end effects are present. As the chain length increases, those distributions show a very clear tendency toward convergence, albeit not completely achieved within the range of lengths studied.

Instead of further increasing the chain length in already demanding computations, we now attempt to decrease the
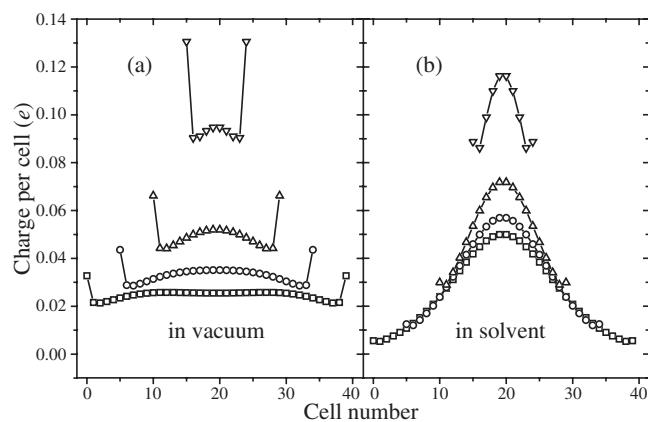

FIG. 3. As in Fig. 2 but for positively charged $C_NH_2^+$ chains with $N=20$, 40, 60, and 80—top to bottom curves, respectively, in their central parts.
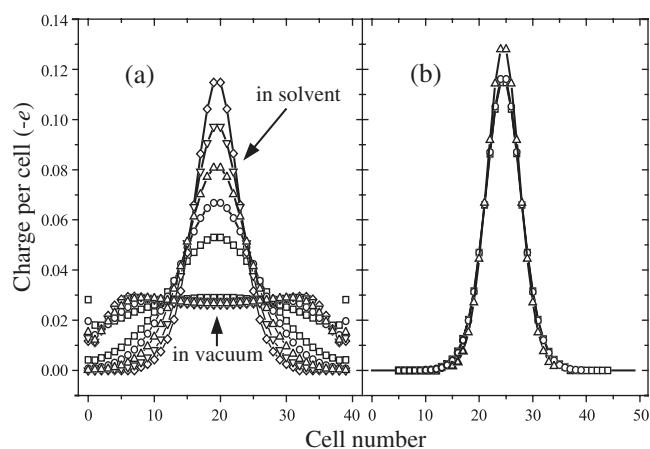

FIG. 4. Excess charge density spatial distribution on charged $C_NH_2^-$ chains. (a) $N=80$. The evolution of the charge distribution upon stretching the single bonds by 0.1 Å successive increments from 1.326 to 1.726 Å—bottom to top in a group of 5 clearly distinct curves shown by different connected symbols and denoted in solvent. The same—but unconnected—data symbols are used to show the results for chains in vacuum, those distributions largely overlap. (b) Comparison of distributions for chains in the solvent with $N=40$, 60, 80 (different data symbols), and 100 (solid line) for the geometry RG2 featuring the longest single bonds. Curves for $N=60$, 80, and 100 practically coincide.

spatial extent of charge localization in model systems. To this end, we recall that, in single-particle models,[3–7] the spatial extent of the polaron is determined by the balance of the gain in the potential energy of the self-localized carrier due to its interaction with the medium and the loss in its kinetic energy due to localization. Decreasing the role of the kinetic energy would lead to a diminished delocalization propensity and is expected to shorten the polaron. This should be achievable with an increased effective band mass of the carrier, or with a narrower electron bandwidth. To affect this, we chose to *artificially* stretch all single bonds in our rigid model system as described in Sec. II thereby making C≡C "dimers" more and more separated from each other. Figure 4(a) (extra electron) and Fig. 5(a) (extra hole) illustrate a *dramatic* difference in the response of the excess charge distributions on $N=80$ chains to successive single-bond stretch-
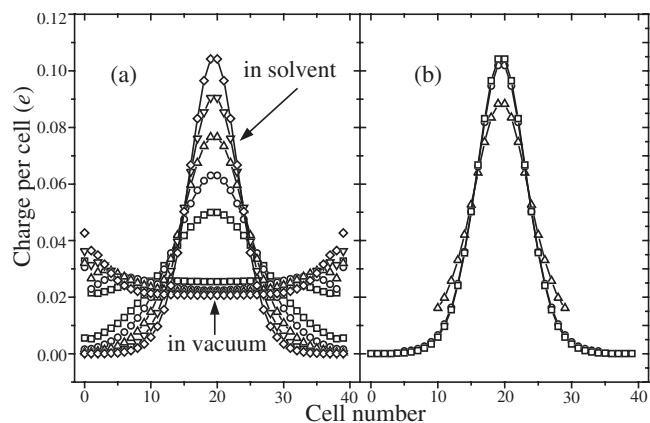

FIG. 5. Excess charge density spatial distributions on charged $C_NH_2^+$ chains. (a) $N=80$. The evolution of the charge density distribution upon stretching bonds as in Fig. 4. (b) Comparison of distributions for chains in the solvent, with $N=40$, 60, and 80 (different data symbols) for the RG2 geometry. Curves for $N=60$ and 80 practically coincide.

ing in vacuum and in solvent. While the charge density in vacuum shows only very little changes in this process and preserves nearly uniform distributions over the whole chain, for chains in solvent, each successive stretching step indeed results in substantially smaller and smaller localization regions. As the extent of localization in the longest-stretched geometry, RG2, appears to be well within the chain length, we can now compare the corresponding excess charge distributions for several chain lengths. Figure 4(b) makes it evident that the distributions for $N=60$, 80, and 100 negatively charged chains in solvent practically coincide. Likewise, distributions for $N=60$ and 80 positively charged chains are practically identical in Fig. 5(b). This confirms that the obtained charge distributions on longer chains correspond to a fully converged self-consistent pattern of excess charge localization. Importantly, self-localization of the excess charge demonstrated here has been achieved *entirely* due to the interaction with the surrounding solvent.

Comparing the results for negatively charged and positively charged species (Fig. 2 versus Fig. 3 and Fig. 4 versus Fig. 5, one, of course, notices some effects of charge-conjugation (CC) symmetry breaking. They depend on the chain length as affected by both the ends (hydrogen atoms) and by the inherent band structure. As the inherent π-orbital bands are nearly CC symmetric, these effects are evidently relatively weak, and basically the localization behavior for electrons and holes appears very similar. This fact should be emphasized in the context of the different status of highest occupied and lowest unoccupied states within DFT computations, and observed differences in electron and hole polarons due to the interaction with lattice distortions in CPs with more complex structures.[22]

B. Molecular orbitals

We now turn from the total excess charge distribution to individual MOs and the resulting electronic structure. In the neutral C_NH_2 chains, π-electron energy levels exhibit a fourfold degeneracy—in addition to the spin degeneracy, there is a twofold degeneracy with respect to the spatial orientation of π-orbitals. If the chain direction is chosen as the z-axis, π-orbitals can be said to be oriented either along the x or along the y axis. In charged chains, spin- and orbital-orientation-degeneracy are generally lifted. Also, in the presence of the polaronic effect, one observes both spatially localized and delocalized (over the chain length) individual electronic states. The overall picture of MO energy levels in neutral and charged chains is illustrated in Fig. 6 ($C_{100}H_2^0$ versus $C_{100}H_2^-$) and Fig. 7 ($C_{80}H_2^0$ versus $C_{80}H_2^+$), while Fig. 8 illustrates the spatial behavior of MOs on charged $C_{100}H_2^-$ chains in more detail.

Looking at the electronic structures of neutral and charged chains in Figs. 6 and 7, one can compare the differences in responses between chains in vacuum and chains in solvent as well as compare the differences caused by the geometry of carbon atom arrangements (RG1 versus RG2). Going to the artificial RG2 geometry with longer C–C bonds allows us here to decrease the polaron size and to illustrate some features that would otherwise be hard to observe within
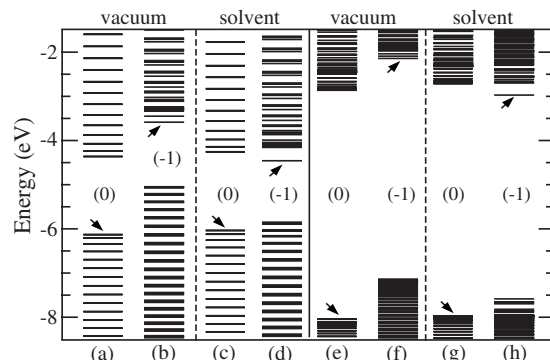

FIG. 6. MO energy levels for neutral (0) and charged (−1) $C_{100}H_2$ chains with rigid RG1 [(a)–(d)] and RG2 [(e)–(h)] geometries both in vacuum and in the solvent. The arrows indicate positions of HOMO levels.

the range of chain lengths studied. Probably the first visually noticeable difference between RG1 and RG2 electronic structures is a much wider band gap in RG2—as indeed one should expect based on a much larger difference in the hopping integrals corresponding to triple and single bonds. As such, however, the size of the band gap is inconsequential for the degree of charge localization due to solvation. Instead, of direct importance here is a much narrower bandwidth in RG2, which is easily detected via a higher density of states [panels (e) versus (a) and (g) versus (c)]. The narrower the bandwidth is, the smaller is the propensity of the excess carrier to delocalize.

A common feature evident in the results for charged chains in vacuum is the appreciable overall energy shifts with respect to neutral chain MO levels: to higher energies for excess electrons and to lower energies for excess holes. These shifts reflect simple electrostatic effects (the electrostatic potential with respect to infinity) for chains of finite lengths. Understandably, shifts of such an origin should become much smaller for chains surrounded by media with high dielectric constants, which is indeed the case for our chains in the solvent environment (see also below in Sec. III C). A much more important and relevant difference in the MO structure of charged chains in vacuum and in solvent is instead that solvated chains feature local electronic levels clearly separated from other states. In the case of negatively charged chains (Fig. 6), it is the highest occupied MO
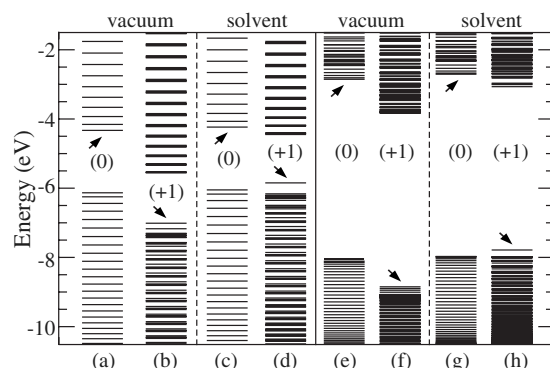

FIG. 7. MO energy levels for neutral (0) and charged (+1) $C_{80}H_2$ chains with rigid RG1 [(a)–(d)] and RG2 [(e)–(h)] geometries both in vacuum and in the solvent. The arrows indicate positions of LUMO levels.
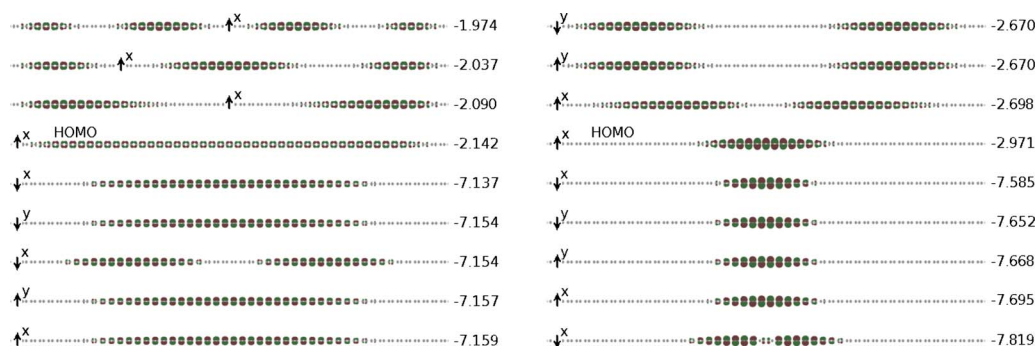
FIG. 8. (Color online) Spatial distribution of several MOs for $C_{100}H_2^-$ chains with RG2 geometry in vacuum (left column) and in solvent (right column). The spin state of orbitals is indicated by arrows, while the spatial orientation by letters "x" and "y" (chains are oriented along the z-axis). Orbital energies in eV are shown in the right of the columns. Compared MOs around HOMOs are sequentially selected from a list ordered in orbital energies.

(HOMO) accommodating an excess electron. In the case of positively charged chains (Fig. 7), it is the lowest unoccupied MO (LUMO) accommodating an excess hole. Comparison of panels (d)–(b) and, especially, panels (h)–(f) in these figures clearly demonstrates the formation of local levels—as would be caused by the appropriate polarization of the environment. The appearance of localized electronic states in self-consistent "potential wells" is one of the hallmarks of the strong polaronic effect.[9,11]

The number of localized electronic states appearing due to the polaronic effect should depend on the nature of the system and the effective potential well. For electron-lattice polarons in CPs, local levels are known[1,2] to split off from both conduction and valence bands. The short-range character of the effective potential well in that case, however, limits the number of such states (in traditional two-band Peierls dielectric models,[1] there would be only two local levels: one close to the conduction and one to the valence band). In the case of the long-range interaction with the polarizable environment, the effective potential well has the long-range Coulomb behavior expected to result, for an infinite system, in a multitude of localized states of various spatial symmetries converging to the onset of the delocalized continuum. This is a standard picture for traditional "single-band" 3D polarons,[9] and we have specifically discussed its realization for 1D systems immersed in the 3D polar medium.[4,7]

Restricting a more detailed illustration now to the negatively charged $C_{100}H_2^-$ chains, Fig. 8 compares the spatial structure of HOMOs and several other MOs (from a list ordered in orbital energies) in vacuum and in the solvent environment as retrieved from the GAUSSVIEW 4 (Ref. 41) rendition of GAUSSIAN 03 outputs. Here we use results only for RG2 geometry displaying better distinguishable localized states. (The figure of course also illustrates the lifting of spin and spatial-orientation degeneracies.) As expected, a stark difference is seen between the HOMOs in vacuum and solvent cases: the former shows a state delocalized over the chain length, while the latter indeed exhibits a well-localized character. In addition to this, however, we also find in the right column of Fig. 8 that the solvation-induced negative polaron features various occupied localized states in the valence band region of energies (nothing like this happens for valence band states in the vacuum case). This observation confirms a reorganization of valence band states apparent in

the corresponding electronic structure in Fig. 6(h). Thus the polaron reveals a many-electron structure, more complex than invoked in simplified single-particle models.[3–7]

Even in RG2 geometry it is difficult though to visually identify the LUMO in the right column of Fig. 8 as an unoccupied localized state expected to be formed in the effective polarization potential well.[4,7] While that state wave function evidently exhibits the right odd symmetry with respect to the inversion of the chain axis, the length of the chain appears insufficient to establish a localized character of the state with certainty. Likewise, within the length of our oligomer, we cannot establish the onset of what would become a continuum of truly delocalized states in the limit of infinite chains. Similar considerations of details of the spatial behavior of MOs can be done for positively charged chains which would then correlate with signatures of the electronic structure in Fig. 7.

C. Energetics

An important energetic quantity in discussions of the polaronic effect is the polaron binding energy referring essentially to the gain in the *total* energy of the system taking place upon self-localization of the excess charge carrier.[1,9,11] Calculations of the binding energy of solvation-induced polarons on 1D structures are very straightforward in simplistic models.[3–7] Unfortunately, we do not feel we have a reliable straightforward procedure for the determination of the binding energy of solvation-induced polarons in our current *ab initio* calculations. One of the reasons for this is that we cannot control the state of the polarization of the solvent as it would be easily done by prescribing desired patterns of atomic displacements in the case of electron-lattice polarons. Some considerations can, however, be put forward based on direct outputs of GAUSSIAN 03 computations.

Figure 9 illustrates such considerations for excess electrons. One very well-defined and physically meaningful quantity characterizing accommodation of an excess electron in the computational outputs is the electron affinity

$$EA = E_{tot}^0 - E_{tot}^-,$$

corresponding to the difference in the total system energies for neutral (superscript "0") and negatively charged ("−") chains. Another readily available energy is the energy E_{LUMO}^0
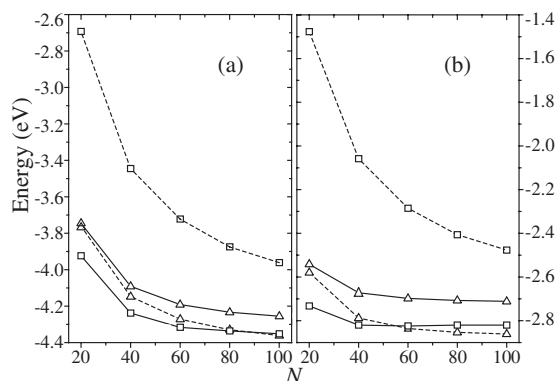
FIG. 9. The negative of electron affinities, −EA, (square symbols) and energies E_{LUMO}^0 of neutral chains (triangles) as functions of the number of carbons in polyyne oligomers $C_N H_2$ with rigid geometries. Vacuum data points are connected by dashed lines, data for chains in solvent by solid lines. Panel (a) displays results for chains with RG1 geometry, panel (b) corresponds to chains with RG2 geometry.

FIG. 10. IPs (square symbols) and the negative of HOMO energies ($-E_{HOMO}^0$) of neutral chains (triangles) as functions of the number of carbons in $C_N H_2$ with rigid geometries. Vacuum data points are connected by dashed lines, data for chains in solvent by solid lines. Panel (a) displays results for chains with RG1 geometry, panel (b) corresponds to chains with RG2 geometry.

of the LUMO in the neutral system. These energies are compared in Fig. 9 as −EA versus E_{LUMO}^0 for various conditions as functions of the number N of carbons in $C_N H_2$. The rationale for this comparison is that in the limit of infinite chains, $N \rightarrow \infty$, one might hope, in the spirit of Koopman's theorem,[28,42] that E_{LUMO}^0 would represent the extra system energy upon an addition of a single electron into the lowest-energy delocalized state with vanishing excess charge density. The negative of the electron affinity, −EA, on the other hand, represents the extra system energy upon the addition of a single electron when the system is allowed to completely reorganize itself to achieve the minimum possible total energy. Both compared "extra energies" are of course negative in our data. We remind the reader that in this section we discuss systems with rigidly positioned carbons so that reorganization here is limited only to the states of other electrons and the polarization of the environment.

A striking difference is observed in Fig. 9 when results for chains in vacuum are compared to chains in solvent. In the former case, the data correspond to $-EA > E_{LUMO}^0$, while in the latter, the order of these energies is reversed: $-EA < E_{LUMO}^0$, clearly showing the significance of screening and reorganization effects taking place in the solvent environment. Vacuum data points are evidently very far from displaying a convergence to the infinite chain limit, and a larger steepness of the vacuum EA as a function of N is indicative of the magnitude of the Coulomb effects involved for finite excess charge densities in oligomers. While data points for chains in solvent, of course, also exhibit an N-dependence, this dependence is shallower than in the vacuum case, and for RG2 geometry [panel (b)] displays a nearly converged behavior for largest N studied. As we discussed in Sec. III A, a self-consistent polaron formation is achieved in RG2 within our range of chain lengths.

Considering the positive energetic "improvement" $E_{LUMO}^0 + EA$ in the solvent environment, its $N = 100$ magnitudes in Fig. 9 are equal to approximately 0.1 and 0.11 eV for RG1 and RG2 geometries, respectively. If one were to take this energetic improvement in the infinite-N limit as
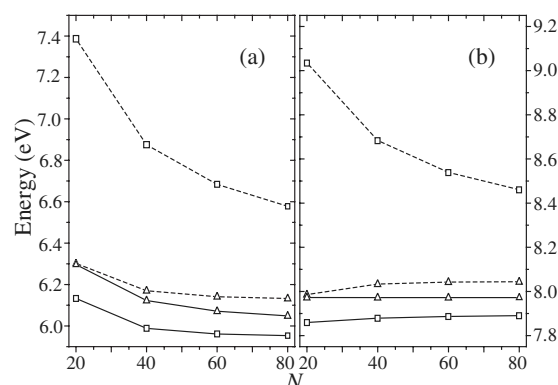
corresponding to the "true" solvation-induced polaron binding energy, then the obtained numbers $\simeq 0.1$ eV would provide estimates of the polaron binding.

An analogous consideration for excess holes involves a comparison of the ionization potential (IP)

$$IP = E_{tot}^+ - E_{tot}^0$$

and the negative $-E_{HOMO}^0$ of the energy of the HOMO in the neutral chain. This comparison of now positive extra system energies is illustrated in Fig. 10. The figure displays qualitative patterns similar to observed above for excess electrons (while, of course, also showing signs of CCS breaking). Particularly, one notes while for chains in vacuum one has IP $> -E_{HOMO}^0$, the relationship reverses for chains in solvent: IP $< -E_{HOMO}^0$. The $N = 80$ values of the energetic improvement $-E_{HOMO}^0 - IP$ in the solvent environment are approximately 0.1 and 0.08 eV for RG1 and RG2 geometries, respectively, which could again suggest polaron bindings close to 0.1 eV.

It appears, however, strange that these naive estimates lead to relatively small differences (and even to a reversal) in polaron bindings for RG1 and RG2 geometries—while the spatial localization has been found much more significant in RG2 (Sec. III A). We believe this indicates that the actual polaron binding energies would be underestimated in discussed energetic comparisons. It is quite likely that E_{LUMO}^0 and $-E_{HOMO}^0$ do not represent fully the lowest extra energy of systems where an excess delocalized electron or an excess delocalized hole would interact with a nonuniform, charge density wave (CDW), background of the polymer chain.

Bond-centric CDWs are known to form on neutral chains upon their dimerization with more electronic density corresponding to shorter ($C \equiv C$) and less electronic density to longer ($C-C$) bonds. Such CDWs have been widely discussed in the context of CPs as Peierls insulators.[1] Being a nonvanishing distribution of the electric charge, a CDW is expected to polarize the solvent, which is indeed how we interpret the data shown in Fig. 11. The figure displays the electrostatic energy U_{pol} stored in the solvent polarization as retrieved from outputs of GAUSSIAN 03 computations. It is
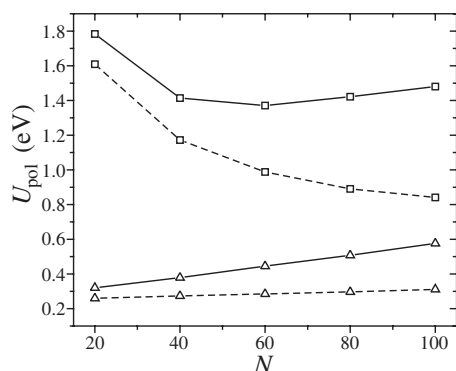
FIG. 11. The electrostatic energy stored in the solvent polarization as a function of the number N of carbons in C_NH_2. Triangular data points are for neutral $C_NH_2^0$, squares for charged $C_NH_2^-$ chains. The dashed lines connect the data for RG1 chain geometry, the solid lines for RG2.

evident that this energy does not vanish for neutral chains and in fact grows linearly with the number of carbons N, as one would expect for a CDW. Since the amplitude of CDW is enhanced in neutral chains with RG2 geometry, they do exhibit a steeper growth with N. It would be interesting to evaluate the interaction of a CDW with the solvent using more tractable analytical approaches based on atomistic models of both the CP chain and the solvent. (A related example of structure-based calculations is given in Ref. 43 treating the Coulomb interaction of CDWs on neighboring polyacetylene chains.) That would allow clarification of the geometrical regimes of the applicability of the continuum solvent description.

Figure 11 also shows the evolution of U_{pol} for negatively charged $C_NH_2^-$ chains. Especially illuminating here are the results for chains with RG2 geometry exhibiting a nonmonotonic behavior of U_{pol} as a function of N. U_{pol} first decreases with N at smaller N, reflecting the decrease in the electric field of the excess charge upon its spreading over longer oligomers. U_{pol} then reaches its minimum in the region of N corresponding to the formation of the self-consistent localized polaron pattern. With a further increase in N, U_{pol} starts growing again with the same slope that is exhibited by neutral chains reflecting the interaction of the CDW with the solvent. The converged large-N difference in U_{pol} of charged and neutral chains with RG2 geometry is evidently quite substantial, close to 0.9 eV. While the minimum of U_{pol} is not

achieved for negative chains with RG1 geometry within the range of chain lengths studied, one could guess from the data in Fig. 11 that the large-N difference in U_{pol} of charged and neutral chains in that case would probably be roughly half of the value for RG2 geometry. This ratio would look like more in line with charge localization patterns observed for RG1 and RG2. The very magnitude of the "excess" polarization energy just discussed may be indicative of the polaron binding energies appreciably larger than 0.1 eV. This speculative conclusion could be verified more directly if we were able to perform *ab initio* computations for charged chains with the polarization state of the solvent corresponding to that for neutral chains.

IV. SOLVATION AND BOND ALTERNATION PATTERNS

We now turn our attention to the results obtained with full geometrical optimizations of underlying carbon lattices. A very convenient and well-known[1,26,27] way to characterize dimerized polymeric structures is via BLA patterns

$$\delta_n = (-1)^n (l_n - l_{n+1}),$$

where l_n is the length of the nth carbon-carbon bond. In the infinite dimerized neutral structure, this pattern would be uniform, that is, independent of the spatial bond position n.

Figure 12 compares BLAs computed for neutral and negatively charged oligomers $C_{40}H_2$, $C_{80}H_2$, and $C_{100}H_2$. This comparison allows one to visually evaluate the magnitude of oligomer end effects. It is clear that a uniform, infinite-polymer, behavior is practically achieved over a long central-part stretch of the neutral $C_{100}H_2^0$. There is very little difference in BLAs of neutral chains in vacuum and in solvent; a small increase in δ_n in the solvent is consistent with our expectation for a CDW interacting with the environment.

Much more significant variations are observed for charged oligomers. As was discussed at length for electron-lattice polarons in CPs,[1,2] the magnitude of BLAs would exhibit a dip in the spatial region containing an excess particle, where the lattice becomes "less dimerized." This expected decrease in δ_n is evident in all panels of Fig. 12. The character of its evolution with the oligomer length, however, is quite different for chains in vacuum and in solvent. The vacuum data just show a progressive reduction in the dip in δ_n for longer oligomers. In the absence of data for much
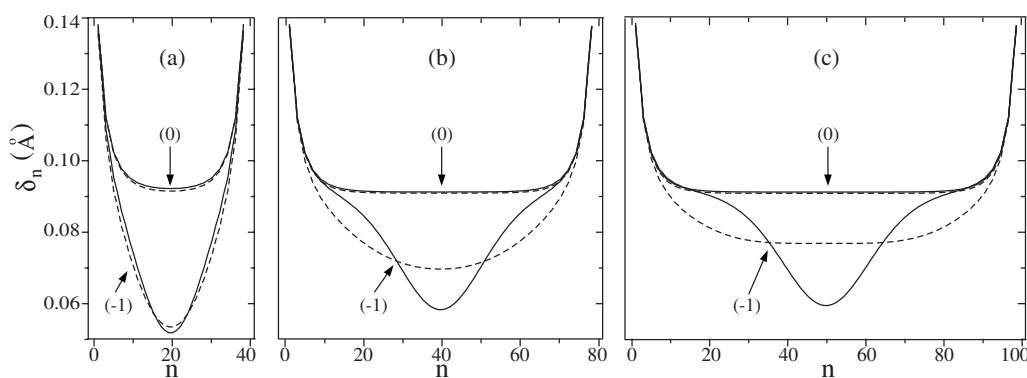

FIG. 12. Carbon-carbon BLA patterns for (a) $C_{40}H_2$, (b) $C_{80}H_2$, and (c) $C_{100}H_2$. Patterns for neutral chains are indicated with symbol (0), patterns for negatively charged chains with (−1). The dashed lines show results for chains in vacuum, the solid lines for chains in the solvent environment.
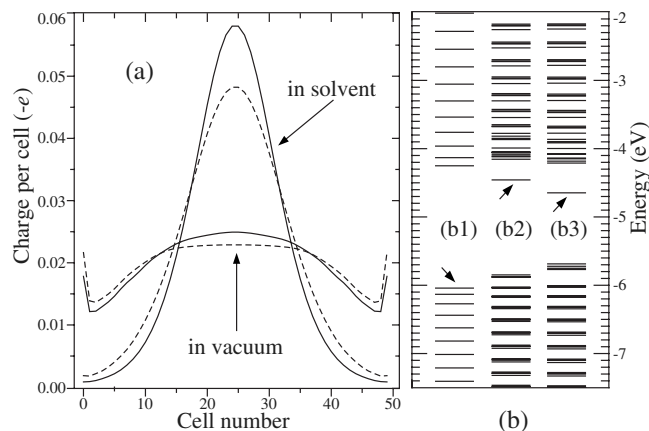
FIG. 13. Comparison of the solvation and BLA effects for $C_{100}H_2$. (a) Excess charge distributions in vacuum and in the solvent for the fully optimized lattice geometry (solid lines) and for the RG1 geometry (dashed lines). (b) The corresponding MO energy levels in the solvent for: (b1) Optimized neutral chain, (b2) Charged chain in RG1 geometry, (b3) Optimized charged chain. The arrows show HOMO levels.
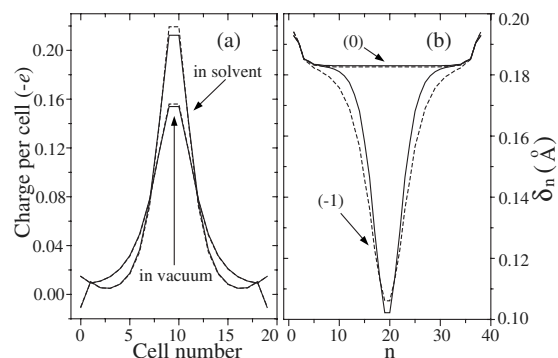

FIG. 14. Results of restricted-HF computations for $C_{40}H_2$ oligomers. (a) Excess charge density distribution on $C_{40}H_2^-$ in vacuum and in solvent. Dashed lines show the distribution on chains with a uniform BLA pattern of the neutral system, solid lines are for chains with relaxed (optimal) geometries. (b) Optimal BLA patterns for neutral (0) and negatively charged (−1) oligomers. The dashed lines are for chains in vacuum, the solid lines are for chains in solvent.

longer chains, all we can conclude is that a very flat pattern of δ_n in the middle of $C_{100}H_2^-$ does not suggest yet an incipient formation of a self-localized pattern characteristic of polarons. This is reminiscent of the apparent failure of DFT computations to detect electron-lattice polarons in computationally tractable oligomers discussed in Sec. I—with our results now extended to hybrid B3LYP computations. On the contrary, the data derived for chains in solvent quite clearly indicate a nearly self-consistent localized pattern of δ_n on $C_{100}H_2^-$, although, of course, longer oligomers would be needed to reveal a truly self-consistent polaron size.

These observations correlate well with the results obtained for excess charge densities on $C_{100}H_2^-$ that are displayed in panel (a) of Fig. 13. The panel compares the excess density on chains with the uniform BLA of neutral chains (RG1 geometry) and on chains where the relaxation of the BLA due to the excess charge has taken place. One can see that while the relaxation of the BLAs does lead to spatial contractions of charge densities both in vacuum and in solvent, the delocalized (over the whole oligomer) nature of the excess charge remains intact in the vacuum case. Excess charge localization due to solvation, on the other hand, gets evidently enhanced by the localized lattice response seen in Fig. 12(c). One could probably say that solvation and lattice relaxation here act synergistically to affect excess charge self-trapping. With our B3LYP computations, the effect of the solvation on the excess charge distribution is evidently much more pronounced. A complementary information is provided by panel (b) of Fig. 13, showing the effects of solvation and BLA relaxation on the electronic structure of MO levels. Particularly relevant here are the intragap levels. Interestingly, for the energies of these levels effects due to each of the mechanisms appear similar in magnitude. This suggests that one has to be careful in evaluating *self-localization per se* based just on the appearance of the MO levels in their overall structure. The spatial behavior of individual MOs, as well as the total spatial distribution of the excess charge, needs to be properly analyzed.

A. Hartree–Fock results

As mentioned in Sec. I, in this paper we do not pursue an extensive comparison of results obtained with various *ab initio* methods. To emphasize the level-of-theory dependence of at least the quantitative aspects, we, however, find it pertinent to provide a glimpse at the nature of results derived with HF computations. HF calculations for conjugated polymeric structures have been discussed[26,27] to result both in overestimated energy gaps and magnitudes of BLAs. At the same time, unlike pure-DFT computations, they have also been shown to yield self-localized polaronic states for excess charge carriers.[22–25] Our findings for polyynic chains agree well with these known trends.

Figure 14 illustrates our restricted-HF results for neutral and negatively charged $C_{40}H_2$ chains both in vacuum and in the solvent environment; they are consistent with a limited set of data we have also computed for longer chains. When compared to B3LYP-derived results discussed earlier in this paper and in Ref. 15, one immediately notices an appreciably higher degree of excess charge density localization and larger magnitudes of BLAs obtained with the HF. Reassuringly, the qualitative effect of the solvent environment remains intact: it does enhance the excess charge localization [panel (a) of Fig. 14] and leads to a shorter and more pronounced associated dip in the optimized BLA pattern [panel (b)]. Differently from the B3LYP-data, however, solvation here does not appear to act as a "primary" source.

In agreement with previous HF studies, we do find the excess charge self-localized already on chains in vacuum. One might be tempted to say—as expected for traditional electron-lattice polarons—that the calculated self-trapping in this case is *caused* by the interaction with displacements of carbon atoms manifested in the relaxed BLA pattern in Fig. 14(b). The comparison made in Fig. 14(a), however, does not seem to support such a viewpoint. Specifically, we compare in that panel the excess charge densities obtained for fully relaxed geometries and for a rigid geometry featuring a *uniform* BLA pattern. The latter corresponds to the BLA derived for neutral chains in their middle portion [Fig. 14(b)]. Despite the uniform lattice background, the excess charge local-

ization evidently takes place, and with minimal variations from the fully geometrically relaxed chains. Moreover, the lattice relaxation, while indeed decreasing the total system energy, counterintuitively results here in slightly smaller localization. (To compare, in B3LYP results geometrical relaxation would always lead to larger spatial charge localization.) Thus, it is rather the treatment of electron-electron interactions within the framework of HF computations that appears to affect the excess charge localization observed in our HF data. In this paper, we forgo a discussion of the physical validity of these results that would require a more focused study.

V. DISCUSSION

Self-localization of excess charge carriers (electrons or holes) into polaronic states on 1D SC structures is an interesting effect that may be consequential for transport, optical, and electrochemical properties of these systems. The basic nature of the self-trapping is easily revealed in a *single-particle* picture within a standard 1D continuum adiabatic framework, where a localized carrier wave function $\psi(x)$ is found as corresponding to the ground-state solution of the *nonlinear* Schrödinger equation,

$$-\frac{\hbar^2}{2m}\frac{\partial^2 \psi(x)}{\partial x^2} - \int dx' V(x-x')|\psi(x')|^2 \psi(x) = E\psi(x).$$

Here x is the coordinate along the structure axis, m is the effective band mass of the carrier, and $V(x)$ is the effective self-interaction mediated by another subsystem. In the case of a short-range electron-phonon mediation, the self-interaction may be approximated as local: $V(x) = g\,\delta(x)$ leading then to the exact solution $\psi(x) \propto \mathrm{sech}(gmx/2\hbar^2)$ for a continuum 1D polaron. This is the result widely known after the pioneering contributions of Rashba[44] and Holstein.[20] Another type of mediation arises due to the long-range polarization interaction of an excess charge carrier with a surrounding polar medium. In that situation, the effective $V(x)$ behaves as $1/|x|$ at large distances, while the short-range behavior depends on specific system details such as, e.g., the actual transverse charge density distribution and the geometry of the dielectric screening.[3,4,7] Numerical studies of this case[4,5] indicate that the binding energy of the resulting polarons could reach an appreciable fraction of the binding energy of the corresponding primary optical excitations, Wannier–Mott excitons.

While illuminating the basic physics of the self-trapping, simplified single-particle descriptions have the drawback of not explicitly including valence band electrons, whose interactions and reorganization may substantially affect the outcomes. Numerous *ab initio* calculations have been dedicated to effects of electron-electron interactions on electron-lattice polarons in CPs. In this paper we have extended our first model *ab initio* study[15] intended to address these effects in the formation of 1D polarons due to the interaction with a surrounding polar solvent. As our study is performed within the framework of the PCM, it could also be thought of as a new avenue for applications of quantum-mechanical continuum solvation models.[17,18]

By studying and comparing various model systems based on long C_NH_2 oligomers with the polyynic structure, we have been able to successfully demonstrate the self-consistent formation of 1D large electron and hole polarons entirely due to solvation. Reorganization of valence band electrons and a more complex many-electron structure of the resulting polarons have been also explicitly illustrated. Full geometrical optimization of the underlying carbon lattice has shown that localized BLA patterns may act synergistically with the solvent reorganization to even further increase the degree of excess charge self-localization.

It should be reiterated that, while providing clear conceptual demonstrations and a seemingly appealing physical picture of solvation-induced self-localization, our current study is limited both in terms of its scope and direct quantitative applicability to real systems. Among other things, we have already discussed and illustrated a relatively strong dependence of the results on the level of *ab initio* theory used, a common feature of such computations.[26,27] DFT computations with hybrid exchange-correlation functionals may be "appropriate" engines for the problem at hand, but a more comprehensive comparative study is required before conclusions can be drawn. The PCM framework as used in this paper may overestimate the effects of solvation on self-localization as it does not take a proper account of the frequency dependence of the actual solvent dielectric functions.[4,5,8,11] This issue could possibly be analyzed within newly developed time-dependent PCM schemes.[45,46] As the computational demand for calculations of 1D large polarons, especially in application to more complex SC structures, may turn out to be excessive, one should also be looking for more efficient computational approaches such as, e.g., the scaling description of solvent effects.[47]

[1] Y. Lu, *Solitons and Polarons in Conducting Polymers* (World Scientific, Singapore, 1988).

[2] J. L. Brédas and G. B. Street, Acc. Chem. Res. **18**, 309 (1985).

[3] D. M. Basko and E. M. Conwell, Phys. Rev. Lett. **88**, 098102 (2002).

[4] Y. N. Gartstein, Phys. Lett. A **349**, 377 (2006).

[5] Y. N. Gartstein, T. D. Bustamante, and S. O. Castillo, J. Phys.: Condens. Matter **19**, 156210 (2007).

[6] Y. N. Gartstein and G. L. Ussery, Phys. Lett. A **372**, 5909 (2008).

[7] G. L. Ussery and Y. N. Gartstein, J. Chem. Phys. **130**, 014701 (2009).

[8] *Polarons and Excitons*, edited by C. G. Kuper and G. D. Whitfield (Plenum, New York, 1963).

[9] J. Appel, in *Solid State Physics*, edited by F. Seitz, D. Turnbull, and H. Ehrenreich (Academic, New York, 1968), Vol. 21, p. 193.

[10] *Polarons in Ionic Crystals and Polar Semiconductors*, edited by J. T. Devreese (North-Holland, Amsterdam, 1972).

[11] A. M. Kuznetsov, *Charge Transfer in Physics, Chemistry and Biology* (Gordon and Breach, Luxembourg, 1995).

[12] *Excess Electrons in Dielectric Media*, edited by C. Ferradini and J. P. Jay-Gerin (CRC, Boca Raton, FL, 1991).

[13] A. Nitzan, *Chemical Dynamics in Condensed Phases* (Oxford University Press, New York, 2006).

[14] E. M. Conwell and D. M. Basko, J. Phys. Chem. B **110**, 23603 (2006).

[15] M. L. Mayo and Y. N. Gartstein, Phys. Rev. B **78**, 073402 (2008).

[16] M. J. Frisch, G. W. Trucks, H. B. Schlegel *et al.*, GAUSSIAN 03, Revision D.01, Gaussian, Inc., Wallingford, CT, 2004.

[17] A. Leach, *Molecular Modelling: Principles and Applications* (Prentice-Hall, Englewood Cliffs, NJ, 2001).

[18] J. Tomasi, B. Mennucci, and R. Cammi, Chem. Rev. (Washington, D.C.) **105**, 2999 (2005).

[19] D. K. Campbell, A. R. Bishop, and K. Fesser, Phys. Rev. B **26**, 6862 (1982).

[20] T. Holstein, Ann. Phys. **8**, 325 (1959).

[21] A. Ye, Z. Shuai, O. Kwon, J. L. Brédas, and D. Beljonne, J. Chem. Phys. **121**, 5567 (2004).

[22] K. Meisel, H. Vocks, and P. Bobbert, Phys. Rev. B **71**, 205206 (2005).

[23] G. Moro, G. Scalmani, U. Cosentino, and D. Pitea, Synth. Met. **108**, 165 (2000).

[24] V. M. Geskin, A. Dkhissi, and J. L. Brédas, Int. J. Quantum Chem. **91**, 350 (2003).

[25] L. Zuppiroli, A. Bieber, D. Michoud, G. Galli, F. Gygi, M. N. Bussac, and J. J. André, Chem. Phys. Lett. **374**, 7 (2003).

[26] S. Yang and M. Kertesz, J. Phys. Chem. A **110**, 9771 (2006).

[27] S. Yang and M. Kertesz, J. Phys. Chem. A **112**, 146 (2008).

[28] R. M. Martin, *Electronic Structure* (Cambridge University Press, Cambridge, 2004).

[29] L. Hornŷ, N. D. K. Petraco, C. Pak, and F. H. Schaefer III, J. Am. Chem. Soc. **124**, 5861 (2002).

[30] L. Hornŷ, N. D. K. Petraco, and F. H. Schaefer III, J. Am. Chem. Soc. **124**, 14716 (2002).

[31] S. Szafert and J. A. Gladysz, Chem. Rev. (Washington, D.C.) **103**, 4175 (2003).

[32] S. Szafert and J. A. Gladysz, Chem. Rev. (Washington, D.C.) **106**, PR1 (2006).

[33] M. J. Rice, A. R. Bishop, and D. K. Campbell, Phys. Rev. Lett. **51**, 2136 (1983).

[34] M. J. Rice, S. R. Phillpot, A. R. Bishop, and D. K. Campbell, Phys. Rev. B **34**, 4139 (1986).

[35] A. Karpfen, J. Phys. C **12**, 3227 (1979).

[36] Q. Fan and G. V. Pfeiffer, Chem. Phys. Lett. **162**, 472 (1989).

[37] B. Mennucci and J. Tomasi, J. Chem. Phys. **106**, 5151 (1997).

[38] E. Cancès, B. Mennucci, and J. Tomasi, J. Chem. Phys. **107**, 3032 (1997).

[39] M. Cossi, V. Barone, B. Mennucci, and J. Tomasi, Chem. Phys. Lett. **286**, 253 (1998).

[40] M. Cossi, G. Scalmani, N. Rega, and V. Barone, J. Chem. Phys. **117**, 43 (2002).

[41] R. Dennington, T. Keith, and J. Millam, GAUSSVIEW, Version 4.1, Semichem, Inc., Shawnee Mission, KS, 2007.

[42] A. Szabo and N. S. Ostlund, *Modern Quantum Chemistry* (Dover, Mineola, NY, 1996).

[43] S. Jeyadev, Phys. Rev. B **28**, 3447 (1983).

[44] E. I. Rashba, Opt. Spektrosk. **2**, 75 (1957).

[45] M. Caricato, F. Ingrosso, B. Mennucci, and J. Tomasi, J. Chem. Phys. **122**, 154501 (2005).

[46] B. Mennucci, Theor. Chem. Acc. **116**, 31 (2006).

[47] C. S. Pomelli and J. Tomasi, J. Mol. Struct. **537**, 97 (2001).

CC: Inga Musselman (Co-PI)

May 11, 2009

To: **Ms. Dina Caplinger**
OSP at UT Dallas

From: DJ Yang (PI)
Chemistry Department at UT Dallas

SPRING REPORT: Novel Proton Conducting Membrane with Well Controlled Nano-morphology for PEM Fuel Cells

If you have any questions on the Report, please feel free to call me to 972-883-6681.

Sincerely,

May 11, 2009

SPRING PROGRESS REPORT:
Novel Proton Conducting Membranes for PEM Fuel Cells

Summary

We report that we have made promising lead in developing polymeric membranes operable as proton exchange membrane (PEM) to meet the DOE guidelines. The successful PEM must have good proton conductivity with mechanical, thermal, and chemical stability under fuel cell operation over a wide range of temperature (-20 to 120 °C) and relative humidity (25 to 100%) conditions. To meet these requirements, we have designed novel polymers with three different design concepts (see Strategies 1-3 as shown below). Since then, we have already prepared several polymers, and we now are in the process of optimizing these to fabricate into new proton exchange membranes.

At present, highest proton conductivity value is up to 0.07 S/cm at 80°C and 90% RH with the polymers made from the Strategy 1. The polymers showed good thermal stability even at 200 ^{o}C. Tests at various conditions with further optimization of the polymers are underway to find if the polymers can perform to meet with the DOE guideline of the conductivity > 0.1 S/cm at 120°C and ≤ 25% RH. Additionally, synthesized polymers from the Strategies 2 and 3 have also been characterized, and testing them under fuel cell conditions will be started soon.

Background

Nafion[®] is the current dominant material for PEM fuel cells and, typically, operates at low temperature (≤80°C) and high relative humidity (R.H.). However, it is unsuitable for operation at higher temperatures (≥120°C) and/or low R.H. conditions because of significant loss in proton conductivity due to dehydration, compromised mechanical strength due to its relatively low glass transition temperature (T_g) in the dry state (~110 ^{o}C), and even lower in the hydrated state,[1] and susceptibility to chemical degradation by peroxide-derived free radicals formed under FC operation. The present DOE's year 2010 guidelines for PEM applications include proton conductivity > 0.1 S/cm and durability for 2-5,000 hrs at 120°C / <25% RH,[2] and Nafion[®] fall short to these required properties.
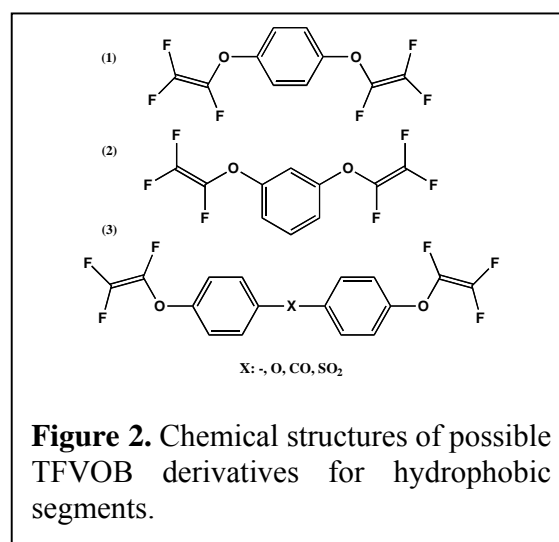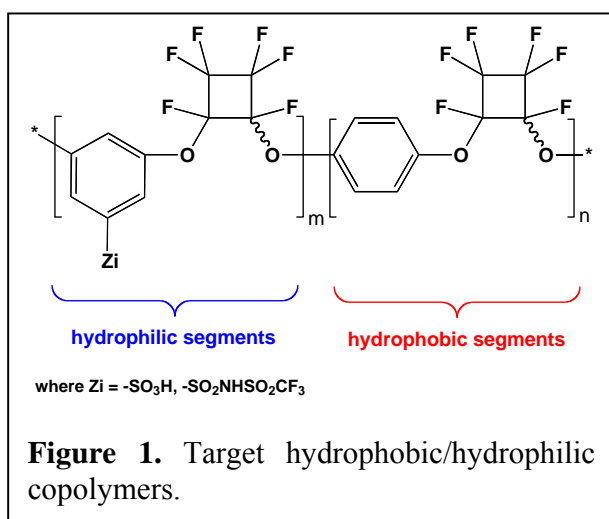
Our PEM designs involve the use of copolymers comprising hydrophobic and hydrophilic domains. The combination of the hydrophilic and hydrophobic segments will result in the incorporation of the desired aggregation of the rigid hydrophobic backbone for mechanical stability and minimal water swelling, and the high concentration of acidic functionalities for better proton conductivity. The use of backbones with glass transition temperatures (T_g) > 120 °C will also enhance membrane stability at high temperatures. The hydrophobic block will consist of perfluorocyclobutane (PFCB) aromatic ether linkages formed by thermal cyclization of trifluorovinyloxybenzene (TFVOB) groups without side products. The linear prepolymers or block segments can be casted into membranes from common organic solvents, and the resultant membranes can be further thermally treated to obtain high molecular weight copolymers or a 3-D cross-linked network. These highly processable PFCB polymers have been reported to be

thermally, mechanically and oxidatively robust with T_g's >200 °C.[3,4,5] This combination of properties makes them promising for the hydrophobic backbone in the proposed copolymers.

Hydrophilic side chains will contain highly acidic functionalities such as sulfonimides and sulfonic acids, thereby maximizing IECs (greater than 1 mmol/g) for the copolymers. The side chains will be flexible, facilitating aqueous micelle formation without disrupting the hydrophobic domains. (Per) fluorinated side chains will also be used to enhance the overall stability under fuel cell operating conditions.

Strategy 1: Copolymers with hydrophobic PFCB-based backbones and highly acidic side chains
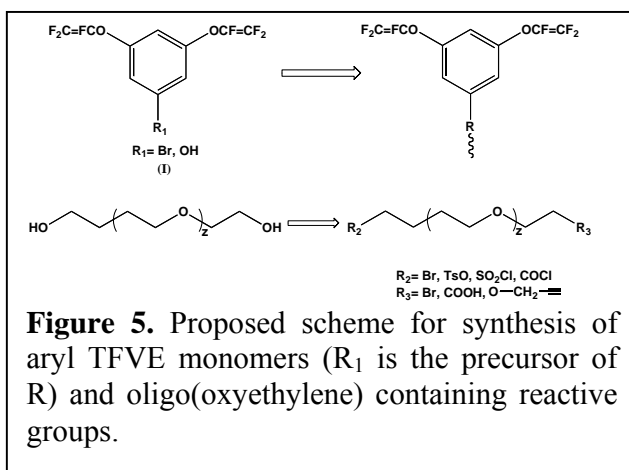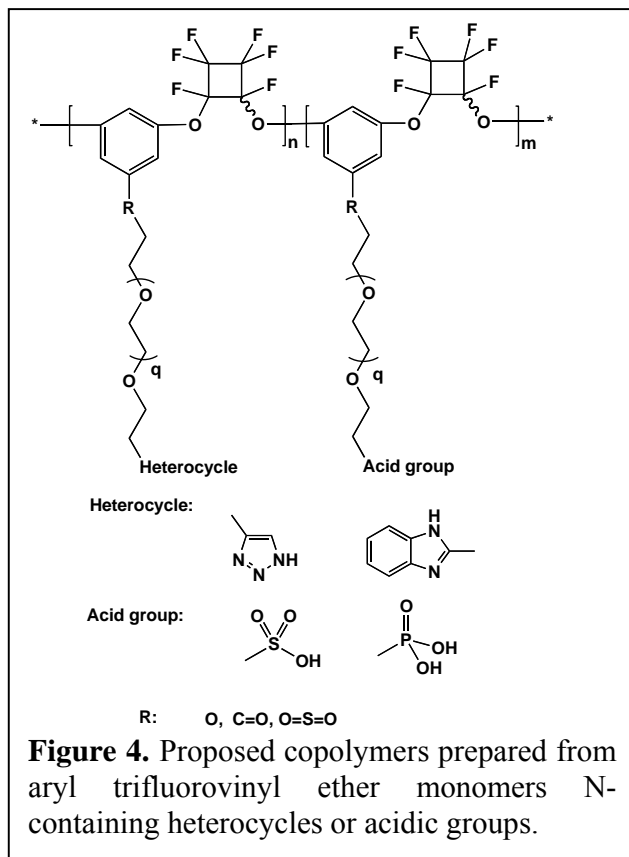
The general structure of the block copolymer, consisting of hydrophobic and hydrophilic segments, is shown in **Fig. 1**. The proposed hydrophobic rigid backbone was derived from the TFVO derivatives shown in **Fig. 2**.

Figure 1. Target hydrophobic/hydrophilic copolymers.

Figure 2. Chemical structures of possible TFVOB derivatives for hydrophobic segments.

The salt form of Z_1 in the perfluorinated side chain will be converted into the acid form by hydrolysis in aqueous acid after membrane fabrication, giving two proton sources for each side chain, which will lead to IEC values up to 2 mmol/g, a two-fold increase vs. Nafion®. The high density of the acid sites in the membrane will enhance the water uptake ability and, therefore, proton conductivity at high temperature and low humidity conditions.

For PFSA polymers such as Nafion®, and sulfonated polyarylenes, IEC increases are typically achieved at the expense of mechanical stability, resulting from polymer swelling. In contrast, our design, which utilizes both rigid hydrophobic backbones and highly acidic hydrophilic side chains, will allow increased values of IECs compared to Nafion® with minimal swelling.

Strategy 2: Copolymers with hydrophobic PFCB-based backbones and hydrophilic side chains containing N-heterocycles and acidic functional groups

Figure 4. Proposed copolymers prepared from aryl trifluorovinyl ether monomers N-containing heterocycles or acidic groups.

Figure 5. Proposed scheme for synthesis of aryl TFVE monomers (R_1 is the precursor of R) and oligo(oxyethylene) containing reactive groups.

Operation of a PEMFC under essentially water-free conditions involves a different mechanism for proton conduction (Grotthuss)[6,7,8] where protons hop from donor to acceptor sites without the transport of associated water molecules. A number of oligomeric and polymeric systems with covalently attached heterocycles have recently shown promise under essentially anhydrous conditions.[9-17] We have extended this concept to copolymers with PFCB-based backbones containing flexible side chains terminating in heterocycles, and acidic functionalities in the other, as shown in **Fig. 4**.

Tethering the functional groups on the side chains allows for high local mobility. We have initially explored polyether side chains of various lengths containing a number of heterocyclic and acid end groups to maximize the proton conductivity. The *meta* bis-1,3-trifluorovinyloxybenzene **(I)** in **Fig 5** contains a reactive functional group R_1 that is used to attach a side chain to the polymer backbone. The precursor of this side chain has two reactive functional groups (R_2 and R_3) (**Fig. 5**). One will be used to attach the side chain to the backbone, while the other will be used to attach either the heterocyclic or acid group. The reactive functional groups may be acyl chloride (COCl or SO_2Cl), halogen (Br or Cl), hydroxy (OH), carboxyl (COOH), or alkynyl (C≡C).

Strategy 3: Copolymers with hydrophobic perfluoro aromatic ether-based backbones and highly sulfonated group

We designed another structure of copolymer containing hydrophilic and hydrophobic domains for developing properties of polymer electrolyte membrane to meet the operation conditions as suggested in DOE guideline. We prepared the rigid-rod type polymer as biphenyl ether and phenyl sulfone. The polymer contains two side chains (Figure 6) that could induce the formation of liquid crystalline property. This property can form nanostructured proton conducting channels. We can also easily control the channel length by changing aliphatic chain length.
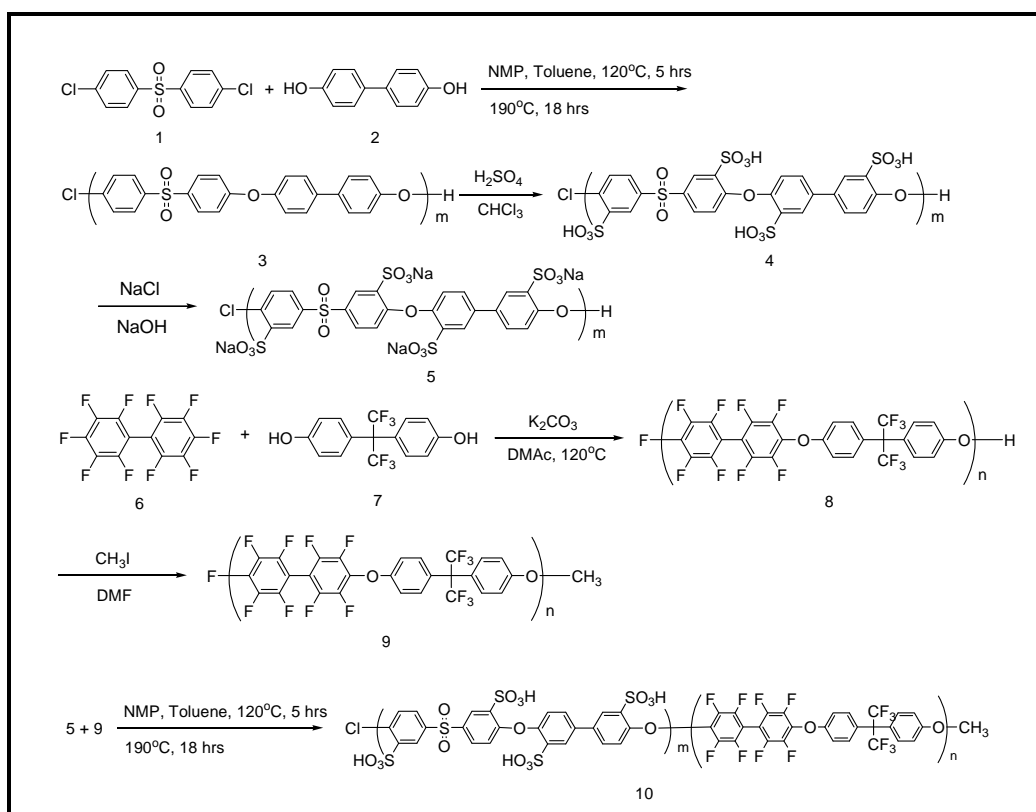

Figure 6. Synthetic route to copolymer

**Experimental Procedure: Results and Discussion**
<u>Progress on Strategy 1-3:</u>

Strategy 1: Copolymers with hydrophobic PFCB-based backbones and hydrophilic side chains containing pendant acidic functional groups

Polysulfone containing at least three sulfonimide acid groups

Using the chemistry derived from the functionalization of commercially-available polymer, Udel®'s polysulfone (PSU), the hydrophilic segments were prepared. Nonetheless, the PSU-based membrane was characterized and tested for proton conductivity.

Synthesis route and digital image of the PSU-based membrane
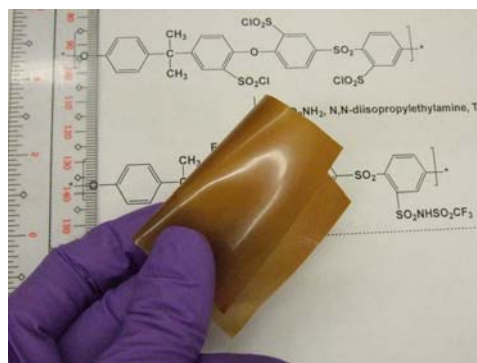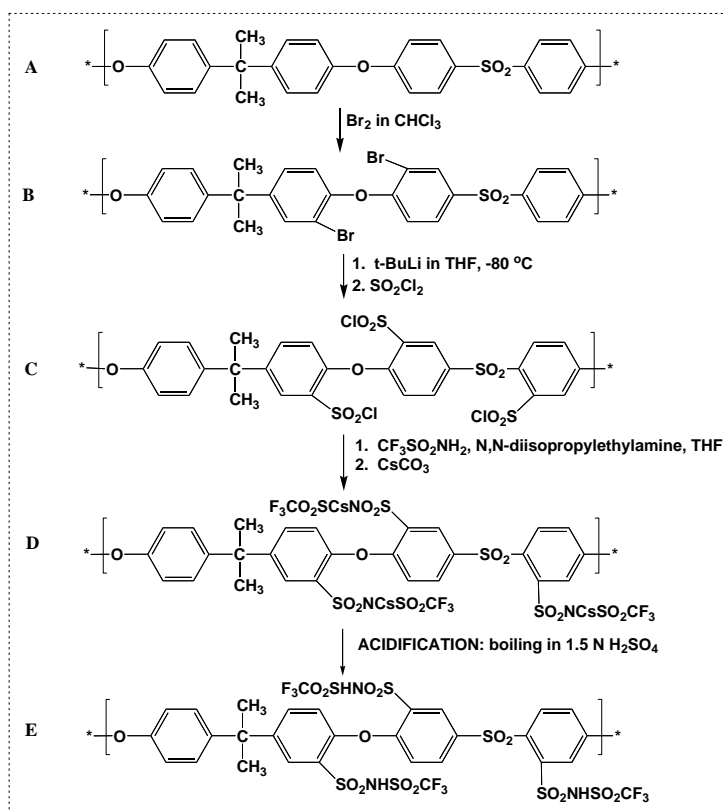
PSU membrane cast from DMSO

PSU membrane cast from THF

Figure 7. Synthetic route to PSU-functionalized PEM; Digital images of PSU-functionalized PEM

Thermal gravimetric analysis (TGA) of the PSU-based membrane shows that the membrane is stable up to 200 °C, even in the acidified form. The acidification process involves refluxing the membrane in 1.5 N H_2SO_4, washing with distilled water, and drying between sheets of task wipers at room temperature overnight.

Preliminary proton conductivity testing of the PSU-based polymer shows promising conductivities up to 0.07 S/cm at 80°C and 90% RH as shown below. Current investigation and optimization of the polymer synthesis is underway.
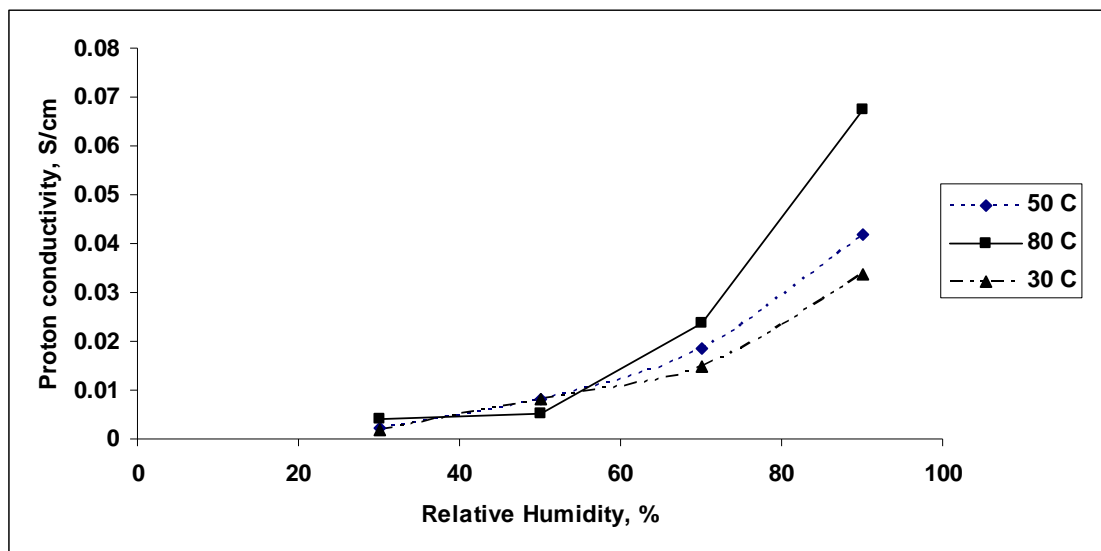
Figure 8. Proton conductivity measurements for PSU-functionalized PEM at various Temp and RH conditions

Perfluorocyclobutane (PFCB) polymers containing sulfonimide acid groups

In the synthesis of the PFCB polymers, two routes were used: pre-polymer functionalization and post-polymerization chemistry.

Via monomer functionalization prior to polymerization: This route was optimized to 5 steps, instead of the original planned route shown below.

Figure 9. General route for monomer functionalization prior to polymerization
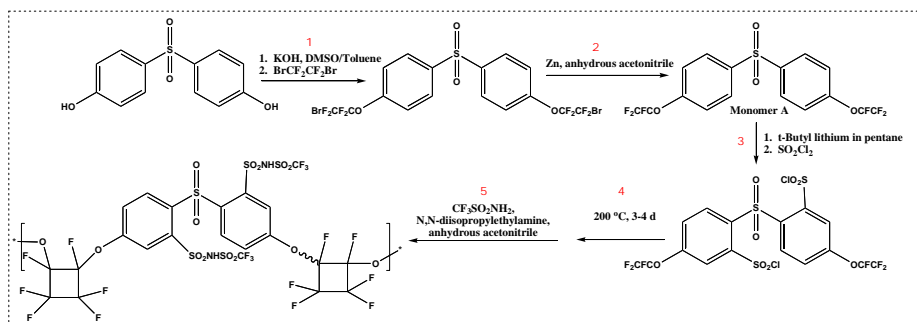
Figure 10. Optimized route for monomer functionalization prior to polymerization

The hydrophilic segment has been prepared, cast and is currently being tested and characterized by spectroscopy techniques, therm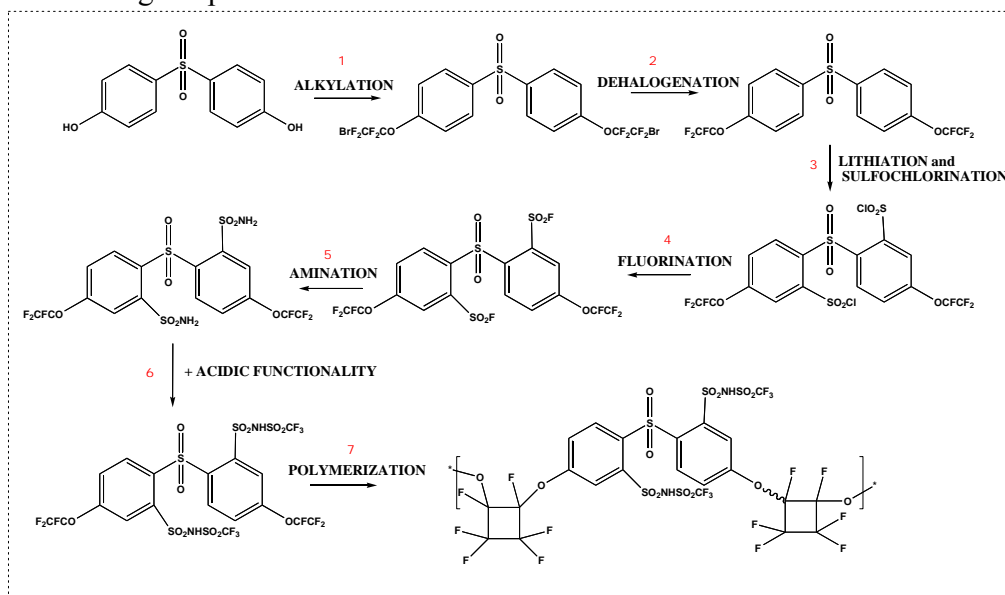al/chemical stability and proton conductivity testing. Future work includes combination of the said hydrophilic segment with the hydrophobic segments synthesized similarly (steps 1, 2 and 7 in Optimized Route) to form block copolymers and blends.

Via post-sulfonation of PFCB via lithiation: Another route is post-sulfonation on the PFCB polymer. Two hydrophilic segments have been by post-sulfonation, the sulfonyl biphenyl and the biphenyl PFCB. The following routes are presented.

Post-sulfonation of Polymer A

Figure 11. Post-sulfonation via lithiation procedures

Post-sulfonation of Polymer B

Figure 12. Post-sulfonation via chlorosulfonation

Both polymers have been functionalized and are currently being characterized and tested for fuel cell measurements and performance.

General Synthetic Procedure
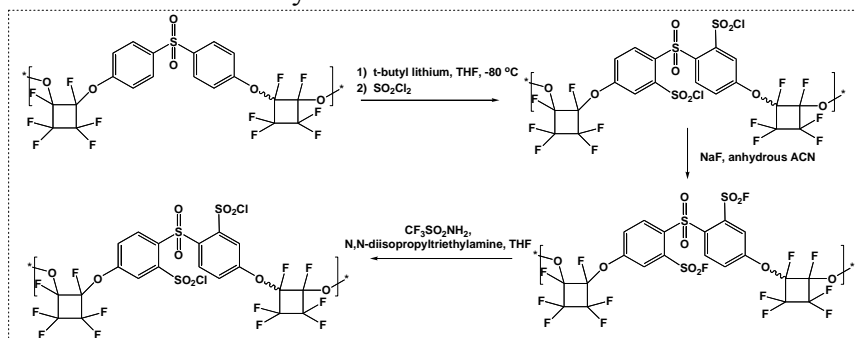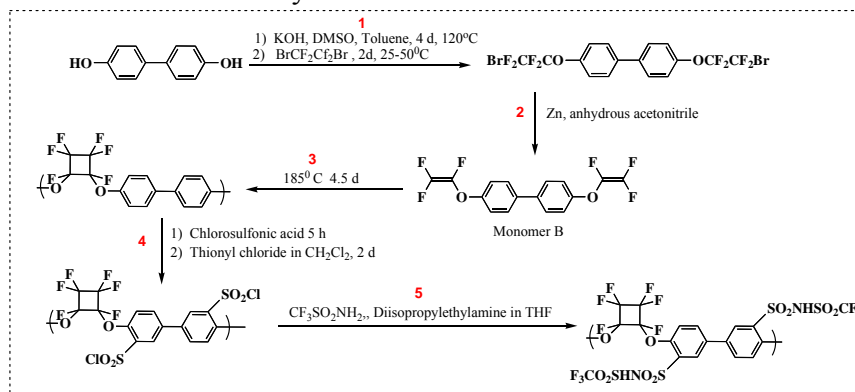
Trifluorovinyloxybenzene Monomer Preparation

Monomers A and B were synthesized based on an adapted published procedure. In a 500-mL 3-neck round bottom flask fitted with a Dean-Stark apparatus and reflux condenser, 25.00 g of phenolic starting material, 2.2 molar equivalents of KOH and 1:4 v/v ratio of dimethylsulfoxide and toluene were combined under N_2. The solution was boiled under reflux 120 ^{o}C for 3-4 d, or until no water is distilled out with toluene in the Dean-Stark apparatus arm. After the reflux, the remaining toluene was removed. The reaction mixture was allowed to cool down to room temperature, and further to 15-20 ^{o}C for the addition of the alkylation reagent, 1,2-dibromotetrafluoroethane ($BrCF_2CF_2Br$) under N_2. Three molar equivalents of $BrCF_2CF_2Br$ was added dropwise to the reaction mixture over at least 1.5 h at less than 20 ^{o}C. After the complete addition of the alkylating agent, the reaction mixture was stirred at room temperature for 12 h, and at 50 ^{o}C for 36 h. The reaction was stopped by adding 100 mL of water. After stirring for 15 min, the organic and aqueous layers were separated. The aqueous layer was extracted with dichloromethane three times (100 mL each). The combined organic layers were washed with water followed by a saturated brine solution. The resulting organic layer was dried using anhydrous Na_2SO_4. Purification of the crude product was performed using column chromatography with silica as the stationary phase, and ethyl acetate/hexane as solvent system.

The alkylated compounds were then dehalogenated using the following procedure: In a 250-mL round bottom flask, the alkylated compound, 8 molar equivalents of freshly activated Zn, and dry acetonitrile were added under N_2. The reaction mixture was boiled under reflux for 3-4 d. Acetonitrile was then removed by vacuum distillation, leaving the crude product, salts and Zn. The crude product was extracted using hexanes, and the other solids separated by filtration. The filtrate was concentrated, and the crude product purified using column chromatography on silica and ethyl acetate/hexane as solvent system to yield the monomer desired.

Polymerization

Three grams of the monomer was placed in a 25-mL round bottom flask. With the heating oil bath at >185 ^{o}C, the flask was immersed, ensuring melting of the polymer. The temperature was raised to the desired temperature, and maintained for 4-5 d. The resulting polymer was dissolved in chloroform, and precipitated out using methanol. A light brown polymer was obtained and dried under vacuum for 12 h at > 50 ^{o}C.

Strategy 2: Copolymers with hydrophobic PFCB-based backbones and hydrophilic side chains containing N-heterocycles and acidic functional groups

We have prepared a polymer consisting of six-carbon polyether side chains containing a number of heterocyclic (1, 2, 3-triazole) and acid (sulfonic and phosphonic acid) end groups. The *meta* bis-1, 3-trifluorovinyloxybenzene was used to attach the polyether side chain to the

polymer backbone. At this point, optimization for the synthetic routes is underway, and at the same time, a proton exchange membrane is ready to be cast and characterized by proton conductivity, ion-exchange determination (IEC), tensile strength, thermal and chemical stability.

Synthesis and characterization of comb-shaped perfluorocyclobutyl aromatic polyethers bearing adjustable phosphonated pendant chain

3
3a, n = 1
3b, n = 2
3c, n = 3

4
4a, n = 1
4b, n = 2
4c, n = 3

6
6a, n = 1
6b, n = 2
6c, n = 3

5
5a, n = 1
5b, n = 2
5c, n = 3

7
7a, n = 1
7b, n = 2
7c, n = 3

8
8a, n = 1
8b, n = 2
8c, n = 3
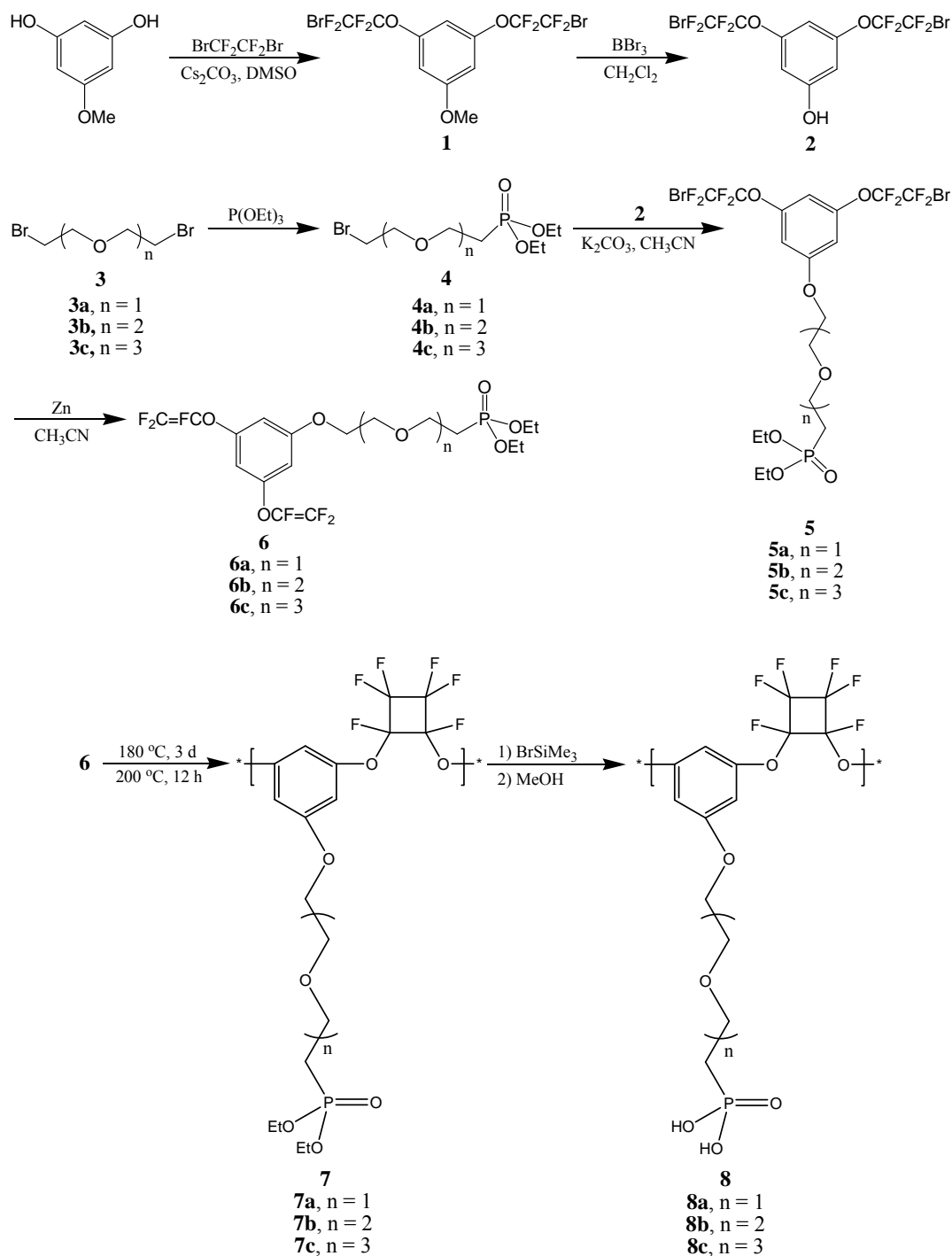
General procedure for synthesis of compound 5

A solution of **2** (4.84 g, 10 mmol), **4** (10 mmol) and K_2CO_3 (2.07 g, 15 mmol) in CH_3CN (30 mL) was stirred at reflux for 48 h. After solvent was removed, H_2O (100 mL) and EtOAc (20 mL) were added. The aqueous phase was separated and extracted with EtOAc (2 × 10 mL). The combined organic phases were washed with H_2O (2 × 10 mL), brine (2 × 10 mL), dried over anhydrous $MgSO_4$. After removal of the solvent, the residue was purified by silica column chromatography using hexane-acetone (1:1, v/v) to give a colorless oil (**5**).

Compound **5a**: 88% yield; ^1H NMR ($CDCl_3$, ppm) δ 6.69 (d, 3H), 3.95–4.12 (m, 6H), 3.68–3.83 (m, 12H), 1.96–2.22 (m, 2H), 1.24 (t, 6 H). ^{13}C NMR ($CDCl_3$, ppm) δ 160.5, 149.8, 115.2 (tt, 1C), 113.2 (tt, 1C), 107.6, 106.9, 70.6, 70.1, 69.2, 68.5, 61.7 (d, 1C), 28.7, 26.2, 16.3 (d, 1C). ^{19}F NMR ($CDCl_3$, ppm) δ − 67.9 (t, 1F), − 86.0 (t, 1F). ^{31}P NMR ($CDCl_3$, ppm) δ 26.4. IR (neat, cm^{-1}) 3098, 2983, 2879, 1605, 1457, 1324, 1102, 793. Compound **5b**: 86% yield; ^1H NMR ($CDCl_3$, ppm) δ 6.69 (d, 3H), 3.95–4.12 (m, 6H), 3.68–3.83 (m, 12H), 1.96–2.22 (m, 2H), 1.24 (t, 6 H). ^{13}C NMR ($CDCl_3$, ppm) δ 160.3, 149.7, 115.5 (tt, 1C), 113.5 (tt, 1C), 107.7, 107.1, 70.8, 70.2, 69.4, 68.3, 61.6 (d, 1C), 28.8, 26.0, 16.4 (d, 1C). ^{19}F NMR ($CDCl_3$, ppm) δ − 67.9 (t, 1F), − 86.0 (t, 1F). ^{31}P NMR ($CDCl_3$, ppm) δ 26.2. IR (neat, cm^{-1}) 3098, 2983, 2879, 1605, 1457, 1324, 1102, 793. Compound **5c**: 84% yield; ^1H NMR ($CDCl_3$, ppm) δ 6.69 (d, 3H), 3.95–4.12 (m, 6H), 3.68–3.83 (m, 12H), 1.96–2.22 (m, 2H), 1.24 (t, 6 H). ^{13}C NMR ($CDCl_3$, ppm) δ 160.1, 149.5, 115.4 (tt, 1C), 113.3 (tt, 1C), 107.4, 106.9, 70.7, 70.3, 69.2, 68.1, 61.4 (d, 1C), 28.7, 25.9, 16.2 (d, 1C). ^{19}F NMR ($CDCl_3$, ppm) δ − 67.9 (t, 1F), − 86.0 (t, 1F). ^{31}P NMR ($CDCl_3$, ppm) δ 26.3. IR (neat, cm^{-1}) 3098, 2983, 2879, 1605, 1457, 1324, 1102, 793.

1.1.5. General procedure for synthesis of compound 6

A solution of **5** (5 mmol) and Zn (0.975 g, 15 mmol) in CH_3CN (20 mL) was stirred at reflux for 48 h. After the solvent was removed, the residue was diluted with CH_2Cl_2 and filtered. The filtration was washed with H_2O (2 × 10 mL), brine (2 × 10 mL), dried over anhydrous $MgSO_4$. After removal of the solvent, the residue was purified by silica column chromatography using hexane-acetone (1:1, v/v) to give a colorless oil (**6**).

General procedure for synthesis of polymer 7

Compound **6** (2.69 g, 5 mmol) was added to a pre-dried 25 mL flask. After three cycles of freeze-pump-thaw, the flask was heated at 180 °C for 3 d and 200 °C for 12 h. After cooling to RT, the residue was dissolved in $CHCl_3$ (10 mL). The resulting solution was precipitated in hexane to give polymer **7**.

Polymer **7a**: 94 % yield; ^1H NMR (DMSO-d_6, ppm) δ 6.98 (s, 3H), 3.75–4.25 (d, 6H), 3.30–3.75 (d, 4H), 1.82–1.93 (m, 2H), 1.22 (s, 6 H). ^{13}C NMR (DMSO-d_6, ppm) δ 161.2, 156.7, 117.0, 115.0, 107.0 105.0, 99.0, 96.8, 70.7, 70.1, 69.4, 68.1, 65.2, 61.6 (d, 1C), 28.0, 26.0. ^{19}F NMR (DMSO-d_6, ppm) δ − 126.7, − 127.2, − 127.9, − 128.5, − 129.4, − 130.0, − 130.7, − 131.3, − 132.1. ^{31}P NMR (DMSO-d_6, ppm) δ 25.6. IR (KBr, cm^{-1}) 3098, 2877, 1604, 1482, 1271, 1158, 1031, 988, 961, 792.

Polymer **7b**: 95 % yield; ^1H NMR (DMSO-d_6, ppm) δ 6.98 (s, 3H), 3.75–4.25 (d, 6H), 3.30–3.75 (d, 8H), 1.82–1.93 (m, 2H), 1.22 (s, 6 H). ^{13}C NMR (DMSO-d_6, ppm) δ 161.2, 156.7, 117.0, 115.0, 107.0 105.0, 99.0, 96.8, 70.7, 70.1, 69.4, 68.1, 65.2, 61.6 (d, 1C), 28.0, 26.0. ^{19}F NMR (DMSO-d_6, ppm) δ − 126.7, − 127.2, − 127.9, − 128.5, − 129.4, − 130.0, − 130.7, − 131.3, −

132.1. ^{31}P NMR (DMSO-d_6, ppm) δ 25.4. IR (KBr, cm^{-1}) 3098, 2877, 1602, 1482, 1271, 1158, 1031, 988, 961, 792.

Polymer **7c**: 92 % yield; ^{1}H NMR (DMSO-d_6, ppm) δ 6.98 (s, 3H), 3.75–4.25 (d, 6H), 3.30–3.75 (d, 12H), 1.82–1.93 (m, 2H), 1.22 (s, 6 H). ^{13}C NMR (DMSO-d_6, ppm) δ 161.2, 156.7, 117.0, 115.0, 107.0 105.0, 99.0, 96.8, 70.7, 70.1, 69.4, 68.1, 65.2, 61.6 (d, 1C), 28.0, 26.0. ^{19}F NMR (DMSO-d_6, ppm) δ − 126.7, − 127.2, − 127.9, − 128.5, − 129.4, − 130.0, − 130.7, − 131.3, − 132.1. ^{31}P NMR (DMSO-d_6, ppm) δ 25.3. IR (KBr, cm^{-1}) 3098, 2877, 1606, 1482, 1271, 1158, 1031, 988, 961, 792.
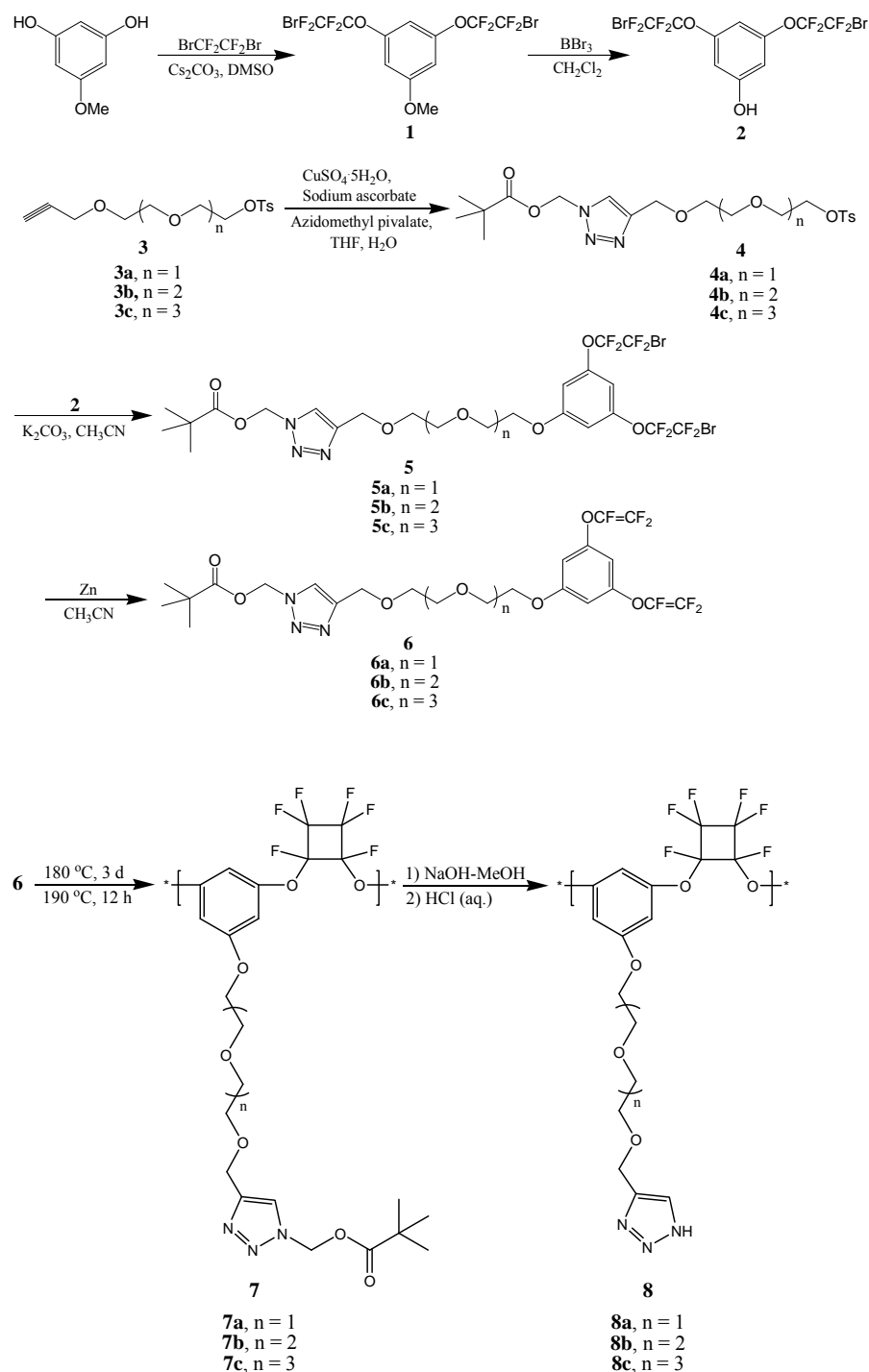
General procedure for synthesis of polymer 8

To a solution of polymer **7** (2 g) in CHCl$_3$ (50 mL) was added bromotrimethylsilane (10 mL). The resulting solution was stirred at RT for 12 h and 40 ^{o}C for 24 h. After removal of any volatile, the residue was dissolved in methanol (50 mL) and then stirred at RT for 12 h. The polymer was subsequently precipitated in 50 mL of water containing 5 vol % fuming hydrochloric acid. After filtration, the polymer was dried at 100 ^{o}C for 24 h.

Polymer **8a**: 89 % yield; ^{1}H NMR (DMSO-d_6, ppm) δ 6.98 (s, 3H), 4.01–4.26 (s, 2H), 3.26–3.78 (d, 4H), 1.82–1.93 (m, 2H). ^{13}C NMR (DMSO-d_6, ppm) δ 161.2, 156.7, 117.0, 115.0, 107.0 105.0, 99.0, 96.8, 70.7, 70.1, 69.4, 68.1, 61.6 (d, 1C), 28.0, 26.0. ^{19}F NMR (DMSO-d_6, ppm) δ − 126.7, − 127.2, − 127.9, − 128.5, − 129.4, − 130.0, − 130.7, − 131.3, − 132.1. ^{31}P NMR (DMSO-d_6, ppm) δ 25.7. IR (KBr, cm^{-1}) 3465, 3098, 2877, 1604, 1482, 1271, 1158, 1031, 988, 961, 792.

Polymer **8b**: 91 % yield; ^{1}H NMR (DMSO-d_6, ppm) δ 6.98 (s, 3H), 3.98–4.26 (s, 2H), 3.26–3.78 (d, 8H), 1.82–1.93 (m, 2H). ^{13}C NMR (DMSO-d_6, ppm) δ 161.2, 156.7, 117.0, 115.0, 107.0 105.0, 99.0, 96.8, 70.7, 70.1, 69.4, 68.1, 61.6 (d, 1C), 28.0, 26.0. ^{19}F NMR (DMSO-d_6, ppm) δ − 126.7, − 127.2, − 127.9, − 128.5, − 129.4, − 130.0, − 130.7, − 131.3, − 132.1. ^{31}P NMR (DMSO-d_6, ppm) δ 25.5. IR (KBr, cm^{-1}) 3465, 3098, 2877, 1604, 1482, 1271, 1158, 1031, 988, 961, 792.

Polymer **8c**: 87 % yield; ^{1}H NMR (DMSO-d_6, ppm) δ 6.98 (s, 3H), 3.96–4.26 (s, 2H), 3.26–3.78 (d, 12H), 1.82–1.93 (m, 2H). ^{13}C NMR (DMSO-d_6, ppm) δ 161.2, 156.7, 117.0, 115.0, 107.0 105.0, 99.0, 96.8, 70.7, 70.1, 69.4, 68.1, 61.6 (d, 1C), 28.0, 26.0. ^{19}F NMR (DMSO-d_6, ppm) δ − 126.7, − 127.2, −127.9, − 128.5, − 129.4, − 130.0, − 130.7, − 131.3, − 132.1. ^{31}P NMR (DMSO-d_6, ppm) δ 25.6. IR (KBr, cm^{-1}) 3465, 3098, 2877, 1604, 1482, 1271, 1158, 1031, 988, 961, 792.

Synthesis and Characterization of Perfluorocyclobutyl Aromatic Polyethers Bearing 1*H*,2,3-Triazole Rings on Oligo(ethylene oxide)s Chains

Scheme 4. Synthesis of polymer **7** and **8**.

General procedure for synthesis of compound 4

3 (10 mmol) and azidomethyl pivalate (1.57 g, 10 mmol) were suspended in THF-H_2O (20 mL, 1:1). To this mixture was added CuSO4·5H_2O (0.125 g, 0.5 mmol) and sodium ascorbate (0.594

g, 3 mmol). The mixture was stirred at room temperature for 48 h. The reaction mixture was diluted with H_2O (20 mL), and extracted with EtOAc (2 × 20 mL). The combined organic layers were washed with brine (2 × 10 mL), dried over anhydrous $MgSO_4$, filtered, and the solvent was removed under reduced pressure. The residue was purified by column chromatography (Hexane-EtOAc, 1:3) to give a colorless oil (**4**).

Compound **4a**: 96% yield; ^{1}H NMR ($CDCl_3$, ppm) δ 7.66 (s, 1H), 7.53 (d, 2H), 7.11 (d, 2H), 6.01 (s, 2H), 4.43 (s, 2H), 3.90 (t, 2H), 3.33-3.45 (m, 6 H), 2.19 (s, 3H), 0.93 (s, 9H). ^{13}C NMR (67 MHz, $CDCl_3$) δ 177.3, 145.3, 144.8, 132.8, 129.8, 127.8, 124.2, 70.5, 70.4, 70.3, 69.6, 69.4, 68.5, 64.2, 38.6, 26.7, 21.5. IR (neat, cm^{-1}) 3148, 2972, 2873, 1745, 1599, 1454, 1359, 1284, 1179, 1137, 1038, 923, 814, 775, 666.

Compound **4b**: 93% yield; ^{1}H NMR ($CDCl_3$, ppm) δ 7.67 (s, 1H), 7.53 (d, 2H), 7.11 (d, 2H), 6.01 (s, 2H), 4.43 (s, 2H), 3.90 (t, 2H), 3.33-3.45 (m, 10H), 2.19 (s, 3H), 0.93 (s, 9H). ^{13}C NMR (67 MHz, $CDCl_3$) δ 177.3, 145.3, 144.8, 132.8, 129.8, 127.8, 124.2, 70.5, 70.4, 70.3, 69.6, 69.4, 68.5, 64.2, 38.6, 26.7, 21.5. IR (neat, cm^{-1}) 3146, 2971, 2874, 1744, 1598, 1455, 1358, 1282, 1179, 1137, 1035, 921, 814, 772, 664.

Compound **4c**: 92% yield; ^{1}H NMR ($CDCl_3$, ppm) δ 7.65 (s, 1H), 7.53 (d, 2H), 7.11 (d, 2H), 6.01 (s, 2H), 4.43 (s, 2H), 3.90 (t, 2H), 3.33-3.45 (m, 14 H), 2.19 (s, 3H), 0.93 (s, 9H). ^{13}C NMR (67 MHz, $CDCl_3$) δ 177.3, 145.3, 144.8, 132.8, 129.8, 127.8, 124.2, 70.5, 70.4, 70.3, 69.6, 69.4, 68.5, 64.2, 38.6, 26.7, 21.5. IR (neat, cm^{-1}) 3144, 2971, 2870, 1743, 1598, 1455, 1357, 1282, 1176, 1134, 1038, 920, 816, 772, 663.

General procedure for synthesis of compound 5

A solution of **2** (4.84 g, 0.01 mol), **4** (0.01 mol) and K_2CO_3 (2.76 g, 0.02 mol) in CH_3CN (50 mL) was stirred at reflux for 48 h. After solvent was removed, the residue was partitioned in water and ethyl acetate. The organic layer was separated and the aqueous layer was extracted with ethyl acetate (2 × 10 mL). The combined organic layers were washed with H_2O and brine, dried over anhydrous sodium sulfate, and evaporated under reduced pressure. The residue was purified by column chromatography (Hexane-EtOAc, 2:7) to give a colorless oil (**5**).

Compound **5a**: 89% yield; ^{1}H NMR ($CDCl_3$, ppm) δ 7.78 (s, 1H), 6.72 (d, 3H), 6.07 (s, 2H), 4.65 (s, 2H), 4.08–4.15 (m, 2H), 3.76–3.85 (m, 2H), 3.64–3.68 (m, 8H), 1.13 (s, 9H). ^{13}C NMR (67 MHz, $CDCl_3$) δ 177.0, 160.4, 149.7, 147.3, 135.5, 115.8 (tt, 1C), 113.4 (tt, 1C), 107.7, 106.9, 74.0, 71.0, 70.7, 70.6, 70.0, 69.4, 68.3, 64.4, 38.9, 26.9. ^{19}F NMR ($CDCl_3$, ppm) δ − 67.9 (t, 1F), − 86.0 (t, 1F). IR (neat, cm^{-1}) 3105, 2980, 2875, 1745, 1609, 1473, 1325, 1277, 1105, 989, 925, 841, 801.

Compound **5b**: 86% yield; ^{1}H NMR ($CDCl_3$, ppm) δ 7.78 (s, 1H), 6.72 (d, 3H), 6.07 (s, 2H), 4.65 (s, 2H), 4.08–4.15 (m, 2H), 3.76–3.85 (m, 2H), 3.64–3.68 (m, 8H), 1.13 (s, 9H). ^{13}C NMR (67 MHz, $CDCl_3$) δ 177.0, 160.4, 149.7, 147.3, 135.5, 115.8 (tt, 1C), 113.4 (tt, 1C), 107.7, 106.9, 74.0, 71.0, 70.7, 70.6, 70.0, 69.4, 68.3, 64.4, 38.9, 26.9. ^{19}F NMR ($CDCl_3$, ppm) δ − 67.9 (t, 1F), − 86.0 (t, 1F). δ 21.3. IR (neat, cm^{-1}) 3103, 2965, 2877, 1746, 1610, 1462, 1325, 1286, 1103, 989, 925, 866, 794.

Compound **5c**: 87% yield; ^{1}H NMR ($CDCl_3$, ppm) δ 7.78 (s, 1H), 6.72 (d, 3H), 6.07 (s, 2H), 4.65 (s, 2H), 4.08–4.15 (m, 2H), 3.76–3.85 (m, 2H), 3.64–3.68 (m, 8H), 1.13 (s, 9H). ^{13}C NMR (67 MHz, $CDCl_3$) δ 177.0, 160.4, 149.7, 147.3, 135.5, 115.8 (tt, 1C), 113.4 (tt, 1C), 107.7, 106.9, 74.0, 71.0, 70.7, 70.6, 70.0, 69.4, 68.3, 64.4, 38.9, 26.9. ^{19}F NMR ($CDCl_3$, ppm) δ − 67.9 (t, 1F), − 86.0 (t, 1F). IR (neat, cm^{-1}) 3104, 2983, 2875, 1742, 1606, 1476, 1323, 1279, 1106, 988, 923, 842, 800.

General procedure for synthesis of compound 6

A solution of **5** (10 mmol) and Zn (1.95 g, 30 mmol) in CH_3CN (30 mL) was stirred at reflux for 48 h. After solvent was removed, the residue was diluted with ethyl acetate and filtered. The organic layer was washed with H_2O and brine, dried over anhydrous sodium sulfate, and evaporated under reduced pressure. The residue was purified by column chromatography (Hexane-EtOAc, 1:3) to give a colorless oil (**6**).

Compound **6a**: 77% yield; ^{1}H NMR (CDCl$_3$, ppm) δ 7.77 (s, 1H), 6.44 (d, 3H), 6.20 (s, 2H), 4.65 (s, 2H), 4.06–4.11 (m, 2H), 3.79–3.85 (m, 2H), 3.62–3.67 (m, 8H), 1.15 (s, 9H). ^{13}C NMR (67 MHz, CDCl$_3$) δ 177.0, 160.3, 156.7, 147.2, 146.5 (ddd, 1C), 135.5, 134.6 (tt, 1C), 99.1, 96.9, 74.0, 71.0, 70.7, 70.6, 70.0, 69.4, 68.3, 64.4, 38.9, 26.9. ^{19}F NMR (CDCl$_3$, ppm) δ − 119.0 (dd, 1F), − 125.7 (dd, 1F), − 134.6 (dd, 1F). IR (neat, cm^{-1}) 3145, 3098, 2983, 2878, 1834, 1746, 1607, 1474, 1278, 1107, 988, 840, 800.

Compound **6b**: 74% yield; ^{1}H NMR (CDCl$_3$, ppm) δ 7.77 (s, 1H), 6.42 (d, 3H), 6.21 (s, 2H), 4.64 (s, 2H), 4.06–4.11 (m, 2H), 3.79–3.85 (m, 2H), 3.62–3.67 (m, 8H), 1.15 (s, 9H). ^{13}C NMR (67 MHz, CDCl$_3$) δ 177.0, 160.3, 156.7, 147.2, 146.5 (ddd, 1C), 135.5, 134.6 (tt, 1C), 99.1, 96.9, 74.2, 70.9, 70.7, 70.6, 69.9, 69.5, 68.3, 64.5, 38.8, 26.8. ^{19}F NMR (CDCl$_3$, ppm) δ − 119.0 (dd, 1F), − 125.7 (dd, 1F), − 134.6 (dd, 1F). IR (neat, cm^{-1}) 3142, 3095, 2985, 2875, 1833, 1745, 1609, 1473, 1276, 1105, 989, 841, 801.

Compound **6c**: 72% yield; ^{1}H NMR (CDCl$_3$, ppm) δ 7.77 (s, 1H), 6.42 (d, 3H), 6.17 (s, 2H), 4.63 (s, 2H), 4.06–4.11 (m, 2H), 3.79–3.85 (m, 2H), 3.62–3.67 (m, 8H), 1.13 (s, 9H). ^{13}C NMR (67 MHz, CDCl$_3$) δ 177.0, 160.3, 156.7, 147.2, 146.5 (ddd, 1C), 135.5, 134.6 (tt, 1C), 99.1, 96.9, 70.9, 70.7, 70.6, 69.9, 69.5, 68.3, 64.5, 38.8, 26.8. ^{19}F NMR (CDCl$_3$, ppm) δ − 119.0 (dd, 1F), − 125.7 (dd, 1F), − 134.6 (dd, 1F). IR (neat, cm^{-1}) 3140, 3092, 2986, 2872, 1832, 1743, 1606, 1475, 1274, 1103, 987, 841, 802.

General procedure for synthesis of polymer 7

Compound 2 (0.345 g, 0.56 mmol) was added to a pre-dried 50 mL flask. The flask was pumped and filled back with nitrogen for 3 times. Then the reaction mixture was stirred at 170 ^{o}C for 16 h and 190 ^{o}C for 4 h. After cooling to RT, the residue was dissolved in CHCl$_3$ (10 mL). The resulting solution was precipitate in hexane to give polymer **7**.

Polymer **7a**: 95 % yield; ^{1}H NMR (CDCl$_3$, ppm) δ 7.66 (s, 1H), 6.58 (d, 3H), 6.20 (s, 2H), 4.62 (s, 2H), 4.03 (s, 2H), 3.56–3.86 (d, 6H), 1.13 (s, 9H). ^{13}C NMR (CDCl$_3$, ppm) δ 177.0, 160.3, 156.7, 147.2, 146.5 (ddd, 1C), 135.5, 134.6 (tt, 1C), 99.1, 96.9, 74.2, 70.9, 70.7, 70.6, 69.9, 69.5, 68.3, 64.5, 38.8, 26.8. ^{19}F NMR (CDCl$_3$, ppm) δ − 126.7, − 127.2, − 127.9, − 128.5, − 129.4, − 130.0, − 130.7, − 131.3, − 132.1. IR (KBr, cm^{-1}) 3114, 2973, 2885, 1744, 1608, 1468, 1306, 1207, 1126, 1018, 914, 841, 736.

Polymer **7b**: 93 % yield; ^{1}H NMR (CDCl$_3$, ppm) δ 7.67 (s, 1H), 6.58 (d, 3H), 6.20 (s, 2H), 4.63 (s, 2H), 4.05 (s, 2H), 3.52–3.91 (d, 10H), 1.14 (s, 9H). ^{13}C NMR (CDCl$_3$, ppm) δ 177.0, 160.7, 153.7, 147.3, 135.5, 102.3, 101.3, 74.0, 70.9, 70.7, 70.6, 70.0, 69.4, 68.1, 64.4, 38.9, 26.9. ^{19}F NMR (CDCl$_3$, ppm) δ − 126.6, − 127.1, − 127.8, − 128.4, − 129.3, − 130.0, − 130.6, − 131.3, − 132.1. IR (KBr, cm^{-1}) 2971, 2878, 1746, 1612, 1467, 1306, 1205, 1126, 1014.

Polymer **7c**: 92 % yield; ^{1}H NMR (CDCl$_3$, ppm) δ 7.67 (s, 1H), 6.55 (d, 3H), 6.19 (s, 2H), 4.60 (s, 2H), 4.03 (s, 2H), 3.54–3.89 (d, 14H), 1.14 (s, 9H). ^{13}C NMR (CDCl$_3$, ppm) δ 177.0, 160.3, 156.7, 147.2, 146.5 (ddd, 1C), 135.5, 134.6 (tt, 1C), 99.1, 96.9, 74.2, 70.9, 70.7, 70.6, 69.9, 69.5, 68.3, 64.5, 38.8, 26.8. ^{19}F NMR (CDCl$_3$, ppm) δ − 126.7, − 127.2, − 127.9, − 128.5, − 129.4, −

130.0, − 130.7, − 131.3, − 132.1. IR (KBr, cm^{-1}) 3110, 2968, 2878, 1743, 1606, 1465, 1306, 1202, 1123, 1016, 913, 840, 731.

General procedure for synthesis of polymer 8

The flask was cooled to room temperature. MeOH (4 mL) and 1 M NaOH (2 mL) were added. The resulting mixture was stirred at room temperature for 12 h and subsequently neutralized with 1 M HCL and diluted with H_2O (4 mL). The liquid was removed and the residue was washed with water, dried under vacuum overnight to give a brown solid (8).

Polymer **8a**: 86 % yield; ^{1}H NMR (DMSO-d$_6$, ppm) ^{1}H NMR (DMSO-d$_6$, ppm) δ 7.76 (s, 1H), 6.65 (d, 3H), 4.53 (s, 2H), 4.10 (s, 2H), 3.53–3.69 (m, 6H). ^{13}C NMR (DMSO-d$_6$, ppm) δ . ^{19}F NMR (DMSO-d$_6$, ppm) δ − 126.7, − 127.2, − 127.9, − 128.5, − 129.4, − 130.0, − 130.7, − 131.3, − 132.1. IR (KBr, cm^{-1}) 3414, 2885, 1618, 1468, 1306, 1213, 1126, 1008, 931, 841, 716.

Polymer **8b**: 88 % yield; ^{1}H NMR (DMSO-d$_6$, ppm) δ 7.70 (s, 1H), 6.61 (d, 3H), 4.48 (s, 2H), 3.38–4.15 (d, 12H). ^{13}C NMR (DMSO-d$_6$, ppm) δ 161.2, 153.5, 146.0, 134.7, 103.0, 100.0 76.2, 70.3, 70.1, 69.7, 69.5, 69.0, 63.7. ^{19}F NMR (DMSO-d$_6$, ppm) δ − 126.7, − 127.2, − 127.9, − 128.5, − 129.4, − 130.0, − 130.7, − 131.3, − 132.1. IR (KBr, cm^{-1}) 3423, 2880, 1612, 1465, 1306, 1205, 1128, 1013, 947.

Polymer **8c**: 82 % yield; ^{1}H NMR (DMSO-d$_6$, ppm) δ 7.75 (s, 1H), 6.66 (d, 3H), 4.52 (s, 2H), 4.08 (s, 2H), 3.51–3.71 (m, 14H). ^{13}C NMR (DMSO-d$_6$, ppm) δ . ^{19}F NMR (DMSO-d$_6$, ppm) δ − 126.7, − 127.2, − 127.9, − 128.5, − 129.4, − 130.0, − 130.7, − 131.3, − 132.1. IR (KBr, cm^{-1}) 3410, 2878, 1616, 1465, 1308, 1209, 1120, 1003, 930, 840, 711.

Synthesis of polymer 7 and 8

The preparation procedure of polymer **7** and **8** was shown in Scheme 2. Polymer **7** was prepared by the thermal [$2\pi + 2\pi$] cyclopolymerization of **6** in bulk. This polymerization process did not require catalysts or initiators and gave polymer **7** in excellent yield. The formation of polymer **7** was confirmed by ^{1}H, ^{13}C, ^{19}F NMR and FT-IR spectra.

Strategy 3: Copolymers with hydrophobic perfluoro aromatic ether-based backbones and highly sulfonated group

We have synthesized side chains for forming well-ordered nanostructure. The side chain without sodium sulfuric acid shows liquid crystalline property. Generally cyanobiphenol shows a nematic mesophase itself. Even if it has a flexible alkyl chain to hydroxyl group, it exhibits the same mesophase. According to these results, 6-bromohexanoxybiphenyl would show mesophase-like nematic phase. When cyanophenyl mesogen was attached to the polymer backbone like polyoxetane, the mesophase changed from nematic to smectic phase. The formation of smectic phase will improve the thermal stability of the mesophase rather than nematic phase so the stability of liquid crystalline polymer will be more stable in mesophase. We are expecting the sulfonated biphenyl moiety for having liquid crystalline property. We are ready to synthesize the sulfonamide groups on the polymer to check if there is liquid crystalline property.
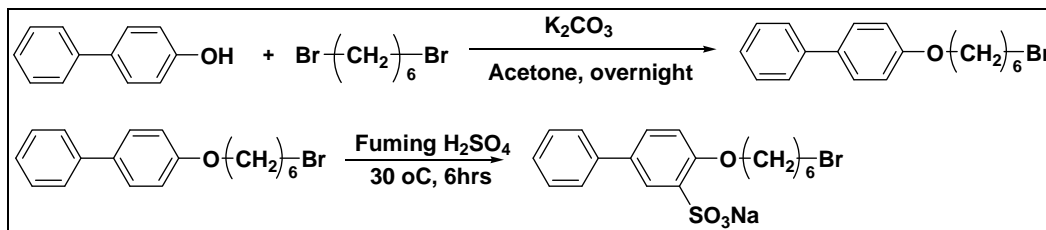
Current and Future Work

Fuel cell tests with the membranes prepared utilizing the three strategies will continue as membrane castings are done. Tests and characterization work (proton conductivity testing, thermo-gravimetric analysis, fuel cell performance, AFM, SEM, etc.) of the membranes prepared will also be undertaken. Further optimization work will also be included along with the tests to meet DOE guidelines.

References

1. Miyatake, K.; Watanabe, M. Emerging membrane materials for high temperature polymer electrolyte fuel cells: durable hydrocarbon ionomers. *J. Mater. Chem*. (**2006**) 16, 4465.
2. 2003 Basic Energy Sciences Advisory Committee Workshop. A Report from the Basic Energy Sciences Advisory Committee.
3. Smith, D.W.; Chem, S.; Kumar, S. M.; Ballato, J.; Topping, C.; Shah, H. V.; Foulger, S. H. Perfluorocyclobutyl copolymers for microphotonics. *Adv. Mat.* (**2002**) *14*(21) 1585-1589.
4. Smith, D.W. Jr.; Babb, D.; Shah, H.; Houeglund, A.; Traiphol, D. Perahia, H.; Boone, H.; Langhoff, C.; Radler, M. Perfluorocyclobutane (PFCB) polyaryl ethers: versatile coatings materials. *J. Fluorine Chem*. (**2000**) *104*, 109.
5. Traiphol, R.; Shah, H. V.; Smith, D.W. Jr.; Perahia, D. Bulk and interfacial studies of a new and versatile semifluorinated lyotropic liquid crystalline polymer. *Macromolecules* (**2001**) 34, 3954.
6. Susan, Md. A. B. H.; Noda, A.; Mitsushima, S.; Watanabe, M.; Bronsted acid-base ionic liquids and their use as new materials for anhydrous proton conductors. *Chemical Communications* (Cambridge, United Kingdom) (**2003**), *8*, 938-939.
7. Smith, D.W.; Chem, S.; Kumar, S. M.; Ballato, J.; Topping, C.; Shah, H. V.; Foulger, S. H. Perfluorocyclobutyl copolymers for microphotonics. *Adv. Mat.* (**2002**) *14*(21) 1585-1589.
8. Kreuer, K. D. Fast proton conductivity: A phenomenon between the solid and the liquid state? *Solid State Ionics*. (**1997**), *94*, 55–62.
9. Schuster M.; Meyer W. H.; Wegner G.; Herz H. G.; Ise M.; Schuster M.; Kreuer K. D. Maier J. Proton mobility in oligomer-bound proton solvents: imidazole immobilization via flexible spacers. *Solid State Ionics*. (**2001**), *145*, 85–92.
10. Herz H. G.; Kreuer K. D.; Maier J.; Scharfenberger G.; Schuster M. F. H.; Meyer W. H. New fully polymeric proton solvents with high proton mobility. *Electrochim. Acta*. (**2003**), *48*, 2165–71.
11. Schuster M. F. H.; Meyer W. H.; Schuster M.; Kreuer K. D. Towards a New Type of Anhydrous Organic Proton Conductor Based on Immobilized Imidazole. *Chem. Mater.* (**2004**)*, 16*, 329–37.

12. **(a)** Persson J. C.; Jannasch P. Self-Conducting Benzimidazole Oligomers for Proton Transport. *Chem. Mater. (***2003***)*, *15*, 3044–5. **(b)** Persson, J. C.; Jannasch, P. Intrinsically Proton-Conducting Benzimidazole Units Tethered to Polysiloxanes. *Macromolecules.* **(2005)**, *38,* 3283–9. **(c)** Persson J. C.; Josefsson, K.; Jannasch, P. *Polymer* **(2006)**, 47, 991–8. **(d)** Persson, J. C.; Jannasch, P. Block Copolymers Containing Intrinsically Proton-Conducting Blocks Tethered with Benzimidazole Units. *Chem. Mater.* **(2006),** *18,* 3096–102. **(e)** Persson J. C.; Jannasch, P. Intrinsically proton-conducting comb-like copolymers with benzimidazole tethered to the side chains. *Solid State Ionics.* **(2006)**, 177, 653–8.

13. Jeske1, M.; Soltmann1, C.; Ellenberg1, C.; Wilhelm1, M.; Koch1, D.; Grathwohl1, G.; Proton Conducting Membranes for the High Temperature-Polymer Electrolyte Membrane-Fuel Cell (HT-PEMFC) Based on Functionalized Polysiloxanes. *Fuel Cells.* **(2007)**, *1*, 40–6.

14. Woudenberg, R.C.; Yavuzcetin, O.; Tuominen, M.T.; Coughlin, E. B.; Intrinsically proton conducting polymers and copolymers containing benzimidazole moieties: Glass transition effects. *Solid State Ionics.* **(2007)**, *178*, 1135–41.

15. Surangkhana. M.; Woudenberg, R. C.; Granados-Focil, Yavuzcetin O.; Tuominen, M. T.; Coughlin, E. B.; Intrinsically conducting polymers and copolymers containing triazole moieties. *Solid State Ionics.* **(2007)**, *178*, 1398–403.

16. Siwen, L.; Zhen; Z.; Meilin, L.; Wen, L.;Heterocyclic monomers and related polymers and hybrid inorganic-organic polymer membranes. US Patent, **2006**.

17. **(a)** Babb, D. A.; Ezzel, R. B.; Clement, K. S.; Richey, W. F.; Kennedy, A. P. *J.;* Perfluorocyclobutane aromatic ether polymers. *Polym. Sci. Part A: Polym. Chem.* **(1993)**, *31*(13), 3465–77. **(b)** Kennedy A.P.; Babb, D. A.; Bremmer, J. N.; Pasztor Jr, A. J. *J.* Perfluorocyclobutane aromatic ether polymers. II. Thermal/ oxidative stability and decomposition of a thermoset polymer**.** *J. Polym. Sci. Part A: Polym. Chem.* **(1995)**, *33*(11), 1859–65. **(c)** Smith, Jr D.W.; Babb, D. A.; Shah, H.; Hoeglund, A.; Traiphol, R.; Perahia, D.; *J. Fluorine Chem.* **(2000)***, 104*(1), 109–17.